

Valorization of carbon dioxide for the production of value-added chemicals in fluidized bed and plasma-catalytic reactors

Presented by

Karla Jennifer Martin del Campo Rodriguez



Department of Chemical Engineering

McGill University

Montreal, Quebec, Canada

December 2020

A thesis submitted to McGill University in partial fulfillment of the requirements of the degree of Doctor of Philosophy

Supervisors:

Dr. Sylvain Coulombe

Dr. Jan Kopyscinski

© by Karla Jennifer Martin del Campo Rodriguez, 2021

Acknowledgements

I want to express my gratitude to my supervisors Dr. Sylvain Coulombe and Dr. Jan Kopyscinski. Thank you for your guidance, your trust and mentorship during this journey. The Ph.D. has been a steep learning curve professionally and personally. Thank you, “*big chief*” and “*chief*”, for giving me the opportunity to join the PPL and CPE groups and challenge me with this complex project.

I would like to thank the technical and administrative staff of the McGill Chemical Engineering Department. Thank you to Frank Caporuscio, Gerald Lepkyj and Luciano Cusmich for “*saving me*” so many times during the Ph.D., for helping me to find out solutions when nothing was clear. I would also like to thank Andrew Golsztajn and Ranjan Roy for helping me and teaching me to use the equipment in the analytical labs. Thank you also to Robert Tariello and Csaba Szalacsi for machining some essential pieces of my reactor and giving me ideas to improve the design. Thanks to Lisa Vopalto, Louise Miller-Aspin and Anna Pollock for their invaluable help in the administrative duties.

Thanks for the financial support of CONACYT-SENER, McGill Engineering Doctoral Award and the Eugenie Ulmer Lamothe Scholarship to complete my Ph.D. studies.

I would also like to thank the Trottier Institute for Sustainability in Engineering and Design (TISED) for giving me the opportunity to share my Ph.D. research with a broader audience through the SEDTalks! and providing me with the tools to make it more impactful. Thank you also to the Graphos team for the inspiring writing sessions.

I would also like to thank the past and current members of the CPE and PPL groups: Ali, Pakpong, Mohsen, Vishnu, Varun, Freya, Larissa, Adya, Katheryn, Robyn, Adna, Dante, Philip, Steven, and Simon. Thank you for being there and for the nice friendship that has developed with a lot of you. A big thanks to Mitch, who helped me build the reactor, and what started as a working relationship

developed into a great friendship. I also would like to thank Pablo for the moments shared in and out of the lab and sharing his expertise with me. A special thanks to Jose, Kanchan and Liz. Guys, my Ph.D. life would have been completely different without you. Thanks for your support in the most difficult moments, for the laughs, the stories, for giving me ideas even when our projects were not related at all, and for all your invaluable knowledge. Thank you also to my *Ph.D. girls*, Elmira and Elena. Girls, this journey with you has been amazing, with all the ups and downs, the friendship we have built and your support in good and bad times. I would also like to thank Marianna, who has become a good friend and also co-author. Thank you for all the help provided during my project.

I would like to thank my friends: Oscar Matus, Paulina, Mayra, Oscar Marin, Adrien, J.D., Norma, Charlie, Aldo, Tania, Cindy, Fanny, Evelyne, Mehdi, Mario A., Oscar A., Karla, Abraham, Joao, Zach, Daniel, Eva, Matheus, Zeyneb, Nathalie, Luiz and Angel. I have shared priceless moments with all of you. Thanks for being part of my life and for becoming part of my new family in Canada. A special thanks to Laura, Claudio and Mario F., who kept me going and inspired me to continue when I felt lost. Thanks for always being there, listening to me and making me laugh even in the worst situations. Thank you to my friends in Mexico, who were regularly checking on me. Especially Pamela, my oldest and best friend, for her support and messages every day.

A huge thanks to my family, my dad Sergio, my mom Norma and my brother Sergio. Being far from you has not been easy but knowing that you are always there encouraging me and supporting me provides me with the energy to keep going. Thank you for always believing in me. I would like to thank also Mrs. Mary, who passed away during my Ph.D. Losing her was a very hard hit, but knowing that she was always so proud of me inspired me to continue to make her even prouder.

To Christian, there are not enough words to say thank you. You are a fundamental part of my life. Thank you for all your love and support, for providing me ideas and guidance not only in the personal but also in professional life. Thank you for extending my family, with now my German family. Thank you for building a home with me and for all the moments we have shared. You are my rock, and you have always believed in me even when I didn't believe in myself. I love you, and I will always do. Together, there is nothing we cannot do.

Abstract

Climate change is one of the major challenges of our current era. The amount of greenhouse gas emissions produced by anthropogenic sources has steadily increased since the industrial revolution, in particular CO₂, which reached a maximum historical concentration of 409.8 ppm in 2019. In recent years, new technologies have been developed to valorize CO₂, which, when used as feedstock for chemical processes, reduces its environmental impact. Two of these technologies are CO₂ methanation and dry reforming of methane (DRM).

CO₂ methanation is the core of the Power-to-Gas process (P2G). P2G is a technology in which the surplus of power produced by renewable energy is converted into a grid compatible gas. However, the P2G process is limited by the intermittency of renewable electricity generation and thus hydrogen production. Hence, the methanation reactor should also be able to operate into a different range of feed flow rates while maintaining fluidized bed conditions. Therefore, the design of fluidized bed reactors for the catalytic CO₂ methanation is a crucial step. The first part of this thesis presents a graphical approach for the design and operation of bubbling fluidized bed reactors through a new type of working diagrams. These working diagrams show the interdependency of operating temperature, pressure, particle diameter, and fluidization characteristics. Moreover, a decision window to (a) determine the reactor diameter and (b) operate the fluidized bed reactor with a turndown ratio of 0.5 to 1.1 is visualized in the working diagrams. When the turndown ratio (i.e., inlet flow rate) is reduced, defluidization could occur. Thus, to maintain fluidization, an increase in temperature or pressure reduction are alternatives to keep good fluidization conditions. However, increasing temperature significantly reduces the CH₄ yield and so the efficiency of the process. A case study of an industrial CO₂ methanation reactor is presented. The results show that operating the reactor in a pressure range at a fixed and low temperature gives more flexibility to carry the reaction out with different catalyst particle sizes and turndown ratio. For example, a reactor that is designed to operate at 10 bar_{abs}, 340 °C with a total inlet flow rate of 5000 m³_N h⁻¹

($H_2/CO_2 = 4$), can operate at a turndown ratio of 0.3 ($1500 \text{ m}^3_{\text{N}} \text{ h}^{-1}$) at the same temperature and the same u_0/u_{mf} ratio by reducing the pressure to 3 bar_{abs}, with only a decrease of 2% in the CO_2 equilibrium conversion, saving the energy cost of the high pressure.

On the other hand, dry reforming of methane is a reaction that simultaneously converts CO_2 and CH_4 to produce syngas, a mix of hydrogen and carbon monoxide. However, the DRM reaction requires temperatures above $700 \text{ }^\circ\text{C}$ and an efficient catalyst to achieve good conversions ($>80\%$). Non-thermal plasma technologies can help the reaction by providing energy to the highly endothermic reaction and by decreasing its activation energy. In the second part of this thesis, a plasma configuration called rotating gliding arc (RGA) is investigated. In the RGA, tangential gas injection combined with a static magnetic field allows the rotation and upward displacement of the arc along the electrodes, forming a large plasma reaction volume. Different operating parameters such as peak current, total gas flow rate, CO_2/CH_4 ratio and gas inlet preheating were studied to determine the most efficient parameter combination based on conversion and yield. Higher CO_2 and CH_4 conversions, as well as H_2 and CO yields, were obtained when doubling the peak arc current. However, increasing the flow rate led to a decrease in CO_2 and CH_4 conversions. For instance, increasing the flow rate from 3.7 to 6.7 SLPM decreased the conversions of CO_2 and CH_4 by 1.7 and 3.7 times, respectively. No significant effect of the peak current or flow rate was found in the H_2/CO ratio. Moreover, the carbon deposition in the reactor decreased by increasing the CO_2 concentration in the inlet flow rate. No significant effect of the gas inlet temperature on the conversions or yields was found. Acetylene and ethylene were identified in trace amounts ($< 0.5\%$ mol) as byproducts of syngas generation. The low amount of byproducts obtained implies cleaner syngas when produced with RGA discharge.

By combining the RGA with other technologies such as catalysis, the DRM reaction can be even more favored. The addition of a catalyst to the plasma discharge can create the so-called “synergistic-effect” in which plasma and catalyst properties combine to improve the performance of the chemical reaction. In the RGA-spouted bed reactor developed in this thesis, the catalyst interacts directly with the plasma discharge. Different nickel-based catalysts were investigated in the plasma-catalytic reactor to determine the effect of these catalysts conditions on the DRM reaction. These catalysts included Ni supported in two different supports, with three different Ni loadings, fresh and pre-reduced catalyst, as well as catalyst pretreated with CH_4 under plasma

conditions. A noticeable increase in selectivity was obtained with a catalytic bed in the plasma zone, reducing acetylene production. For instance, CO selectivity increased by 9.9% when the pre-reduced 30 wt % Ni catalyst supported in SiO₂ was present in the plasma zone, compared to just the plasma reaction. Furthermore, carbon and coke deposition were strongly reduced in the reactor just by adding a catalyst. The results suggest that the reaction pathway for the plasma -catalytic DRM is different from the thermal-catalytic reaction. On the other hand, the catalyst characterization shows that the plasma introduces defects on the Ni catalyst, making it more electronegative, but without affecting its crystalline structure, suggesting that the change in the surface chemistry might affect the performance of the catalyst during the DRM reaction.

Résumé

Le changement climatique est l'un des défis majeurs de notre époque. La quantité d'émissions de gaz à effet de serre produites par des sources anthropiques n'a cessé d'augmenter depuis la révolution industrielle, en particulier le CO₂, qui a atteint une concentration historique maximale de 409.8 ppm en 2019. Ces dernières années, de nouvelles technologies ont été développées pour valoriser le CO₂, qui, lorsqu'il est utilisé comme matière première pour des processus chimiques, réduit son impact sur l'environnement. Deux de ces technologies sont la méthanisation du CO₂ et le reformage à sec du méthane (DRM).

La méthanisation du CO₂ est au cœur du procédé *Power-to-Gas* (P2G). Le P2G est une technologie dans laquelle le surplus d'électricité produit par les énergies renouvelables est converti en un gaz compatible avec le réseau. Cependant, le processus P2G est limité par l'intermittence de la production d'électricité renouvelable et donc de la production d'hydrogène. Par conséquent, le réacteur de méthanisation devrait également être capable de fonctionner dans une gamme différente de débits d'alimentation tout en maintenant des conditions de lit fluidisé. Pour cette raison, la conception de réacteurs à lit fluidisé pour la méthanisation catalytique du CO₂ est une étape cruciale. La première partie de cette thèse présente une approche graphique pour la conception et le fonctionnement des réacteurs à lit fluidisé bouillonnant à travers un nouveau type de diagrammes de travail. Ces diagrammes de travail montrent l'interdépendance de la température de fonctionnement, de la pression, du diamètre des particules et des caractéristiques de fluidisation. De plus, une fenêtre de décision permettant (a) de déterminer le diamètre du réacteur et (b) de faire fonctionner le réacteur à lit fluidisé avec une capacité opérationnelle de 0,5 à 1,1 est visualisée dans les diagrammes de travail. Lorsque la capacité opérationnelle (c'est-à-dire le débit d'entrée) est réduit, une défluidisation pourrait se produire. Ainsi, pour maintenir la fluidisation, une augmentation de la température ou une réduction de la pression sont des alternatives pour conserver de bonnes conditions de fluidisation. Cependant, une augmentation de la température

réduit considérablement le rendement en CH₄ et donc l'efficacité du processus. Une étude de cas d'un réacteur industriel de méthanisation du CO₂ est présentée. Les résultats montrent que le fonctionnement du réacteur dans une plage de pression à une température fixe et basse donne plus de flexibilité pour effectuer la réaction avec différentes tailles de particules de catalyseur et différentes capacités opérationnelles. Par exemple, un réacteur conçu pour fonctionner à 10 bar_{abs}, 340 °C, avec un débit total à l'entrée de 5000 m³_N h⁻¹ (H₂/CO₂ = 4), peut fonctionner avec une capacité opérationnelle de 0.3 (1500 m³_N h⁻¹) à la même température et avec le même ratio u_0/u_{mf} en réduisant la pression à 3 bar_{abs}, avec seulement une diminution de 2% de la conversion d'équilibre du CO₂, ce qui permet d'économiser le coût énergétique de la haute pression.

D'autre part, le reformage à sec du méthane est une réaction qui convertit simultanément le CO₂ et le CH₄ pour produire du gaz de synthèse, un mélange d'hydrogène et de monoxyde de carbone. Cependant, la réaction DRM nécessite des températures supérieures à 700 °C et un catalyseur efficace pour obtenir de bonnes conversions (>80 %). Les technologies à plasma non thermique peuvent aider la réaction en fournissant de l'énergie à la réaction hautement endothermique et en diminuant son énergie d'activation. Dans la deuxième partie de cette thèse, une configuration d'arc glissant rotatif (RGA) est étudiée. Dans le RGA, l'injection tangentielle de gaz combinée à un champ magnétique statique permet la rotation et le déplacement vers le haut de l'arc le long des électrodes, formant ainsi un grand volume de réaction. Différents paramètres de fonctionnement tels que le courant de crête, le débit total de gaz, le ratio du CO₂/CH₄ et le préchauffage de l'entrée de gaz ont été étudiés afin de déterminer la combinaison de paramètres la plus efficace en fonction de la conversion et du rendement. Des conversions de CO₂ et de CH₄ plus élevées, ainsi que des rendements en H₂ et CO, ont été obtenus en doublant le courant de crête. Cependant, l'augmentation du débit a entraîné une diminution des conversions de CO₂ et de CH₄. Par exemple, l'augmentation du débit de 3.7 à 6.7 SLPM a réduit les conversions de CO₂ et de CH₄ de 1.7 et 3.7 fois, respectivement. Aucun effet significatif du courant de crête ou du débit n'a été constaté dans le ratio H₂/CO. En outre, le dépôt de carbone dans le réacteur a diminué en augmentant la concentration de CO₂ dans le débit d'entrée. Aucun effet significatif de la température d'entrée du gaz sur les conversions ou les rendements n'a été constaté. L'acétylène et l'éthylène ont été identifiés à l'état de traces (< 0.5% mol) comme sous-produits de la production de gaz de synthèse. La faible quantité de sous-produits obtenue implique un gaz de synthèse plus propre lorsqu'il est produit avec une décharge de RGA.

En combinant le RGA avec d'autres technologies telles que la catalyse, la réaction DRM peut être encore plus favorisée. L'ajout d'un catalyseur à la décharge de plasma peut créer ce que l'on appelle un "effet synergique" dans lequel les propriétés du plasma et du catalyseur se combinent pour améliorer les performances de la réaction chimique. Dans le réacteur à lit fluidisé développé dans le cadre de cette thèse, le catalyseur interagit directement avec la décharge de plasma. Différents catalyseurs à base de nickel ont été étudiés dans le réacteur plasma-catalytique afin de déterminer l'effet des conditions de ces catalyseurs sur la réaction de DRM. Ces catalyseurs comprenaient du Ni supporté sur deux supports différents, avec trois charges de Ni différentes, un catalyseur frais et un catalyseur pré-réduit, ainsi qu'un catalyseur prétraité au CH₄ dans les conditions du plasma. Une augmentation notable de la sélectivité a été obtenue avec un lit catalytique dans la zone du plasma, réduisant la production d'acétylène. Par exemple, la sélectivité du CO a augmenté de 9,9 % lorsque le catalyseur pré-réduit à 30 % en poids de Ni supporté sur le SiO₂ était présent dans la zone du plasma, par rapport à la réaction uniquement avec le plasma. En outre, le dépôt de carbone et de coke a été fortement réduit dans le réacteur par le simple ajout d'un catalyseur. Les résultats suggèrent que la voie de réaction pour la réaction plasma-catalytique DRM est différente de la réaction thermo-catalytique. D'autre part, la caractérisation du catalyseur montre que le plasma introduit des défauts sur le catalyseur de Ni, le rendant plus électronégatif, mais sans affecter sa structure cristalline, ce qui suggère que le changement de la chimie de surface pourrait affecter la performance du catalyseur pendant la réaction DRM.

Table of Contents

1	Introduction	1
1.1	Motivation	1
1.2	Objectives	4
1.3	Thesis structure	5
2	Theoretical Background	6
2.1	CO ₂ valorization	6
2.2	CO ₂ methanation	8
2.2.1	Bubbling Fluidized Bed Reactors	10
2.3	Dry Reforming of Methane	13
2.3.1	Catalysis reforming	15
2.3.2	Plasma reforming	16
2.3.3	Plasma-catalysis	20
3	Methodology	24
3.1	Experimental Setup	24
3.2	Power Supply	28
3.2.1	Electrical Measurements	30
3.3	Instrumentation	31
3.3.1	Mass Spectrometry	31
3.3.2	Gas Chromatography	32
3.3.3	Optical Emission Spectroscopy	33
3.4	Fluidization Tests	33
3.5	Catalyst Preparation	34

3.6	Catalyst Characterization	36
3.6.1	Inductively Coupled Plasma-Optical Emission Spectroscopy.....	36
3.6.2	Adsorption/desorption measurements.....	37
3.6.3	Temperature Programmed Reduction	37
3.6.4	Activity Test.....	38
3.6.5	Temperature Programmed Oxidation	39

4 CO₂ methanation: A graphic approach for the design of Bubbling

Fluidized Bed reactors40

4.1	Preface.....	40
4.2	Introduction	43
4.3	Methodology	45
4.4	Results and Discussion.....	48
4.4.1	Equilibrium composition	48
4.5	Bed diameter	49
4.5.1	Temperature effect	49
4.5.2	Pressure effect.....	54
4.6	Turndown ratio.....	56
4.6.1	Temperature effect	56
4.6.2	Pressure effect.....	57
4.7	Conclusions	59

5 Plasma Assisted Dry Reforming of Methane62

5.1	Preface.....	62
5.2	Introduction	65
5.3	Experimental	67
5.4	Results and discussion.....	72
5.4.1	Thermodynamic Analysis	72
5.4.2	Conversion and Yield	74
5.4.3	Effect of inlet gas temperature.....	83
5.4.4	Energy	86
5.4.5	Qualitative Analysis of the Optical Emission Spectrum.....	90

5.4.6	Morphology of the deposited particulates.....	91
5.5	Conclusions	94
5.6	Supplementary material.....	96
6	Plasma-Driven Catalytic Dry Reforming of Methane.....	98
6.1	Preface.....	98
6.2	Introduction	101
6.3	Experimental	103
6.3.1	Catalyst synthesis.....	103
6.3.2	Catalyst characterization.....	103
6.3.3	Thermo-catalytic activity	104
6.3.4	Plasma-catalytic activity	105
6.4	Results and discussion.....	107
6.4.1	Activity measurements.....	107
6.5	Conclusions	126
6.6	Supplementary material.....	128
7	Conclusions and Future work.....	141
7.1	Summary and main findings	141
7.2	Contributions to knowledge	145
7.3	Future work	147
	Nomenclature.....	149
	References.....	154

List of Figures

Fig. 1-1 Flow diagram of the Power-to-Gas process. Adapted from [11].	2
Fig. 1-2 Flow diagram of DRM carried out using plasma generated using renewable energies. Adapted from [12].	3
Fig. 2-1 Roadmap of CO ₂ valorization technologies. The symbols are defined as ○ direct use, ◇ production of chemicals/fuels, □ mineralization, and △ biological utilization. Adapted from [15].	7
Fig. 2-2 Combination of DRM and methanation process in a closed-loop for TCHP. Adapted from [21].	8
Fig. 2-3 Equilibrium composition of CO ₂ methanation as a function of (a) temperature, 200 to 500 °C at 1 bar, and (b) pressure, 1 to 20 bar at 350 °C for H ₂ /CO ₂ = 4.	9
Fig. 2-4 Geldart classification of particles in BFB. Taken from [31].	12
Fig. 2-5 Equilibrium composition of DRM as a function of temperature, 20 to 1000 °C at 1 bar for CO ₂ /CH ₄ = 1.	13
Fig. 2-6 Phases of gliding arc evolution: (A) gas break-down ;(B) quasi-equilibrium stage; (C) non-equilibrium stage. Adapted from [75].	19
Fig. 2-7 Interaction between plasma and catalysis. Adapted from [36].	23
Fig. 3-1 (a) Photograph of the RGA setup. (b) Infrared photograph of the RGA reactor during DRM reaction. Taken with Cat S61 FLIR camera.	24

Fig. 3-2 Technical drawings of (a) the conical electrode, (b) Delrin TM plate, and (c) ceramic base. (d) Digital photograph of the assembly. An extra ceramic piece (cylinder) was added for the plasma-catalytic experiments to the setup.	26
Fig. 3-3 Gas injector assembly (a) technical drawing and (b) digital photograph.....	27
Fig. 3-4 Gas heater wrapped with heating tape (a) before being covered with insulation, (b) after being insulated to avoid heat losses. (c) Nylon tubing for gas injectors, (d) Cooper tubing for gas injectors for the high-temperature experiment.....	28
Fig. 3-5 Detailed schematic of the base assembly.	28
Fig. 3-6 (a) Photograph of the igniter circuit. (b) Electrical circuit of the homemade power supply. On top, the CWM and on the bottom the current driver power supply. Adapted from [96].	30
Fig. 3-7 Acrylic reactor (a) technical drawing and (b) digital photography of the reactor with catalyst support inside.....	34
Fig. 3-8 Scheme of catalyst preparation procedure with incipient wetness impregnation method.	36
Fig. 3-9 Schematic of the fix bed reactor (FBR). Taken from [11].	39
Fig. 4-1 Equilibrium composition of CO ₂ methanation based on (A, B) the molar flow rate and (C, D) the volumetric flow rate as a function of (A, C) temperature at 1 bara and (B, D) pressure at 350 °C. Total inlet flow rate: 5000 m _N ³ h ⁻¹ (220 kmol h ⁻¹) with H ₂ /CO ₂ = 4/1. Blue shaded parts represent volume contraction. Normal inlet refers to the inlet at standard conditions (273 K and 1 bara), whereas inlet refers to the volumetric flow rate at operating conditions.....	49
Fig. 4-2 Bed diameter as a function of temperature (300-500 °C) at 3 bara for a laboratory-scale reactor. Total inlet flow rate 0.5 m _N ³ h ⁻¹ , H ₂ /CO ₂ = 4/1. Blue shaded area represents the zone between 6· <i>u_{mf}</i> (bold black line) and 12· <i>u_{mf}</i> (blue line) for a particle size of 250 μm (decision window). Dashed lines (<i>u_t</i>).	50

Fig. 4-3 Bed diameter as a function of temperature at (A) 3 bara and (B) 10 bara for different particle diameters (150, 250, and 500 μm) for an industrial-scale reactor. Total flow rate of 5000 $\text{m}_\text{N}^3 \text{h}^{-1}$ with $\text{H}_2/\text{CO}_2 = 4/1$ ($6 \cdot u_{mf}$ (bold lines), $12 \cdot u_{mf}$ (blue lines), u_t (dashed lines))..... 53

Fig. 4-4 Bed diameter as a function of pressure at 340 °C for different particle diameters (150, 250, and 500 μm) for an industrial-scale reactor. Total flow rate of 5000 $\text{m}_\text{N}^3 \text{h}^{-1}$ with $\text{H}_2/\text{CO}_2 = 4/1$ ($6 \cdot u_{mf}$ (solid lines), $12 \cdot u_{mf}$ (blue line), u_t (dashed lines)). 54

Fig. 4-5 Energy output in MW_{CH_4} as a function of temperature for different operating pressures (1, 3, 10, and 20 bar). Total inlet flow rate of 5000 $\text{m}_\text{N}^3 \text{h}^{-1}$ and $\text{H}_2/\text{CO}_2 = 4/1$ 55

Fig. 4-6 Energy output in MW_{CH_4} as a function of temperature for different operating pressures (1, 3, 10, and 20 bar). Total inlet flow rate of 5000 $\text{m}_\text{N}^3 \text{h}^{-1}$ and $\text{H}_2/\text{CO}_2 = 4/1$ 56

Fig. 4-7 Capacity as a function of pressure assuming volume contraction at 340 °C for different particle diameters (150, 250, and 500 μm) and empty tube reactor diameter of 1.06 m for an industrial-scale reactor. Total flow rate with $\text{H}_2/\text{CO}_2 = 4/1$ ($6 \cdot u_{mf}$ (solid lines), $12 \cdot u_{mf}$ (blue line), u_t (dashed lines)). 58

Fig. 5-1 RGA setup. (a) Photograph of the RGA reactor. (b) Schematics of the RGA setup and (c) six tangential gas injectors configuration (top view). 68

Fig. 5-2 Characteristic RGA discharge voltage, current and instantaneous power signals for DRM reaction at $\text{CO}_2/\text{CH}_4 = 1.0$, 3.7 SLPM, and peak arc current of 1.50 A 69

Fig. 5-3 Equilibrium composition of DRM as a function of temperature for $\text{CO}_2/\text{CH}_4 = 1.0$, 1.5, and 2.0 at 1 bar. Note the absolute composition of Ar (in mol) is constant throughout the whole temperature range. Hence, Ar is not reported in the graphs. 74

Fig. 5-4 (a) Average conversions of CO_2 and CH_4 and (b) average yields of H_2 and CO as a function of total gas flow rate for peak arc currents of 0.74 and 1.50 A. Dashed lines are used only for guidance. Note that the error bars are smaller than the symbol..... 76

Fig. 5-5 Temporal evolution of H₂ yields at peak currents of (a) 0.74 and (b) 1.50 A, for CO₂/CH₄ = 1.0 and total flow rates of 3.7, 4.7, 6.7 SLPM. Dashed lines are used only for guidance. 78

Fig. 5-6 Influence of the CO₂/CH₄ ratio on the H₂/CO ratio, the symbols represent the average values. Dashed lines are used only for guidance. 79

Fig. 5-7 Yield of acetylene concentration for DRM for CO₂/ CH₄ ratios of 1.0, 1.5 and 2.0, total gas flow rates of 3.7, 4.7 and 6.7 SLPM, and peak current of 1.50 A..... 81

Fig. 5-8 (a) Conversion of CO₂ and CH₄, and yield of H₂ and CO and (b) temperature profile as a function of time of the DRM at a total flow rate of 3.7 SLPM, CO₂/CH₄=1.5 and peak current of 1.50 A..... 83

Fig. 5-9 (a) CO₂ conversion, (b) CH₄ conversion, (c) CO yield and (d) H₂ yield as a function of time for not preheated (open symbols) and preheated (full symbols) gas at a total flow rate of 3.7 SLPM, CO₂/CH₄=1.5, and peak current of 1.50 A. The error bars represent the standard error of the mean. Dashed lines are used only for guidance..... 84

Fig. 5-10 Gas temperature of the inlet (T₁) and inside the reactor (T₀) versus time for 3 DRM periods separated by two periods of electrode regeneration. Total flow rate of 3.7 SLPM during DRM and 3.26 SLPM during electrode regeneration, CO₂/CH₄=1.5, peak current of 1.50 A..... 85

Fig. 5-11 Temporal evolution of the accumulated energy deposited for DRM for CO₂/CH₄ ratios of 1.0, 1.5 and 2.0 at a total flow rate of 3.7 SLPM and peak current of 1.50 A..... 86

Fig. 5-12 Power provided to the RGA (a, b), specific energy input (SEI) (c, d) and energy efficiency (η) (e, f) for DRM with CO₂/CH₄ ratios of 1.0, 1.5 and 2.0, total gas flow rate of 3.7, 4.7 and 6.7 SLPM, and peak currents of 0.74 and 1.50 A..... 88

Fig. 5-13 Emission spectra observed in the RGA for DRM at CO₂/CH₄ = 1.5, a total flow rate of 3.7 SLPM and peak currents of 0.74 (less intense) and 1.50 A (more intense)..... 91

Fig. 5-14 Left: (a) stainless steel cathode covered with black carbon, a by-product of DRM, (b) stainless steel particle found in the black carbon, as a result of electrode erosion, (c) black

carbon. On the right: (d) top view of the stainless steel anode with some black carbon powder, (e) black carbon and stainless steel particles, (f) carbon structure. 93

Fig. 5-15 (a) Stainless steel particle from the anode covered by a carbon-containing structure, (b) EDS spectrum of the stainless steel particle. The cross in (a) shows the exact location where the EDS analysis was carried out. 93

Fig. 5-16 Raman spectrum of one carbon sample produced during the DRM reaction by the RGA discharge after approx. 20 h. 94

Fig. 5-17 A Kinetics plot of the power law for a total inlet flow rate of 3.7SLPM and peak current of 1.5 A. 96

Fig. 6-1 Average conversions of (a) CO₂ and (b) CH₄. Average selectivities of (c) CO and (d) H₂ under catalytic conditions at 700 °C and 1 bar_{abs} with different Ni-based catalysts at GHSV = 148 L_N g_{cat}⁻¹ h⁻¹. 109

Fig. 6-2 Characteristic RGA discharge voltage, current and instantaneous power signals for plasma-catalytic DRM reaction at CO₂/CH₄ = 1.5, with a total flow rate of 3.7 L_N min⁻¹ over NiO/Al₂O₃ catalyst. 110

Fig. 6-3 Average conversions of (a) CO₂ and (b) CH₄. Average selectivities of (c) CO and (d) H₂ under plasma and plasma-catalytic conditions for different Ni/Al₂O₃ catalysts at GHSV = 148 L_N g_{cat}⁻¹ h⁻¹. Note: P = reduced – passivated, CH₄ = plasma pretreated with methane. 112

Fig. 6-4 Average conversions of (a) CO₂ and (b) CH₄. Average selectivities of (c) CO and (d) H₂ under plasma and plasma-catalytic conditions for different Ni/SiO₂ catalysts at GHSV = 180 L_N g_{cat}⁻¹ h⁻¹. Note: P = reduced – passivated, CH₄ = plasma pretreated with methane. 113

Fig. 6-5 H₂/CO ratio for different catalysts under (a) thermal catalysis and (b) plasma-catalytic conditions for Al₂O₃ and SiO₂ based Ni catalysts. 114

Fig. 6-6 Stainless steel cathode after DRM reaction under (a) plasma-only and (b) plasma-catalytic conditions.....	115
Fig. 6-7 (a) Normalized weight change and (b) CO ₂ evolution during temperature-programmed oxidation (TPO) of the spent Ni-catalysts. Note: P = reduced + passivated, CH ₄ = plasma pretreatment with CH ₄	119
Fig. 6-8 SEM pictures and EDS spectra for 30NiO/Al ₂ O ₃ for (a, b) fresh and (c, d) spent catalyst (after plasma).	120
Fig. 6-9 (a) N ₂ adsorption/desorption isotherms and (b) pore size distribution for 15NiO/SiO ₂ catalysts. (F) Fresh catalyst (AP) catalyst analyzed after interaction with plasma, (CH ₄) Pretreated with methane.	122
Fig. 6-10 XRD patterns of fresh catalyst and after plasma (a) 30NiO/Al ₂ O ₃ and (b) 30NiO/SiO ₂ support. Reference patters of NiO and γ -Al ₂ O ₃ and SiO ₂ , PDF #044–1159, PDF #050-0741 and PDF #016-0152, respectively.....	123
Fig. 6-11 XPS survey spectra of the catalyst materials before (F) and after contact with plasma (AP) for (a) 30NiO/Al ₂ O ₃ and (b) 30NiO/SiO ₂ . High-resolution spectral analysis for catalyst materials at the (c) Ni 2p edge of 30NiO/Al ₂ O ₃ , d) Ni 2p of 30NiO/SiO ₂	125
Fig. 6-12 Reduction temperatures for (a) Al ₂ O ₃ and (b) SiO ₂ based catalyst.....	129
Fig. 6-13 Conversion of CO ₂ and CH ₄ over time for (a)30Ni/Al ₂ O ₃ , (b) 30Ni/SiO ₂ , (c) 15Ni/Al ₂ O ₃ and (d) 15Ni/SiO ₂	130
Fig. 6-14 Water signal over time for different Ni-based catalyst supported on Al ₂ O ₃ and SiO ₂	131
Fig. 6-15 Characteristic RGA discharge voltage, current and instantaneous power signals for plasma - catalytic DRM reaction at CO ₂ /CH ₄ = 1.5, with a total flow rate of 4.5 L _N min ⁻¹ over Ni/SiO ₂ catalyst.....	131
Fig. 6-16. Reactor assembly (on the left) and infrared photograph of the RGA reactor during DRM reaction (on the right). Taken with Cat S61 FLIR camera.	132

Fig. 6-17 [C ₂ H ₂]/[Ar] signal for the different catalyst supported on (a)Al ₂ O ₃ , total flow rate 3.7 L _N min ⁻¹ and (b) SiO ₂ , total flow rate 4.5 L _N min ⁻¹	136
Fig. 6-18 TGA-TPO results for Ni-based catalysts (a, b) fresh, (c,d) used in thermo-catalytic experiments and (e,f) used in plasma-catalytic experiments.	137
Fig. 6-19 SEM pictures and EDS spectra for 30NiO/SiO ₂ for (a, b) fresh and (c, d) spent catalyst (after plasma).	138
Fig. 6-20 High-resolution spectral analysis for fresh (F) and spent (AP) catalysts at the (a) Al 2p of 30NiO/Al ₂ O ₃ , and (b) Si 2p of 30NiO/SiO ₂	139
Fig. 6-21 High-resolution spectral analysis for fresh (F) and spent (AP) catalysts at the O 1s (a) 30NiO/Al ₂ O ₃ , and (b) 30NiO/SiO ₂	139
Fig. 6-22 Fresh and spent catalyst (after contact with plasma) (a) 30NiO/Al ₂ O ₃ and (b) 30NiO/SiO ₂	140

List of Tables

Table 3–1 Composition in vol% of the calibration gases.	32
Table 4–1 Parameters and assumptions used for the operating diagrams	47
Table 5–1 Residence times in the RGA discharge zone for different total flow rates.....	70
Table 5–2 Percentage of electrical power input that contributed to the H ₂ and CO production, for peak currents of 0.74 and 1.50 A, CO ₂ /CH ₄ =1.0, 1.5, 2.0 and total flow rates of 3.7, 4.7 and 6.7 SLPM	89
Table 5–3 Comparison of performance parameters for different plasma sources for DRM	90
Table 5-4 Summary of the order of reaction for C ₂ H ₂ production	97
Table 6–1 Turnover frequency for Ni/Al ₂ O ₃ and Ni/SiO ₂ catalysts	108
Table 6–2 Carbon balance for the different plasma and plasma-catalytic experiments.	117
Table 6–3 N ₂ adsorption/desorption results (total surface area, average pore size and pore volume) for fresh and spent catalysts (AP = after plasma, P = passivated, CH ₄ = after plasma pretreatment with CH ₄).	121
Table 6-4. H ₂ -uptake [$\mu\text{mol g}^{-1}$], specific surface area [$\text{m}^2 \text{g}^{-1}$], average nickel crystallite size [nm] and metal dispersion [%] for fresh and spent Ni-catalysts.	122
Table 6-5 Crystallite size of NiO catalysts fresh and after plasma DRM.....	124
Table 6-6 Target and actual nickel loadings for Al ₂ O ₃ and SiO ₂ supported catalyst determined by ICP-OES	128
Table 6-7 ANOVA results for plasma-catalytic experiments with Ni/Al ₂ O ₃ catalysts.	133
Table 6-8. t-test results for plasma-catalytic experiments with Ni/Al ₂ O ₃ catalysts.....	134

Table 6-9 ANOVA results for plasma-catalytic experiments with Ni/SiO ₂ catalysts	135
Table 6–10. t-test results for plasma-catalytic experiments with Ni/SiO ₂ catalysts.	135
Table 6–11 Atomic compositions of the catalyst.....	140
Table 6–12 Change in Ni 2p 3/2 peak ratios for catalysts.	140

1

Introduction

1.1 Motivation

The current climate crisis that the world is facing is the result of the rise in atmospheric greenhouse gas (GHG) levels, predominantly carbon dioxide (CO₂), produced from anthropogenic sources over the past 200 years [1]. Globally, about 78% of GHG emissions from human activity are related to the production and consumption of energy [2]. In 2015, CO₂ accounted for 76% of the global GHG emissions [3], originating mainly from the combustion of fossil fuels such as oil, coal, and natural gas. In particular, the consumption of natural gas has increased over the last few decades due to its lower CO₂ emissions when combusted (25 to 45 % less compared to oil or coal) and its vast available quantities in the forms of conventional and shale gas [4]. Besides fuel for energy generation, natural gas is used as a feedstock to produce chemical building blocks such as methanol, ethylene, benzene, and hydrogen. The main component ($\leq 95\%$) of natural gas is methane (CH₄). CH₄ leakage into the atmosphere during shale recovery, transportation, storage, and distribution has become a serious issue that contributes to the atmospheric GHG emissions [4]. CH₄ is 25 times more potent as a GHG compared to CO₂, and it represented 16% of the global GHG emissions in 2015 [3]. In Canada, CH₄ emissions contribute to 15% of total GHG emissions [5]. The utilization of CO₂ and CH₄ to produce commodity chemicals is essential to control/reduce the impact of GHG in the atmosphere.

CO₂ can be used as a raw material for the production of chemicals such as urea, carboxylic acids, polymeric materials, alcohols, and heterocyclic compounds [4, 6]. Furthermore, as the demand for renewable energies grows, being even mandatory by law in some European countries and recently in Québec [7, 8], research is being done to convert CO₂ into renewable natural gas. This can be

addressed by the Power-to-Gas (P2G) concept (Fig. 1-1). P2G uses the excess of electricity from renewable sources to produce H_2 via water electrolysis. The H_2 produced reacts with CO_2 via thermal catalysis through the Sabatier reaction to produce CH_4 . The resulting CH_4 can be directly injected in the existing natural gas infrastructure or used for storage services [9, 10]. CO_2 methanation is the core of P2G. Hence, the determination of design and operating parameters for a methanation reactor is critical for a successful operation. The theoretical part of this dissertation contributes towards better design of CO_2 methanation fluidized bed reactors. This method can also be used for other gas phase reactions.

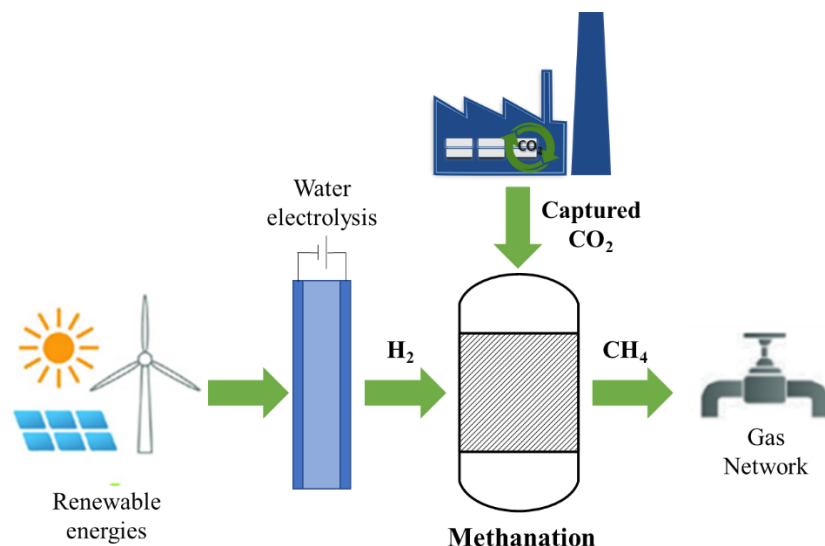


Fig. 1-1 Flow diagram of the Power-to-Gas process. Adapted from [11].

Similarly, CH_4 can be converted into higher hydrocarbons, hydrogen, synthesis gas, aromatics, etc. via thermal catalysis, biological processes, or plasma activation techniques [4]. However, the dissociation of CO_2 and CH_4 is challenging due to the high dissociation energies of the C–O ($\Delta H_{298K} = 532 \text{ kJ mol}^{-1}$) and C–H ($\Delta H_{298K} = 439 \text{ kJ mol}^{-1}$) bonds. Hence, the catalytic conversion of CO_2 and CH_4 requires high temperatures and presents several challenges, such as coking and catalyst sintering, low conversion rate, and product selectivity. For these reasons, plasma-assisted conversion technologies offer an attractive solution. In the plasma environment, electron-impact excitation, dissociation, and ionization reactions can generate excited species, such as radicals, neutral atoms, ions, and metastable species, while remaining close to room temperature. This type of plasma is known as non-thermal or non-equilibrium plasma. This state

of non-equilibrium is closely linked to the large difference of masses between the electron and heavy species, which results in inefficient exchanges of kinetic energy between these two species. The highly energetic species created in the plasma can dissociate strong molecular bonds, like in the case of CO_2 and CH_4 , and provide energy to carry out reactions that would require high temperatures and an efficient catalyst to make them happen.

Dry reforming of methane (DRM) is a reaction that simultaneously converts two greenhouse gases, CH_4 and CO_2 , into valuable chemicals, i.e., synthesis gas (syngas). DRM is a highly endothermic reaction and is conventionally carried out at temperatures $> 700\text{ }^\circ\text{C}$ using an efficient catalyst. Hence, for the abovementioned reasons, plasma technologies are well suited for this reaction. Moreover, plasmas can be sustained using electrical power from renewable sources. Since plasma reactors can easily be switched on and off, the intermittency of some renewable energy services can be accommodated (Fig. 1-2) [12].

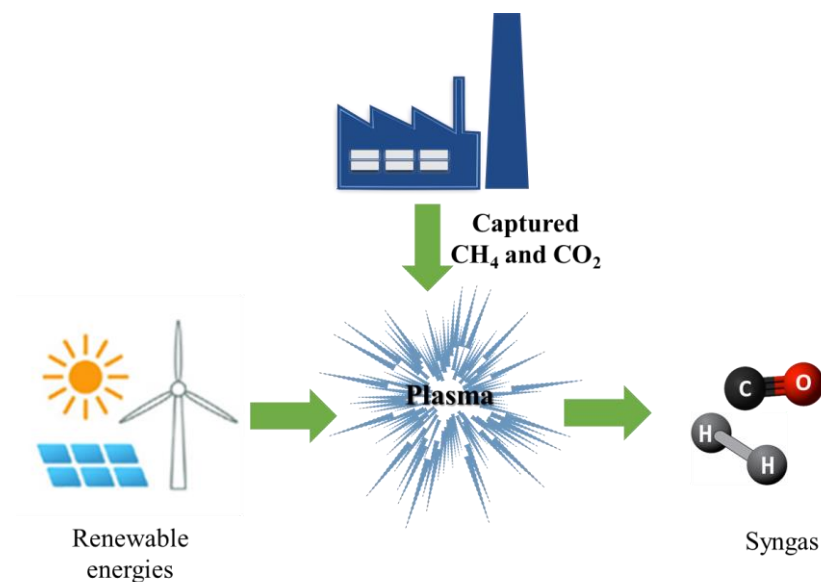


Fig. 1-2 Flow diagram of DRM carried out using plasma generated using renewable energies.

Adapted from [12].

One type of non-thermal plasma discharge is the rotating gliding arc (RGA), in which the reactant gas is injected tangentially to form a swirling flow field in the reactor. As the arc is pushed away from the breakdown area, it swirls and elongates, creating a large plasma volume [13]. The formation of products in the plasma volume can be controlled by regulating certain parameters such as gas flow rate, discharge power, and feed gas composition [4]. Additionally, the

introduction of a suitable catalyst in or close to the discharge zone can improve the conversion of the reactants, as well as product selectivity and yield [14]. The interaction between the plasma and the catalyst modifies the properties of both at the same time. This technology is known as plasma-catalysis.

The experimental work presented in this dissertation provides the design, validation, and characterization of a RGA reactor system used for DRM considering plasma and plasma-catalysis technologies.

1.2 Objectives

CO₂ is the main atmospheric greenhouse gas; however, existing reactions and technologies can use this gas while producing value-added chemicals. The first two objectives of this dissertation provide a new graphical method for reactor and process design for the CO₂ methanation reaction. The other objectives address and study plasma and plasma-catalytic approaches to valorize CO₂, also considering another relevant greenhouse gas, CH₄. The following specific objectives are addressed in this thesis:

1. To graphically identify and determine the operating range of a fluidized bed reactor for the CO₂ methanation reaction, the core of the Power-to-Gas technology.
2. To determine the hydrodynamics of the fluidized bed for CO₂ methanation, considering the cases of industrial and laboratory-scale reactors.
3. To design and build a laboratory-scale RGA reactor.
4. To investigate the best combination of operating conditions of a RGA reactor to achieve high CO₂ and CH₄ conversion, as well as CO and H₂ yield.
5. To determine the relationships between the chemical composition and structure of the catalyst, and the mechanisms responsible for the plasma-catalytic activity, efficiency, selectivity and stability.
6. To investigate and understand the interactions (positive or negative effects) between plasma (RGA discharge) and catalysis (fluidized-bed catalytic reactor) for DRM.

1.3 Thesis structure

This manuscript-based thesis is organized in seven chapters, including introductory chapters that cover background and methodology.

Chapter 2 provides a comprehensive background and theory that covers the concepts needed to complete the work presented in this dissertation. These concepts are related to CO₂ valorization reactions, such as CO₂ methanation and CO₂ reforming of methane, as well as the current technologies to carry out these reactions. In the case of the thermodynamically favored CO₂ methanation reaction, which also is more technologically mature, literature related to bubbling fluidized bed reactors is revised. On the other hand, CO₂ reforming of methane is still a technology in development, and methods to carry out the reaction more efficiently, such as catalysis, plasma, and plasma-catalysis, are discussed.

Chapter 3 presents an overview of the methods and procedures used to carry out the experiments presented in each manuscript. The core of the thesis consists of three manuscripts that follow the objectives mentioned in the previous section. Each of the following chapters includes a preface that summarizes the connection with the subsequent chapters.

Chapter 4 is titled “*Working diagrams to identify the operating range of a bubbling fluidized bed reactor for CO₂ methanation*”, published in The Canadian Journal of Chemical Engineering, and addresses objectives 1 and 2.

Chapter 5 is titled Plasma Assisted Dry Reforming of Methane and addresses objectives 3 and 4. The corresponding manuscript was published under the title “*Influence of Operating Parameters on Plasma-Assisted Dry Reforming of Methane in a Rotating Gliding Arc Reactor*” in the Plasma Chemistry and Plasma Processing journal.

Chapter 6 addresses objectives 5 and 6. The corresponding manuscript has been accepted in the Journal of CO₂ utilization under the title “*Plasma-Catalytic Dry Reforming of Methane over Ni-supported catalyst in a Rotating Gliding Arc - Spouted Bed Reactor*”.

Finally, Chapter 7 summarizes the main findings of this work as well as the recommendations for future work.

2

Theoretical Background

This chapter presents some concepts and theory used throughout the thesis. Concepts covered in the presented manuscripts are not repeated in this chapter.

2.1 CO₂ valorization

CO₂ valorization and utilization technologies offer the possibility of having a sustainable carbon cycle while creating a circular economy and producing value-added products. In this way, CO₂ would not be considered a waste, and revenues from it would also be generated [15]. Over the past decades, CO₂ has been used in several industries such as carbonation of beverages, food, agro-chemistry, welding, foaming, blanketing agent, fire-extinguisher, solvent, etc. [16, 17]. Nevertheless, due to the high amounts of CO₂ generated every year (~33 Mt in 2017 [3]), new processes need to be developed that involve CO₂ as a reactant or feedstock [17]. Even though CO₂ is highly versatile, it presents some disadvantages as a chemical reactant due to its stability, non-reactive property, and low Gibbs energy [15, 16, 18]. Fig. 2-1 shows the roadmap of valorization technologies for captured CO₂. The utilization of CO₂ can be classified in (a) production of chemicals and fuels, (b) direct use of CO₂ (as a reactive solvent), (c) mineralization, and (d) enhanced biological utilization [15, 17, 19]. The first method mainly produces two types of products: fully reduced carbon derivatives, e.g., hydrocarbons, and products where a C=O or a O=C=O is introduced into a molecule [18]. From a thermodynamic standpoint, the conversion of CO₂ ($\Delta G_f^\circ = -394 \text{ kJ mol}^{-1}$) is easier when it is paired with a co-reactant with higher (or less negative) Gibbs energy, such as CH₄ ($\Delta G_f^\circ = -50.7 \text{ kJ mol}^{-1}$) or H₂ ($\Delta G_f^\circ = 0 \text{ kJ mol}^{-1}$) [20]. Two of the most interesting technologies involving the latter co-reactants, are showed in Fig. 2-1 (in red diamonds), are the hydrogenation of CO₂, also known as CO₂ methanation, and dry reforming

to syngas or dry reforming of methane. From the industrial ecology point of view, CH₄ production (CO₂ methanation) is suitable due to the synergies with the existing infrastructure; besides, it can be considered a simple and fast reaction. Although these technologies are not yet ready for commercialization, they have gained a lot of interest over the last few years since both technologies use CO₂ as a feedstock to produce fuels towards a circular economy.

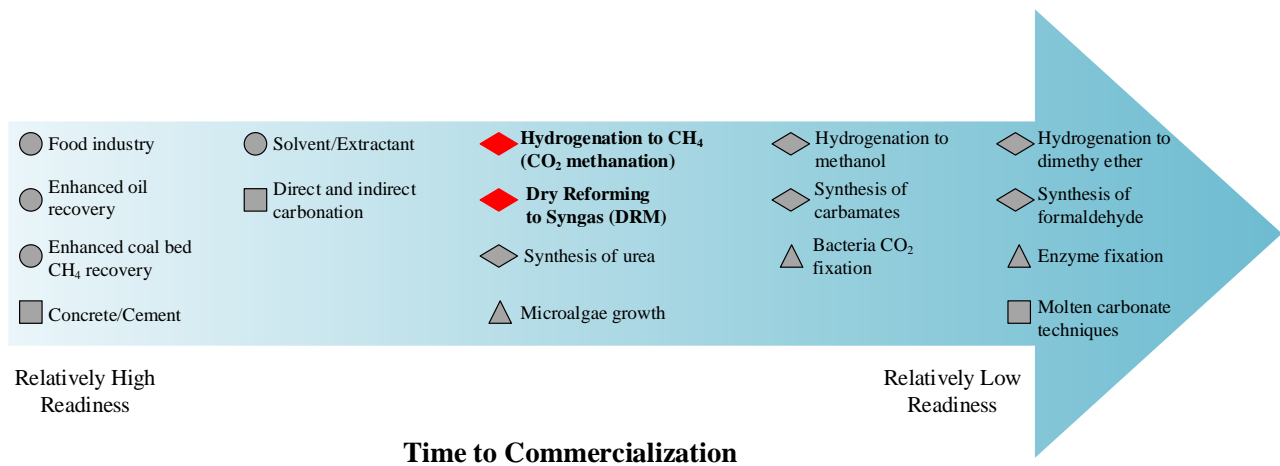


Fig. 2-1 Roadmap of CO₂ valorization technologies. The symbols are defined as ○ direct use, ◇ production of chemicals/fuels, □ mineralization, and △ biological utilization. Adapted from [15].

DRM and the methanation reaction can be combined in a closed-loop process that could be used for thermochemical heat pipe (TCHP) applications as proposed by Edwards *et al.* [21] for energy storage and transmission (Fig. 2-2). The process involves high-temperature, or an alternative method such as plasma discharge to drive the strongly endothermic CO₂/CH₄ reforming reaction. The reaction products, CO and H₂, and the unreacted or excess CO₂ can be stored, transported to a separate site, or used in-situ for the reverse reaction (CO/CO₂ methanation), releasing the stored chemical energy. Finally, the products of the methanation reaction are sent back to the endothermic reactor to complete the closed-loop cycle [21]. However, these types of applications can only be successful if the optimization of individual technologies, i.e., DRM and CO₂ methanation, is achieved. In the following sections, some aspects related to CO₂ methanation and dry reforming of methane are discussed.

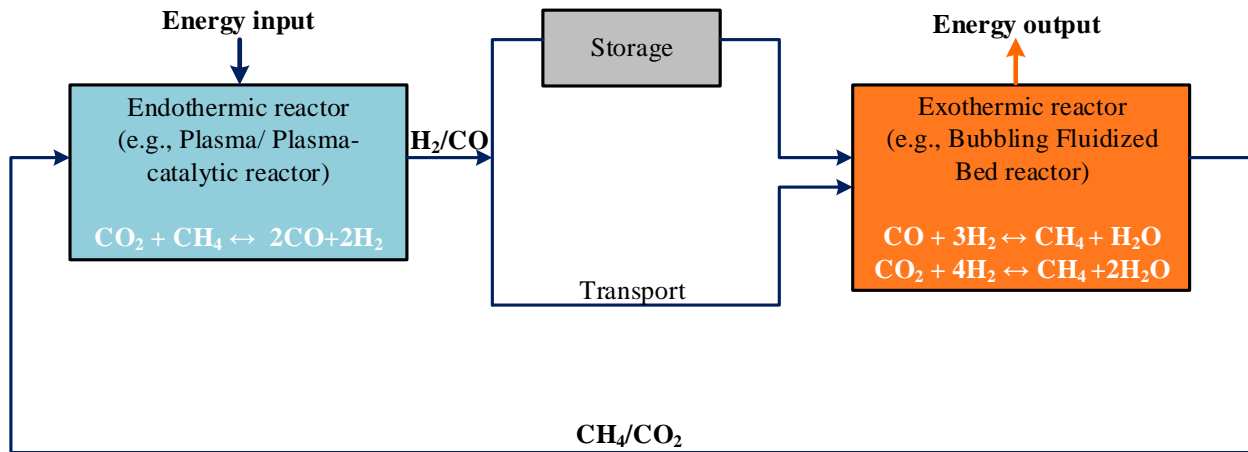


Fig. 2-2 Combination of DRM and methanation process in a closed-loop for TCHP. Adapted from [21].

2.2 CO₂ methanation

As mentioned earlier, the widely studied CO₂ methanation is the core of Power-to-Gas (P2G) (refer to Fig. 1-1). Recently, new CO₂ methanation pilot-scale plants and commercial projects have been built, whereas the majority of them are located in Europe. According to [11], there are approximately 128 P2G research and demonstration projects currently in operation or testing stage. In the catalyzed methanation reaction, CO₂ is reduced with H₂ over noble metal-based catalysts such as nickel (Ni), ruthenium (Ru), or rhodium (Rh) to produce CH₄ and water ($\text{CO}_2 + 4\text{H}_2 \leftrightarrow \text{CH}_4 + 2\text{H}_2\text{O}$) [15]. The CH₄ produced is a preferable technique to store energy, which can close the gap between energy supply and demand.

The catalytic methanation reaction has been known since 1902 [7], and it can be seen as a combination of CO hydrogenation ($\text{CO} + 3\text{H}_2 \leftrightarrow \text{CH}_4 + \text{H}_2\text{O}$) and reverse water gas shift (RWGS) ($\text{CO}_2 + \text{H}_2 \leftrightarrow \text{CO} + \text{H}_2\text{O}$) reactions. A thermodynamic equilibrium analysis of CO₂ methanation using the minimization of Gibbs energy approach (HSC Chemistry 9) is shown in Fig. 2-3, as a function of temperature at 1 bar (a), and as a function of pressure at 350 °C (b). A complementary thermodynamic analysis of the reaction is discussed in Chapter 4.

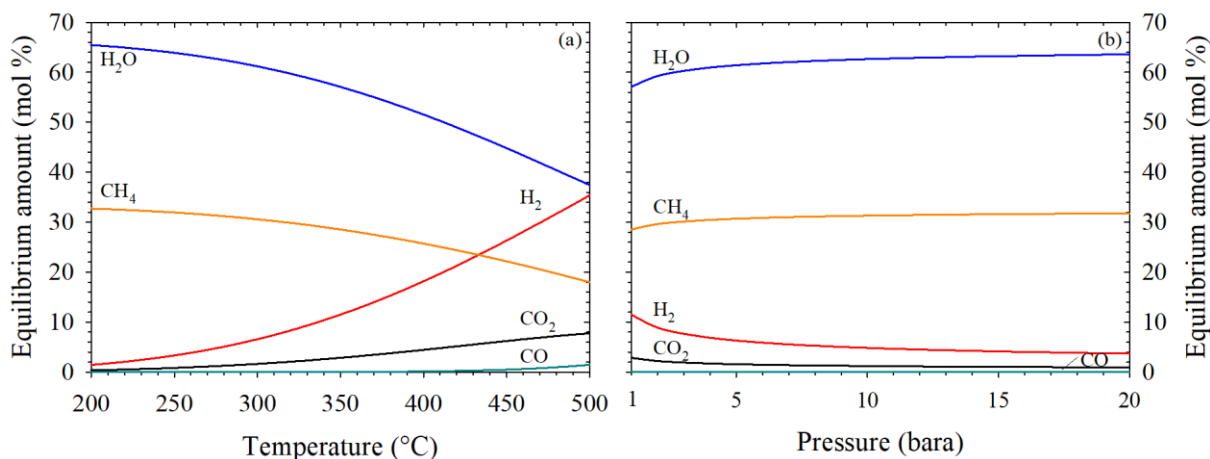


Fig. 2-3 Equilibrium composition of CO₂ methanation as a function of (a) temperature, 200 to 500 °C at 1 bar, and (b) pressure, 1 to 20 bar at 350 °C for H₂/CO₂ = 4.

The catalytic methanation reaction usually operates at low temperatures (200 to 550 °C) and pressures between 1 to 20 bar, using mostly Ni as a catalyst due to its high CH₄ selectivity ($\approx 100\%$) and low cost. Thermodynamic equilibrium models show that the CO₂ methanation reaction can be completed at low temperature (< 300 °C) at atmospheric pressure (Fig. 2-3a). However, conventional Ni catalysts are not fully active at those temperatures, limiting the conversion of the reactants. Thus, higher temperatures (> 320 °C) are needed to reach equilibrium. Nonetheless, higher temperatures are non-favorable for the reaction, and CH₄ yields $> 95\%$ are not obtained at stoichiometric conditions [22]. Moreover, above 450 °C the formation of CO through the RWGS dominates. On the other hand, higher pressures are usually required to carry out the CO₂ methanation reaction, as high pressures increase the conversion of CO₂ and selectivity of CH₄ while reducing the concentration of the byproduct CO (Fig. 2-3b) [11]. Therefore, increasing the pressure while operating a temperature high enough to keep the catalyst completely active is the conventional method to carry out CO₂ methanation.

Furthermore, the CO₂ methanation reaction is highly exothermic ($\Delta H_{298K} = -165$ kJ mol⁻¹), and a significant amount of heat needs to be removed from the reactor to prevent thermodynamic limitations and catalyst sintering [7]. Hence, the type of reactor chosen and its design is crucial for a successful operation. Different reactor concepts have been investigated for methanation, such as fixed-bed [23–25], fluidized-bed [9, 25, 26], and structured reactors [11, 27, 28]. Among the reactor concepts mentioned before, fixed-bed and fluidized-bed reactors are well-established

technologies, whereas the other reactor types are still in the development stage [7]. In the case of fixed bed reactors, the formation of hotspots in the catalyst bed is one of the major challenges as it can lead to catalyst sintering and deactivation. An alternative to deal with the exothermic nature of the reaction are fluidized-bed reactors, in which the mixing of fluidized solids leads to isothermal conditions in the reactor that simplify the operation control [29]. According to [24], two types of fluidized bed reactors have been developed for CO₂ methanation: a) bubbling fluidized bed (BFB) methanation reactors, in which the catalyst particles are suspended in the upwards flowing reacting gas and b) bubble columns, in which particles and gas are suspended in a non-reactive liquid that is used to improve the heat transport. However, the flexibility of fluidized-bed reactors is limited by their hydrodynamics [30]. For instance, the superficial gas velocity needs to be high enough to hold minimum fluidization conditions, but low enough to avoid catalyst entrainment [7]. In the following section, hydrodynamics related to BFB reactors will be discussed.

2.2.1 Bubbling Fluidized Bed Reactors

One of the limitations of the CO₂ methanation in the P2G technology is that the operating capacity of the reactor depends on the H₂ availability. Therefore, adapting the geometry of the BFB reactor for changing operational conditions (dynamic mode) such as temperature, pressure, or input flow rate is essential to ensure proper fluidization inside the reactor [22]. The fluidization of the particles depends on the gas velocity. As the gas velocity increases, the pressure also increases until it balances the weight of the bed, and bubbles start to appear in the catalyst bed [31]. This velocity is known as the minimum fluidization velocity, u_{mf} , and represents the transition between packed bed and particulate fluidization behavior (see eq. 4.4 in Chapter 4). For very small particles (< 250 μm), u_{mf} can be simplified as follows:

$$u_{mf} = \frac{d_p^2(\rho_s - \rho_g)g}{150\mu} \frac{\varepsilon_{mf}^3 \varphi_s^2}{1 - \varepsilon_{mf}} \quad Re_{p,mf} < 20 \quad (2.1)$$

Where u_{mf} is the minimum fluidization velocity (m s⁻¹), ρ_s and ρ_g are the densities of the solid and gas, respectively (kg m⁻³). The gravitational acceleration is stated by g (kg m s⁻²), μ is the dynamic viscosity (Pa s), d_p and φ_s are the particle diameter (m), and sphericity of the catalyst, respectively, and ε_{mf} is the bed voidage at minimum fluidization conditions [31].

The minimum fluidization velocity is an important parameter needed for the design of fluidized beds. Temperature and pressure affect u_{mf} since the parameters described earlier are influenced by these operating conditions. For instance, ε_{mf} increases from 1 to 4% with rising operating pressure. Also, with increasing temperature, ε_{mf} varies up to 8% for temperatures up to 500 °C for fine particles but is unaffected for coarse particles. On the other hand, u_{mf} decreases with increasing operating pressure. This decrease in the u_{mf} is negligible for fine particles ($d_p < 100 \mu\text{m}$) but becomes important (up to 40%) for larger particles ($d_p \approx 360 \mu\text{m}$) [31].

The superficial gas velocity, u_o , is especially influenced by the u_{mf} . As mentioned before, u_o needs to be high enough to provide proper fluidization but low enough to avoid catalyst entrainment. Fluidization in BFB reactors occurs at u_o of less than about $10u_{mf}$ [31]. Furthermore, the behavior of the fluidization is affected by the particle characteristics. Geldart [32] investigated the behavior of different kinds of particles in a BFB, and he classified the difference between the groups by the density difference between particles and fluid, $(\rho_p - \rho_F)$ and the average particle size d_p . The four groups described below for the Geldart classification (Fig. 2-4) are for $u_o < 10u_{mf}$ and air fluidization at ambient conditions [31]:

- Group C: cohesive or very fine powders. Difficult to fluidize since the interparticle forces are greater than the force resulting from the action of the gas. The particles tend to rise as clumps of solids in small bed diameters.
- Group A: aeratable or particles with small diameter and/or low density ($< 1.4 \text{ g cm}^{-3}$). Easy to fluidize with smooth fluidization at low gas velocities. The bed expands before bubbles appear.
- Group B: sandlike or particle diameters between 40 and 500 μm and density between 1.4 and 4 g cm^{-3} . These particles fluidize well, and bubbles form as soon as the gas velocity exceeds u_{mf} . Thus, the minimum bubbling velocity, u_{mb} , and u_{mf} are approximately equal ($u_{mb}/u_{mf} \approx 1$), with bubbles growing large. Vigorous bubbling enhances the gross circulation of solids.
- Group D: spoutable, large or dense particles. Low voidage and difficult to fluidize in large beds, hence big amounts of gas are needed to fluidize these particles. Large exploding bubbles.

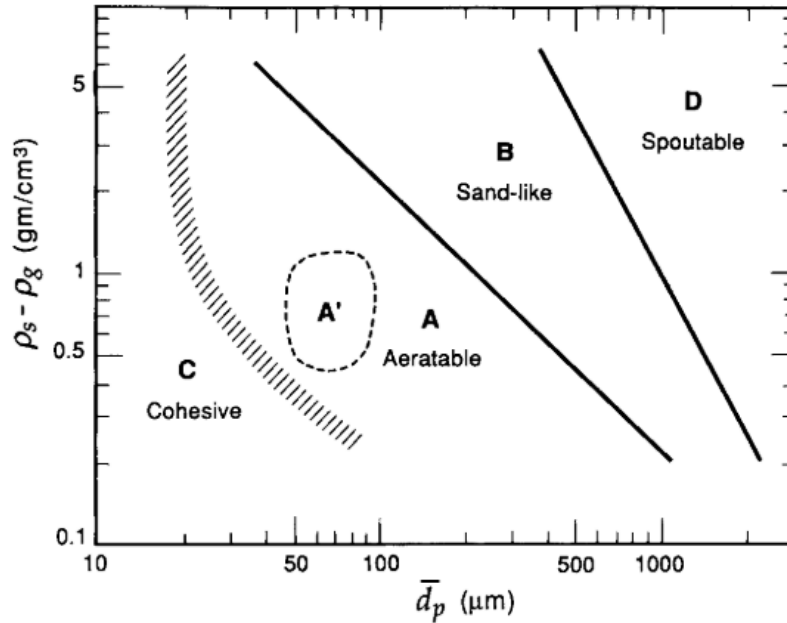


Fig. 2-4 Geldart classification of particles in BFB. Taken from [31].

As stated before, $u_o < 10u_{mf}$ is a good criterion to determine the superficial gas velocity in BFB reactors. Ideally, in a BFB reactor, the u_o , should be kept between the u_{mf} and the terminal velocity, u_t , to assure that the catalyst particles are fluidized and to avoid or reduce the carryover of particles from the bed [7, 31, 33]. The terminal velocity represents the maximum operating velocity for a fluidized bed before the particles start to be entrained out of the bed (see eq. 4.5, Chapter 4).

The operation of BFB reactors depends not only on the gas-solid properties as described before but also on the chemical reaction itself [34], i.e., the thermodynamics of the reaction. For the CO_2 methanation reaction, there is a volume contraction of 40% after the reaction is completed. This change in gas volume as a result of the chemical reaction can significantly affect the hydrodynamics [35] in the BFB reactor. Hence, the proper u_o should be chosen to assure good fluidization and to avoid the collapse of the bed when carrying out the reaction. Both hydrodynamics and reaction thermodynamics must be considered in the reactor design and operation.

The work presented in Chapter 4 discusses the design of working diagrams for BFB reactors based on hydrodynamics and the thermodynamics of the CO_2 methanation reaction to determine (a) a suitable reactor diameter at established operating conditions, and (b) the operating capacity range for a given reactor diameter.

2.3 Dry Reforming of Methane

Carbon dioxide and methane are stable molecules that need high energy inputs to dissociate and convert into new products. DRM was invented by Fischer and Tropsch in 1928 to convert CO_2 and CH_4 simultaneously ($\text{CO}_2 + \text{CH}_4 \leftrightarrow 2 \text{H}_2 + 2 \text{CO}$) [36]. In DRM, high temperatures are the traditional method to deliver enough energy to drive the endothermic reaction ($\Delta H_{298K} = + 247 \text{ kJ mol}^{-1}$), and achieve high conversions of CO_2 and CH_4 to syngas, a mix of H_2 and CO [37]. Syngas can be upgraded to higher alcohols or used as fuel or as feedstock for the Fischer-Tropsch (FT) synthesis to produce chemicals such as higher alkanes and oxygenates [15, 36]. A thermodynamic equilibrium analysis of DRM using the minimization of Gibbs energy approach (HSC Chemistry 9) is shown in Fig. 2-5, as a function of temperature at 1 bar. A complementary thermodynamic analysis of the reaction is discussed in Chapter 5.

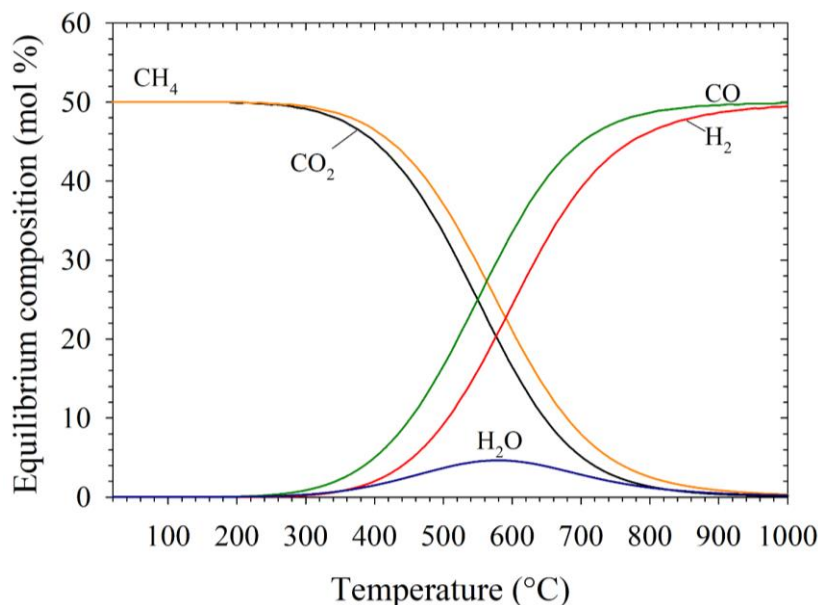


Fig. 2-5 Equilibrium composition of DRM as a function of temperature, 20 to 1000 °C at 1 bar for $\text{CO}_2/\text{CH}_4 = 1$.

For years, DRM has been carried out via thermal catalysis, at temperatures >700 °C, since catalysts lower the activation energy of the reaction [36]. Noble metals such as ruthenium, rhodium, platinum, iridium, and palladium present a good catalytic activity for the reaction. However, the use of noble metals as catalysts increases the total cost of the process, making it economically unsustainable. Nickel-based catalysts represent a good alternative for DRM reaction due to their

low cost, good availability, efficiency, and good turnover numbers, i.e., number of moles of substrate that a mole of catalyst can convert before becoming inactivated [38, 39]. Nevertheless, catalyst deactivation due to carbon deposition represents a big obstacle to scale up the catalytic reforming process [20, 36]. Thermodynamic equilibrium models [40] show that the DRM reaction can be completed at high temperatures (> 900 °C) and at atmospheric pressure (Fig. 2-5). However, high operating temperatures lead to catalyst sintering and deactivation. Moreover, at stoichiometric conditions, carbon deposition is favored at temperatures < 900 °C (see Fig. 5-3, Chapter 5), which leads to catalyst poisoning and thus deactivation. On the other hand, the competitive reverse water gas-shift (RWGS) reaction ($\text{CO}_2 + \text{H}_2 \leftrightarrow \text{CO} + \text{H}_2\text{O}$) occurs simultaneously with DRM, producing higher water contents between 575 and 585 °C. The formation of water decreases the production of H_2 , affecting the H_2/CO ratio and hence the further applicability of syngas for various processes. For instance, at stoichiometric conditions, a ratio of $\text{H}_2/\text{CO} > 0.98$ is obtained > 900 °C, which can be used for FT to produce liquid fuel such as DME [40].

An alternative for DRM are plasma technologies. Plasma processes are powered by electricity and are characterized by low turn-on and turn-off times, as they do not require preheating, long stabilization, and no cool-down times. Plasma reactors can thus be directly connected to intermittent renewable electricity sources [12, 41]. In fact, the conversion of the reactant gas starts immediately after plasma ignition, since plasma allows the activation of stable molecules in an energy-efficient way. In non-equilibrium plasmas, the applied electric field selectively heats up the electrons without a similarly large heating of the heavy species gas (atoms, molecules, ions) [12]. Hence, plasma technologies can assist the conversion process by providing energy and reducing the activation barrier for the $\text{CO}_2 - \text{CH}_4$ reaction. However, depending on the type of plasma discharge, the conversions of CO_2 and CH_4 are lower compared to the ones obtained via catalytic conversion. Furthermore, carbon byproducts, i.e., coke and higher hydrocarbons, are inevitably formed during the plasma discharge [36].

The combination of plasma and catalysis may induce complex synergistic effects and potentially overcome the drawbacks of both technologies [36, 42]. Such a concept is known as plasma-catalysis, and it consists of taking a material with catalytic properties and combining it with a plasma [14]. Plasma-catalysis might enhance CO_2 and CH_4 conversions and improve syngas selectivity.

Even though plasma and plasma-catalytic technologies represent a good alternative for CO₂ valorization, they are still in the research stage and further development is needed to scale up and commercialize these technologies. In the following sections, a more detailed analysis of DRM via thermal catalysis, plasma, and plasma-catalysis is provided.

2.3.1 Catalysis reforming

CO₂ is the most oxidized state of carbon. This characteristic makes CO₂ inert and gives it good thermal stability, and therefore, its chemical transformation is thermodynamically unfavorable [18, 36]. A thermodynamic analysis for DRM is presented in Chapter 5 for a temperature range of 20 to 900 °C using the minimization of Gibbs energy approach for three different CO₂/CH₄ ratios. The results presented in Fig. 5-3 show that an operating temperature > 700 °C is needed to reach a conversion of at least 80% for CO₂ and CH₄. However, in practice, the retention time in the reactor is shorter than the time to reach thermodynamic equilibrium [36]. Hence, a catalyst is needed to reduce the activation energy for DRM. Several studies have been conducted to determine the best catalyst for DRM. For instance, Fischer *et al.* [43] in 1928 tested different metals (Fe, Co, Ni, Cu, Mo, and W) supported on clay, silica (SiO₂), magnesium carbonate (MgCO₃) or mixed with alumina (Al₂O₃) and found that Ni and Co supported on clay and silica were the best catalysts, while Fe, Cu, Mo, and W did not show a good catalytic activity. Later, Nakamura *et al.* [44] performed experiments for different noble metals (Ru, Rh, Ni, Pt, Pd) supported on SiO₂ and MgO. The results showed that the catalytic activities for the metals supported on SiO₂ are Ru > Rh > Ni > Pt > Pd and Ru > Rh > Ni > Pd > Pt for MgO-supported catalyst, with 1 % wt. metal loading and operating temperature of 700 °C. On the other hand, Ferreira-Aparicio *et al.* [45] showed that the order of the activities for SiO₂ - supported catalysts is Ru > Rh > Ni > Ir > Pt > Co, and Rh > Ni > Pt > Ir > Ru > Co supported on Al₂O₃, at an operating temperature of 750 °C.

Among all the metals studied for DRM, nickel is the most extensively used. However, Ni-based catalysts undergo severe deactivation due to carbon deposition [46]. Carbon deposition cannot be avoided, as both CH₄ and CO₂ are C-containing molecules, but it should be minimized [36]. Mainly, three reactions are involved in carbon and coke formation on the catalyst surface. These reactions are CO disproportionation, CH₄ cracking, and RWGS reaction, which are stated in

Chapter 5. With fresh catalysts, carbon formation comes mostly due to CH₄ dissociation since CO is not present in the reactant feed [46]. Although carbon deposition is inevitable, its extent can be reduced by increasing the CO₂/CH₄ ratio (> 1) and operating temperature of the reaction (see Chapter 5, section 4.4.1) [40, 47]. Moreover, supports with high surface area (160–300 m² g⁻¹) allow greater dispersion of active metal through the pore structure on the surface support, which limits carbon deposition [46]. However, high surface area supports have small pores and can inhibit reactant diffusion. In this dissertation, two types of supported Ni catalysts were studied for DRM. The widely used Ni supported on Al₂O₃ and a Ni/SiO₂, which presents a high surface area.

The Ni/Al₂O₃ catalyst presents a strong interaction between Ni and Al₂O₃, which makes the catalyst less prone to sintering [48] and gives the catalyst a greater ability to dehydrogenate CH₄ [49]. Additionally, the surface basicity of Al₂O₃ enhances coke resistance capability of the catalyst [48, 50], and it provides, at the same time, high activity towards CO formation (and CO₂ conversion) since there is an increase in the adsorption of the acidic gas CO₂ [36, 51]. However, the strong metal-support interaction may result in the formation of the NiAl₂O₄ spinel structure, which complicates the reduction of the catalyst and leads to low metal dispersion [52]. In the case of Ni/SiO₂, due to the high surface area of SiO₂ and hence, high metal dispersion, the initial catalytic activity is high [48]. Furthermore, Takayasu *et al.* reported that a SiO₂ based catalyst leads to less carbon deposition [53]. Even though the weak interaction between metal and support facilitates the reduction of the catalyst, it may also lead to quick deactivation due to metal agglomeration [45, 48, 52].

Regarding the mechanism for DRM, several authors agreed that the mechanism is bi-functional [54, 55], i.e., CH₄ is activated on the metal while CO₂ is activated on the acidic/basic supports (e.g. Al₂O₃). However, for catalysts supported on inert materials such as SiO₂, the mechanism follows a mono-functional pathway, where CO₂ and CH₄ are activated by the metal alone [46].

2.3.2 Plasma reforming

Non-thermal plasma technologies represent an alternative to the catalytic processes, as they can achieve conversions of the reactant gases at relatively low temperatures and without the use of a catalyst. Plasma for DRM was used for the first time in 1976 by Capezutto *et al.*, in a low-pressure (26.6 mbar) radiofrequency plasma reactor [36, 56].

Processing plasmas contain highly energetic, neutral, and ionized particles, free electrons, and photons. The fraction of charged particles is typically larger than 1%. Plasma maintenance involves numerous electron-impact reactions (excitation, dissociation, and ionization, amongst the most important ones), which are responsible for the high reactivity of the medium. The excited species, ions, and radicals will react further to create new molecules [12]. In thermal plasmas, the temperature of all species (electrons and heavy species) are approximately equal and high. On the other hand, non-thermal or non-equilibrium plasma (NTP) discharges can produce excited and reactive species at gas temperatures much lower than combustion flames. In NTP, the electron temperature, T_e , can be significantly higher (10^4 - 10^5 °C) than the temperature of the heavy species (25 - 730 °C) [14], T_h , (ions, neutral, excited neutrals, also referred to as the gas temperature) since the exchange of kinetic energy between the electrons and heavy species is very inefficient. Hence, most reaction processes are rate-controlled by the electron temperature [36, 57].

Non-thermal plasma technologies represent an attractive alternative for DRM since expensive high temperature-resistant materials and complex assemblies are not required for reactor construction. Non-thermal plasmas allow CO_2 to be activated efficiently via electron impact at mild temperature conditions [41]. Currently used technologies for the generation of non-thermal plasmas for DRM include dielectric barrier discharges (DBD) [58–62], glow discharges [63, 64], corona discharges [65–68] and gliding arcs [42, 69–73]. Among these technologies, gliding arcs have the most potential and applicability for CO_2 conversion since they operate at atmospheric pressures, and high energy efficiencies can be achieved [41]. In this thesis, the use of a rotating gliding arc (RGA) is investigated for DRM (see Chapter 5 and 6). RGA is a special configuration of a gliding arc, which will be described in the following section.

The reforming of CO_2 - CH_4 by plasma is very complex. However, Tao et al. [74] proposed the simplified reactions occurring in plasma-assisted DRM:



Equations (2.2) and (2.3) are highly endothermic reactions that can be induced by electron impacts. On the other hand, equations (2.4) and (2.5) are radical reactions, which occur without the activation barrier [74]. More detailed reactions regarding the plasma-assisted DRM are stated in Chapter 5, section 5.4.2.

Gliding arc

A gliding arc discharge relies on an auto-oscillating periodic phenomenon that develops between two diverging electrodes submerged in a flowing gas [57]. To sustain the gliding arc, a high-voltage generator (several tens of kVs) produces the electric field required for gas breakdown at the shortest inter-electrode distance ($\sim 30 \text{ kV cm}^{-1}$ in atmospheric air). At the same time, a second, mid-voltage range (a few kVs) but higher-current capability power supply takes over for arc maintenance [75, 76]. However, some specific configurations of the gliding arc, only require a single high-voltage power supply [77–81].

Plasmas generated by gliding arc discharges are also known as “warm” plasmas since they have thermal and non-thermal properties [77, 82, 83]. Three phases occur during the gliding arc evolution, as shown in Fig. 2-6. Phase A) is the thermal stage, where the gas breakdown takes place at the narrowest inter-electrode gap (typically 1–2 mm) and an arc forms. Phase B) the quasi-equilibrium stage when the arc is then forced to move away from the shortest gap area by a gas flow (or natural convection in vertical gliding arc systems). In phase B), the arc length increases, which is associated with a voltage increase, and the plasma evolves to a non-equilibrium state. C) Once the arc voltage (arc length) becomes too large for the power supply, the arc extinguishes. The next arc is ignited at the lowest inter-electrode gap [42, 75, 76, 84].

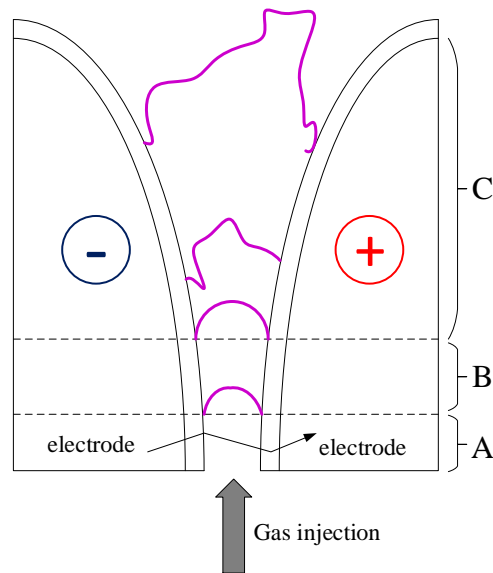


Fig. 2-6 Phases of gliding arc evolution: (A) gas break-down ;(B) quasi-equilibrium stage; (C) non-equilibrium stage. Adapted from [75].

As the length of the arc increases, the gas temperature decreases because the heat losses from the plasma column begin to exceed the energy supplied by the source. Therefore, it is not possible to sustain the plasma in thermodynamic equilibrium anymore. Thus, the heavy species (gas) cool down rapidly, while the electrons maintain a high temperature, $T_e \sim 1$ eV (11,600 K) [75, 76, 80]. The relatively high gas temperature (1000 – 4000 K) in the gliding arc creates favorable conditions for chemical reactions. Theoretically, GA discharges are very promising for the conversion of CO_2 ; however, in practice, they are limited by the low treated gas fraction [41].

To enhance the reactive plasma volume and its uniformity between the electrodes, a special configuration, called a rotating gliding arc (RGA) has been developed by different authors [13, 85–87]. The RGA consists of a conical electrode surrounded by a hollow cylindrical electrode (see Fig. 5-1 in Chapter 5). In this configuration, the reactant gas is injected tangentially to form a swirling flow field. The arc ignites at the shortest gap. Then the arc is pushed away from the break-down area, swirling and elongating around the cone to form a larger and more uniform plasma volume [13, 76]. The arc can also be forced to rotate by the action of an external magnetic field (Lorentz force) [13, 76, 85]. Gas swirl and magnetic forces accelerate the rotation of the arc, increasing the residence time of the reactants, as well as the contact area between the reactants and the plasma, thus enhancing the performance of the conventional gliding arc discharge [13].

Gliding arc discharges have been extensively studied for reforming reactions, pollutant degradation, combustion enhancement, waste and exhaust gas treatment [42, 75, 85, 87, 88], amongst other applications. They present several advantages compared to other plasma sources. For instance, gliding arc discharges can operate at atmospheric pressure (or higher), the reactor construction is simple, which translates in low cost compared to several currently used reactors, and they operate over a wide range of flow rates and power levels (W to several kW). Besides, the high energy content generated by gliding arcs is attractive for chemical processing since endothermic reactions, such as DRM, can use up to 80% of the energy provided by the arc [75]. The properties of the gliding arc discharge depend on the system parameters such as power input and flow rate. However, the optimization of plasma parameters and efficient reaction pathways for CH₄ and CO₂ conversions in GA are still unclear [41]. Hence, a deeper understanding of this plasma technology is required to improve conversion and reduce energy cost, which would lead to further technological development.

The work presented in Chapter 5 studies the influence of operating parameters such as total flow rate, peak current, inlet gas temperature, and CO₂/CH₄ ratio on DRM in a RGA.

2.3.3 Plasma-catalysis

The combined action of a catalytic material with a plasma is known as plasma-catalysis [14]. Plasma-catalysis combines the high reactivity of the plasma with the selectivity of the catalyst, which may lead to products with high yield and selectivity [12]. Combining plasma and catalysis technologies may induce complex synergistic effects since plasma, and catalytic reforming by themselves provide different mechanisms, active species, and reactor characteristics for the reforming reaction. Thus, in plasma-catalysis, both technologies can interact with each other, which changes the performance of the chemical reaction and makes the mechanisms more complex than catalysis and plasma alone [36, 42, 62].

Plasma can influence the catalyst, particularly during the discharge phase, where its structure can be changed by particle bombardments or thermal effects [36]. Kinetic energy and motion of gas molecules are affected by the presence of the catalyst, which alters the electron energy distribution (EED) [2]. The EED in the plasma is determined by the electric field strength and determines the yield of chemical species in the discharge [14]. Besides, when the catalyst is in contact with the

plasma discharge, the catalyst acts as a dielectric barrier that generates micro-discharges inside of the catalyst pores [36]. The nature of the catalyst surface, i.e., roughness and pores, influence the local electric field [14].

Moreover, the adsorbed species on the catalyst are more likely to collide with electrons as the electron-impact reactions take place frequently due to the energy kept inside the pores and gaps [36]. Therefore, the dielectric constant of the catalyst is an important parameter in plasma-catalysis. In fact, a plasma-catalytic reactor can be considered as the combination of conductors and resistors in series, where the catalyst works as a conductor when the electric resistance is small or as a resistor when the electric resistance is large, and the gap between the catalyst particles is considered as another conductor or resistor [36].

On the other hand, plasma can make adsorption of the reactant gases more effective by lowering energy barriers and by increasing the number of active sites on the catalyst, which increases the residence time of the adsorbed species in the plasma zone. As a result, the operating temperature will be reduced, and the yield under plasma conditions will increase [14].

Depending on the catalyst packing strategy, plasma-catalytic reactors can be classified into three classes. (1) Single-stage, in-plasma-catalysis (IPC), or plasma-driven catalysis, where the catalyst is partially or completely placed in the discharge zone, so plasma and catalyst interact directly. (2) Double-stage, post-plasma catalysis (PPC), or plasma-assisted catalysis, where the catalyst is placed downstream the discharge zone. (3) Multistage plasma-catalytic reactors in where each catalyst bed has a different purpose along the flow direction. Multistage reactors are more interesting for industrial applications compared to the previous configurations (i.e., IPC and PPC) [4, 37, 89]. In many cases, single-stage reactors were found better than double stage reactors for different reactions, including DRM [4, 89]. For instance, Wang *et al.* [90] investigated three different packing modes of the Ni/Al₂O₃ catalyst in a DBD reactor for DRM. They concluded that the synergy between plasma and catalyst was only observed when the catalyst was completely placed in the discharge zone, i.e., single-stage reactor. However, incorporating a catalyst inside the plasma reactor does not necessarily induce a synergistic effect, i.e., better conversion rate or product selectivity [4]. For instance, in the case of a DBD reactor, where the catalyst was fully packed into the gap, the formation of filamentary micro-discharges was suppressed as the discharge volume decreased [91]. As a result, the conversion could be reduced to a large extent

[4]. Wang *et al.* [92] studied the reforming of CO₂ and CH₄ into high-value liquid chemicals in a plasma-catalytic DBD reactor. They found that plasma-catalysis yields slightly lower conversion of CO₂ and CH₄ than plasma alone, and they attributed this effect to the change of discharge behavior as a result of the full packing of the catalyst in the reactor. However, the selectivity towards specific liquid products increased when combining plasma-catalysis. Lee *et al.* [80] studied the reforming of methane in a single-stage gliding arc reactor. They concluded that there was a decline in CH₄ conversion because of the distortion of the discharge by the catalyst; however, an increase in product selectivity was also observed. Li *et al.* [77] investigated the DRM in a double-stage gliding arc-fixed bed reactor. They concluded that the combination of plasma and catalyst increased CH₄ and CO₂ conversion, as well as the energy efficiency of the process. Gallon *et al.* stated [93] that the synergistic effect of the combination of plasma and catalyst at constant discharge power and low temperatures for reforming reactions depends on the balance between the change in discharge behavior induced by the catalyst and the plasma-generated activity of the catalyst.

In general, the interactions between plasma and catalyst depend on several factors (Fig. 2-7), such as operating temperature, power input, dielectric constant, reactor geometry, packing method of the catalyst, basicity of the catalyst, etc. [36]. Whereas, the kinetics of the rate determining step of the reaction will depend on the reaction conditions, including pressure, means of plasma excitation, nature of the catalyst, and occupancy of the surface sites on it [14].

The use of plasma-catalysis in reactions, such as DRM, has the potential to enhance gas conversion, improve selectivity towards syngas, increase energy efficiency, improve stability of the catalyst, reduce sintering and poisoning of the catalyst, as well as coke formation [14, 37, 62]. Besides, plasma-catalysis could decrease the activation barrier of CO₂ and CH₄, and therefore improve the reaction rate [94].

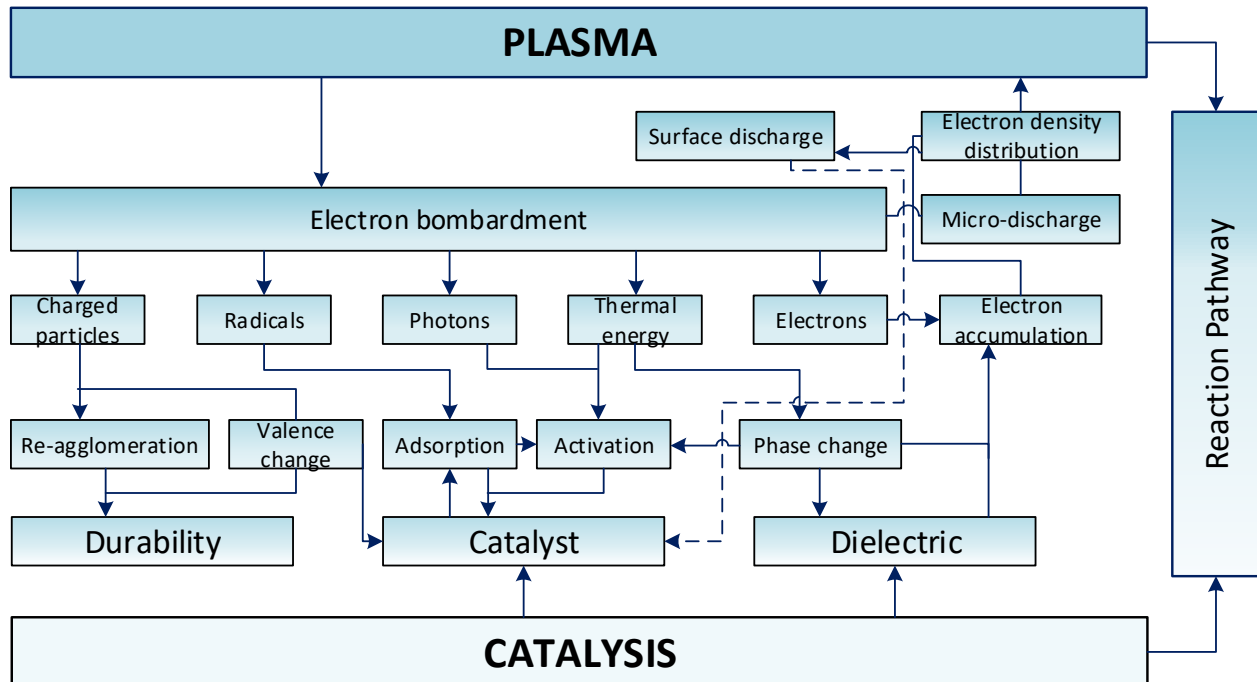


Fig. 2-7 Interaction between plasma and catalysis. Adapted from [36].

In this dissertation, the effects of plasma-catalysis have been studied for DRM in a single-stage plasma-catalytic reactor, i.e., rotating gliding arc combined with a spouted bed, to answer the question if there is a synergistic or antagonistic effect when combining plasma and catalyst. The work presented in Chapter 6 studies the influence of different catalyst characteristics on CO_2 and CH_4 conversions, as well as H_2 and CO yields for plasma-driven catalysis of DRM. These catalyst characteristics include: two different Ni-based catalysts ($\text{Ni}/\text{Al}_2\text{O}_3$ and Ni/SiO_2), percentage of metal loading (15 and 30% wt.), reduced and non-reduced catalysts.

3

Methodology

3.1 Experimental Setup

Fig. 3-1a shows a picture of the whole reactor assembly, this includes the homemade dual stage pulsed DC power supply (on the left) and the mass spectrometer (on the right), described in the following sections.



Fig. 3-1 (a) Photograph of the RGA setup. (b) Infrared photograph of the RGA reactor during DRM reaction. Taken with Cat S61 FLIR camera.

The plasma reactor is made of stainless steel 316, and it consists of a cone surrounded coaxially by a hollow cylinder. The cone (Fig. 3-2a) screws to a $\frac{1}{4}$ inch hollow tube. This assembly acts as a cathode and allows the cone to be replaced whenever needed. At the other end of the tube, a

SwagelokTM tee was adapted to connect the dual-stage power supply to the cathode. Two spacer pieces serve as a base for the reactor while also act as an electric insulator between the two electrodes: (1) A DelrinTM piece (polyoxymethylene, later PEEK, polyether ether ketone) (Fig. 3-2b) and (2) a ceramic piece (glass-ceramic, MacorTM) (Fig. 3-2c).

The reactor is mounted vertically on the two pieces described above, and it has on both ends two 6-hole flanges of 1/2 inch thickness each. The lower flange of the reactor bolts to the DelrinTM piece while the reactor sits on an O-ring on the ceramic piece. The process gases are injected in the reactor by two sets of three equally-spaced tangential tubular inlets that uniformly cover the circumference of the reactor, one set on top of the other. The gas injectors are mounted at an angle of 20° from the horizontal plane of the system and allow the gas to swirl counterclockwise (Fig. 3-3). On the upper part, the reactor is terminated with ConFlat (CF) tee adaptor that enables direct line-of-sight view along the reactor axis on the top, and a gas exhaust on the side. A stack of four ring magnets is mounted around the grounded anode cylinder to add a static axial magnetic field. The magnets are oriented such as to provide a Lorentz force acting along the gas drag force. More details about the complete setup, as well as the corresponding schematic, are stated in Chapter 5, section 5.3 (Fig. 5-1).

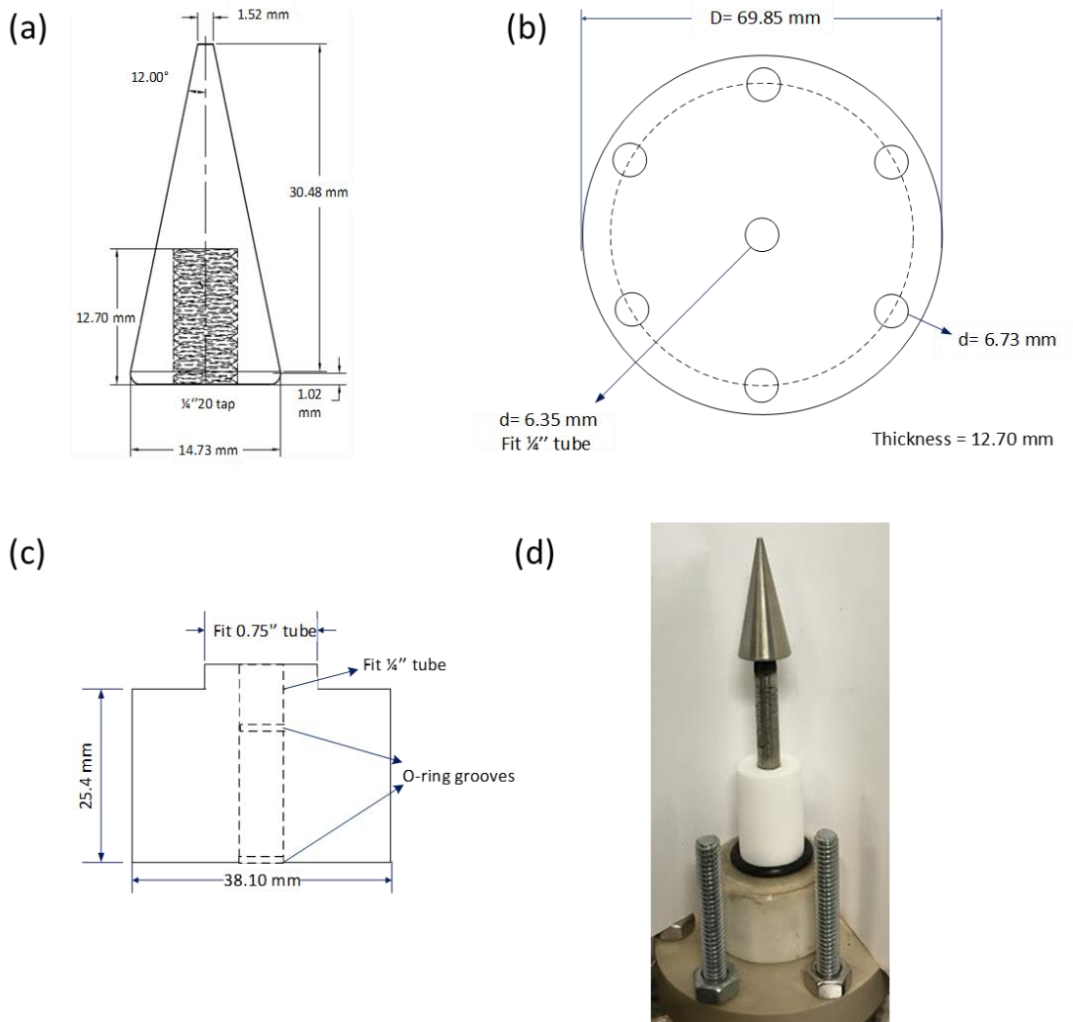


Fig. 3-2 Technical drawings of (a) the conical electrode, (b) Delrin™ plate, and (c) ceramic base. (d) Digital photograph of the assembly. An extra ceramic piece (cylinder) was added for the plasma-catalytic experiments to the setup.

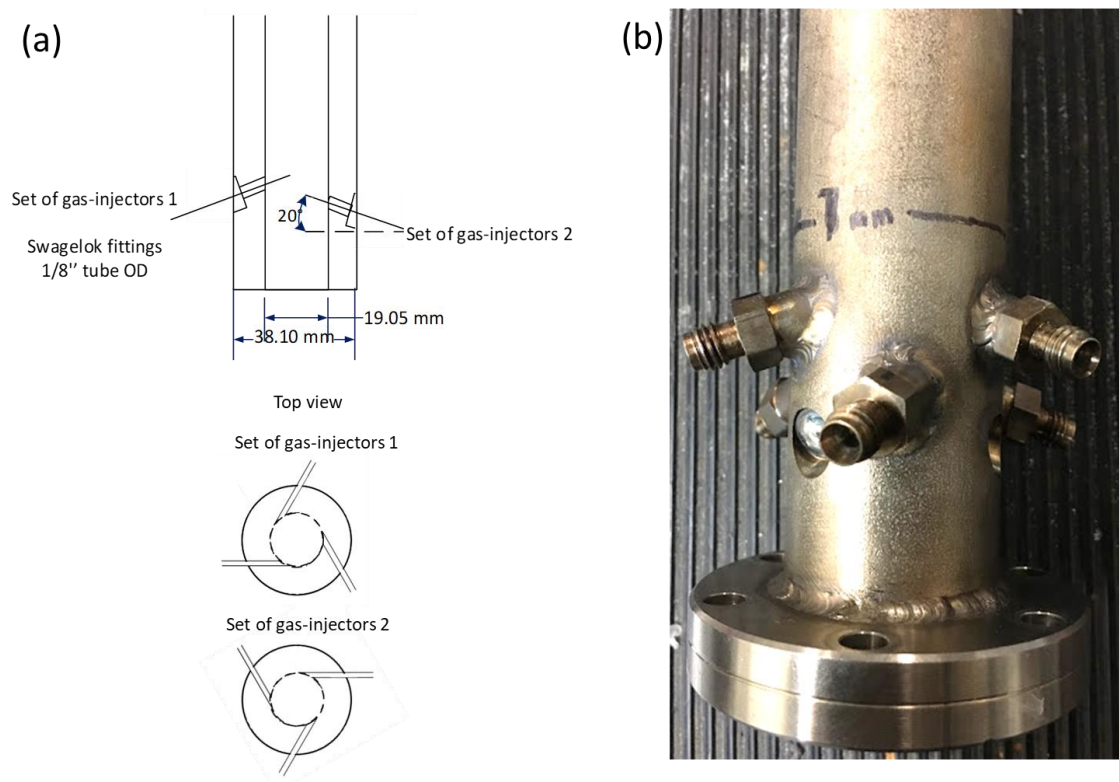


Fig. 3-3 Gas injector assembly (a) technical drawing and (b) digital photograph.

For the experiments described in Chapter 5, section 5.4.3, an additional component was added to the setup to preheat the gas. A gas heater was developed by filling a tube (91.4 cm long by 2.54 cm diameter) with approx. 700 g of silicon carbide (SiC, carborundum, Fisher Scientific, mesh 12, 1.70 mm). The carborundum has a high thermal conductivity ($120 \text{ W m}^{-1} \text{ K}^{-1}$) that allows heating the gas when it passes through the space between the SiC particles. Then, the tube was covered entirely with electrical heating tape, and a thermocouple measured the wall temperature (Fig. 3-4a, b). The gas heater was placed after the gas mixer and before the manifold that distributed the gases through the six gas inlets. An additional thermocouple measured the temperature of the gas just before the reactor (in the manifold). Moreover, the material of the gas lines was replaced by copper tubing instead of nylon tubing (Fig. 3-4c, d) to prevent melting during the high-temperature experiment. All the gas lines and manifold were wrapped with ceramic fiber insulating strip to avoid heat losses through the walls as much as possible.

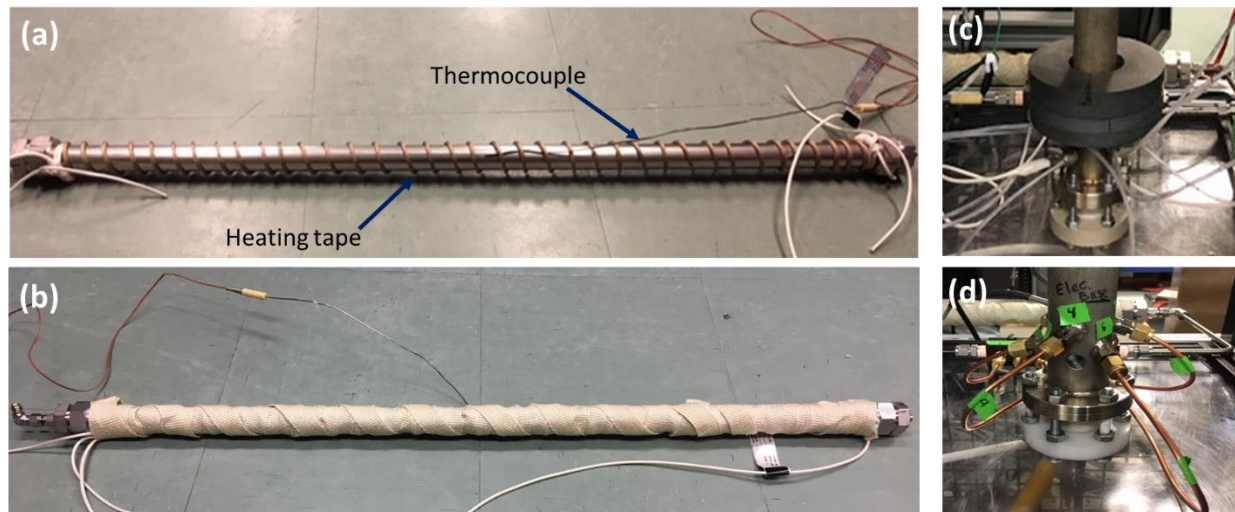


Fig. 3-4 Gas heater wrapped with heating tape (a) before being covered with insulation, (b) after being insulated to avoid heat losses. (c) Nylon tubing for gas injectors, (d) Cooper tubing for gas injectors for the high-temperature experiment.

For the experiments described in Chapter 6, an additional ceramic piece (glass-mica) was added to fill the gap between the base of the reactor and the gas inlets, and thus avoiding the catalyst falling to the base and not fluidize (Fig. 3-2d and Fig. 3-5).

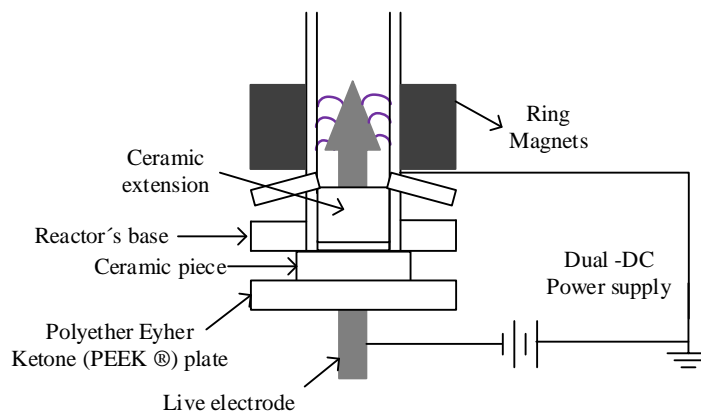


Fig. 3-5 Detailed schematic of the base assembly.

3.2 Power Supply

A homemade dual-stage pulsed DC power supply was used to ignite and sustain the plasma discharges. The power supply combines an arc igniter and a current driver. The arc igniter produces

a constant train of high-voltage pulses, of magnitude above the breakdown voltage of the gaseous gap. The igniter was designed based on [76, 95]. It consists of a 5-stage Cockcroft-Walton Voltage Multiplier (CWVM) that converts a low voltage high-frequency AC to a pulsed negative high-voltage DC signal (output voltage ~ -4.5 kV).

Fig. 3-6 shows the electric circuit for the arc igniter, it consists of a 12 V, 2 A DC charger, a DC - to -high voltage AC inverter (3 kV, 15 mA, Plasma Power Generator, MINIMAX30), a 5-stage CWVM, a 3 M Ω current limiting resistor, and a charging capacitor (1 nF). Each stage of the CWVM consists of 2 capacitors (100 pF) and 2 diodes (1 kV/1 A). Once that the gaseous breakdown has taken place, the current driver takes over and provides the required current to sustain the gliding arc while providing enough voltage for the arc to elongate through the inter-electrode gap. The current driver consists of a resistor-capacitor (RC) circuit driven by a 2.5 kW negative polarity capacity-charging power supply with -1000 V open-circuit voltage (Analog Modulus, Inc. model 5743). An additional set of high-voltage diodes is used to prevent current or high voltage exposure on each power supply [96].

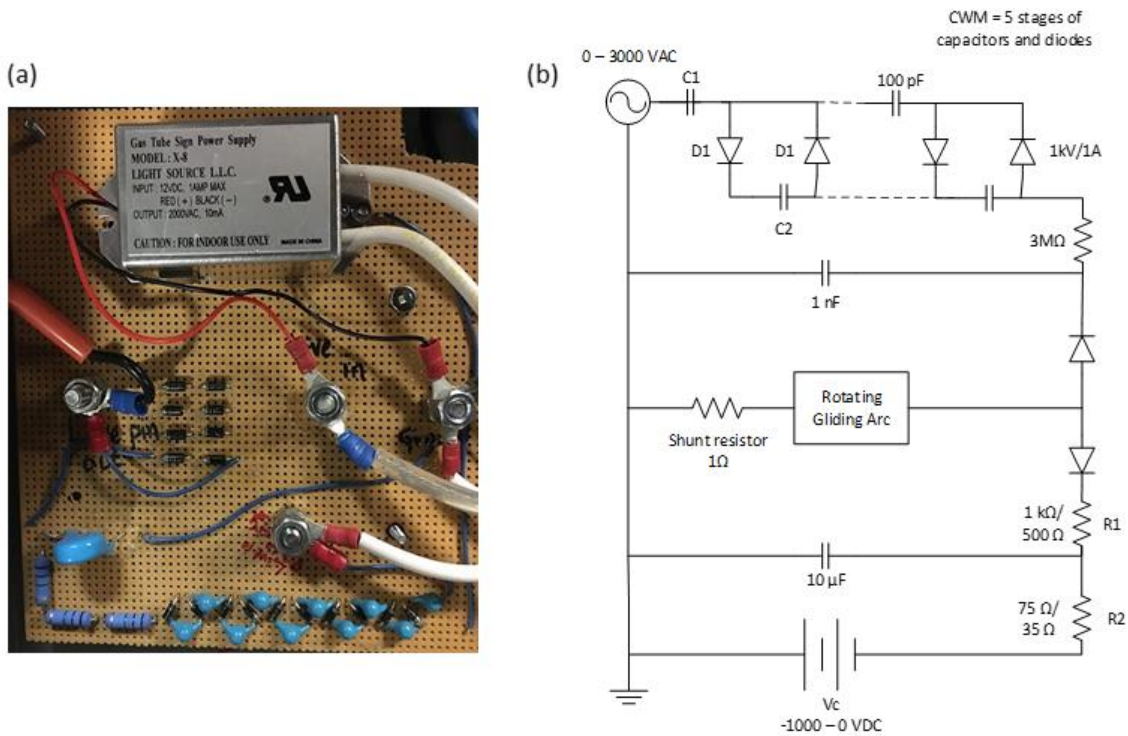


Fig. 3-6 (a) Photograph of the igniter circuit. (b) Electrical circuit of the homemade power supply. On top, the CWM and on the bottom the current driver power supply. Adapted from [96].

3.2.1 Electrical Measurements

The electrical characteristics of the plasma discharge, i.e., voltage and current, were monitored using a high-voltage probe (B&K Precision PR55) and a passive voltage probe (Tektronix P2200) across of a 1 Ω shunt resistor connected to a digital oscilloscope. The electrical measurements obtained were used to calculate the instantaneous and average discharge powers, and cumulative energy deposition in the plasma discharge.

One of the main problems was the interference of the high-frequency noise caused by the igniter power supply to the electronic equipment. Hence, a Tektronix model MSO2012 benchtop oscilloscope was used to monitor the electrical signals during the experimental phase, to ensure that the plasma discharge was working correctly. However, these data could not be saved directly from the oscilloscope, due to the high-frequency interference. To solve this issue, a PC oscilloscope (PicoScope 2408B) connected directly to the computer was used to record the electrical characteristics of the discharge as it was not affected by the high frequencies. The PC

oscilloscope was set to record 50 frames for every experimental condition (sample rate 1 GS/s), and a low pass filter was activated to filter the noise of the signals. The obtained waveforms were processed using a script written in MATLAB® for further processing.

3.3 Instrumentation

All experiments described in the chapters that follows were performed by using the instruments described below. Gas flow rates were controlled by calibrated rotameters. Gas products were analyzed on-line by a calibrated mass spectrometer and off-line by a gas chromatographer equipped with a thermal conductivity detector. Carbon byproducts were analyzed by Scanning Electron Microscopy (SEM) and Raman Spectroscopy. The catalysts were characterized by Inductively Coupled Plasma-Optical Emission Spectroscopy (ICP-OES), X-Ray Diffraction (XRD), X-Ray Photoelectron Spectroscopy (XPS), SEM, physisorption and chemisorption methods, as well as temperature-programmed reduction and oxidation methods.

3.3.1 Mass Spectrometry

Mass spectrometry (MS) is a simple technique to analyze the composition of the gas. The mass spectrometer measures the mass-to-charge ratio of ions, and a plot of intensity in amperes as a function of the mass-to-charge ratio is displayed as the result of the measurement. Throughout the thesis, mass spectroscopy was used as the main analytical technique to analyze/quantify the composition of the reforming products. The Faraday-type detector (measures percentage levels) with a secondary electron multiplier (SEM, ppm level detection) can acquire mass spectra from 0 to 200 atomic mass units (amu). The MS (Pfeiffer Ominstar GSD 301) operation and data acquisition were controlled by the computer using the Quadstar 32-bit software. The following instrument parameters were set for the MS operation: Ion – ref (150 V), Cathode (80 V), Focus (7.00 V), Field axis (5.88 V), and Extract (31V), Mode (Emission), Speed (1 s).

The capillary of the MS was connected on-line at the exit of the reactor and before the gas exhaust. A particle filter with a 2 μm frit was adapted to the capillary to ensure that no solid particles were transported inside the MS. The capillary heater was on and its temperature was maintained at 200 °C at all times.

Argon was used as an internal standard with a calibration factor of 1. The calibration factors of the other gases were calculated using eq. 3.1:

$$Cal. factor_i = \frac{[A_i]}{[A_{Ar}]} \cdot \frac{Conc. Ar}{Conc. i} \quad (3.1)$$

[A] is the intensity of the species in amperes and conc. stands for concentration of the calibration gas in vol %. Typical values of calibration factor for other gases are between 0.7 and 1.2. The MS was calibrated using three different calibration gas mixtures with compositions presented in Table 3-1.

Table 3-1 Composition in vol% of the calibration gases.

Calibration gas	H ₂ [vol%]	CO [vol%]	CO ₂ [vol%]	CH ₄ [vol%]	Ar [vol%]
1	0.502	--	--	--	Balance
2	20.00	--	4.979	10.03	Balance
3	14.93	15.19	14.98	14.90	Balance

Note: According to the supplier (MEGS, Specialty Gases) the composition of the calibration gases is reported with an uncertainty of $\pm 2\%$ for concentrations $> 5\%$ and $\pm 5\%$ for concentrations $< 0.5\%$. The uncertainties are calculated in relative percentage

The contribution of CO₂ fragmentation to the CO signal (mass 28) was considered in the calibration.

3.3.2 Gas Chromatography

Gas chromatography is another analytical technique used to quantify the concentration of a gas mixture once its composition is known. Gas chromatography was used to measure/analyze the byproducts of the reforming reaction, i.e., acetylene and ethylene, for which the MS was not calibrated. The gas chromatographer (GC, Agilent 6890N) was used offline, and it was equipped with a thermal conductivity detector (TCD). Hence, the gas samples obtained as a product of the DRM reaction were collected in gas sample bags (SupelTM Inert Multi-Layer Foil) and injected into the GC using a 1 mL syringe (Hamilton, 1000 series GASTIGHT). Argon was the carrier gas that transported the gas sample through the column and into the detector.

The GC was equipped with two 10 m capillary columns: a CP-Molecular sieve 5 Å for permanent gases such as CH₄, H₂, CO, N₂, O₂, and a Plot-Q for CO₂ and C₂-C₄ hydrocarbons. These columns retain each gas for a specific time depending on the column and injector temperature, and the intermolecular interactions with the stationary phase. The GC was calibrated by injecting different amounts of the calibration gas 3 (from Table 3-1) as well as C₂H₂ (99%, MEGS Specialty Gases) and C₂H₄ (99.999%, MEGS Specialty Gases) to obtain a linear calibration curve. Once the chromatogram was recorded, the peaks for the different gas components were integrated to obtain the area under the curve, which is related to the concentration of the gas by the calibration curve.

3.3.3 Optical Emission Spectroscopy

Optical Emission Spectroscopy (OES) is a technique that uses the light emitted by the plasma discharge to identify various species. The optical spectrometer used was an Ocean FX spectrometer (Ocean Optics, 25 μm slit, extended range 200 – 1100 nm) with an optical resolution of 0.78 nm. The measurement of the optical emission spectra was performed using an optical fiber placed on top of the quartz viewport (approx. 49 cm on top of the arc region) to collect the plasma radiation face-on. The spectra were collected for off-line analyses.

3.4 Fluidization Tests

Fluidization tests were performed for the plasma-catalytic experiments reported in Chapter 6. These experiments were made to visualize the catalyst fluidization in the plasma reactor as the plasma reactor is made of stainless steel, the fluidization cannot be seen in it. Hence, a transparent acrylic (Plexiglass™) reactor with similar dimensions was used to determine the best fluidization conditions, i.e., amount of catalyst, catalyst particle size, and total flow rate. The acrylic reactor consists of a conical electrode (which height inside of the reactor can be adjusted) mounted coaxially inside of a hollow cylindrical CF 1–1/3 fitting, with an inner diameter of 17.47 mm and an outer diameter of 19.05 mm. The acrylic reactor sits on top of the CF fitting, while an O-ring is used to seal the connection between the two parts. Unlike the stainless-steel reactor, the six tangential gas inlets are at the same height (misunderstanding with the manufacturer). However, no major impact of this difference was expected for the final results. This diameter continues

downstream for 241.0 mm, and then it expands up to 63.5 mm to reduce the gas velocity to avoid particle entrainment. The experiments to determine the best fluidization conditions were performed with Ar and using the catalyst supports only (i.e., Al_2O_3 and SiO_2); keeping the same gas velocity in both reactors.

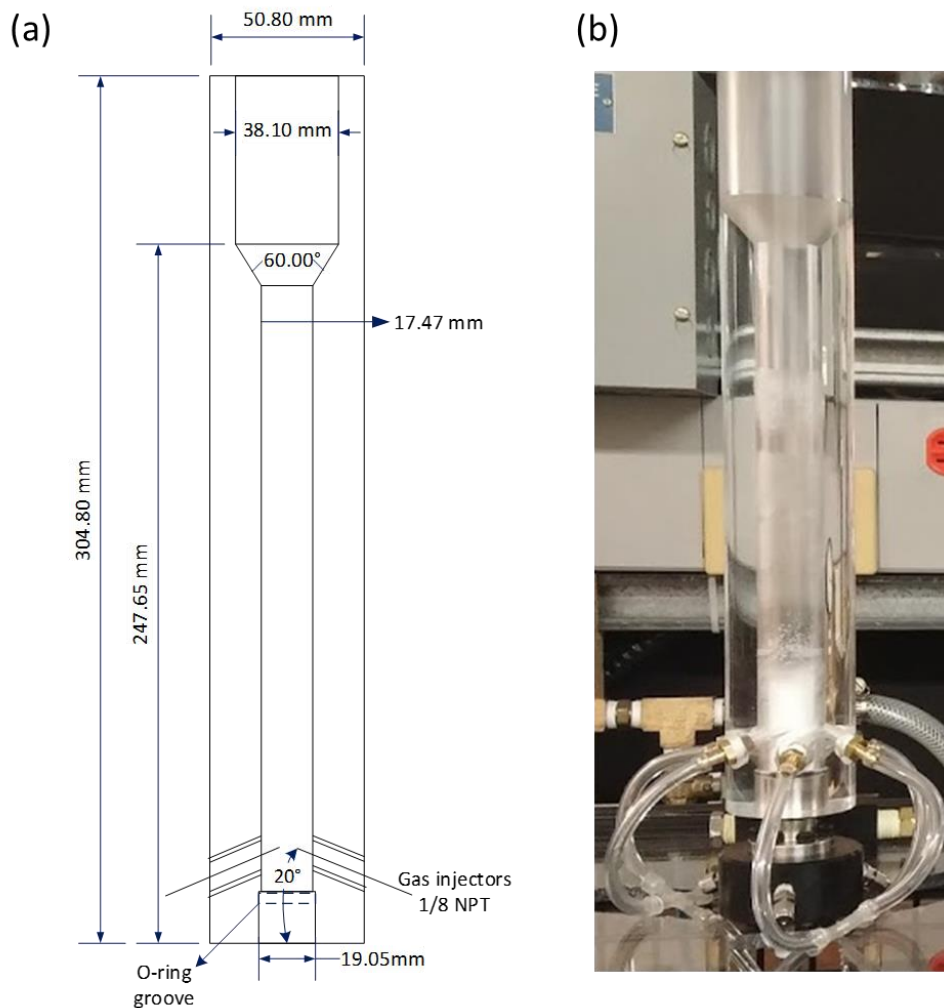


Fig. 3-7 Acrylic reactor (a) technical drawing and (b) digital photography of the reactor with catalyst support inside.

3.5 Catalyst Preparation

For the experiments performed in Chapter 6, the effect of catalyst and plasma in the DRM reaction was studied. The incipient wetness impregnation method was chosen to prepare the catalysts. In this method, the support is in contact with a solution of appropriate metal concentration of the

precursor, which in quantity corresponds to slightly more than the total known pore volume or until it looks wet. However, one of the drawbacks of this method is that the redistribution inside of the pores is very slow [97].

In incipient wetness impregnation, nickel nitrate hexahydrate ($\text{Ni}(\text{NO}_3)_2 \cdot 6\text{H}_2\text{O}$, $\geq 98.5\%$, Sigma Aldrich) was dissolved in water ($\sim 1.80 \text{ mL g}^{-1}$ for Al_2O_3 and $\sim 1.75 \text{ mL g}^{-1}$ for SiO_2). Note that the Ni salt contains water, which significantly contributes to the total amount of H_2O added to the support, making the support wetter than it should be. To solve this issue, the correct amount of water was measured previously in the vial, and the volume marked. Then, the needed amount of Ni salt was weighed in the vial. Later, water was added until the meniscus of the solution was at the line previously marked and stirred until complete dissolution. Next (see Fig. 3-8), the Ni solution was added drop by drop to a flat layer of the alumina (catalyst support, Alfa-Aesar) or silica ($\geq 99\%$, Sigma-Aldrich) using a micropipette. The impregnated support was left at room temperature overnight to allow the Ni to distribute in the pores of the support. Afterwards, the sample was dried for 8 h at $80 \text{ }^\circ\text{C}$ and subsequently calcined in a muffle furnace with a heating rate of $1 \text{ }^\circ\text{C min}^{-1}$ for 5 h at $500 \text{ }^\circ\text{C}$.

Samples with two different nickel loadings (15 and 30 wt. %) and two different supports (Al_2O_3 and SiO_2) were prepared. The particle size for all the alumina samples was 90 to $125 \text{ }\mu\text{m}$ (support previously crushed and sieved) and 150 to $250 \text{ }\mu\text{m}$ for the silica samples (provided by the supplier).

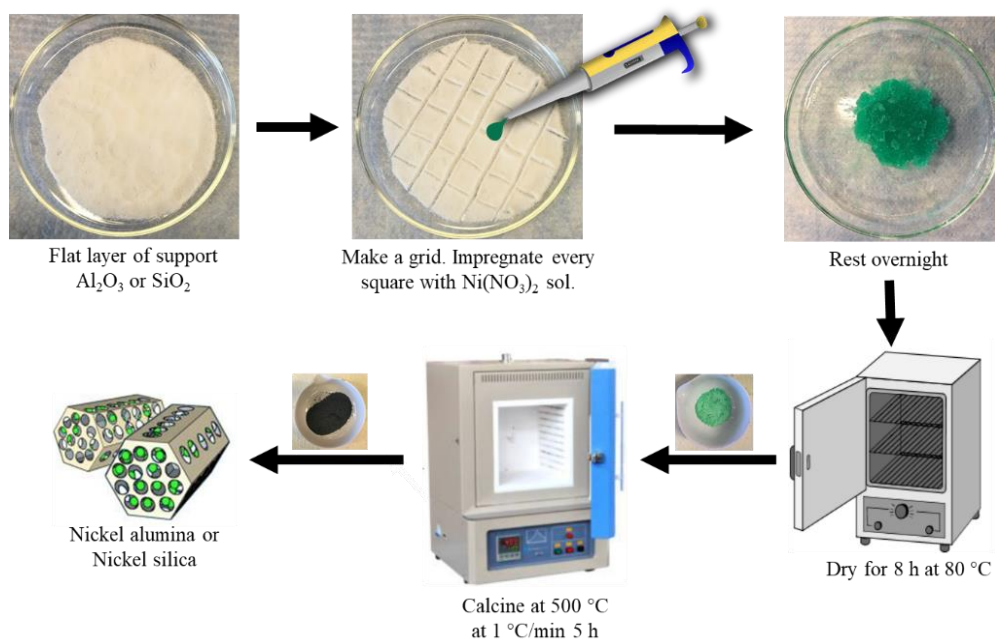


Fig. 3-8 Scheme of catalyst preparation procedure with incipient wetness impregnation method.

3.6 Catalyst Characterization

Different characterization techniques were used to study the catalysts according to pore size, surface area, composition, and reduction temperature of the catalyst. For SEM, XRD and XPS, more details are provided in Chapter 6.

3.6.1 Inductively Coupled Plasma-Optical Emission Spectroscopy

The actual nickel content of the catalysts was determined by Inductively Coupled Plasma-Optical Emission Spectroscopy (ICP-OES). The catalysts supported on alumina (100 mg) were first digested using a mixture of 2 mL of hydrochloric acid (37 wt.%, Fisher Scientific) and 5 mL nitric acid (67 wt.%, Fisher Scientific) at $95\text{ }^\circ\text{C}$ for 2 h. The resulting liquid samples were diluted and analyzed using an ICP-OES (iCAP 6500 dual view, Thermo Scientific). The ICP-OES was calibrated previously using nickel standards diluted at 0.5, 5, 50 ppm and the concentration of the nickel in the samples was measured at a wavelength of 231.6 nm.

For the catalyst samples supported on silica, a digestion method called fusion flux was used. The catalyst was fused with twice the amount (by weight) of lithium tetraborate (SCP science) in a 9 mL graphite crucible (SCP science). The fusion was heated up in a muffle furnace to 950 °C, and held at this temperature for 30 min. Once the samples were cooled down, acid digestion was applied to them by using a mixture of 6 mL of hydrochloric acid and 2 mL nitric acid at 95 °C for 3 h. The resulting liquid samples were diluted and analyzed using an ICP-OES.

3.6.2 Adsorption/Desorption Measurements

Nitrogen adsorption/desorption measurements (196 °C) were conducted using a Micromeritics Gemini VII 2390t analyzer to determine the total surface area, pore size distribution, and pore volume of fresh samples. Previous to the analysis, the samples (100 mg) were degassed with helium overnight at 250 °C.

The volumetric hydrogen uptake or chemisorption was conducted using an Autosorb iQ (Quantachrome) gas sorption instrument. Fresh catalyst (100 mg) was placed in a U-shape quartz tube. The samples were preheated first with He at a heating rate of 20 °C min⁻¹ up to 120 °C and maintained at this temperature for 0.5 h, then 5 vol% of H₂ was introduced to reduce the samples for 3 h at the reduction temperature obtained previously from TPR at a heating rate of 10 °C min⁻¹. Afterwards, the gas mixture was evacuated for 1 h, and the catalyst was cooled down to 40 °C. The active surface area (m² g⁻¹), metal dispersion (%), and average crystallite size (Å) were calculated based on the amount of H₂ absorbed, the stoichiometry of the reaction H/Ni = 1, and a hemispherical cluster with a nickel density of 8.9 g cm⁻³.

3.6.3 Temperature Programmed Reduction

Temperature Programmed Reduction (TPR) of the catalysts was carried out in the fixed bed reactor (FBR) setup connected to a calibrated mass spectrometer (Pfeiffer Ominstar GSD 301). The catalyst samples (100 mg) were heated up under Ar atmosphere (50 mL_N min⁻¹, 99.999%, Praxair) with a rate of 5 °C min⁻¹ to 200 °C maintained at the same temperature for two hours to remove moisture. Then, Ar flow was reduced to 80% (40 mL_N min⁻¹), and 20 % of H₂ was introduced to the reactor (10 mL_N min⁻¹, 99.999%, Megs Specialty Gases) to reduce the sample. Finally, the

catalyst was heated up at $4.5\text{ }^{\circ}\text{C min}^{-1}$ to $700\text{ }^{\circ}\text{C}$ and held at this temperature for 3 h while recording the mass to charge ratio for water ($m/z = 18$) with the MS.

3.6.4 Activity Test

The activity test of the catalysts was carried out in the fixed bed reactor (FBR) setup (Fig. 3-9). The FBR consists of a quartz tube (I.D. 7 mm) with a 15-40 μm frit at the bottom. The quartz tube was inserted into a 0.5 in. stainless steel 316 reactor with a counter-current flow configuration. The reaction temperature was controlled by a K-type thermocouple inserted into the catalytic bed. The gas flow rates were controlled by calibrated high-precision Vögtlin red-y smart controller GSC (Switzerland). The exit gas line was electrically heated between 110 and $120\text{ }^{\circ}\text{C}$ to avoid water condensation. A split stream of the exit gas was analyzed using a calibrated mass spectrometer (Pfeiffer Omnistar GSD 301). The activity test was performed considering the same Gas Hourly Space Velocity (GHSV) used for the plasma-catalytic reactor, i.e., $148\text{ L h}^{-1}\text{ g}_{\text{cat}}^{-1}$. Thus, the catalyst samples (approx. 40.05 mg) were diluted with approx. 59.95 mg of catalyst support (Al_2O_3 or SiO_2) and placed in the reactor. Afterwards, the samples were heated up under Ar atmosphere ($100\text{ mL}_N\text{ min}^{-1}$, 99.999%, Praxair) with a rate of $4.5\text{ }^{\circ}\text{C min}^{-1}$ to $200\text{ }^{\circ}\text{C}$ and held at this temperature for two hours to remove moisture. Then, Ar flow was reduced to 80% ($80\text{ mL}_N\text{ min}^{-1}$), and 20 % of H_2 was introduced to the reactor ($20\text{ mL}_N\text{ min}^{-1}$, 99.999%, Megs Specialty Gases) to reduce the sample at its respective reduction temperature previously determined via H_2 -TPR (see section 3.6.3) for 2 hours. Once reduced, the catalyst was heated at $4.5\text{ }^{\circ}\text{C min}^{-1}$ to $700\text{ }^{\circ}\text{C}$ and this temperature was maintained for 3 h. H_2 flow was closed, while Ar flow was reduced to 70% ($70\text{ mL}_N\text{ min}^{-1}$), and 18% of CO_2 ($18\text{ mL}_N\text{ min}^{-1}$, 99.999%, Megs Specialty Gases), as well as 12% of CH_4 ($12\text{ mL}_N\text{ min}^{-1}$, 99.999%, Megs Specialty Gases), were introduced to the reactor to keep a CO_2/CH_4 ratio of 1.50. The mass to charge ratios for all the species were recorded with the MS.

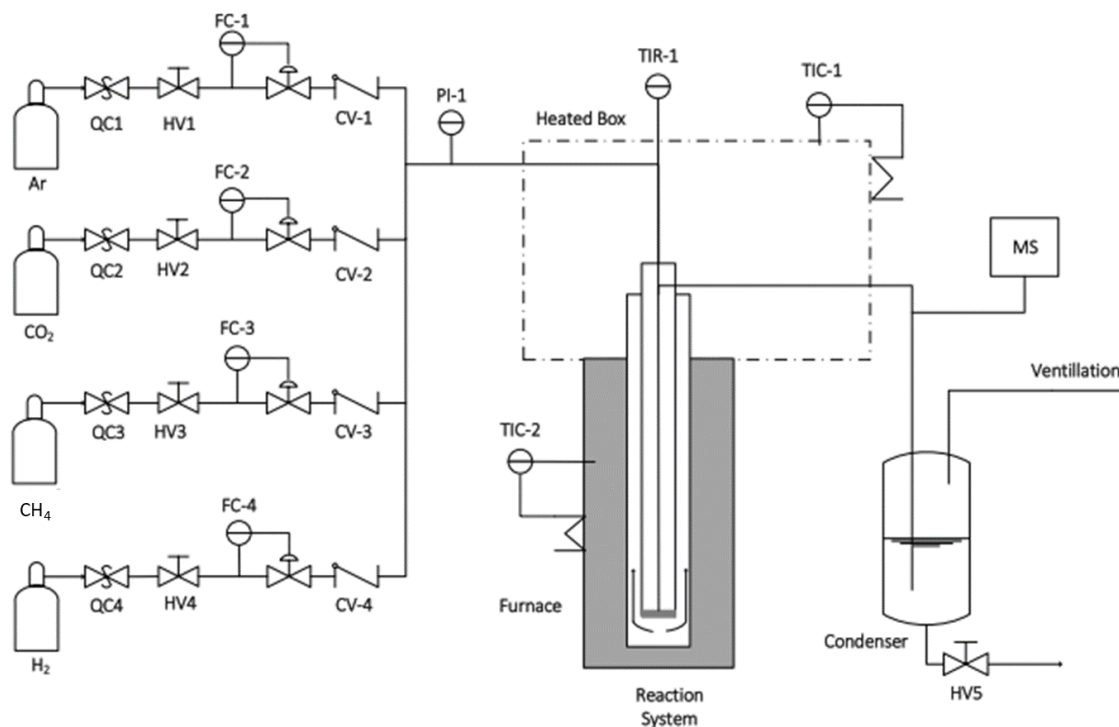


Fig. 3-9 Schematic of the fixed bed reactor (FBR). Taken from [11].

3.6.5 Temperature Programmed Oxidation

Temperature-programmed oxidation with thermogravimetric analysis and mass spectrometry (TPO-TGA-MS) was carried out for the fresh and spent catalysts (TG 209 F1 Libra, Netzsch Instruments) to determine the amount of carbon present on the samples. Approximately, 25–30 mg of catalyst were placed in a ceramic crucible inside of the equipment. Then, the sample was heated with Ar at the rate of $5\text{ }^{\circ}\text{C min}^{-1}$ to $110\text{ }^{\circ}\text{C}$ and held at this temperature for 2 h to remove moisture. After, the sample was heated up to $950\text{ }^{\circ}\text{C}$ at $2.5\text{ }^{\circ}\text{C min}^{-1}$ with 66% air and held at this temperature for 40 min to combust possible carbon deposition. The CO_2 evolution was recorded during the whole process.

4

CO₂ methanation: A graphic approach for the design of Bubbling Fluidized Bed reactors

4.1 Preface

This chapter presents the development of working diagrams for the design of Bubbling Fluidized Bed Reactors for the CO₂ methanation reaction results. The work was executed and analyzed by J. Martin-del-Campo. J. Kopyscinski did the supervision of the research and manuscript reviewing. The citation for this chapter is:

Martin-del-Campo, Jennifer and Jan Kopyscinski. 2020. “*Working Diagrams to Identify the Operating Range of a Bubbling Fluidized Bed Reactor for the CO₂ Methanation*” The Canadian Journal of Chemical Engineering 99 (3):803-12. <https://doi.org/10.1002/cjce.23868>

CO₂ methanation is a technologically mature process currently used for CO₂ valorization. The CO₂ methanation reaction is the core of P2G. Hence, the adequate selection of the methanation reactor is decisive for the effective operation of the process. Fluidized bed methanation reactors offer the required flexibility for the P2G process. However, Bubbling Fluidized Bed reactors are limited by the hydrodynamics. In this chapter, working diagrams to visualize a decision window for determining the reactor diameter, as well as to determine the operating range for a given reactor size, have been developed. The diagrams are based on the hydrodynamic equations for BFB

reactors and the reaction thermodynamics. The influence of temperature, pressure, and catalyst particle size on the design and operating parameters were investigated. The variation of each parameter produced a change in the minimum fluidization velocity, superficial gas velocity, and terminal velocity, which consequently affected reactor diameter and turndown ratio.

It was found that changing pressure provides higher flexibility in terms of turndown ratio, whereas increasing the operating temperature increases the reactor diameter as a consequence of gas expansion. These diagrams can be used as a base for reactor design and to determine operating conditions for BFB reactors. The same methodology explained in this manuscript can be used to other reactions besides CO₂ methanation, such as reforming reactions. In any case, the reaction thermodynamics must be considered.

Working diagrams to identify the operating range of a bubbling fluidized bed reactor for the CO₂ methanation

Jennifer Martin-del-Campo, Jan Kopyscinski

Catalytic Process Engineering, Department of Chemical Engineering, McGill University,
Montreal, Quebec, Canada

Abstract. Fluidized bed reactors for the catalytic CO₂ methanation is a promising concept within the Power-to-Gas (methane) process. Due to the intermittency of renewable electricity generation and thus hydrogen production, the subsequent methanation reactor should also be able to operate at lower feed flow rates, while maintaining fluidized bed conditions. Bubbling fluidized bed reactors offer the required flexibility as shown with the new type of working diagrams. These working diagrams visualize a decision window for (1) determining the reactor diameter and (2) operating the fluidized bed reactor with a turndown ratio of 0.5 to 1.1. Reducing the turndown ratio (i.e., inlet flow rate) could lead to defluidization, thus increasing temperature or reducing the pressure are alternatives to maintain fluidization conditions. The former method is not desired, as a temperature increase would significantly reduce the CH₄ yield due to thermodynamic constraints and therefore reduce the overall efficiency. An industrial CO₂ methanation reactor, for example, that is designed for 10 bara and 340 °C with a total inlet flow rate of 5000 m³_N h⁻¹ (H₂/CO₂ = 4) can be operated at a turndown ratio of 0.5 (2500 m³_N h⁻¹) at the same temperature and the same u_0/u_{mf} ratio by reducing the pressure to 5 bara with only a slight decrease in the CO₂ equilibrium conversion from 96.7% to 94.6%.

4.2 Introduction

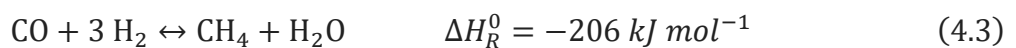
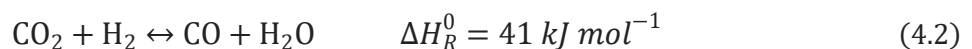
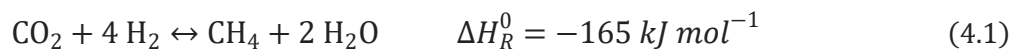
Fluidized bed reactors operating in the bubbling regime are ideal for heterogeneous catalyzed reactions, as they allow high heat and mass transfer rates [31]. In bubbling fluidized bed reactors (BFBR), the mixing of the solid catalyst leads to isothermal conditions along the reactor axis and provides excellent temperature control [31]. These features make fluidized bed reactors suitable for fast and highly exothermic and endothermic reactions [98–101]. Moreover, in the case of catalyst deactivation due to coking, the catalyst can easily be replaced or regenerated in the same reactor [30, 102]. For instance, for the Fischer-Tropsch (FT) process, BFBR have been developed at the Cartage Hydrocol FT plant in the USA for High-Temperature FT (HTFT), operating at 305–345 °C and 21–45 bara. SASOL I plant integrated HTFT (340 °C, 20 bara in a Circulating Fluidized Bed) with Low-Temperature FT (LTFT) operating at 230 °C, 27 bara in a BFBR [103]. On the other hand, BFBR have also proven to be reliable for CO methanation [26, 29], whereas BFBR for the direct methanation of biogas were studied in a pilot plant in Zurich with stable operation over 1100 h and an average of methane yield of 96% [9].

Various quantitative and qualitative working diagrams have been published to classify fluidized bed reactors [31, 104–109]. Kunii and Levenspiel [31] presented a general flow regime diagram, which has been adapted from Grace [109] and is valid for the whole range of gas-solid contacts. Most reported working diagrams are made for fast fluidization and circulating fluidized beds. Rabinovich and Kalman published a flow regime diagram for pneumatic conveying and fast fluidized bed systems [108]. Takeuchi *et al.* proposed a qualitative flow regime diagram for a catalytic cracking catalyst for fast fluidization [110]. The diagrams are based on experimental studies and define the limits of the fast-fluidization regime in terms of solid mass flux as a function of the superficial gas velocity. In the case of circulating fluidized beds, operating diagrams for the riser operation have been proposed based on the different solid circulation flux and superficial air velocity through the riser [104, 107]. However, the proposed diagrams do not provide specific information for design parameters.

Working diagrams for the bubbling fluidized bed reactors (BFBR) are scarce. The influence of the bed height to diameter ratio for different particle sizes on the minimum bubbling and slugging velocities has been analyzed and plotted in a generalized flow diagram of Reynolds number as a function of Archimedes number [105]. Besides geometric factors, the operation of a bubbling

fluidized bed reactor depends on the properties of the gas-solid system and the chemical reaction itself [34]. The most important hydrodynamic parameters are the minimum fluidization velocity (u_{mf}), the terminal velocity (u_t), and the bubble velocity (u_b), which are functions of particle properties (i.e., size, density, sphericity) and fluid properties (i.e., viscosity, density). Ideally, BFBR should operate between the minimum fluidization velocity (u_{mf}) and the terminal velocity (u_t) to assure that the catalyst particles are fluidized but not entrained [7, 33]. Usually, the superficial gas velocity (u_0) is 3–10 times the minimum fluidization velocity [31]. Temperature and pressure have different effects on the fluid properties and on the reaction kinetics (e.g., volume contraction vs. expansion), which must be considered in the reactor design. The change in gas volume due to the chemical reaction can significantly affect the hydrodynamics [35].

For the reactor and process design, two main questions should be answered: (1) *What catalyst particle size should be used?* (2) *What temperature and pressure should be used?* However, additional questions dealing with the operating range of the reactor are important. For example, for a given reactor size: *What range of pressure, temperature, catalyst diameter, and total flow rate can the reactor be operated in?* The latter is essential for processes in which the actual flow rate can vary between 50–120% of the designed flow rate (i.e., capacity utilization ratio or turndown ratio). The highly exothermic CO₂ methanation used within the Power-to-Gas process is such a case [9, 22, 111]. Power-to-Gas is a three-step process in which excess of renewable electricity is used to produce hydrogen via water electrolysis. The hydrogen is subsequently converted with captured carbon dioxide through the Sabatier reaction (CO₂ methanation, see eq. 4.1) to produce methane (CH₄), which can be stored in the existing natural gas distribution network [10, 112]. By doing so, electricity storage and carbon capture can be combined. Besides the CO₂ methanation (eq. 4.1), the competing reverse water gas shift reaction (eq. 4.2) and the CO methanation (eq. 4.3) occur.



Both the CO₂ and CO methanation are reactions with a considerable volume contraction (max. 40% and 50%, respectively), which might influence the fluidization behavior [34]. From the

thermodynamic standpoint, the CO₂ methanation is favored at low temperatures (300 - 350 °C) and high pressures (up to 20 bar). However, high operating pressures are not economical, whereas low operation temperatures require a highly efficient catalyst. Thus, a techno-economical deal must be found [112, 113]

Due to the inherent intermittency of renewable electricity, the hydrogen production fluctuates. Even with intermediate H₂ storage, the subsequent methanation reactor should be flexible and have the ability to operate at a lower gas feed (i.e., lower turndown ratio) [114]. Conventionally, bubbling fluidized bed reactors are not designed with the highest flexibility in mind. Therefore, this work presents a new type of operating diagram for BFBR that allows (1) to determine a suitable reactor diameter for a given operating condition and (2) to determine the operating range for a given reactor diameter for the CO₂ methanation. The presented methodology can be applied for other reactions, such as Fischer-Tropsch synthesis or reforming reactions.

4.3 Methodology

The minimum fluidizing velocity (u_{mf}) is the velocity at which the solids will be suspended, i.e. when the pressure drop exceeds the weight of solids (eq. 4.4) [31].

$$u_{mf} = \frac{\mu}{2 \cdot d_p \cdot \rho_g} \left(-\frac{K_2}{K_1} + \sqrt{\left(\frac{K_2}{K_1}\right)^2 + \frac{1}{K_1} \frac{4 \cdot d_p^3 \cdot \rho_g \cdot (\rho_s - \rho_g) \cdot g}{\mu^2}} \right) \quad (4.4)$$

with $K_1 = \frac{1.75}{\varepsilon_{mf}^3 \cdot \varphi_s}$ and $K_2 = \frac{150 \cdot (1 - \varepsilon_{mf})}{\varepsilon_{mf}^3 \cdot \varphi_s^2}$. Eq. (4.4) takes into account all particles ranges, where u_{mf} is the minimum fluidization velocity (m s⁻¹), ρ_s is the solid density (kg m⁻³), ρ_g is the gas density (kg m⁻³), g is the gravitational acceleration (kg m s⁻²), d_p is the particle diameter (m), μ is the dynamic viscosity (Pa s), φ_s is the sphericity of the particle and ε_{mf} is the bed voidage [31]. On the other hand, the terminal velocity (u_t) refers to the velocity at which the particles are entrained from the bed (eq. 4.5) [31].

$$u_t = \left[\frac{4 \cdot d_p \cdot (\rho_s - \rho_g) \cdot g}{3 \cdot \rho_g \cdot C_D} \right]^{1/2} \quad (4.5)$$

Terminal velocity depends on gas density, solid density, particle size, and drag coefficient, C_D . The latter is described by eq. (4.6) [115].

$$C_D = \frac{24}{Re_t} \left[1 + (8.1716e^{-4.0655\varphi_s}) Re_t^{0.0964+0.5565\varphi_s} \right] + \frac{73.69(e^{-5.0748\varphi_s}) Re_t}{Re_t + 5.378e^{6.2122\varphi_s}} \quad (4.6)$$

Where Re is the Reynolds number evaluated at u_t . The Reynolds number depends strongly on the temperature and pressure, as they predominately influence the fluid viscosity and density, respectively.

Considering the assumptions stated above and based on eqs. (4.4) and (4.5), working diagrams can be designed to determine the bed diameter and the operating range for different catalyst particle diameters. By fixing one variable, the effect on temperature and pressure changes can be analyzed. The diagrams include a set of curves using constant velocity values, denoted as isotachs. The bed diameter, d_{FB} (m), can be determined by considering the superficial gas velocity, ($u_o = \dot{V}/A$) and the cross-section of the reactor ($A = 0.25 \cdot \pi \cdot d_{FB}^2$) as:

$$d_{FB} = \sqrt{\frac{4 \cdot \dot{V}}{\pi \cdot u_o}} \quad (4.7)$$

where \dot{V} is the actual volumetric flow rate at reaction conditions (T, p). Using ideal gas relation $\frac{\dot{V} \cdot p}{T} = \frac{\dot{V}_0 \cdot p_0}{T_0}$, the reactor diameter can be expressed with the volumetric flow rate (\dot{V}_0) at standard conditions (i.e., STP, temperature and pressure of $T_0 = 273.15$ K and $p_0 = 1$ bara):

$$d_{FB} = \sqrt{\frac{4 \cdot \dot{V}_0 \cdot p_0 \cdot T}{\pi \cdot u_o \cdot T_0 \cdot p}} \quad (4.8)$$

By plotting eq. (4.8) as a function of temperature or pressure, the required bed diameter can be determined for various particle sizes. Working diagrams were developed considering two cases, a laboratory and an industrial-scale fluidized bed reactor for the CO₂ methanation with the assumptions stated in Table 4-1.

Carbon dioxide captured from biogas plants is a good source for the CO₂ methanation reaction. Assuming that a typical biogas plant produces $\sim 1000 \text{ mN}^3 \text{ h}^{-1}$ of CO₂ [116] and a stoichiometric H₂ to CO₂ ratio, a total volumetric flow rate of $5000 \text{ mN}^3 \text{ h}^{-1}$ (i.e., 100% capacity) was used. In the

current study, we considered that the reactor should be able to operate between 50 to 110% of their design capacity (i.e., 2500 to 5500 m_N³ h⁻¹) due to the H₂ fluctuations, which represents a turndown ratio of 0.5 – 1.1. The turndown ratio for the fluidized bed reactor is defined as the actual feed flow rate divided by the designed feed flow rate (both in STP). A superficial gas velocity of $u_o = 6 \cdot u_{mf}$ was chosen to ensure that the reactor operates in the bubbling regime [22, 31]. Besides, we have assumed three different catalyst particle sizes (150, 250, and 500 μm) and not a particle size distribution. The values for catalyst sphericity and bed voidage at minimum fluidization velocity were taken from the literature [31].

Table 4-1 Parameters and assumptions used for the operating diagrams.

Parameter	Assumption
Feed composition	H ₂ /CO ₂ = 4/1 (stoichiometric)
Designed capacity (total inlet flow rate)	0.5 m _N ³ h ⁻¹ (laboratory/pilot scale), 5000 m _N ³ h ⁻¹ (industrial scale)
Capacity range	50% - 110%
Temperature, T	300 - 500 °C
Pressure, p	1 – 20 bara
Velocity ratio u_o/u_{mf}	6 - 12
Particle sizes, d_P	150, 250 and 500 μm (Geldart B)
Sphericity φ_s	0.58 [31]
Bed voidage ε_{mf}	0.57, 0.55 and 0.54 [31]
Catalyst density ρ_s	1500 kg m ⁻³

As the operating conditions and turndown ratio will affect the amount of methane formed, the associated chemical energy (E_{CH_4} in MW) is calculated assuming that all unconverted CO₂ and H₂, as well as the produced H₂O, are separated from CH₄. Thus, the chemical energy is directly proportional to the lower heating value (i.e., heat of combustion) from CH₄.

4.4 Results and Discussion

4.4.1 Equilibrium composition

Temperature and pressure have different and opposite effects on the equilibrium composition as illustrated in Fig. 4–1A and B. The main products of the CO₂ methanation, i.e., H₂O and CH₄, are thermodynamically favored at low temperatures and high pressures [117]. On the other hand, the formation of CO, a product of the competitive reverse water-gas-shift reaction, is favored at higher temperatures (> 450 °C) but not at higher pressures [7, 112, 117]. The equilibrium composition was calculated using the HSC Chemistry v9 software that uses the minimization of the Gibbs energy approach.

The total outlet molar flow rate increased with increasing temperature and slightly decreased with increasing pressure (pink line in Fig. 4–1A and B). In other words, the volume contraction (blue shaded area) decreased when the temperature increased. At 300 °C, a 36% volume reduction is observed; however, as the temperature increases to 500 °C, the gas expands, and hence the volume contraction reduces to 27%.

During the reaction, the influence of temperature and pressure on the actual volumetric flow rates (inlet and outlet) are more pronounced, as visualized in Fig. 4-1C and D, respectively. These effects are very important as the actual volumetric flow rate dictates the gas velocity in the reactor, and hence, the fluidization behavior. For example, the outlet volume flow rate increased from 6,500 m³ h⁻¹ at 300 °C to 10,500 m³ h⁻¹ at 500 °C for 1 bara (Fig. 4-1C). Whereas, the outlet volume flow rate decreased significantly from 7,000 m³ h⁻¹ at 1 bara to less than 500 m³ h⁻¹ at 20 bara at 350 °C (Fig. 4-1D). Therefore, the design and operating conditions of the fluidized bed reactor will be different in each case.

The subsequent calculations have been done with the standard inlet flow rates considering the volume contraction instead of the outlet flow rates as the volume contraction is assumed to occur along the height of the reactor as the reaction progresses.

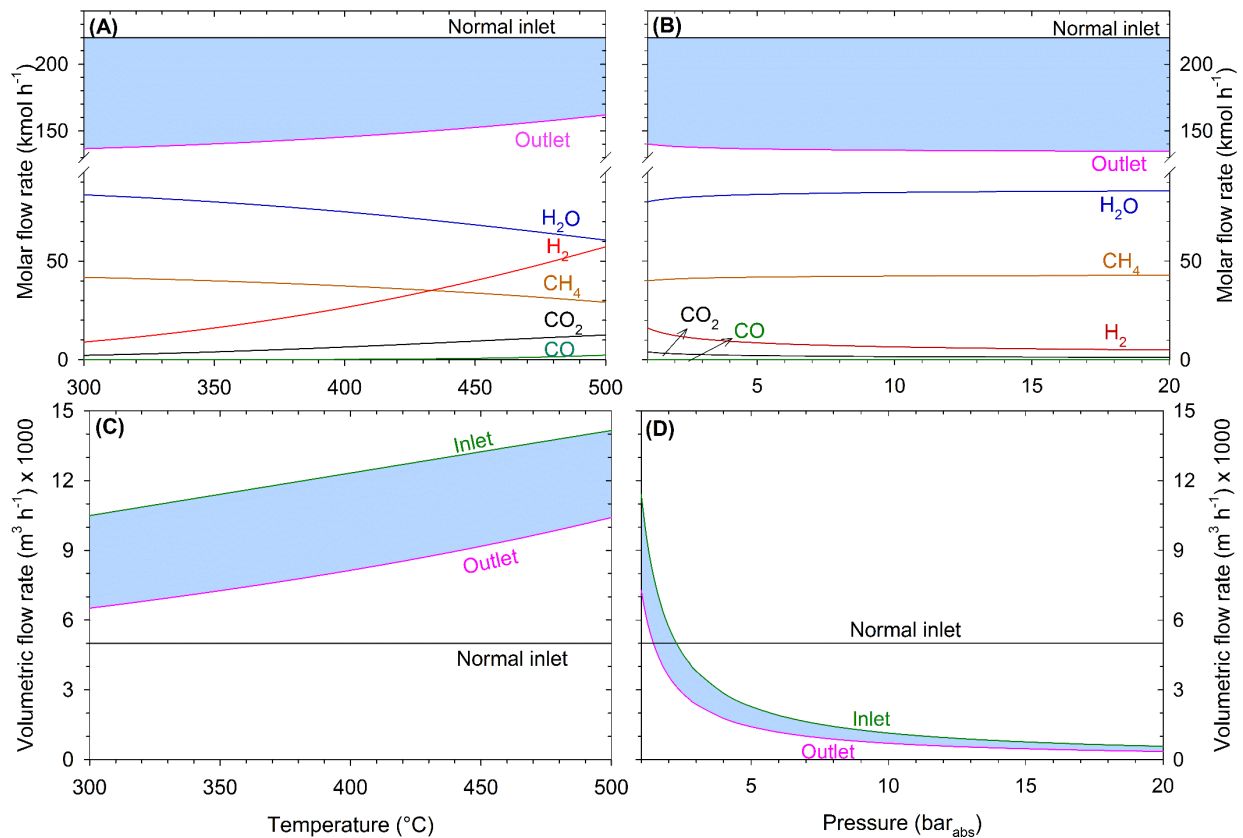


Fig. 4-1 Equilibrium composition of CO₂ methanation based on (A, B) the molar flow rate and (C, D) the volumetric flow rate as a function of (A, C) temperature at 1 bara and (B, D) pressure at 350 °C. Total inlet flow rate: 5000 m_N³ h⁻¹ (220 kmol h⁻¹) with H₂/CO₂ = 4/1. Blue shaded parts represent volume contraction. Normal inlet refers to the inlet at standard conditions (273 K and 1 bara), whereas inlet refers to the volumetric flow rate at operating conditions.

4.5 Bed diameter

The calculations shown in the following diagrams rely on the fact that at the same gas flow rate, different gas velocities can be set by changing the cross-sectional area of the reactor where the bed diameter is directly proportional to the square root of this parameter.

4.5.1 Temperature effect

Figure 4-2 depicts the calculated bed diameter (eq. 4.8) (empty tube diameter) as a function of temperature at a constant pressure of 3 bara for a laboratory-scale reactor. The total inlet flow rate

was set to $0.5 \text{ m}_N^3 \text{ h}^{-1}$ with an H_2/CO_2 ratio of 4/1 (Table 4-1). The grey lines denote the isotachs (constant gas velocity), the black solid and dashed lines refer to the superficial gas velocity ($u_0 = 6 \cdot u_{mf}$) and the terminal velocity (u_t), respectively, for catalyst particles with a size of 150, 250 and 500 μm . Since bubbling fluidized beds should operate far from the terminal velocity, the maximum u_0/u_{mf} ratio of 12 was assumed (blue line), resulting in a decision window indicated by the blue shaded area. To fluidize particles with a size of 250 μm , the bed diameter of the BFBR should be within that blue area to ensure proper fluidization.

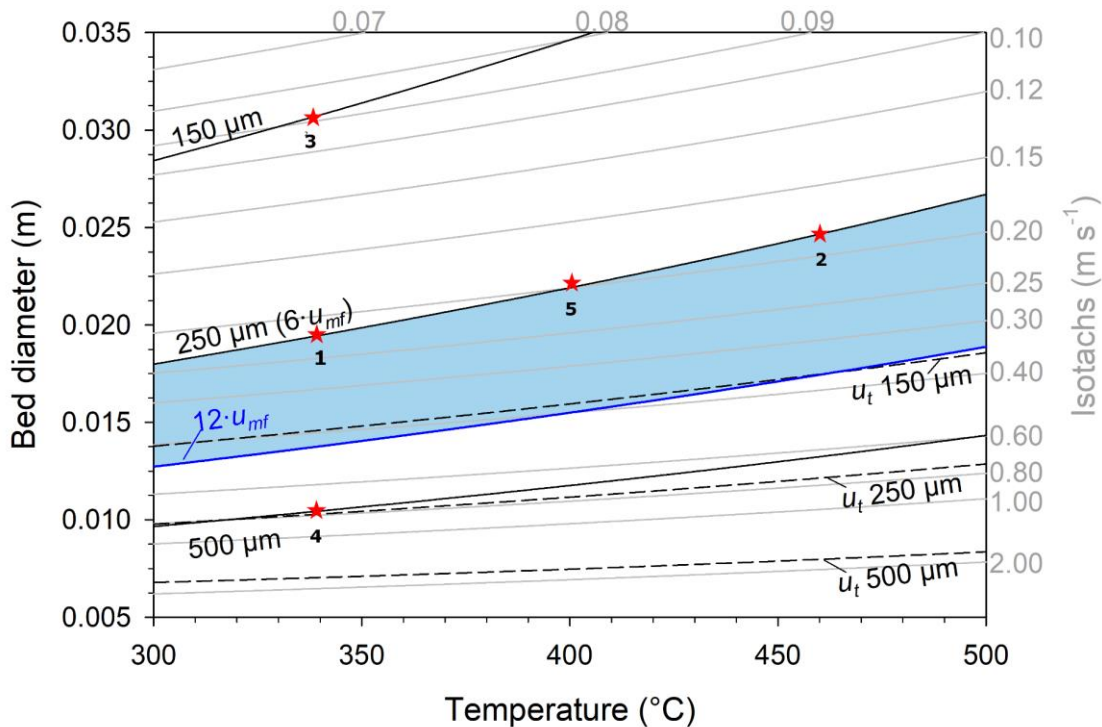


Fig. 4-2 Bed diameter as a function of temperature (300-500 °C) at 3 bara for a laboratory-scale reactor. Total inlet flow rate $0.5 \text{ m}_N^3 \text{ h}^{-1}$, $\text{H}_2/\text{CO}_2 = 4/1$. Blue shaded area represents the zone between $6 \cdot u_{mf}$ (bold black line) and $12 \cdot u_{mf}$ (blue line) for a particle size of 250 μm (decision window). Dashed lines (u_t).

The analysis showed that a larger bed diameter is required to achieve the necessary gas velocity to fluidize smaller particle sizes with the same flow rate and temperature at 3 bara (Fig. 4-2). A larger bed diameter is also required to fluidize the same particle size (e.g., 250 μm) but at higher temperatures. The plot allows determining a suitable bed diameter as a function of particle size and temperature for a given total volumetric flow rate (STP) and operating pressure. For example, if the laboratory-scale reactor operates at 340°C and 3 bara with 250 μm particles at $6 \cdot u_{mf}$, a bed

diameter of 19.5 mm is required. Additionally, the superficial gas velocity of $u_o = 0.22 \text{ m s}^{-1}$ for these conditions can be determined by following the isotachs and their correspondent scale (star 1). If the reactor is operated at a temperature of 460 °C instead of 340 °C, the gas expands, and hence, the cross-sectional area of the reactor increases 1.6 times ($d_{FB} = 24.7 \text{ mm}$) (star 2). For both operating points, the nominal volumetric flow rate and velocity ratio were the same (i.e., $0.5 \text{ m}_N^3 \text{ h}^{-1}$ and $6 \cdot u_{mf}$). Equally, to fluidize smaller catalyst particles of 150 μm an increase of 1.6 times of the reactor diameter is required at 340 °C and 3 bara, whereas a decrease of approx. 50% in the bed diameter is observed when the particle size of the catalyst is increased to 500 μm (stars 3 and 4).

The particle size of the catalyst influences not only the design of the bed diameter but also the bed height to diameter ratio (H/D). For instance, considering that the reactor is operated with the same gas velocity to catalyst amount ratio ($L_N \text{ h}^{-1} \text{ kg}_{\text{Cat}}^{-1}$) for all particle sizes, H/D ratio changes significantly (i.e., by a factor 3), which could further affect the hydrodynamics (i.e., bubble size), mass transfer as well the final conversion. Assuming the equilibrium conversion is achieved, an increase in temperature would decrease the CO₂ conversion from 94.7% at 340 °C to 90.3% at 400 °C (star 5) and 84.3% at 460 °C.

For an industrial reactor, the CO₂ methanation reaction would be carried out at higher pressures, thus affecting the bed diameter. The reactor diameters are illustrated as a function of temperature at 3 and 10 bara in Fig. 4-3A and B, respectively, with a nominal inlet flow rate of $5000 \text{ m}_N^3 \text{ h}^{-1}$ and a ratio $\text{H}_2/\text{CO}_2 = 4$. Increasing the pressure reduces the reactor diameter to keep the same fluidization velocity [22]. For instance, considering the previous example of a reactor operating at 340 °C and 3 bara, with catalyst particles of 250 μm and $u_o/u_{mf} = 6$, a diameter of $\sim 1.9 \text{ m}$ is required (star 1) for the industrial-scale reactor. However, if the operating temperature increases to 460 °C, the diameter doubles to 3.9 m, to fluidize 250 μm catalyst particles at $6 \cdot u_{mf}$ (star 2). On the other hand, if the temperature is fixed at 340 °C due to thermodynamics, kinetics or any other constraints, a larger reactor diameter is needed to fluidize smaller particles and vice-versa (i.e., $\sim 3.1 \text{ m}$ diameter for 150 μm and $\sim 1 \text{ m}$ diameter for 500 μm (stars 3 and 4)). Equally, for a more realistic industrial process in which a higher pressure of 10 bara will favor the CO₂ methanation reaction, the same analysis can be conducted. In this case, the cross-sectional area of the reactor is approx. 3.3 times smaller to keep the gas velocity constant and hence suitable catalyst fluidization. In detail, a diameter of approx. 1.06 m is needed to fluidize 250 μm catalyst particles at $6 \cdot u_{mf}$ at

340 °C (star 5). Hence, it is paramount to decide the total operating pressure prior to determining the reactor size.

As mentioned in section 4.4.1, the CO₂ conversion is favored at low temperatures and higher pressures due to the exothermicity and volume contraction nature of the reaction. At 340 °C and 10 bara, an equilibrium CO₂ conversion of 96.7% is achieved, which translates to a total energy output of 9.6 MW_{CH₄} (based on the lower heating value of methane). If the temperature is kept constant at 340 °C, and the pressure is reduced to 3 bara, the equilibrium conversion of CO₂ is 94.7%, which corresponds to an energy output of 9.4 MW_{CH₄}. It can be noticed that the energy output between the industrial reactor operating at 3 bara and the 10 bara differs only by 2%. However, the operating cost of the compression increase when increasing the operating pressure. Hence, the advantage of operating at a lower pressure.

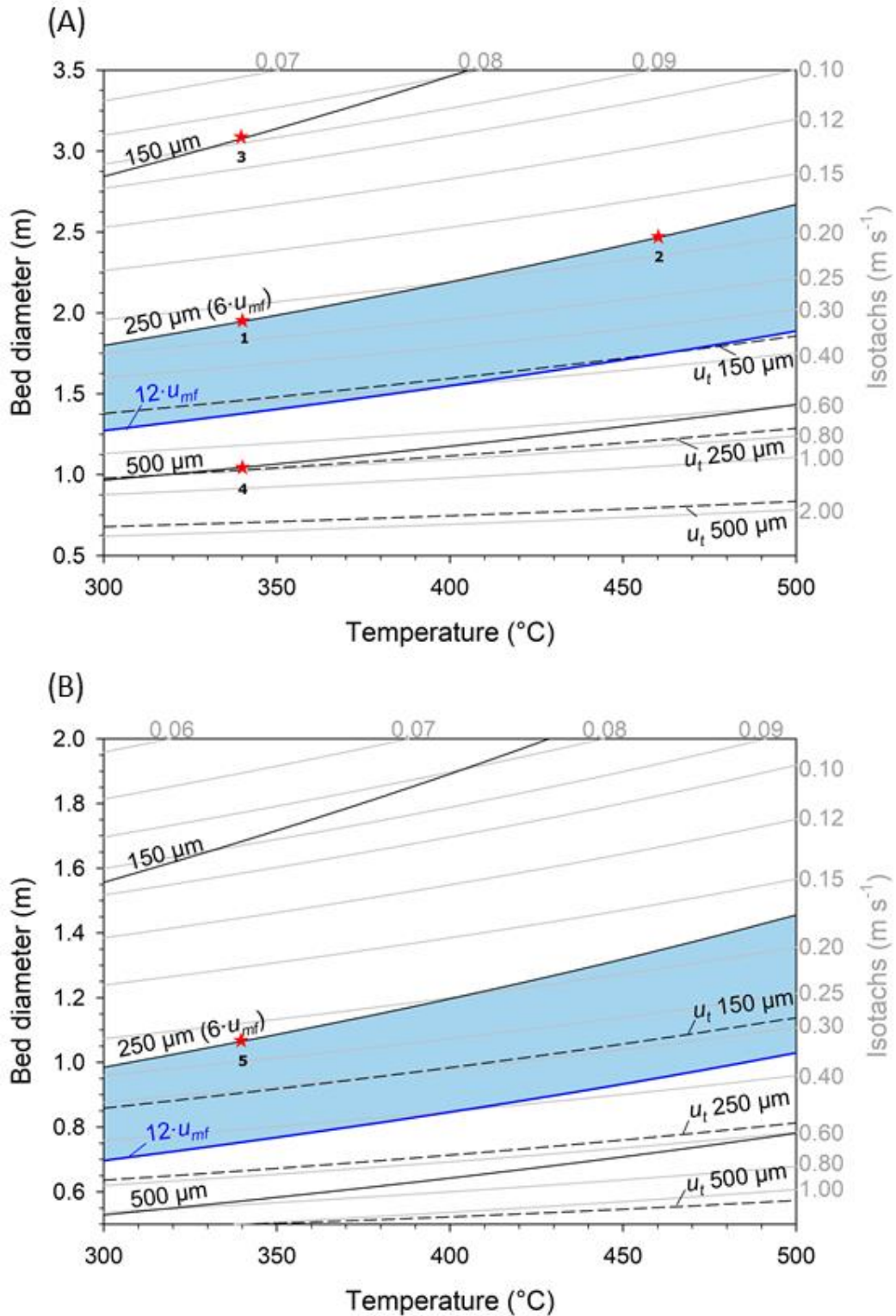


Fig. 4-3 Bed diameter as a function of temperature at (A) 3 bara and (B) 10 bara for different particle diameters (150, 250, and 500 μm) for an industrial-scale reactor. Total flow rate of 5000 m_N³ h⁻¹ with H₂/CO₂ = 4/1 ($6 \cdot u_{mf}$ (bold lines), $12 \cdot u_{mf}$ (blue lines), u_t (dashed lines)).

4.5.2 Pressure effect

Figure 4-4 presents the effect of pressure on the bed diameter at 340 °C shown for different particle sizes for an industrial-scale reactor. The pressure has an important effect on the bed diameter. At higher pressures, the reactor becomes narrower but higher to keep the volume and mass of the catalyst constant [118]. For fluidizing bigger particles, the reactor could operate at lower pressures, which reduces the operating costs associated with the compression, whereas at higher values of pressure, smaller particles are required. In this case, the particle size needs to be chosen carefully so the catalyst can be fluidized.

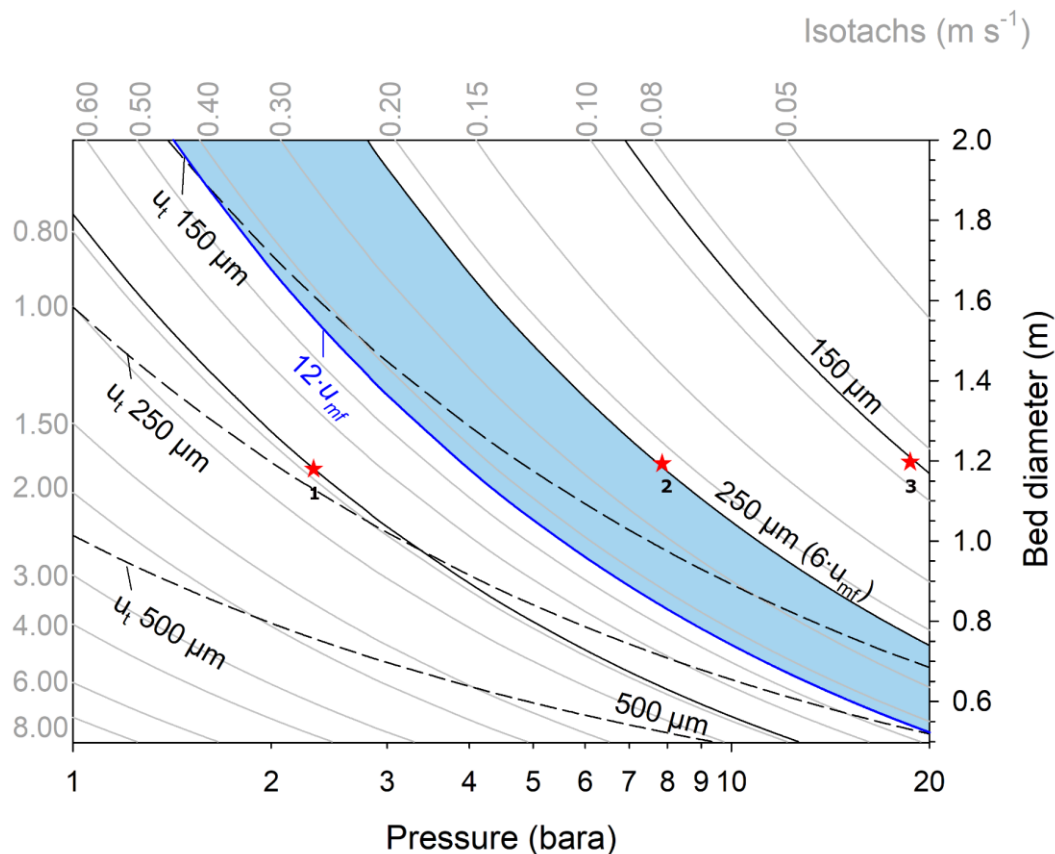


Fig. 4-4 Bed diameter as a function of pressure at 340 °C for different particle diameters (150, 250, and 500 μm) for an industrial-scale reactor. Total flow rate of 5000 m_N³ h⁻¹ with H₂/CO₂ = 4/1 (6·u_{mf} (solid lines), 12·u_{mf} (blue line), u_t (dashed lines)).

The blue shaded zone represents a decision window to operate the reactor between 1 and 20 bara for a particle size of 250 μm. Working at 20 bara would lead to a slimmer reactor with diameters of 0.52 to 0.74 m. In contrast to the temperature diagrams, it is possible to have one empty tube diameter for the fluidization of particles from 150 to 500 μm with superficial gas velocities

between 0.08 and 0.8 m s⁻¹. For example, a fluidized bed with a 1.2 m empty tube diameter can operate with 150, 250, and 500 μm particles at 2.2, 8, and 19 bara (stars 1, 2, and 3), respectively. Figure 4-5 shows the energy output (in MW_{CH₄}) of an industrial-scale reactor at a temperature range of 300 to 500 °C for different operating pressures. A CH₄ yield of 100% means that all carbon from CO₂ is being converted to CH₄, which corresponds to a maximum energy output of 9.94 MW_{CH₄}. However, due to thermodynamic constraints, a maximum of 9.6 MW_{CH₄} is possible at 340 °C and 10 bara. Even though increasing the operating pressure leads to higher CO₂ conversions, the CH₄ energy output depends strongly on the operating temperature. For instance, the energy output only differs by 3% when increasing the pressure from 3 to 20 bar at 340 °C; however, this difference increases to 13% when the temperature increases up to 500 °C. Equally, when the CO₂ methanation reaction is carried out at higher pressures, a change in temperature has a reduced influence on the energy output as a result of the high density of the gas.

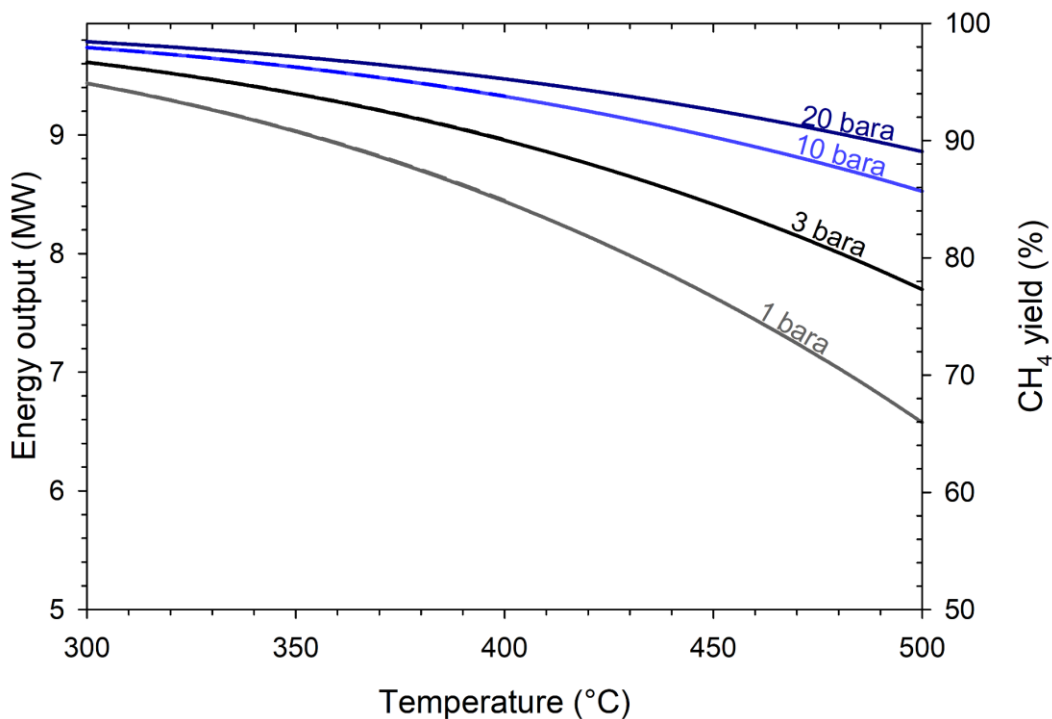


Fig. 4-5 Energy output in MW_{CH₄} as a function of temperature for different operating pressures (1, 3, 10, and 20 bar). Total inlet flow rate of 5000 m_N³ h⁻¹ and H₂/CO₂ = 4/1.

4.6 Turndown ratio

4.6.1 Temperature effect

Once the bed diameter for the reactor has been chosen, a working diagram can be designed to visualize the capacity or turndown ratio. An example is shown in Fig. 4-6 for an industrial-scale reactor operating at 10 bara and an empty tube diameter of 1.06 m, the reactor diameter was chosen based on Fig. 4-3 with a designed capacity of 100% (i.e., inlet flow rate of 5000 m_N³ h⁻¹), reaction temperature of 340 °C, and particle size of 250 μm (star 5 in Fig. 4-3 corresponds to star 1 in Fig. 4-6). As the temperature increases, the turndown ratio decreases, as well as the superficial gas velocity represented by the isotachs.

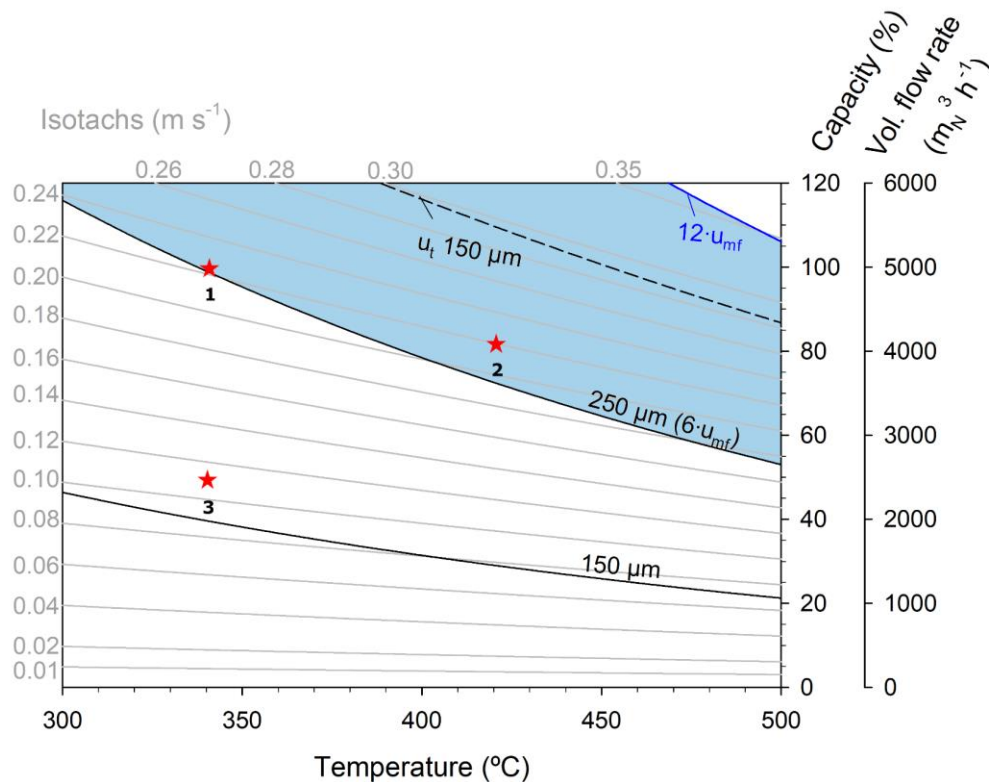


Fig. 4-6 Energy output in MW_{CH₄} as a function of temperature for different operating pressures (1, 3, 10, and 20 bar). Total inlet flow rate of 5000 m_N³ h⁻¹ and H₂/CO₂ = 4/1.

The blue shaded area defines a theoretical maximum working range for 250 μm particles with capacity utilization of 50 to 120% (i.e., turndown ratio of 0.5–1.2). If the temperature increases to 400 °C at the same superficial gas velocity (i.e., 0.22 m s⁻¹), the capacity decreases to approx. 80%, which means that the inlet flow rate reduces to 4000 m_N³ h⁻¹ (star 2). If less feed gas is available for the CO₂ methanation reactor due to low H₂ production, then the temperature can be

increased to maintain the same velocity ratio. However, this would result in a lower CH₄ yield and CO₂ conversion due to equilibrium constraints, as depicted in Fig. 4-1. Hence, the CO₂ conversion and energy output would decrease from 96.7% and 9.6 MW_{CH₄} (10 bara, 340 °C, 100% capacity) to 92.7% and 7.7 MW_{CH₄} (10 bara, 420 °C, 80% capacity). This not only represents a decrease of 20% in the CH₄ energy output but also increases the operating temperature by 80 °C, which raises the energy consumption of the system.

On the other hand, keeping pressure and temperature constant at 50% capacity (i.e., inlet flow rate of 2500 m_N³ h⁻¹) would reduce the velocity ratio to $u_0/u_{mf} = 3$ ($u_0 = 0.11$ m s⁻¹) and the total energy produced to 4.8 MW_{CH₄} (star 3). Considering a volume contraction of 26 – 38 vol%, it follows that the fluidized bed is likely to destabilize and collapse.

4.6.2 Pressure effect

Increasing the temperature to deal with a lower feed flow rate is not the best solution. Thus, in this section, the effect of pressure on the capacity of the industrial-scale reactor is visualized and discussed (Fig. 4-7). The blue shaded area depicts the operating window to fluidize particles of 250 μm at a temperature of 340 °C in a 1.06 m fluidized bed. Operating pressure of 10 bara corresponds to a design capacity of 100% (i.e., inlet flow rate of 5000 m_N³ h⁻¹) (star 1). Operating the reactor at 50% capacity with the same velocity ratio ($6 \cdot u_{mf}$) would require lowering the total pressure to 5 bara at the same temperature (star 2). At this condition, the CO₂ conversion is slightly lower, with 94.6% compared to 96.7% at 10 bara. The corresponding rated CH₄ output would be 4.8 MW.

In contrast, an increase to 110% capacity (i.e., inlet flow rate of 5500 m_N³ h⁻¹) would require a slight increase in the total pressure to maintain the same velocity ratio. If the pressure is kept constant at 10 bara at 110% capacity, the velocity ratio would slightly increase to $u_0 = 6.5 u_{mf}$, which is well within the blue shaded area that defines the operating window (star 3). At this condition, a total energy output of 10.6 MW_{CH₄} could be achieved.

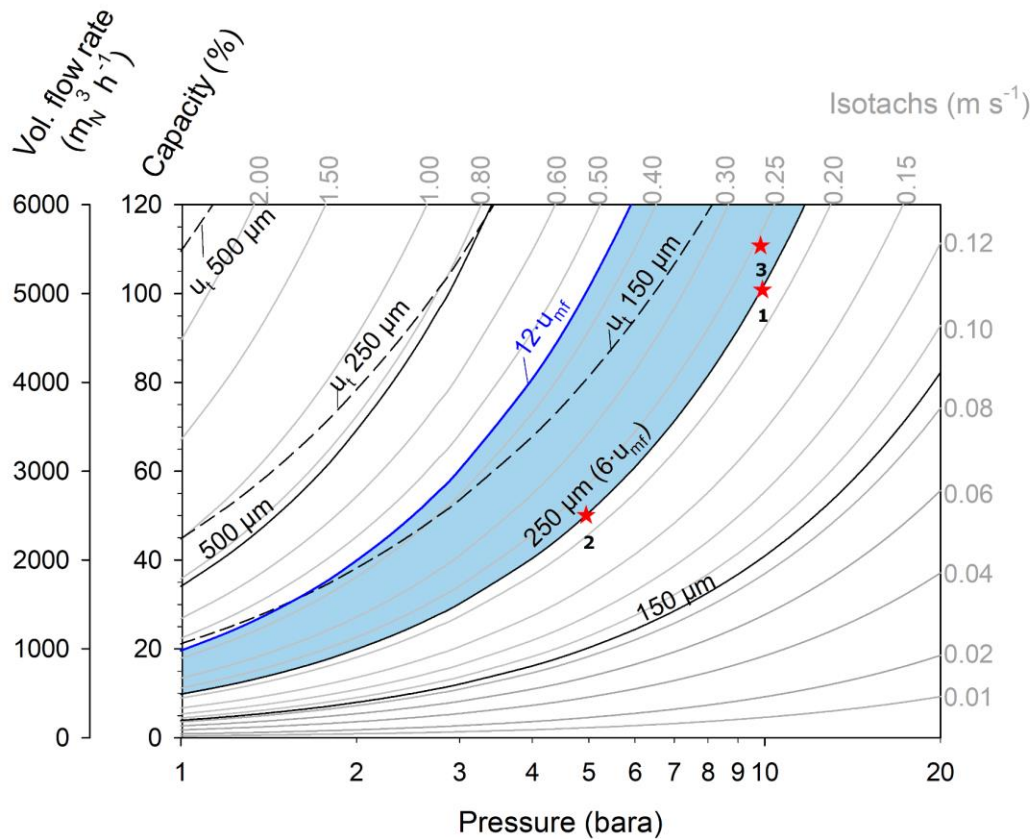


Fig. 4-7 Capacity as a function of pressure assuming volume contraction at 340 °C for different particle diameters (150, 250, and 500 μm) and empty tube reactor diameter of 1.06 m for an industrial-scale reactor. Total flow rate with H₂/CO₂ = 4/1 (6·u_{mf} (solid lines), 12·u_{mf} (blue line), u_t (dashed lines)).

This short analysis shows that changing the pressure provides greater flexibility than changing the temperature in terms of turndown ratio/capacity.

Furthermore, the plot shows that the reactor with an empty tube diameter of 1.06 m can be used with a different range of particle sizes (150 to 500 μm). For 500 μm catalyst particles, the operating window decreases, while for 150 μm catalyst particles, the operating window would be larger compared to the reference case with 250 μm. Larger particles would shift the operation to lower pressure (i.e., 3-5 bara), whereas smaller particles would allow operating the reactor up to 20 bara at 80% capacity at the same velocity ratio of $u_0/u_{mf} = 6$. Operating at 20 bara, would not significantly increase the equilibrium conversion of CO₂ and thus the energy output, but will increase the compression operating costs.

4.7 Conclusions

Power-to-Gas is an industrially relevant process that might be the key to satisfy the increasing global demand for renewable energy. In the Power-to-Gas technology, CO₂ methanation is a fundamental step to produce CH₄ that can be subsequently injected in the current gas grid distribution or gas storage. In this manuscript, we have developed working diagrams for the CO₂ methanation reaction in a bubbling fluidized bed reactor considering different operating temperatures (300 to 500 °C) and pressures (1 to 20 bara). The diagrams shown in this work are a graphical representation of the hydrodynamic equations for BFB reactors and can be used as a base for the reactor design. Moreover, the same methodology to determine design (bed diameter) and operating (turndown ratio) parameters can be applied to other reactions besides CO₂ methanation by considering the thermodynamics of the reaction. Adjusting the geometry of the BFB reactor for changing operating conditions such as temperature, pressure, and total flow rate is critical to ensure proper fluidization. These working diagrams consider a given reactor design (bed diameter) and turndown ratio. This means that the reactor can operate in a flexible range of operating conditions depending on the availability of the reactants. Increasing the operating temperature increases slightly the bed diameter due to the gas expansion, whereas increasing the pressure leads to slimmer reactors in order to keep the fluidization velocity. The results showed that the CO₂ methanation reaction should be carried out at a lower and more importantly, at a fixed temperature (e.g., 340 °C) to allow a more flexible operation in terms of pressure, particle size of the catalyst and thus turn-down ratio and energy output. Altering the pressure while maintaining the same velocity ratio might be a good option to adjust for changing turndown ratios of 50 to 110%.

Acknowledgments

The authors acknowledge funding from the Natural Sciences and Engineering Research Council of Canada (NSERC RGPIN–2014-04685). Jennifer Martin-del-Campo gratefully acknowledges funding from the Consejo Nacional de Ciencia y Tecnologia (CONACyT, Mexico scholarship program) and the Faculty of Engineering through the McGill Engineering Doctoral Award.

Nomenclature

Symbol	Units	Parameter
u_{mf}	[m s ⁻¹]	Minimum fluidization velocity
d_p	[m]	Particle diameter
ρ_s	[kg m ⁻³]	Solid density
ρ_g	[kg m ⁻³]	Gas density
g	[m s ⁻²]	Gravity
μ	[Pa s]	Viscosity
ε_{mf}	[-]	Bed voidage
φ_s	[-]	Sphericity
Re	[-]	Reynolds number
V_o	[m ³ s ⁻¹]	Volumetric flow rate at outlet conditions
T_o	[K]	Temperature at standard conditions (273.15 K)
P_o	[bara]	Pressure at standard conditions (1 bara)
T	[°C]	Temperature
p	[bara]	Pressure
u_t	[m s ⁻¹]	Terminal velocity
M	[kg kmol ⁻¹]	Molecular weight
x_i	[-]	Molar fraction of the component in the mixture
C_D		Drag coefficient

Complementary equations

$$Re = \frac{u \cdot d_p \cdot \rho_g}{\mu}$$

$$\mu_m = \sum_{i=1}^{Ncc} \frac{x_i \cdot \mu_i}{\sum_j^{Ncc} x_j \cdot \phi_{ji}}$$

$$\phi_{ij} = \frac{\left[1 + \left(\frac{\mu_i}{\mu_j} \right)^{0.5} \cdot \left(\frac{M_j}{M_i} \right)^{0.25} \right]^2}{\left[8 \cdot \left(1 + \frac{M_i}{M_j} \right) \right]^{0.5}}$$

$$\mu = \frac{A \cdot T^B}{1 + \frac{C}{T} + \frac{D}{T^2}}$$

5

Plasma assisted Dry Reforming of Methane

5.1 Preface

This chapter presents the results of studying the influence of peak current, total flow rate, CO₂/CH₄ ratio, and preheated flow rate in the Dry Reforming of Methane reaction carried out in a Rotating Gliding Arc reactor. The work was planned, analyzed, and executed by J. Martin-del-Campo. Supervision of the research and manuscript reviewing were shared between S. Coulombe and J. Kopyscinski. The citation for this chapter is:

Martin-Del-Campo J, Coulombe S, Kopyscinski J (2020) *Influence of Operating Parameters on Plasma-Assisted Dry Reforming of Methane in a Rotating Gliding Arc Reactor*. *Plasma Chem Plasma Process*: 40:857–881. <https://doi.org/10.1007/s11090-020-10074-2>

In this Chapter, a different reaction for CO₂ valorization was studied. Compared to the previous valorization reaction stated in Chapter 4, dry reforming of methane is an immature technology. Besides, DRM is highly energetic, and new technologies are still under research and development to make the reaction more efficient and economically feasible. In this chapter, a non-thermal plasma discharge known as rotating gliding arc was used as the energy input for DRM. The effects of operating parameters such as CO₂/CH₄ ratio, peak current, total flow rate, as well as preheated

and non-preheated inlet flow on the DRM reaction were investigated. The variation in each parameter produced a change in the reaction product composition, and efficiency of the process.

It was found that changing the peak arc current had the strongest effect on the conversion of reactive gas and hence, the yield of products and byproducts formation. Moreover, increasing the inlet temperature up to 473 K did not affect the reforming reaction, regardless of the endothermic nature of the reaction. The concentration of products as a function of time was also measured. We found that the plasma discharge presents a transient behavior of the products concentration at the beginning of the reaction, and only after approximately 5 min, the concentration on the stream was steady.

The solid by-products of the reaction were also analyzed. The analysis of the Raman Spectroscopy results showed the formation of some graphene sheets that can have potential use for industry or research, which would add value to the DRM reaction.

Influence of operating parameters on plasma-assisted dry reforming of methane in a rotating gliding arc reactor

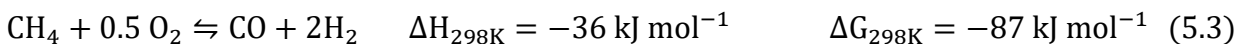
Jennifer Martin-del-Campo^{1,2}, Sylvain Coulombe¹, Jan Kopyscinski²

Plasma Processing Laboratory¹, Catalytic Process Engineering², Department of Chemical Engineering, McGill University, Montreal, Quebec, Canada

Abstract. The environmental impact of greenhouse gases such as carbon dioxide and methane can be reduced if they are used as feedstock to synthesize chemical building blocks such as syngas (CO, H₂) via dry reforming. Methane dry reforming is investigated using an Ar/CO₂/CH₄ rotating gliding arc (RGA) reactor powered by a dual-stage pulsed DC power supply. Tangential gas injection combined with a static magnetic field enabled the rotation and upward displacement of the arc along the conical cathode and the grounded anode, yielding to a larger plasma volume. Different parameters such as peak arc current (0.74 and 1.50 A), total gas flow rate (3.7, 4.7 and 6.7 SLPM), CO₂/CH₄ ratio (1.0, 1.5, 2.0) and gas inlet preheating (room temperature, 200 °C) were studied to determine the most efficient parameter combination. Gas conversion was measured online using a calibrated mass spectrometer and offline using a gas chromatograph. Noticeable increases in CO₂ and CH₄ conversions, as well as H₂ and CO yields, were obtained when doubling the peak arc current. For the larger peak current, higher H₂ yields were obtained at a CO₂/CH₄=1.0, and the best energy efficiencies were obtained at the lowest specific energy input values. No significant effect of the gas inlet temperature on the conversions or yields was found. Trace amounts of acetylene and ethylene, as well as some carbon deposits, were observed as by-products of syngas generation. The low amount of by-products obtained implies a good selectivity for CO and H₂, i.e., a cleaner syngas when produced with RGA discharge.

5.2 Introduction

The world is moving towards the use of greener and renewable technologies to meet the ever increasing energy demand; however, fossil fuels are still important in our current energy mix [46]. With the dependence on fossil fuels, the emission of pollutants, such as greenhouse gases (GHG), is an unavoidable problem [119]. Climate change is the major consequence of the enormous amount of greenhouse gases released to the atmosphere, with global and local effects such as an increase in the atmospheric temperature, massive ice melting, ocean acidification, and an enhanced rate of violent localized atmospheric events [120–122]. Carbon dioxide (CO₂) and methane (CH₄) are two of the most significant GHG. Reducing carbon emissions is the most desirable way, but closing the loop on carbon through capture, storage, and utilization is another promising avenue. Dry reforming of methane (DRM) is a reaction that upcycles these two GHG to form syngas, which consists of carbon monoxide (CO) and hydrogen (H₂) (eq. 5.1). Syngas can subsequently be converted into liquid hydrocarbons and value-added chemicals for diverse applications. Today, syngas is produced industrially mainly by steam reforming (eq. 5.2) and partial oxidation of methane (eq. 5.3).



Even if DRM is thermodynamically the most unfavorable reaction (eq. 5.1), it is also the most environmentally friendly due to the use of CO₂ as oxidizing agent [123]. Moreover, sources with large amounts of CO₂ such as biogas can be used from the feed gas without previous separation in the DRM process [42, 69]. Nonetheless, one of the major drawbacks of DRM is that it is a highly energy-intensive process as the C-H bond in methane and C-O bond in carbon dioxide are very stable. Thus, for a thermocatalytic conversion process, high temperatures (> 800 °C) and an efficient catalyst, resistant to coke and carbon deposition, are required [42, 124, 125]. CO₂ and CH₄ can also be activated by means of plasma technology (e.g., non-thermal plasma) that can assist the reaction by providing energy to the highly endothermic process as energetic species such as electrons, ions, free radicals intervene in the chemical reactions and hence, reduce the activation barrier of CO₂ and CH₄ [42, 94]. Additionally, in an increasing number of countries, plasma

reactors can be powered by renewable electricity, thus offering a new route for renewable electricity-to-gas processes and applications (e.g., intermittent energy storage and valorization). Plasma technologies such as dielectric barrier discharge (DBD) [58–62], glow discharges [63, 64], microwave discharges (MW) [94], corona discharges [65, 66], radio-frequency discharges (RF) [126] and gliding arc discharges [42, 69–73] have been extensively investigated for reforming reactions. However, corona discharges and dielectric barrier discharges present high energy cost of syngas ($>10 \text{ kWh m}^{-3}$) and low energy efficiency ($<10\%$) in biogas reforming [77, 127]. On the other hand, RF and MW discharges need to operate at low pressure to achieve high conversions and good hydrogen selectivity but with low hydrogen rate and extra energy cost. Moreover, MW technologies are hard to scale up due to the inherently complicated configurations and high installation costs [36, 128]. A promising technology, the gliding arc discharge, produces a plasma classified by some authors as a “warm plasma” [77, 82, 83]. Gliding arc discharges present properties between thermal and non-thermal plasmas, such as high electron temperatures ($>1 \text{ eV}$), high electron density of 10^{13} to 10^{15} cm^{-3} , and gas temperatures of 1000 to 3000 K, while the non-equilibrium between electron and heavy particles is still maintained enabling conversion and selectivity [82, 83, 85, 129]. Furthermore, up to 45% of the electrical energy provided to the gliding arc may be directly absorbed by endothermic chemical reactions, as in the case of DRM. In fact, without any catalyst, the gliding arc allows the generation of syngas at low temperatures ($475 \text{ }^\circ\text{C}$) and chemical efficiency (ratio of energy required to carry out the reaction at $25 \text{ }^\circ\text{C}$ to the used electrical energy) up to 40% [75]. These features make the gliding arc discharge a promising plasma source to satisfy high productivity and good adaptability for plasma-assisted chemical processes [42].

The rotating gliding arc (RGA) is a configuration that makes more efficient use of the energy and arc-cold gas contact, and that is consequently better adapted to scale-up than the traditional knife-shaped gliding arc. In the RGA, the reactant gas is injected tangentially to form a swirling flow field in the reactor. As the arc is pushed away from the breakdown area, it swirls and elongates, thus forming a larger plasma reaction volume compared to the conventional gliding arc. In addition, the arc can be forced to rotate by the action of an external magnetic field through the Lorentz force [13, 85]. The RGA provides a homogeneous distribution of active species in the plasma zone [13, 86].

In this article, a RGA discharge co-driven by tangential gas injection and an external magnetic field was used for dry reforming of methane. Different parameters such as total flow rate, CO₂ to CH₄ stoichiometric ratio, peak arc current, and gas inlet temperature were varied to determine the most efficient parameters combination for DRM. Product gas composition was determined using a calibrated mass spectrometer and gas chromatograph. The influence of the operating parameters on RGA power, specific energy input, and energy efficiency are discussed. Optical emission spectroscopy was used to determine qualitatively the reactive species interacting in the plasma discharge. Scanning electron microscopy and Raman spectroscopy were used to analyze the deposited carbon on the electrodes after the reaction.

5.3 Experimental

An adapted version of the rotating gliding arc (RGA) reactor from [76] was developed. The RGA reactor consists of a vertically-mounted conical electrode of 38.5 mm height, which acts as a cathode mounted coaxially inside a hollow cylinder that acts as a grounded anode (Fig. 5–1). The electrodes are made of stainless steel 316, with a shortest inter-electrode gap of 2.16 mm, increasing up to 8.76 mm in the downstream direction. The angle of the cone cathode is 12.2°, and the maximum and minimum diameters are 14.7 mm and 1.5 mm, respectively. The inner diameter of the anode tube is 19.05 mm, with a wall thickness of 9.5 mm, and a total length of 482.6 mm. The reactor is mounted on two pieces that provide electrical insulation between the electrodes. First, a ceramic base (glass-mica) and second, a polyoxymethylene (Delrin™) plate. On the upper part, the reactor is terminated with a ConFlat (CF) tee adaptor that enables direct line-of-sight view along the reactor axis (from the top), and gas exhaust on the side. The plasma-forming gas mixture is injected tangentially through the reactor by two sets of three equally-spaced and angled gas injectors covering the circumference of the reactor (the two sets are separated by 10 mm). The gas injectors are mounted at an angle of 20° axially and 30° radially to the system, providing a counter-clockwise vortex flow up and around the cathode cone (as viewed from the top viewport). No external heating is provided to the reactor. The live cone cathode is powered by a custom-built dual-stage pulsed DC power supply consisting of a high-voltage arc igniter (peak voltage ~4.5 kV) and a current driver power supply (maximum output voltage –1000 V). The arc igniter consists of a Cockcroft-Walton (CW) voltage multiplier that converts a low-voltage high-frequency AC

signal to a pulsed high-voltage negative DC signal. The current driver consists of a resistor-capacitor (RC) circuit driven by a 2.5 kW negative polarity capacitor-charging power supply with a -1000 V open-circuit voltage [76]. Once the breakdown of the gas is achieved by the arc igniter at the shortest inter-electrode gap, the current driver provides the necessary current to the system and enough voltage for the arc to elongate and be sustained along the live electrode. During the elongation stage, the voltage rises while the current falls, resulting in a typical negative voltage-current characteristic of an arc. A stack of four ring magnets mounted around the anode cylinder adds a static axial magnetic field. The magnets are oriented such as to provide a Lorentz force along the gas drag force [76].

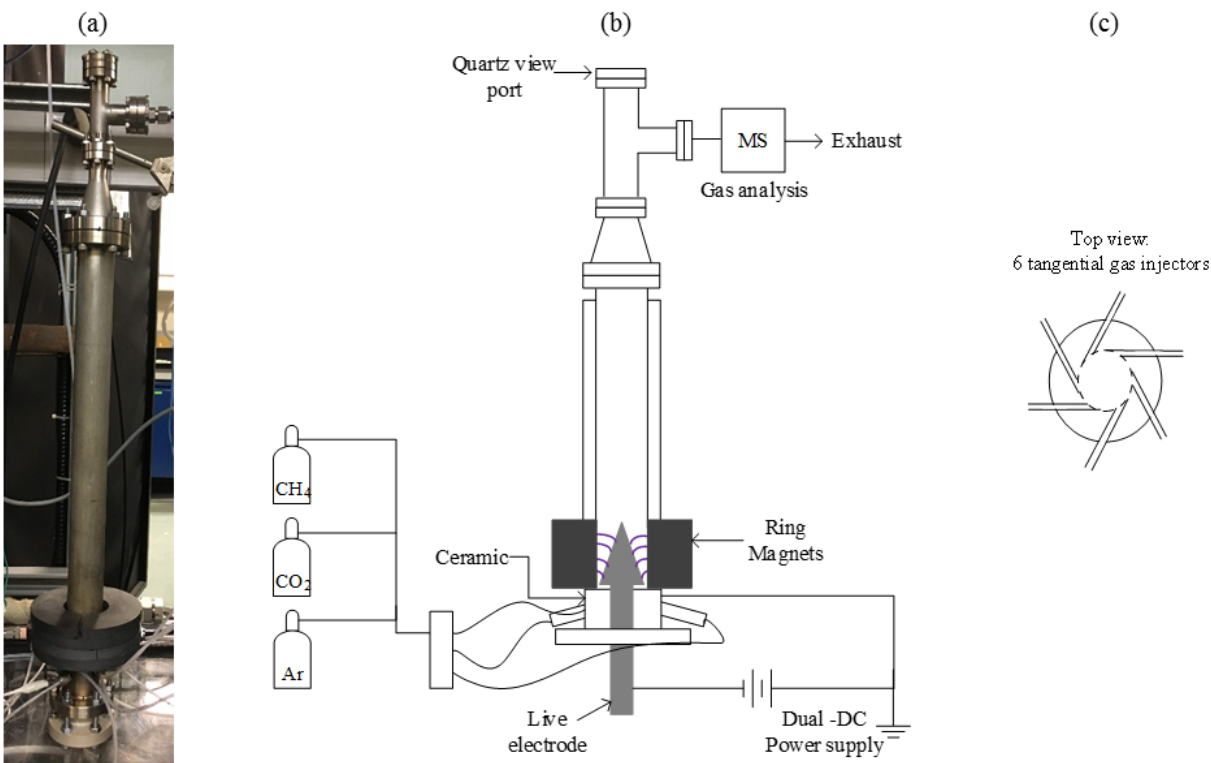


Fig. 5-1 RGA setup. (a) Photograph of the RGA reactor. (b) Schematics of the RGA setup and (c) six tangential gas injectors configuration (top view).

The RGA voltage and circuit current signals were measured online using a high-voltage probe (B&K Precision PR55) and a passive voltage probe (Tektronix P2200) across a 1Ω shunt resistor, respectively, and displayed/recorded with a digital oscilloscope (PicoScope 2207B). The exhaust gas was analyzed online by a calibrated mass spectrometer (Pfeiffer Ominstar GSD 301), and

offline by a gas chromatograph (Agilent 6890N, PLOT-Q Molesieve column) equipped with a thermal conductivity detector (TCD). A mix of gas containing Ar (99.998%, MEGS Specialty Gases), CO₂ (99.9 %, MEGS Specialty Gases), and CH₄ (99.99 %, MEGS Specialty Gases) was used. To ensure stable plasma operation, the Ar concentration was fixed at 70 vol%. The volumetric CO₂/CH₄ ratios were 1.0, 1.5, and 2.0, with total flow rates of 3.7, 4.7, and 6.7 SLPM. The maximum current delivered by the current driver was set by changing its internal resistance (1075 Ω, 535 Ω), giving rise to two peak arc current values of 0.74 and 1.50 A, with peak arc power levels of 595 and 1196 W, respectively. Each experiment was conducted 3 times, and the error bars reported were calculated as the standard error of the mean. Typical voltage, current, and calculated instantaneous power (eq. 5.13) signals are reported in Fig. 5-2 for CO₂/CH₄ = 1.0, total gas flow rate of 3.7 SLPM, and a peak arc current of 1.50 A. For these conditions, the average pulsing frequency was 28 Hz for a pulse duration of ~16 ms.

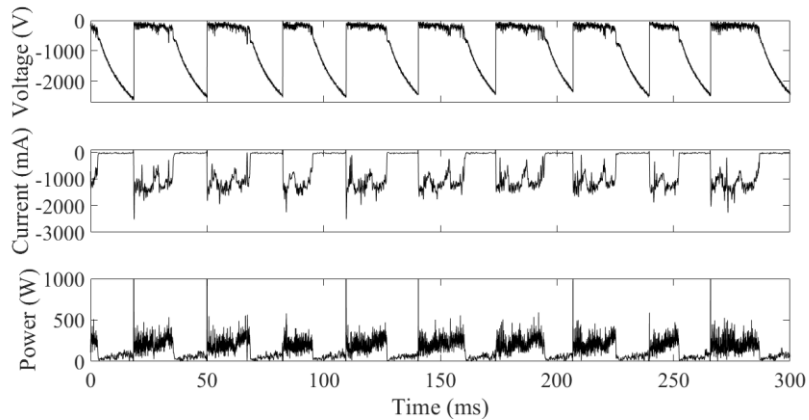


Fig. 5-2 Characteristic RGA discharge voltage, current and instantaneous power signals for DRM reaction at CO₂/CH₄ = 1.0, 3.7 SLPM, and peak arc current of 1.50 A

The gas residence time in the plasma zone (θ) was estimated as the volume accessible for the plasma (eq. 5.4) divided by the volumetric flow rate (Q), and the values are shown in Table 5-1.

$$V_{plasma\ zone} = \pi r_1^2 h - \frac{1}{3} \pi h (R^2 + r_2^2 + R r_2) \quad (5.4)$$

Where $r_1 = 9.525$ mm is the inner radius of the ground electrode, $R = 7.366$ mm and $r_2 = 0.762$ mm are the larger and small radii of the cone, and $h = 30.48$ mm is the height of the cone electrode.

The calculation of the accessible volume in the plasma zone was made by assuming that the arc goes upwards along all the height of the cone, considering the same value of height for the ground electrode.

Table 5-1 Residence times in the RGA discharge zone for different total flow rates.

Total flow rate (SLPM)	θ (ms)
3.7	~ 110
4.7	~ 86
6.7	~ 61

Carbon and coke deposition on the electrodes was observed during the reforming reaction. Cyclic reforming-cleaning protocols were developed to avoid the build-up of soot inside the reactor during long experimental runs. The RGA was operated for 15 min under reforming conditions, followed by 5 min Ar/CO₂ cleaning periods (methane flow was turned off while the other flows were kept at the same level, under the same plasma conditions). Lesueur *et al.* [130] also reported the introduction of CO₂ in a gliding arc reactor to burn off the soot produced in pure CH₄. The cleaning stage enabled the reverse Boudouard reaction (eq. 5.5) to take place and proven to be enough to remove the accumulated solid carbon deposits, as carbon oxidizes to produce CO (observed by mass spectra analysis; not reported here).



The performance of the reforming reaction was calculated based on hydrogen and carbon monoxide yields (eq. 5.6 and 5.7), and the conversions of methane and carbon dioxide (eq. 5.8 and 5.9):

$$Y_{\text{H}_2}(\%) = \frac{\dot{n}_{\text{H}_2\text{out}}}{2 \cdot \dot{n}_{\text{CH}_4\text{in}}} \times 100 \quad (5.6)$$

$$Y_{\text{CO}}(\%) = \frac{\dot{n}_{\text{COout}}}{\dot{n}_{\text{CO}_2\text{in}} + \dot{n}_{\text{CH}_4\text{in}}} \times 100 \quad (5.7)$$

$$X_{\text{CH}_4}(\%) = \frac{\dot{n}_{\text{CH}_4\text{in}} - \dot{n}_{\text{CH}_4\text{out}}}{\dot{n}_{\text{CH}_4\text{in}}} \times 100 \quad (5.8)$$

$$X_{CO_2}(\%) = \frac{\dot{n}_{CO_2in} - \dot{n}_{CO_2out}}{\dot{n}_{CO_2in}} \times 100 \quad (5.9)$$

The yield of minor byproducts such as acetylene was calculated as:

$$Y_{C_2H_2}(\%) = \frac{\dot{n}_{C_2H_2out}}{\dot{n}_{CO_2in} + \dot{n}_{CH_4in}} \times 100 \quad (5.10)$$

The H₂/CO molar ratio and the carbon balances were defined as:

$$\frac{H_2}{CO} = \frac{\dot{n}_{H_2out}}{\dot{n}_{COout}} \quad (5.11)$$

$$B_C(\%) = \frac{\dot{n}_{CO_2out} + \dot{n}_{CH_4out} + \dot{n}_{COout}}{\dot{n}_{CO_2in} + \dot{n}_{CH_4in}} \times 100 \quad (5.12)$$

Where, \dot{n}_i is the molar flow rate in (mol min⁻¹). The quantity of other hydrocarbons (C₂H₂, C₂H₄) was rather small (<0.5 mol%) and was neglected in the carbon balance.

The instantaneous power $P(t)$ was calculated by multiplying the voltage $V(t)$ and current $I(t)$ (eq. 5.13):

$$P(t) = V(t) I(t) \quad [W] \quad (5.13)$$

The evolution of the cumulative energy deposited in the RGA up to time t , $E(t)$, was calculated by integrating the product of the arc voltage $V(t)$ and circuit current $I(t)$ signals (eq. 5.14):

$$E(t) = \int_0^t V(t) I(t) dt \quad [J] \quad (5.14)$$

By determining the slope of the cumulative energy curve (assuming a linear trend, validated with Fig. 5–12), the time-averaged power was determined, which can also be obtained by eq. (5.15):

$$P_{avg} = \frac{1}{T} \int_0^T P(t) dt \quad [W] \quad (5.15)$$

where T is the total time frame observed (typically 1 s).

The Specific Energy Input (SEI) defines the amount of energy input per mol of gas injected, defined as:

$$SEI = \frac{P_{avg}}{\dot{n}_{reactants}} \quad [kJ \text{ mol}^{-1}] \quad (5.16)$$

Where $\dot{n}_{reactants}$ is the molar flow rate of CO₂ and CH₄

The energy efficiency (η) of the process was defined as the ratio of the chemical energy from the products (H₂ and CO) to the energy given to the system, i.e., CH₄ and power input (eq. 5.17)

$$\eta(\%) = \frac{\dot{n}_{H_2out} LHV_{H_2} + \dot{n}_{COout} LHV_{CO}}{P_{avg} + \dot{n}_{CH_4in} LHV_{CH_4}} \times 100 \quad (5.17)$$

where LHV_i stands for the Low Heating Value of the species in (J mol⁻¹).

Optical emission spectroscopy (OES) was used to identify reactive species in the plasma for the DRM reaction. Optical emission spectra were logged using an Ocean FX spectrometer (Ocean Optics, 25 μ m slit, extended range 200–1100 nm) with an optical resolution of 0.78 nm. The integration time per scan was 300 ms, and the resulting spectrum was the average of 5 scans. Scanning electron microscopy (SEM) (Hitachi SU8000) was performed on samples of the deposited solid carbon with an accelerating voltage of 10 to 20 kV, and working distance between 5.4 and 15.4 mm. In addition, Raman spectroscopy (Bruker SENTERRA confocal) with a wavelength of 532 nm was used to analyze the solid carbon samples collected after approximately 20 h of processing.

5.4 Results and discussion

5.4.1 Thermodynamic Analysis

Dry reforming of methane involves the most oxidized form of carbon, CO₂, combined with its most reduced form, CH₄, (eq. 5.1). In DRM, carbon dioxide can be considered as a soft oxidizing agent [40]. As an oxidant, it requires significant energy to activate the molecule in order to interact. Since CO₂ is a stable molecule, DRM is a highly endothermic reaction [123]. Figure 5-3 shows the equilibrium composition as a function of temperature for the DRM based on the minimization of Gibbs energy (HSC Chemistry 9) for CO₂/CH₄ = 1.0, 1.5, and 2.0 at 1 bar. The main products included in the reaction are CH₄, CO₂, H₂, CO, and C_(s). Water was not included in the thermodynamic calculations as it was not observed during the reaction (no peak of OH in OES

spectra). The concentration of other byproducts such as C_2H_2 and C_2H_4 are negligible ($<0.01\%$) and are not reported. Noticeable CH_4 conversion is obtained at $375\text{ }^\circ\text{C}$ (22 to 26%) for all the stoichiometric ratios. On the other hand, the conversion of CO_2 is favored at temperatures $>500\text{ }^\circ\text{C}$. Increasing CO_2/CH_4 ratio leads to an increase in CH_4 conversion, especially meaningful above $400\text{ }^\circ\text{C}$. For instance, the conversion of CH_4 increases 1.17 times when the CO_2/CH_4 ratio increases from 1.0 to 2.0 at approx. $420\text{ }^\circ\text{C}$. Conversely, CO_2 acts as the limiting reactant for the conversion of CH_4 at $CO_2/CH_4=1.0$, leaving 1% of CH_4 unreacted at $900\text{ }^\circ\text{C}$.

Hydrogen production is limited by the amount of CH_4 injected in the feed, as less CH_4 is available for dehydrogenation. Whereas the production of H_2 starts to be appreciable at $250\text{ }^\circ\text{C}$ (4 to 5%), CO yield starts to be noticeable above $450\text{ }^\circ\text{C}$ (3 to 4%) for all CO_2/CH_4 ratios. Conversely, the H_2/CO ratio decreases with increasing temperature for all the CO_2/CH_4 ratios. In addition, at $CO_2/CH_4 = 2.0$, an equimolar H_2 - CO mix is obtained at lower temperatures ($650\text{ }^\circ\text{C}$) compared to temperatures $>900\text{ }^\circ\text{C}$ for $CO_2/CH_4 = 1.0$.

On the other hand, a higher concentration of CO_2 in the mixture leads to a decrease in solid carbon formation. For instance, higher solid carbon formation can be found at $CO_2/CH_4=1.0$ at $550\text{ }^\circ\text{C}$ (6.7%), compared to $CO_2/CH_4=1.5$ (5.1%) and $CO_2/CH_4=2.0$ (4.0%) at the same temperature. Moreover, the temperature for maximum carbon formation is shifted from 550 to $500\text{ }^\circ\text{C}$ when the CO_2/CH_4 increases from 1.0 to 2.0. Higher concentrations of CH_4 in the feed favor the methane cracking reaction ($CH_4 \leftrightarrow C_{(s)} + 2 H_2$) and lead to (a) higher carbon deposition, and (b) higher temperature where the solid carbon can be suppressed. By increasing the CO_2/CH_4 from 1.0 to 2.0, solid carbon formation can be suppressed $>650\text{ }^\circ\text{C}$ instead of at $>875\text{ }^\circ\text{C}$.

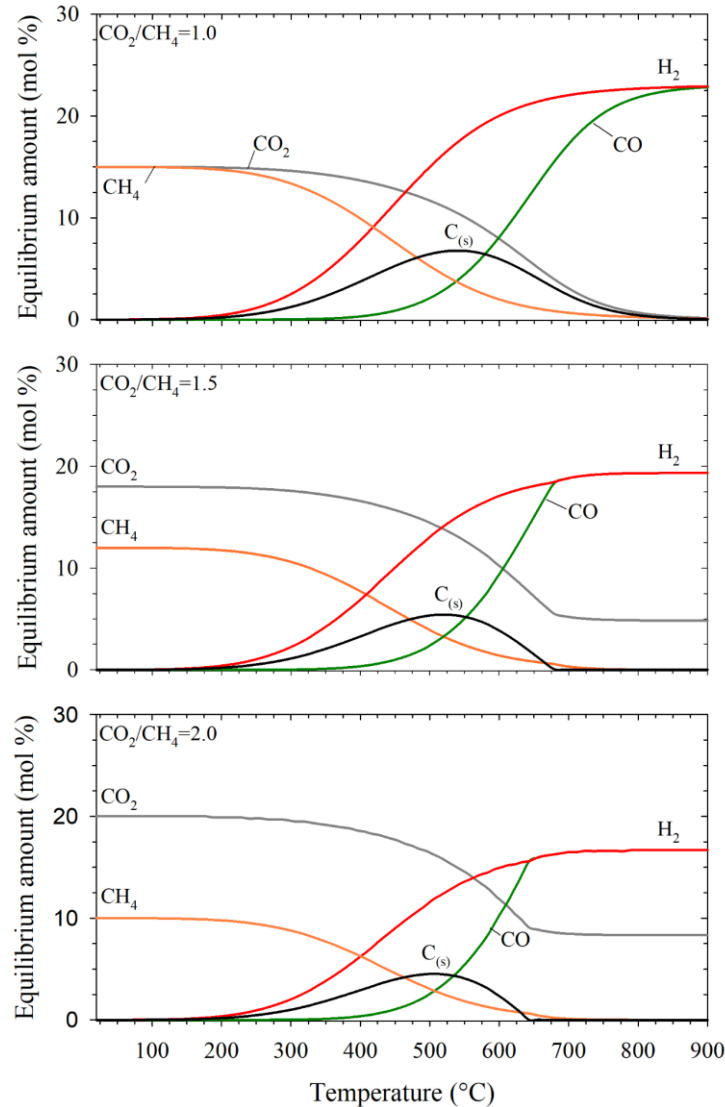


Fig. 5-3 Equilibrium composition of DRM as a function of temperature for $\text{CO}_2/\text{CH}_4 = 1.0, 1.5,$ and 2.0 at 1 bar. Note the absolute composition of Ar (in mol) is constant throughout the whole temperature range.

Hence, Ar is not reported in the graphs.

5.4.2 Conversion and Yield

Hydrogen and carbon monoxide were the main products obtained by DRM, while solid carbon (C), as well as C_2 -species such as acetylene (C_2H_2) and ethylene (C_2H_4), were minor by-products (<1% yield). The latter were observed in considerably smaller amounts when compared to other plasma sources, such as DBDs [42, 72, 131], which can be explained by a higher electron density in the rotating gliding arc lowering the activation energy and yielding a clean syngas.

The temporal evolution of the conversion of CO₂ and CH₄, as well as the yield of CO, was similar to the presented hydrogen yields (Fig. 5-5) and is not reported in this article. The average conversions of CO₂ and CH₄, as well as the H₂ and CO yields at steady-state are reported in Fig. 5-4a and 5-4b, respectively. At lower stoichiometric ratios of CO₂/CH₄, the amount of CO₂ converted was higher than the CH₄ for total gas flow rates of 3.7 and 4.7 SLPM. Conversely, when the total flow rate was increased to 6.7 SLPM, CO₂ and CH₄ conversions had mostly the same values, independently of the peak current or the stoichiometric ratio. When the peak current was set at 0.74 A, the CO₂ conversion reached a maximum value when the total flow rate increased from 3.7 to 4.7 SLPM and decreased afterwards for CO₂/CH₄ = 1.0 and 1.5. According to Zhang *et al.* [129], under certain conditions, the increase of flow rate could improve the CO₂ conversion in a RGA, which probably directs to the CO₂ activation into a more efficient pathway through vibrational excitation. Besides, increasing the total flow rate leads to an increase in the length of the arc, which enhances the conversion rate [132].

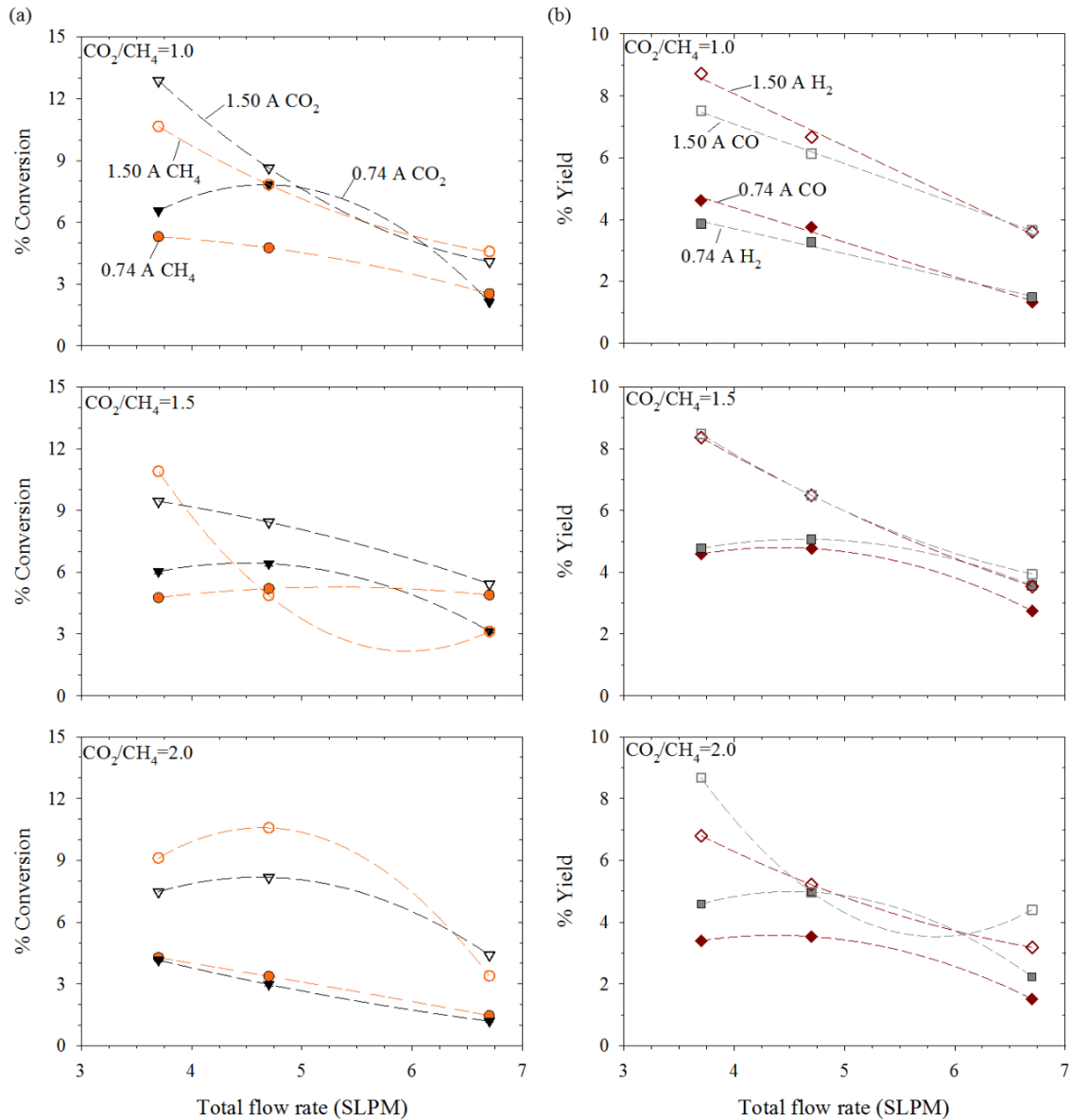


Fig. 5-4 (a) Average conversions of CO_2 and CH_4 and (b) average yields of H_2 and CO as a function of total gas flow rate for peak arc currents of 0.74 and 1.50 A. Dashed lines are used only for guidance. Note that the error bars are smaller than the symbol.

On the other hand, doubling the peak current from 0.74 to 1.50 A also increased the plasma input power, and consequently, the electron density and gas temperature. These parameters can influence CO_2 and CH_4 conversions in different ways [42]. When the peak current doubled from 0.74 to 1.50 A for a total flow rate of 3.7 SLPM, an increase in CO_2 and CH_4 conversion was particularly evident at $\text{CO}_2/\text{CH}_4=2.0$. Under these conditions, the extent of CO_2 and CH_4 conversion increased 1.8 and 2.1 times, respectively. Similarly, at 4.7 SLPM, the CO_2 and CH_4 conversion increased

from 3.0 and 3.4% to 8.2 and 10.6%, respectively, which represented increments of 2.7 and 3.1 times. By further increasing the flow rate to 6.7 SLPM, the conversion of CO₂ increased 3.7 times when the current increased from 0.74 to 1.50 A. A similar trend for the conversion of CO₂ and CH₄ can be observed for CO₂/CH₄=1.0; however, in the case of CO₂ only an increment of 10% for 4.7 SLPM was obtained when the current doubled from 0.74 to 1.50 A. The co-feeding of CH₄ and CO₂ has a synergistic effect in the conversion of each other [133]. As mentioned before, CO₂ is a soft oxidant that first dissociates into CO and O radicals (eq. 5.18), generating some oxygen species, such as metastable O (¹D). Reactive oxygen species can break the C-H bond and generate methyl and hydroxyl radicals from CH₄ [42, 133].

Hydrogen yields as a function of time for two different peak current levels at CO₂/CH₄=1.0 are depicted in Fig. 5-5. These yields vary with time, presenting a transient behavior in the first minutes, i.e., reaching a maximum value (and more variability) between 3 and 5 min and stabilizing afterwards, with constant values and low variability. This finding could be helpful in determining the more convenient time to measure gas concentrations with consistent results, especially with offline measurements. On the other hand, an increase in yield was observed when the peak arc current was doubled. A higher arc current is associated with a higher electron density, thus providing high rates for breaking the strong C-O and C-H bonds, resulting in higher conversions of CO₂ and CH₄ and higher production of CO and H₂.

The residence time in the RGA discharge zone is a function of the total flow rate, whereas a higher total gas flow rate means a lower gas residence time in the plasma zone (Table 5-1), hence less time for CO₂ and CH₄ to react and collide with electrons and active species to produce syngas. This effect was clearly seen with the peak arc current of 1.50 A, where higher H₂ and CO yields at lower total flow rates were obtained. However, when the peak arc current was 0.74 A, there was almost no observable effect of the total flow rates of 3.7 and 4.7 SLPM on the yields. In addition, increasing the total flow rate from 3.7 to 6.7 SLPM decreased CO₂ and CH₄ conversions. When the CO₂/CH₄ ratio was set to 1.0, a high concentration of H₂ was observed, as more CH₄ was available for dehydrogenation. Equally, when the CO₂/CH₄ ratio was set to 2.0, there was a higher production of CO. Once steady state was achieved, the maximum values of H₂ and CO obtained with a peak arc current of 1.50 A and 3.7 SLPM were 8.7% for both H₂ and CO at CO₂/CH₄ of 1.0 and 2.0, respectively.

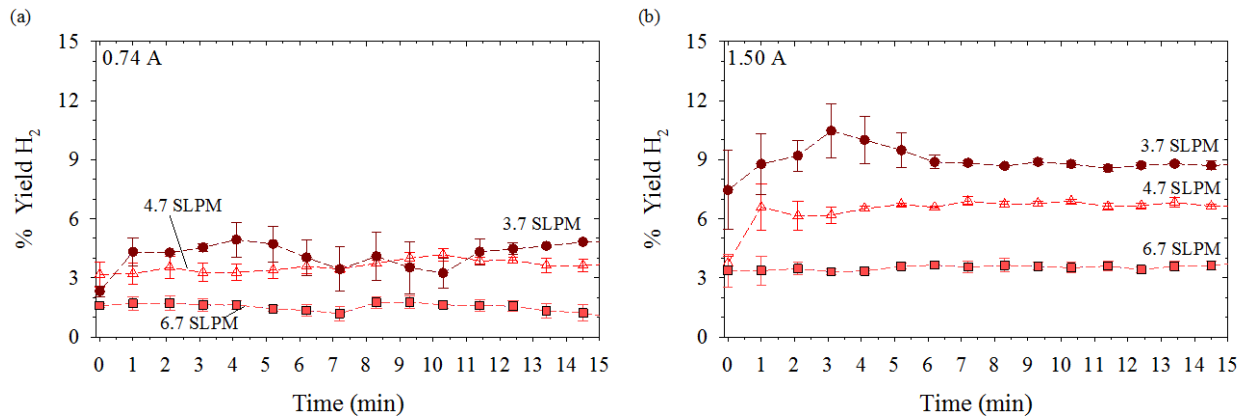


Fig. 5-5 Temporal evolution of H₂ yields at peak currents of (a) 0.74 and (b) 1.50 A, for CO₂/CH₄ = 1.0 and total flow rates of 3.7, 4.7, 6.7 SLPM. Dashed lines are used only for guidance.

The residence time in the RGA discharge zone is a function of the total flow rate, whereas a higher total gas flow rate means a lower gas residence time in the plasma zone (Table 5-1), hence less time for CO₂ and CH₄ to react and collide with electrons and active species to produce syngas. This effect was clearly seen with the peak arc current of 1.50 A, where higher H₂ and CO yields at lower total flow rates were obtained. However, when the peak arc current was 0.74 A, there was almost no observable effect of the total flow rates of 3.7 and 4.7 SLPM on the yields. In addition, increasing the total flow rate from 3.7 to 6.7 SLPM decreased CO₂ and CH₄ conversions. When the CO₂/CH₄ ratio was set to 1.0, a high concentration of H₂ was observed, as more CH₄ was available for dehydrogenation. Equally, when the CO₂/CH₄ ratio was set to 2.0, there was a higher production of CO. Once steady state was achieved, the maximum values of H₂ and CO obtained with a peak arc current of 1.50 A and 3.7 SLPM were 8.7% for both H₂ and CO at CO₂/CH₄ of 1.0 and 2.0, respectively.

The total gas flow rate and peak arc current had a stronger influence on DRM than changing the CO₂/CH₄ ratio. The CO₂/CH₄ ratio did not affect the DRM reaction significantly, but influenced the H₂/CO ratio, as shown in Fig. 5-6. Controlling the H₂/CO ratio in syngas might be useful for valorization purposes [134], as it influences the downstream process. For instance, syngas very rich in CO is valuable for the production of oxygenated chemicals [58, 135]. In Fig. 5-6, the error bars represent the standard error of the mean considering the variations between the different flow rates and peak currents. The CO₂/CH₄ ratio presented an inversely proportional behavior to the H₂/CO₂ ratio, i.e., the higher the CO₂ concentration in the feed mixture, the lower the amount of

H₂ produced, as less CH₄ was available for dehydrogenation. There was no significant effect of the peak arc current or the total flow rate on the H₂/CO ratio.

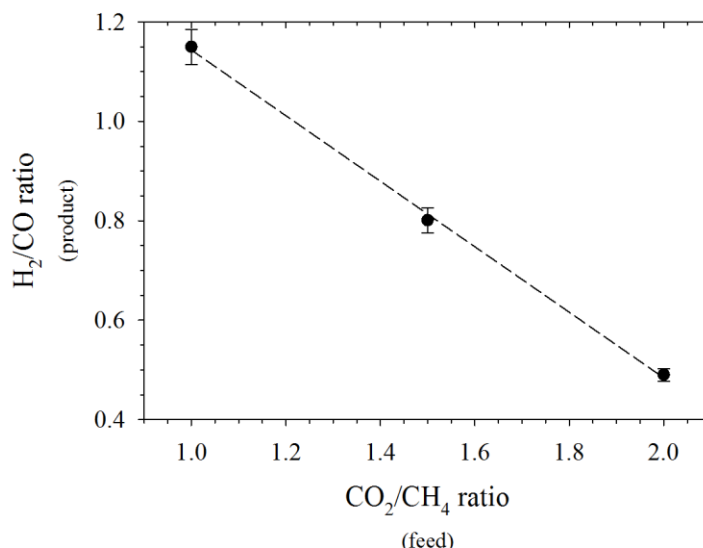


Fig. 5-6 Influence of the CO₂/CH₄ ratio on the H₂/CO ratio, the symbols represent the average values.

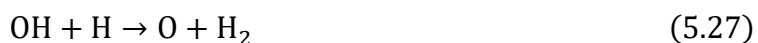
Dashed lines are used only for guidance.

Carbon monoxide is mainly formed via dissociation of CO₂ (eq. 5.18) upon collision with electrons [136, 137]. Recombination of radicals in the reactive plasma can lead to the formation of carbon monoxide (eq. 5.19 to 5.21) and carbon dioxide (eq. 5.22). Some of the elementary steps for CO and CO₂ formation are stated by the following equations [58, 71]:



The dissociation of methane by electron collisions produces the CH₃ radical that by further dissociation produces hydrogen. Some of the reactions leading to H₂ production are stated by equations 5.23 to 5.28 [58, 71]





Trace amounts of acetylene were measured in the gas product, which might have been formed via various C-C coupling reactions such as dimerization of radical CH (eq. 5.29) or CH₂ with subsequent H₂ elimination (eq. 5.30) or via ethylene dehydrogenation (eq. 5.33). Ethylene was most likely formed via CH₃ or CH₂ coupling, instead of dehydrogenation of ethane as the latter was not observed with mass spectrometry (eqs. 5.34 and 5.35).

Some of the possible reactions for the formation of acetylene are stated by equations 5.29 to 5.33 [71]:



Conversely, possible reactions for ethylene formation are stated by equations 5.34 and 5.35 [71]:



Acetylene production decreased significantly with increasing the CO₂/CH₄ ratio as well as with increasing the total gas flow rate (Fig. 5-7). For CO₂/CH₄ = 1.0, an acetylene concentration of 0.23 mol% was measured, which decreased to less than half (0.11 mol%) at a ratio of 1.5 and decreased further to 0.05 mol% at a ratio of 2.0. The formation of C₂H₂ was directly proportional to the inlet partial pressure of CH₄ with an apparent reaction order of 3.7 ± 0.2 at a flow rate of

3.7 SLPM. At higher flow rates the reaction order in CH_4 decreased to 2.9 ± 0.1 and 2.7 ± 0.3 at 4.7 SLPM and 6.7 SLPM, respectively (see supplementary material A). This implies that increasing the CH_4 partial pressure by a factor of 2 increases the acetylene formation by at least a factor of 8. At a higher total gas flow rate and thus, for lower residence time, less CH radicals and therefore less C_2H_2 were produced. This effect was more pronounced at lower CO_2/CH_4 ratios (i.e., higher CH_4 partial pressure). A small amount (< 0.02 mol%) of ethylene (C_2H_4) was measured; however, no clear trend was visible. Especially at high flow rates and low peak currents, no ethylene was observed.

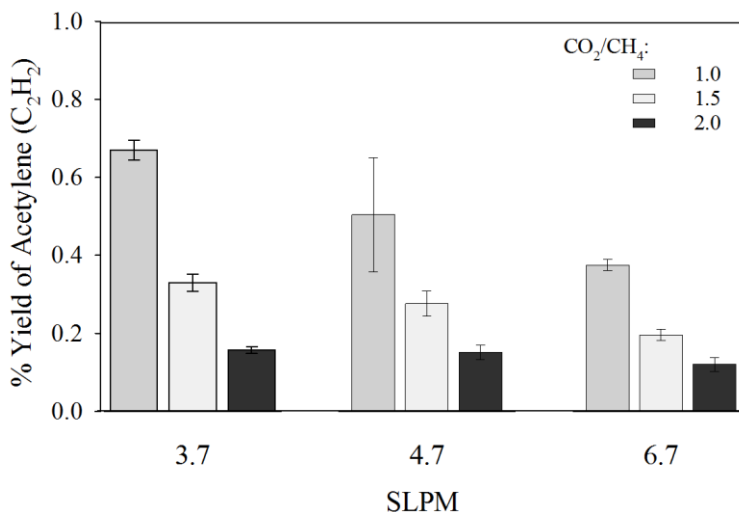


Fig. 5-7 Yield of acetylene concentration for DRM for CO_2/CH_4 ratios of 1.0, 1.5 and 2.0, total gas flow rates of 3.7, 4.7 and 6.7 SLPM, and peak current of 1.50 A.

The carbon balance for all the experiments was $>95\%$. Ethylene and acetylene were not considered in the carbon balance due to their small concentrations (<0.25 mol %, $<1\%$ yield). The main carbon product was CO , and the C_2 products were more than 100 times less than the CO produced. The low concentrations of byproducts imply good selectivity for H_2 and CO when the DRM is carried out in the rotating gliding arc discharge.

A 3 h experiment was carried out in the RGA reactor to determine the temporal evolution of the CO_2 and CH_4 conversions, and the CO and H_2 yields with a total gas flow rate of 3.7 SLPM, CO_2/CH_4 ratio of 1.5 and peak arc current of 1.50 A (Fig. 5-8a). Initial conversions of 13 and 14 % were achieved in the first 10 min for CO_2 and CH_4 , respectively. Thereafter, the CO_2 conversion dropped to 10 % and stabilized until the end of the 3 h run, while the CH_4 conversion steadily

decreased from 14% to 10%. As for CO and H₂, an equimolar amount was observed during the 3 h as per the dry reforming reaction ($\text{CO}_2 + \text{CH}_4 \rightarrow 2\text{CO} + 2\text{H}_2$). This also indicates the absence of water gas shift and steam reforming reactions. The CO and H₂ yields decreased slightly towards the end of the run, most likely due to carbon deposition on the electrodes.

Fig 5-8b shows the temperature inside the reactor (~76 mm above the cathode, to avoid interactions between the thermocouple and the arcs) as a function of time. The reactor itself was insulated to reduce heat losses through the walls. It took more than 60 min to reach a stable temperature at around 227 °C. The sudden temperature drop of 5 °C between minutes 15 and 20 could be attributed to the energy given to the RGA was mostly transformed into chemical energy, as more CH₄ and CO₂ converted before min. 20, rather than into thermal energy. This thermal induction period in the RGA reactor has been reported by others using non-thermal plasma discharges as well [62, 138–141]. When the RGA discharge was operating, faster heating in the gas was observed because the power was directly applied through the RGA and not through the walls, like in the case of a conventional gas heater. Nonetheless, regardless of the gas heating, the RGA discharge is mostly considered non-thermal or “warm” plasma as the electron temperature is conventionally >1 eV, whereas the gas temperature could reach 1000–3000 K, but still sustaining a non-equilibrium between heavy particles and electrons [83]. During the first 15 min of operation, there was a rapid increase in temperature, $\Delta T=135$ °C, while the conversion and yields presented higher values. After 100 minutes, the reaction temperature achieved steady-state, with a temperature of 227 °C and an overall $\Delta T=206$ °C. Carbon dioxide and methane are polyatomic molecules with vibrational, translational, and rotational modes. Hence, the kinetic energy transferred from the electrons to the molecules and between the molecules themselves is mainly converted into thermal energy, translating in an increase of temperature. Note that even in the context of a highly endothermic reaction, the increase of the gas temperature did not enhance the performance of the DRM reaction. Actually, CO₂ and CH₄ conversions decreased by 20 and 25%, respectively, when calculated at the beginning of the reaction (between 10 to 15 min) compared to the conversion determined at the end of the reaction (between 170 to 175 min), possibly due to accumulation of carbon deposited on the electrodes. Decreased CO₂ and CH₄ conversions have also been reported by [140] when increasing the temperature in a DBD catalytic reactor, without an explanation provided by the authors.

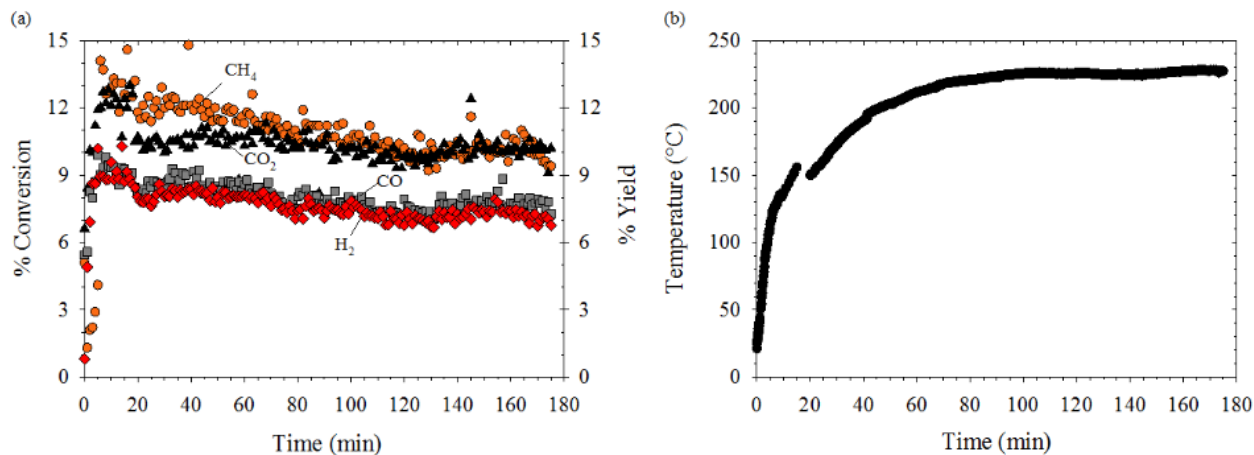


Fig. 5-8 (a) Conversion of CO₂ and CH₄, and yield of H₂ and CO and (b) temperature profile as a function of time of the DRM at a total flow rate of 3.7 SLPM, CO₂/CH₄=1.5 and peak current of 1.50 A.

5.4.3 Effect of inlet gas temperature

Some studies have reported preheating the reactants [82, 131] for DRM in gliding arc discharge, whereas others have carried out the reaction with gases being fed at room temperature [42, 73, 132]. However, the effect of inlet gas temperature on CO₂ and CH₄ conversions and H₂ and CO yields for RGA discharge is still not clear. Maqueo *et al.* [119] reported that preheating the inlet gas did not affect the plasma-assisted dry reforming reaction in a nanosecond pulsed discharge. Zhou *et al.* [58] reported that increasing the temperature up to 250 °C in a DBD reactor hardly influenced the conversion of CO₂ and CH₄. An ANOVA statistical analysis was performed to the results to determine whether the means of the two groups, i.e., preheated and not-preheated flow, were statistically different from each other (see supplementary material B). Figure 5-9 shows the conversions of CO₂ and CH₄ and the yields of CO and H₂ as a function of time for non-preheated and preheated (200 °C) inlet gas feeding. The results of the ANOVA tests indicated that there was not enough evidence to state a significant statistical difference between the means of the conversions and yields for pre-heated and not preheated gas inlet. On the other hand, the H₂/CO ratio decreased from 0.86 to 0.77 when the inlet temperature was increased to 200 °C. However, this can still be considered as part of the error reported previously in Fig. 5-6 (lower limit of error bar).

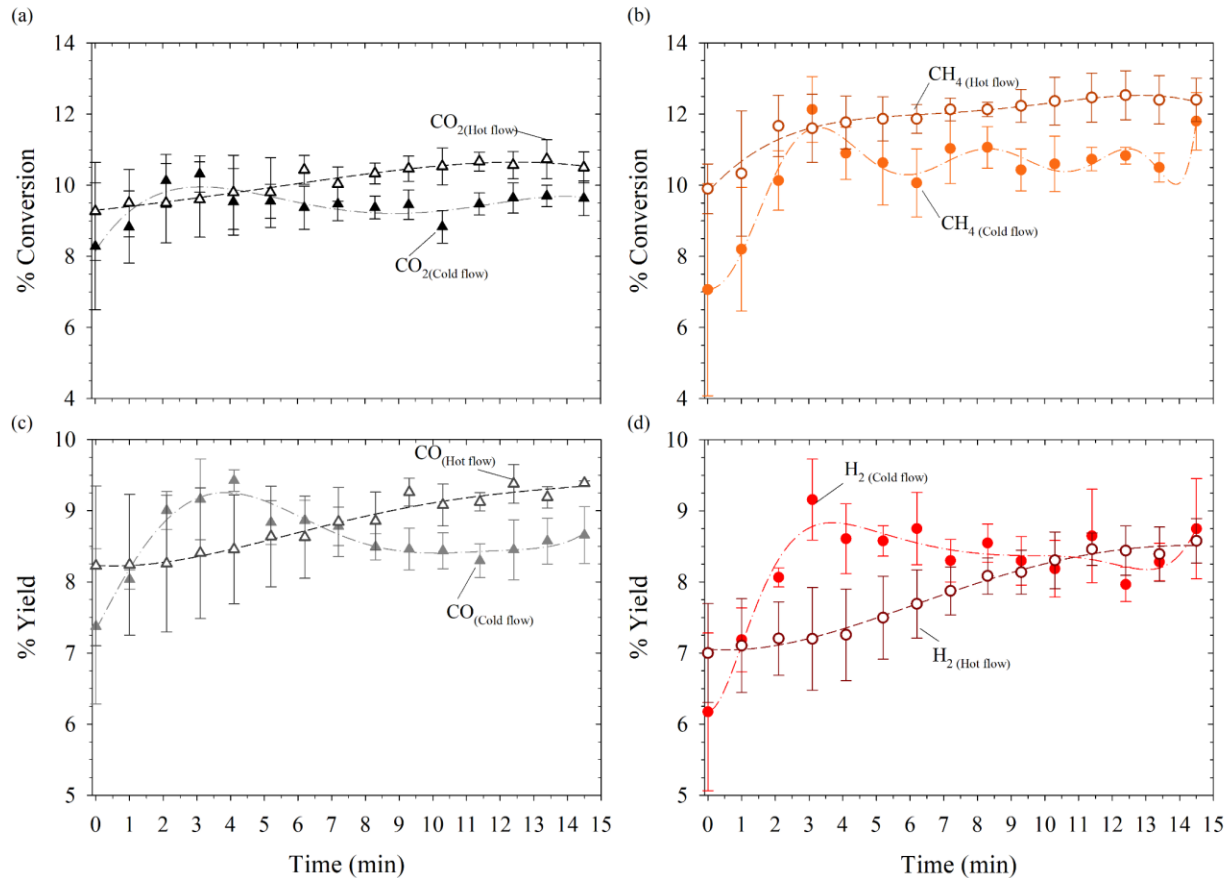


Fig. 5-9 (a) CO_2 conversion, (b) CH_4 conversion, (c) CO yield and (d) H_2 yield as a function of time for not preheated (open symbols) and preheated (full symbols) gas at a total flow rate of 3.7 SLPM, $\text{CO}_2/\text{CH}_4=1.5$, and peak current of 1.50 A. The error bars represent the standard error of the mean.

Dashed lines are used only for guidance.

The energy needed to preheat the inlet flow was provided by a gas heater wrapped with heating tape. Considering the power supplied by the heating tape, the total input power was determined (discussed further in the next section). The input power, i.e., RGA power and power provided by the heating tape, increased from 166 to 590 W (3.5 times more) when the temperature was 200 °C. Thus, the energy efficiency (eq. 5.17) dropped from 8.1 to 4.7%, which represents a drop of 60%, reducing the effectiveness of the process when the temperature was increased from room temperature to 200°C. As discussed in the previous section, plasma discharges induce gas heating. This result is shown in Fig. 5–10, where T_1 is the inlet temperature measured in the manifold, before the distribution of the gas through the gas injectors. T_0 was measured during the first 20 min just above the cathode cone (no arcing) and 76 mm above it when the RGA was active. Note

that the thermocouple was placed first on top of the cathode cone to the gas inlet in the reactor to determine the temperature of the gas compared to the temperature measured at the manifold. Then the thermocouple was moved away during the RGA experiment to avoid interactions between the thermocouple and the arcs. Three periods of DRM reaction were carried out at a total flow rate of 3.7 SLPM, $\text{CO}_2/\text{CH}_4=1.5$, and peak arc current of 1.50 A, separated by two periods of electrode regeneration (CH_4 flow was stopped during regeneration phase; hence, total flow rate decreased to 3.26 SLPM).

The gas heating caused by the RGA is clearly seen in Fig. 5–10. We also noticed that the gas heating appeared to be faster during the regeneration phase (carried out in Ar/CO_2) as the specific heat value of CO_2 ($c_p = 0.844 \text{ J g}^{-1} \text{ K}^{-1}$) is ~ 2.6 times lower than for CH_4 ($c_p = 2.22 \text{ J g}^{-1} \text{ K}^{-1}$). Therefore, more energy was needed to change the temperature of the mix, CH_4 and CO_2 , than when the RGA was operating only with CO_2 , making the gas heating faster in the last case. Besides, during the regeneration phase there was a decrease of the total flow rate from 3.70 to 3.26 SLPM whilst the RGA was operating at the same power conditions, which also made the gas heating faster during this phase. The overall temperature change associated with RGA heating was $\Delta T_0 = 241 \text{ }^\circ\text{C}$.

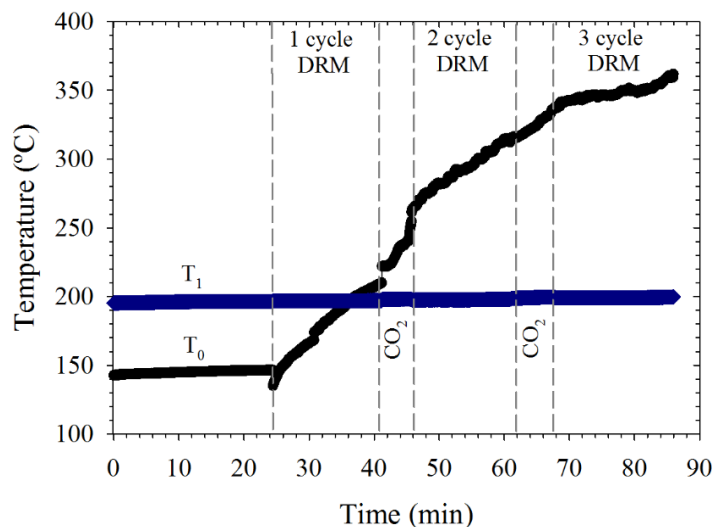


Fig. 5-10 Gas temperature of the inlet (T_1) and inside the reactor (T_0) versus time for 3 DRM periods separated by two periods of electrode regeneration. Total flow rate of 3.7 SLPM during DRM and 3.26 SLPM during electrode regeneration, $\text{CO}_2/\text{CH}_4=1.5$, peak current of 1.50 A.

5.4.4 Energy

Figure 5-11 shows the cumulative energy deposition in the RGA (eq. 5.14) over 25 s for DRM with CO_2/CH_4 ratios of 1.0, 1.5 and 2.0 with a total flow rate of 3.7 SLPM and peak arc current of 1.50 A. The trend is linear, revealing the steadiness of the RGA power over this time scale. Using the slope of the cumulative energy lines, average powers (eq. 5.15) of 155.0 ± 0.4 W, 166.0 ± 0.5 W, and 142.1 ± 0.6 W were obtained, respectively. This reveals that the average power not only changed with the gas composition but also with the total gas flow rate (Fig. 5-11 and 5-12 a, b). The changes between the average powers of the mixtures can be attributed to the differences between the resistivity of the gas mixture and the radiative losses.

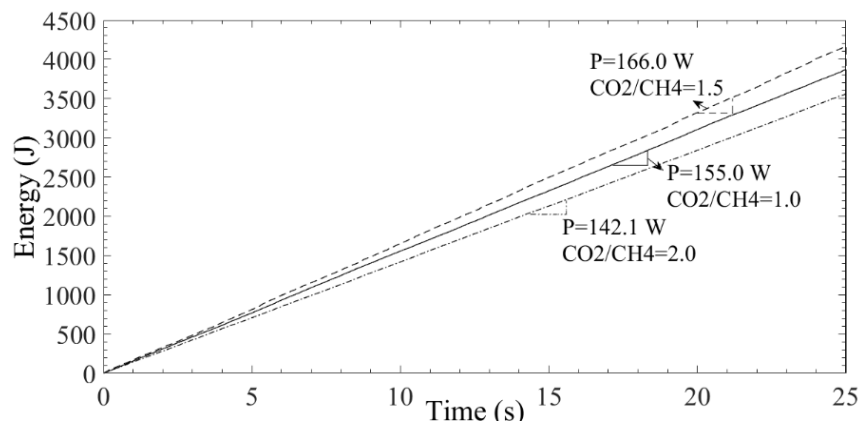


Fig. 5-11 Temporal evolution of the accumulated energy deposited for DRM for CO_2/CH_4 ratios of 1.0, 1.5 and 2.0 at a total flow rate of 3.7 SLPM and peak current of 1.50 A.

An increased RGA current led to an increased deposition of solid carbon on the electrodes and increased the production of C_2H_2 . These undesired by-products were not considered in the energy efficiency calculations, which can lead to an underestimation of the overall process efficiency [119]. For instance, considering the carbon balance, approximately 5% of the solid carbon contributes up to ~ 19.7 kJ for the energy balance. However, only major gas components were considered in the calculation of energy efficiency (eq. 5.17). Energy efficiency increased in a range of 1.1 to 2.3 times when the peak arc current was doubled (Fig. 5-12 e, f), but decreased when the total gas flow rate was increased. This effect can be explained due to the smaller yields of H_2 and CO production, as shown in Fig. 5-4b. The energy efficiency also increased by increasing the amount of CO_2 in the feed, i.e., at higher CO_2/CH_4 ratios, when the current doubled from 0.74 to 1.50 A. At higher RGA current and CO_2/CH_4 ratio in the inlet gas composition, the amount of

carbon deposited on the electrodes was lower than in the other cases, which affected not only the reaction products but also the overall energy efficiency. In Fig. 5-12(c, d), the SEI decreased linearly when increasing the total gas flow rate for both peak arc currents and for all stoichiometric ratios. Furthermore, when the arc current was doubled, the best energy efficiencies were obtained at lower SEI values. This effect has also been reported in [142]. In our study, it could be observed that the best energy efficiencies were obtained at $\text{CO}_2/\text{CH}_4 = 2.0$, and peak current of 1.50 A for each flow rate. These results indicate that higher concentrations of CO_2 in the inlet stream are beneficial for the DRM reaction, most likely as the C-C coupling is hindered due to lower CH_4 partial pressure; consequently, producing less coke. In contrast, when the arc current was set at 0.74 A, the highest energy efficiencies and SEI values were obtained at $\text{CO}_2/\text{CH}_4=1.5$ for all total gas flow rates.

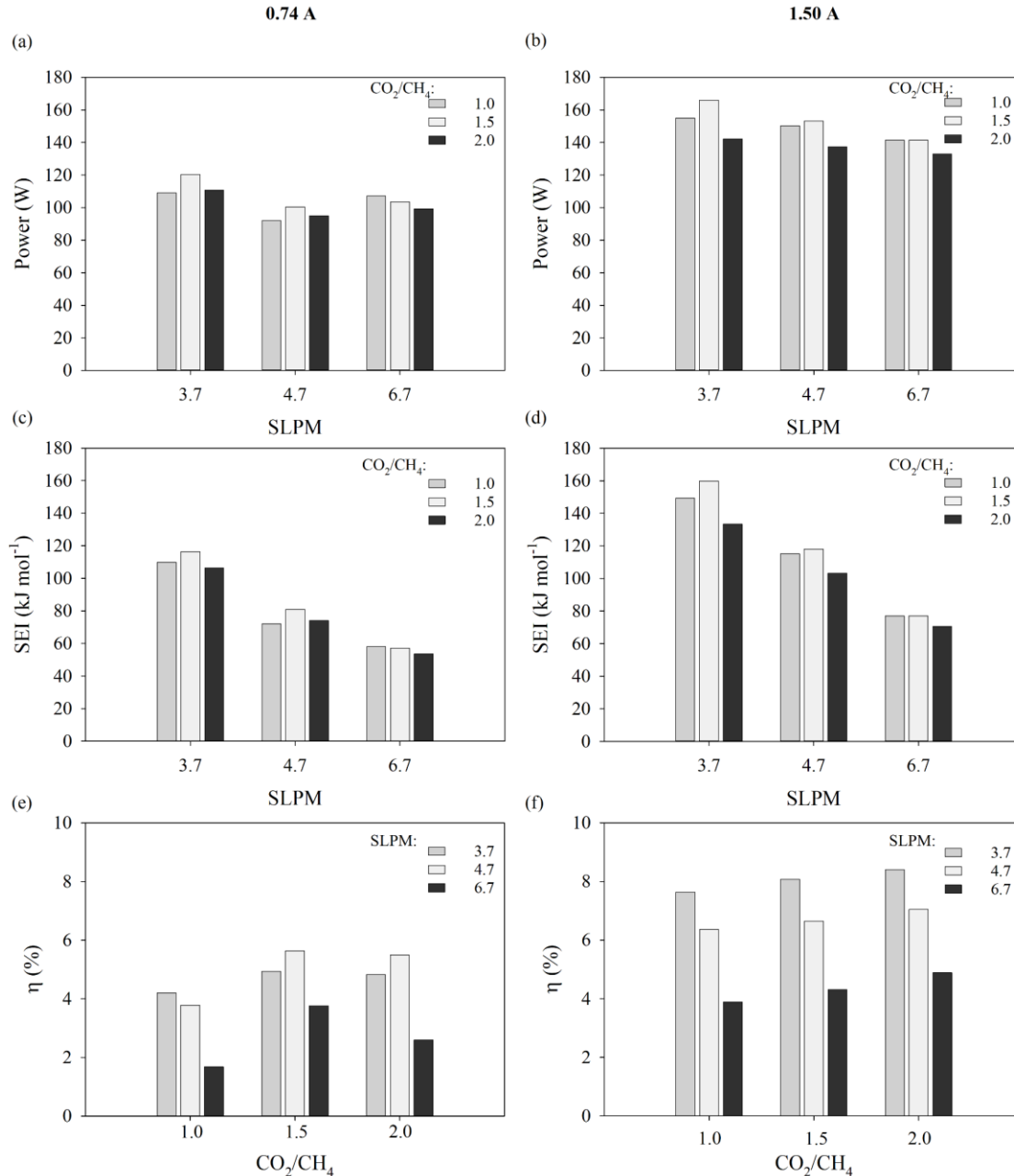


Fig. 5-12 Power provided to the RGA (a, b), specific energy input (SEI) (c, d) and energy efficiency (η) (e, f) for DRM with CO_2/CH_4 ratios of 1.0, 1.5 and 2.0, total gas flow rate of 3.7, 4.7 and 6.7 SLPM, and peak currents of 0.74 and 1.50 A.

Table 5-2 shows the percentage of electrical power that contributed to H_2 and CO production. This value was calculated by considering only the power in the denominator of eq. 5.17. It can be noticed that the electrical power input contributed in a range of ~15 to 30% to the conversion of CH_4 and CO_2 to H_2 and CO . When the current was 0.74 A, there was a higher use of the electrical

power input for a total flow rate of 4.7 SLPM, as increasing the flow rate could direct to an increase in the arc length and CO₂ activation into a more efficient pathway, as mentioned before [129, 132], also leading to higher CO production. In the case of the peak current of 1.50 A, there is no significant difference in the percentage of electrical power contribution between the different conditions studied.

Table 5-2 Percentage of electrical power input that contributed to the H₂ and CO production, for peak currents of 0.74 and 1.50 A, CO₂/CH₄=1.0, 1.5, 2.0 and total flow rates of 3.7, 4.7 and 6.7 SLPM

CO ₂ /CH ₄	1.0		1.5		2.0	
	0.74 A	1.50 A	0.74 A	1.50 A	0.74 A	1.50 A
Total flow rate (SLPM)						
3.7	19.8	29.0	19.9	26.1	17.0	26.7
4.7	26.5	30.1	29.8	26.6	26.6	27.1
6.7	14.6	25.7	28.1	24.6	17.0	25.1

Table 5-3 shows a comparison of the performance parameters for different plasma sources for DRM. It can be noticed that the SEI of the DRM reaction using gliding arc discharges is 4 to 167 times lower compared to other plasma sources such as corona discharges or dielectric barrier discharges. This means that more energy needs to be supplied to the discharge to treat the same amount of gas than for gliding arcs. As a transitional plasma discharge (or warm plasma), gliding arc discharges possess characteristics of thermal and non-thermal plasmas, providing higher gas temperatures and electron densities compared to non-thermal plasmas, but still working under at low current and power density [72, 82, 137]. As reported by [42] the electron density in the gliding arc discharges (10^{23} m^{-3}) is higher compared to corona (10^{15} - 10^{19} m^{-3}), glow discharges, and DBDs (10^{16} - 10^{19} m^{-3}). Hence, it is easier to achieve higher conversions at higher flow rates with GA [72]. The RGA is a promising technology to conduct highly endothermic reactions like the DRM. Improvements in the performance of this plasma source can be achieved by optimizing the power delivery.

Table 5-3 Comparison of performance parameters for different plasma sources for DRM

Plasma source	Feed flow (mL min ⁻¹)	CO ₂ /CH ₄	Conversion (%)		Yield (%)		Power discharge (W)	SEI (kJ L ⁻¹)	Ref.
			CH ₄	CO ₂	H ₂	CO			
DBD	50	1/1	30.0	19.2	8.7	10.0	50	60.0	[62]
DBD	200	4/1	64.0	54.0	52.0	14.0	1000	300.0	[58]
DBD	20	1/1	79.7	52.7	59.8	NR	NR	NR	[61]
Nanosecond pulsed dis.	100	3/2	30.0	NR	12.0	7.5	10	6.3	[119]
DC corona dis.(positive)	60	2/1	86.0	65.0	55.7	NR	45	45.0	[66]
Glow dis.	2200	6/4	61.0	49.9	54.4	NR	NR	NR	[63]
AC Gliding arc	7500	7/3	13.1	8.4	4.1	NR	NR	NR	[42]
Gliding arc Plasmatron	10000	3/1	41.0	24.0	20.9	NR	500	3.0	[88]
Gliding arc	1000	1/1	40.0	31.0	20.0	NR	190	11.4	[72]
RGA	12000	1/1	36.0	35.0	9.8	NR	471	2.4	[73]
RGA	6000	1/1	48.0	54.0	48.0	51.0	175	1.8	[82]
RGA	3700	1/1	10.9	12.8	8.7	7.5	155	6.7	This work

*NR states for Non-Reported. The italic fonts are calculated values based on eq. 5.16 for SEI (values divided by 22.4 L mol⁻¹ to get kJ L⁻¹)

5.4.5 Qualitative Analysis of the Optical Emission Spectrum

Figure 5-13 shows the characteristic optical emission spectra (200-700 nm) obtained for a RGA operating with CO₂/CH₄ = 1.5, total gas flow rate of 3.7 SLPM and peak currents of 0.74 and 1.50 A. Due to the strong molecular emissions from C₂ Swan bands (468-473, 500-516, and 530-563 nm), the arc appeared bright green. C₂ was formed during hydrocarbon degradation in the discharge [143] and is considered an indicator for nanostructured solid carbon formation [73]. We observed that increasing the relative concentration of CO₂ in the inlet gas mixture led to an overall decrease in the intensity of the C₂ Swan bands (spectra not reported here). The latest observation was confirmed visually as the visual appearance of the arc went from green to white when the amount of CO₂ in the inlet flow increased. Moreover, higher amount of H₂ was produced at lower

CO₂ concentrations, i.e., CO₂/CH₄ = 1.0, meaning a reduced degree of dehydrogenated CH₄. CH bands were identified around 387 and 430 nm (A²Δ → X²Π transitions) [62], which according to Ray *et al.* [144] is due to the excitation of C²Σ⁺ → X²Π and indicates the formation of higher hydrocarbons (first band). Additionally, some molecular emission bands related to CO₂ were identified around 357, 374 and 435 nm [143, 145]. An intense emission line was observed at 588.7 nm, which is most likely attributed to carbon ions, C⁺ [146]. The H_α emission line was also observed at 656 nm, whereas a weak emission band for CO was identified at 283 nm [62, 143]. These reactive species participate directly in the reforming reaction where CO₂ and CH₄ are ionized and dissociated to produce ions and radicals that interact and convert mainly into CO and H₂.

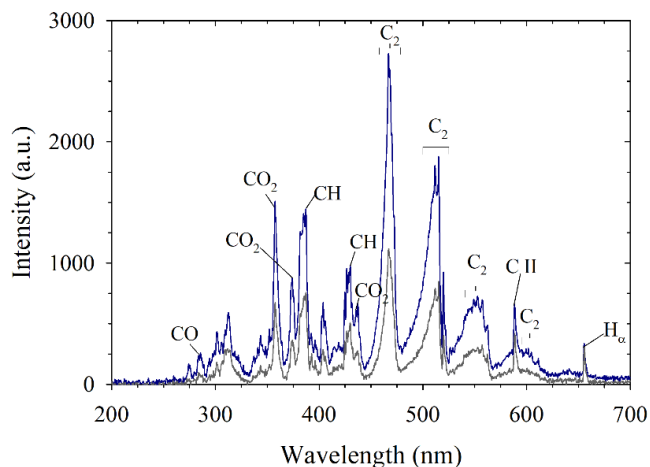
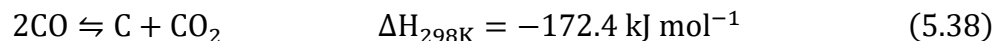
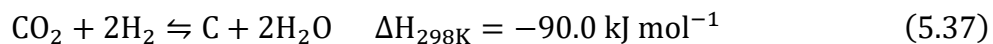
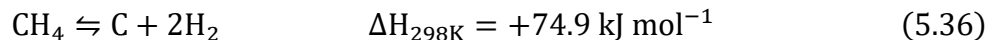


Fig. 5-13 Emission spectra observed in the RGA for DRM at CO₂/CH₄ = 1.5, a total flow rate of 3.7 SLPM and peak currents of 0.74 (less intense) and 1.50 A (more intense).

5.4.6 Morphology of the deposited particulates

One of the main drawbacks of DRM is the occurrence of carbon deposition. This process is unavoidable and thermodynamically favored [40] as shown by equations 5.36 to 5.38



Equation (5.36) is known as methane cracking or methane pyrolysis; equation (5.37) involves steam generation via CO₂ reforming, i.e., CO₂ reduction, whereas equation (5.38) is the Boudouard reaction (opposite of eq. 5.5) [36, 123]. According to their origin, two different types of deposits can be identified: solid carbon and coke. Solid carbon is a product of CO-disproportionation, whilst coke occurs as decomposition or condensation of hydrocarbons on the catalyst surface [26]. Carbon deposition depends on the CO₂/CH₄ ratio, being favored at lower ratio [42]. The methane decomposition process not only leads to higher production of H₂ but also to more solid carbon deposited on the electrodes [40]. Particulate deposition was observed not only on both electrodes (Fig. 5-14) but also in the upper and colder sections of the reactor, towards the gas exhaust. Furthermore, micron-sized particles of stainless steel, mostly produced by arc erosion of the cathode, were found in the deposits (confirmed with Energy Dispersive X-ray Spectroscopy (EDS)). In the samples collected on the anode surface (Fig. 5-14e and 5-15), the stainless-steel microparticles were mostly covered by a carbon-containing structure (Fig. 5-14f and 5-15).

Carbon samples collected from the cathode were also analyzed by Raman spectroscopy (Fig. 5-16). The D, G, and G'-bands can be clearly identified. The D-band at 1327 cm⁻¹ corresponds to the amorphous carbon (non-graphitized) and disordered structure. The G-band at 1582 cm⁻¹ is linked to the tangential mode of the graphene sheet and graphitized structure [42, 73]. Finally, the G'-band, also known as the 2D band, at 2665 cm⁻¹ is the result of different interlayer interactions occurring at different depths within the graphene [147]. The intensity of the D band relative to the G band quantifies the degree of crystallinity of the graphite layers, in this study I_D/I_G = 1.5, which suggests a low degree of graphitization [42].

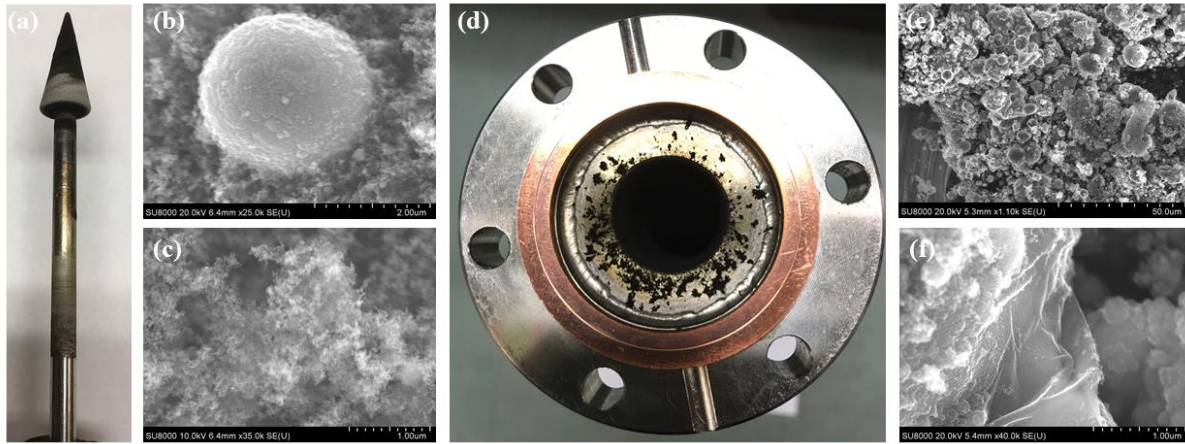


Fig. 5-14 Left: (a) stainless steel cathode covered with black carbon, a by-product of DRM, (b) stainless steel particle found in the black carbon, as a result of electrode erosion, (c) black carbon. On the right: (d) top view of the stainless steel anode with some black carbon powder, (e) black carbon and stainless steel particles, (f) carbon structure.

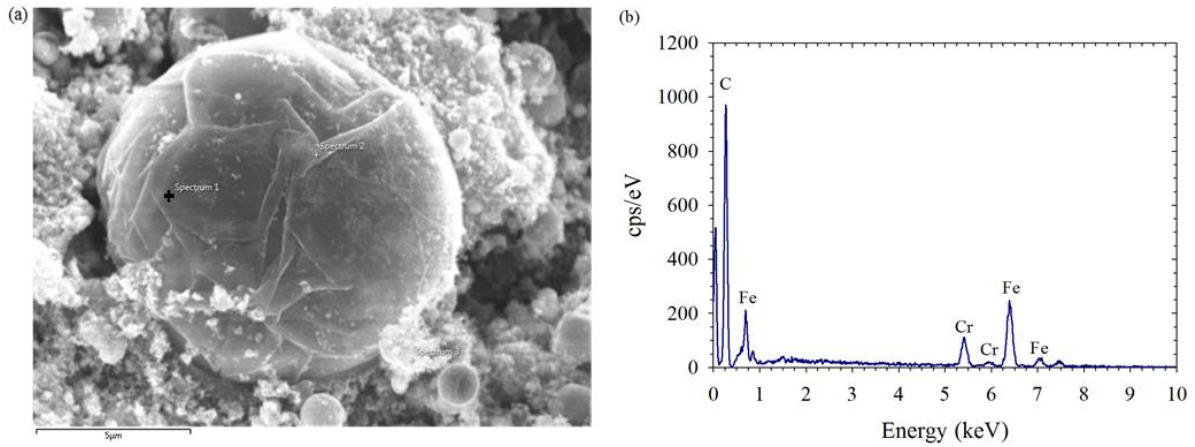


Fig. 5-15 (a) Stainless steel particle from the anode covered by a carbon-containing structure, (b) EDS spectrum of the stainless steel particle. The cross in (a) shows the exact location where the EDS analysis was carried out.

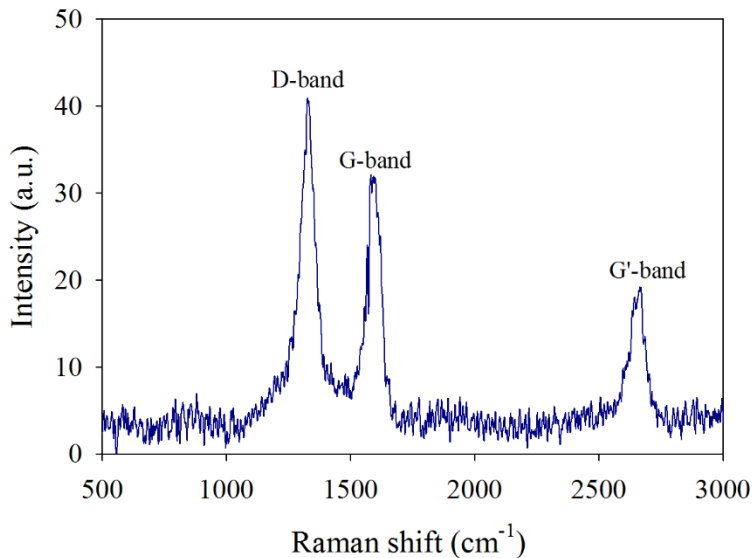


Fig. 5-16 Raman spectrum of one carbon sample produced during the DRM reaction by the RGA discharge after approx. 20 h.

5.5 Conclusions

An atmospheric pressure rotating gliding arc co-driven by a magnetic field has been developed for the plasma-assisted dry reforming of the methane reaction. Operating parameters such as total gas flow rate, peak arc current, and CO₂/CH₄ ratio were varied to determine the most efficient combination for dry reforming of methane. The RGA discharge has shown to be a good plasma source in the generation of cleaner syngas, as only trace concentrations of by-products were found in the effluent gas, whereas the carbon balance was >95% for all the combinations of parameters studied. The optical emission spectrum showed the formation of active species in the plasma zone that are involved in the DRM, such as H_α, C₂, CH, C⁺, and CO₂. The results suggested that plasma acts as a catalyst in the generation of H₂ and CO, where the yield of these products presented a transient behavior in the first minutes to finally stabilized. These results can possibly be used to determine the best time to measure the gas concentrations, especially when sampling offline. Moreover, increasing the peak current mostly increased the conversions of CH₄ and CO₂ and the by-products concentration, such as C₂H₂ and solid carbon. However, increasing the flow rate led to a decrease in CO₂ and CH₄ conversions. Conversely, when the arc current was set at 0.74 A, an increase of the flow rate from 3.7 to 4.7 SLPM seemed to be beneficial for CO₂ and CH₄

conversions for $\text{CO}_2/\text{CH}_4=1.0$ and 1.5 as the increase in the arc length enhanced the conversion. Besides, vibrational excitation could lead to CO_2 activation in a more efficient pathway. This explanation also applied for a peak current of 1.50 A and $\text{CO}_2/\text{CH}_4=2.0$. On the other hand, the H_2/CO_2 ratio was inversely proportional to the CO_2/CH_4 ratio, i.e., the higher the CO_2 concentration in the reactive gas, the lower the H_2 produced. No significant effect of the peak current or flow rate was found in the H_2/CO ratio. Increasing the energy input by preheating the gas inlet did not show a significant effect on the CH_4 and CO_2 conversions as well as the H_2 and CO yields, as the gas temperatures in the plasma zone are much higher (1000 to 3000 K) compared to the preheated gas temperature (200 °C, 473 K). On the other hand, the plasma discharge induced gas heating, resulting in an increased temperature of roughly 200 K. For the larger peak current, i.e., 1.50 A, the best energy efficiency values were obtained at the lowest specific energy input values. Higher values of energy efficiency were obtained at lower flow rates and higher CO_2/CH_4 ratios. As a result of electrode erosion, microparticles of stainless-steel with a structure containing carbon were obtained as a by-product of DRM in the RGA. Raman spectroscopy suggested that the carbon deposits contain amorphous carbon and graphene sheets, which can be potentially useful in industrial/research applications, adding value to the DRM process. Further studies are needed to identify better the nature of the carbon structures. Further work focuses on the addition of a fluidized bed of catalyst for the plasma-catalytic DRM reaction.

Acknowledgments

J. Martin-del-Campo acknowledges the financial support of CONACyT and the Faculty of Engineering through the McGill Engineering Doctoral Award. The authors acknowledge the contributions of Mitchell McNall in the construction of the RGA, Elmira Pajootan for conducting the SEM analysis and Marianna Uceda for conducting the Raman Spectroscopy. The authors thank the technical staff from the Department of Chemical Engineering of McGill University, especially Luciano Cusmich, Gerald Lepkyj, and Frank Caporuscio, for their assistance. This work was financially supported by the Natural Sciences and Engineering Research Council of Canada, the Canadian Foundation for Innovation, and the Gerald Hatch Faculty Fellowship.

5.6 Supplementary material

A. Order of reaction

The relationship between the rate of reaction and the concentration of the reactants is expressed by the power law. The reaction order of the acetylene (C_2H_2) is defined as:

$$r_{C_2H_2} = k \cdot p_{CH_4}^\alpha \quad (a.1)$$

Where $r_{C_2H_2}$ is the rate of reaction in [$mol\ s^{-1}$] of acetylene, k is the constant of reaction, p is the partial pressure of methane in [$mol\ s^{-1}$], and α is the reaction order.

Equation (a.1) can be linearized by taking its natural logarithm (eq (a.2)) to determine the reaction order α and the constant of reaction k :

$$\ln r_{C_2H_2} = \ln k + \alpha \ln p_{CH_4} \quad (a.2)$$

By plotting C_2H_2 concentration obtained vs. CH_4 concentration and making a linear regression, the order of reaction α was obtained for every condition of total inlet flow rate. Fig. 5-17 shows the kinetics plot of the power law for a total inlet flow rate of 3.7 SLPM and peak current of 1.5 A. From Fig 5-17 can be determined that the order of reaction for C_2H_2 formation is 3.7.

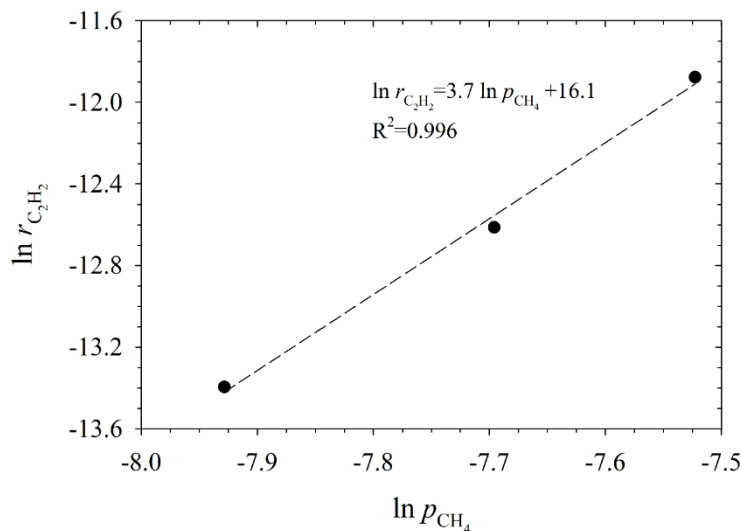


Fig. 5-17 A Kinetics plot of the power law for a total inlet flow rate of 3.7SLPM and peak current of 1.5 A.

Table 5-4 Summary of the order of reaction for C₂H₂ production.

Total inlet flow rate (SLPM)	Order of reaction α
3.7	3.7 ± 0.2
4.7	2.9 ± 0.1
6.7	2.7 ± 0.3

B. ANOVA Statistical Analyses

For Fig. 5-8, ANOVA Statistical analyses were performed using the tool ANOVA: Single-factor from Microsoft Excel. The significance level was set at $\alpha = 0.05$, and the null hypothesis failed to be rejected when $F < F_{crit}$ and p-value $> \alpha$. The acceptance of the null hypothesis stated that there is not enough evidence to state that there is a significant statistical difference between the evaluated means, with 95% confidence. Note that for all the cases, the value of F -critical was 7.71.

Tested with ANOVA	Figure section	Description	Time (min)	F	p-value	Null hypothesis rejected
Hot flow vs cold flow	a	CO ₂ conversion	0	0.19	0.69	no
			5	0.04	0.84	no
			10	6.08	0.07	no
			15	2.58	0.18	no
	b	CH ₄ conversion	0	0.81	0.42	no
			5	0.85	0.41	no
			10	2.84	0.17	no
			15	0.36	0.58	no
	c	CO yield	0	0.29	0.62	no
			5	0.06	0.81	no
			10	2.79	0.17	no
			15	3.29	0.14	no
	d	H ₂ yield	0	0.40	0.56	no
			5	3.01	0.16	no
			10	0.05	0.84	no
			15	0.30	0.61	no

6

Plasma-Driven Catalytic Dry Reforming of Methane

6.1 Preface

This chapter presents the results of studying the influence of different catalyst characteristics such as the plasma-driven catalysis of Dry Reforming of Methane reaction carried out in a rotating gliding arc-fluidized bed reactor. The work was planned, analyzed, and executed by J. Martin-del-Campo. M. Uceda conducted, executed and analyzed the results for X-Ray Photoelectron Spectroscopy, and contributed to the analysis of Scanning Electron Microscopy. Supervision of the research and manuscript reviewing were shared between S. Coulombe and J. Kopyscinski. The citation for this chapter is:

Martin-Del-Campo J., Uceda M., Coulombe S., Kopyscinski J. *Plasma-Catalytic Dry Reforming of Methane over Ni-supported Catalysts in a Rotating Gliding Arc- Spouted Bed Reactor*. Journal of CO₂ Utilization (accepted)

Building on the work developed in Chapter 5, a catalytic material was added to the plasma reactor to create a single-stage plasma-catalytic reactor for the dry reforming of methane. The performance of a rotating gliding arc-spouted bed reactor on the DRM reaction was investigated. The influence of different catalyst characteristics on the performance of DRM was studied. The nickel-based

catalyst characteristics studied were the influence of two catalysts supports, the percentage of metal loading, as well as reduced and non-reduced catalysts.

It was found that the addition of a catalytic material to the plasma discharge highly influences the selectivities of CO and H₂, reducing the production of byproducts such as acetylene and carbon deposition. For the Al₂O₃-supported catalyst, the fresh catalyst showed a better performance regarding yield and selectivity than the pre-reduced catalyst since the plasma discharge might induce a different reaction pathway between the plasma species interacting with the pre-reduced catalyst compared to the fresh catalyst. In the case of the SiO₂-supported catalyst, no statistical difference in the yield of products was found between the pre-reduced catalyst and the fresh one with 15% and 30 % wt. Ni loading. This is attributed to the weak bonding between the Ni and the SiO₂ support. More stable plasma-catalytic performance was achieved with Al₂O₃-supported catalyst rather than with the SiO₂-supported one, which melted and agglomerated in the reactor at lower gas flow rates (>4.5 L_N min⁻¹). The plasma discharge affected the surface chemistry of the catalyst, slightly increasing the binding energy of the Ni in the catalyst. However, no effect of plasma in the crystalline structure of the catalyst was found, confirming that its contact with the plasma discharge did not cause agglomeration.

The reactor has the potential to increase not only selectivity but also reactants conversion and product yield while decreasing the formation of coke and carbon deposition, an undesired byproduct of the DRM reaction.

Plasma-Catalytic Dry Reforming of Methane over Ni-Supported Catalysts in a Rotating Gliding Arc-Spouted Bed Reactor

Jennifer Martin-del-Campo^{1,2}, Marianna Unceda³, Sylvain Coulombe¹, Jan Kopyscinski²

Plasma Processing Laboratory¹, Catalytic Process Engineering², Department of Chemical Engineering, ³Department of Mining and Materials Engineering, McGill University, Montreal, Quebec, Canada

Abstract. A combination of a rotating gliding arc and a spouted catalytic bed was investigated in a plasma-catalytic system for dry reforming of methane. Different nickel-based catalysts, including Ni supported on Al₂O₃ or SiO₂ (fresh and passivated) with 0, 15, and 30 wt % Ni, were investigated. It was found that a more stable operation of the plasma-catalytic system was obtained with the Al₂O₃-supported catalyst rather than with the SiO₂ catalyst. A noticeable increase in selectivity towards CO and H₂ was obtained with a catalytic bed in the plasma zone, reducing acetylene production, a byproduct of DRM, when carried out under plasma conditions. A maximum selectivity of CO of 96.7 % was obtained for the combination of plasma and passivated 30Ni/SiO₂. For H₂, the maximum selectivity achieved was 84.9 % for plasma + fresh 15NiO/SiO₂. Additionally, the formation of soot and coke in the reactor was strongly reduced by the presence of a catalyst. The catalyst characterization showed that the plasma introduces defects on the Ni catalyst, making it more electronegative. However, the crystalline structure of the catalyst was not affected by contact with the plasma, suggesting that the change in the surface chemistry might affect the performance of the catalyst during the DRM reaction.

6.2 Introduction

Carbon dioxide conversion into useful chemicals is an emerging concept for the next generation of greenhouse gas mitigation technology [148]. Dry reforming of methane (DRM) offers an alternative pathway to simultaneously convert CO₂ and CH₄, into valuable synthesis gas (i.e., a mixture of CO and H₂, hereafter referred to as “syngas”). The corresponding reaction is highly endothermic ($\text{CO}_2 + \text{CH}_4 \leftrightarrow 2 \text{CO} + 2 \text{H}_2$, $\Delta H_{298\text{K}} = +247 \text{ kJ mol}^{-1}$) and requires an efficient catalyst as well as process concept. Nonetheless, requirements of high temperatures (>700 °C) for DRM, and the unavoidable carbon deposition of the reaction, limit the industrial application of the thermal catalytic process and result in the deactivation of the catalyst due to poisoning and sintering [37, 42, 149].

Non-thermal plasma (NTP) technologies can assist the valorization of CO₂ and CH₄ since many active and energetic species such as radicals, electrons, ions, neutral atoms, metastable species, and photons are generated at temperatures far below the temperatures required for the thermocatalytic process (i.e., 200 °C vs. 700–1000 °C) [4]. The highly endothermic reaction can occur at low temperatures, and in addition, the activation energy is reduced [149]. However, the conversions of CO₂ and CH₄ in a non-thermal plasma are lower than for the thermo-catalytic process. Moreover, in NTP, due to the low gas temperatures and the long lifetimes of the radicals, the formation of hydrocarbons is favored [36], which decreases the syngas selectivity.

Plasma-catalytic technologies present a potential alternative to overcome the drawbacks of both technologies while benefiting from a possible synergistic effect of the plasma and the catalyst [37, 149]. Plasma-catalysis consists of taking a material with catalytic properties and combining it with a gaseous electrical (plasma) discharge [14]. On the one hand, the plasma discharge possesses reactivity due to the ionized and excited states of the atoms, molecules, radicals, and energetic electrons and photons. Simultaneously, the catalyst accelerates the chemical reaction by providing an alternative reaction pathway with a lower energy barrier [14]. Plasma-catalysis can potentially enhance gas conversion, improve reaction selectivity, increase energy efficiency, improve catalyst stability, and reduce catalyst poisoning and coke formation [14, 37, 60].

Plasma-catalysis has the potential to enhance highly endothermic reactions such as DRM. This technology may also decrease the activation barrier of CO₂ and CH₄, improve the reaction rate [94], and enhance hydrogen yield [42]. Among the non-thermal plasma-catalytic technologies, dielectric

barrier discharges (DBDs) have been extensively studied [37, 148, 150–154], followed by gliding arcs (GA) [77–81, 155, 156]. In particular, gliding arcs produce transitional or warm plasmas, with characteristics in between the non-thermal (cold) and thermal (hotter) plasmas, which allows creating excited and reactive species in the gas at low temperatures (close to room temperature) while maintaining a high electron density (10^{23} m^{-3} in GA [42]). Therefore, these reactive gases can interact with the catalyst at temperatures where conventional thermal catalysis is non-active [14].

Gliding arc fluidized bed is a special configuration of a gliding arc for gas conversion applications, and it combines the advantages of both systems. On the one hand, the warm conditions of the gliding arc provide high reaction rates and selectivity. On the other hand, the fluidized bed system provides excellent mixing of particles, high heat and mass transfer rates, minimizes carbon deposition and offers the possibility of continuous process coupled with high throughput [101, 151, 157, 158]. The spouted bed system investigated in this article is one type of fluidized bed in which coarse particles show circular movement, while at the same time, the gas injected keeps the catalyst particles moving in the inter-electrode space [80, 158, 159]. Considering the potential synergetic effects of a plasma-catalysis system and the benefits associated with a gliding arc-fluidized bed configuration, it is expected that the active species generated in the plasma zone can immediately make contact with the catalyst as the catalytic bed is located between the electrodes in the plasma reactor [80]. Several authors have investigated the gliding arc-spouted bed system for CH_4 reforming [80, 155, 156]. In all cases, the authors reported an increase in product selectivity. Moreover, Mlotek *et al.* [156] reported a reduction of carbon formation. However, Lee *et al.* [80] reported a decrease of CH_4 conversion due to the distortion of the discharge by the catalyst when using plasma-catalysis.

In this study, DRM is investigated in a rotating gliding arc-spouted bed hybrid system using Ni-based catalysts. The influence of two catalyst supports, i.e., alumina and silica, nickel loading, reduced and non-reduced catalysts on CH_4 and CO_2 conversions, and H_2 and CO selectivities are investigated. The product gas composition was determined using a calibrated mass spectrometer. The fresh and spent catalysts were analyzed using Scanning Electron Microscopy (SEM), nitrogen physisorption, hydrogen chemisorption, X-Ray Diffraction (XRD), X-Ray Photoelectron Spectroscopy (XPS) and temperature-programmed oxidation (TPO) to understand better the effect of the plasma discharge on the catalyst properties.

6.3 Experimental

6.3.1 Catalyst synthesis

Two different nickel-based catalysts were synthesized, NiO/Al₂O₃ and NiO/SiO₂, with different metal loadings (0, 15, and 30 wt%). Catalyst samples supported on alumina (Al₂O₃, Alfa-Aesar) presented a particle size of 90 – 125 μm, whereas silica (SiO₂, ≥ 99 %, Sigma Aldrich) based catalysts had a particle size of 150 – 250 μm to ensure proper fluidization for both catalysts since Al₂O₃ catalyst is heavier than the SiO₂ one (i.e., bulk density ~0.68 g cm⁻³ vs. ~0.47 g cm⁻³, respectively). Nickel was added via incipient wetness impregnation using a solution of nickel (II) nitrate hexahydrate (Ni (NO₃)₂ 6 H₂O, ≥ 98.5 %, Sigma Aldrich). Then, the catalysts were dried at 80 °C for 8 h and calcined at 500 °C with a heating rate of 1 °C min⁻¹ for 5 h

6.3.2 Catalyst characterization

Different characterization techniques were used to study the catalyst morphology, crystallinity and composition before and after use in the plasma-catalytic reactor. Inductively coupled plasma optical emission spectrometry (ICP-OES) was used to determine the actual nickel content in the catalyst (Table 6-6, supplementary material A.1). N₂ adsorption/desorption measurements (– 196 °C, pressure range 0.01 – 0.99 *p/p*₀) were conducted using a Micromeritics Gemini VII 2390 t surface analyzer to determine the total surface area, pore size distribution and pore volume. Prior to data collection, the samples were outgassed at 250 °C overnight with He in a Micromeritics FlowPrep 60 degasser. The pore size distribution was determined via the Barret-Joyner-Halenda (BJH) model using the desorption data, whereas the pore volume was determined based on the amount of adsorbed N₂ at *p/p*₀ = 0.97. The total Brunauer-Emmett-Teller (BET) surface area was calculated based on BET measurements in the pressure range 0.05 – 0.3 *p/p*₀.

Volumetric hydrogen uptake (chemisorption) measurements were conducted with an Autosorb iQ (Quantochrome) gas sorption instrument. Approximately 100 mg of the fresh and spent catalyst (recovered after contact with plasma) were placed in a U-shaped quartz tube, where the sample was preheated in He at 120 °C with a heating rate of 20 °C min⁻¹ and maintained at this temperature for 0.5 h. The catalyst sample was then reduced with H₂ at the previously determined reduction temperature from H₂-TPR (see supplementary material B.1.1). Finally, the gas was evacuated, and the sample was cooled to 40 °C. The adsorption measurements were taken at a pressure ranging from 0.05 to 0.75 bar_{abs}. The specific surface area, metal dispersion, and average crystallite size

were calculated based on the amount of H₂ adsorbed, assuming H/Ni = 1 and a hemispherical cluster with a nickel density of 8.9 g cm⁻³.

Temperature-programmed oxidation (TPO) analyses were performed using a thermogravimetric analyzer (TG 209 F1 Libra, Netzsch) connected to a calibrated mass spectrometer (Hidden Analytical, HPR-20). The catalyst samples (25–35 mg) were first dried with Ar at 110 °C at a heating rate of 5 °C min⁻¹ and held at this temperature for 2 h. Subsequently, the catalysts were heated up to 950 °C at 2.5 °C min⁻¹ with 66 vol% air and held at this temperature for 40 min to combust possible carbon deposition, while the evolved gas CO₂ was monitored.

A more extensive characterization was performed on two catalyst samples (30NiO/Al₂O₃ and 30NiO/SiO₂) before and after use in the plasma-catalytic reactor using XRD, XPS and SEM-EDS. X-ray powder diffraction was used to identify the crystallinity of the samples. Analyses were conducted on a Bruker D8 Discovery X-Ray diffractometer with a two-dimensional VANTEC - 500 detector and CuK α ($\lambda = 1.54056 \text{ \AA}$) radiation source. The measurements were carried out at a tube voltage of 40 kV and a tube current of 20 mA, and a scan rate of 5 °C min⁻¹. In addition, X-Ray Photoelectron Spectroscopy was performed using a Thermo Scientific K-alpha XPS instrument to obtain surveys and high-resolution spectra at the edges of C 1s, Al 2p, O 1s, Ni 2p, and Si 2p. The powder samples were degassed in a vacuum oven at 60 °C for 15 h and then mounted on copper tape. A flood gun was used to minimize charging, and the attained survey and high-resolution spectra were charge-corrected with respect to the C 1s C–C peak at 284.7 eV. Scanning Electron Microscopy (Hitachi SU8000) was performed with an accelerating voltage of 10–15 kV and working distance between 15 and 16 mm. In addition, Energy Dispersive X-Ray Spectroscopy (EDS) experiments were performed on the catalyst samples for elemental analysis.

6.3.3 Thermo-catalytic activity

Thermo-catalytic DRM experiments were conducted in a fixed bed reactor. The setup included mass flow controllers, gas mixing station, tube furnace, condenser and gas analyzer (mass spectrometer). The flow rates of reactant gases, Ar (99.999 %, Megs), CH₄ (99.999 %, Praxair) and CO₂ (99.99 %, Praxair), were controlled using calibrated Vögtlin red-y smart controller GSC (Switzerland). The reactor consisted of an inner quartz tube (I.D. 7 mm) with a 15–40 μ m frit at the bottom. The reactor was placed into a 0.5" stainless steel 316 tube with a counter-current flow configuration. The reaction temperature was controlled by a K-type thermocouple inserted into the

catalytic bed. The exit gas line was electrically heated between 110 and 120 °C to avoid water condensation. A split stream of the exit was gas analyzed using a calibrated mass spectrometer (Pfeiffer Ominstar GSD 301). The experiments were performed at 700 °C and 1 bar_{abs} with a gas hourly space velocity (GHSV) of 148 L_N g_{cat}⁻¹ h⁻¹ (Note: N refers to standard conditions, i.e., 273 K and 1 atm). Approximately 40 mg of catalyst diluted in 60 mg of support were loaded in the quartz tube and then purged with Ar (100 mL_N min⁻¹) for 1 h to remove air. Then, the temperature was increased to 200 °C at a heating rate of 4.5 °C min⁻¹ and held for 2 h to remove moisture. Afterwards, the temperature was increased to each sample's reduction temperature (previously determined, see supplementary material B.1.1) under 20 vol% H₂ (99.999 % Praxair) in Ar at the same heating rate and held for 2 h. Finally, the temperature was increased to 700 °C and held for 3 h, while CO₂ and CH₄ were introduced at a concentration of 18 vol% and 12 vol% (i.e., CO₂/CH₄ = 1.5), respectively, with balance Ar. After the reaction, all the catalysts were passivated, removed and stored for further analysis. The reported bars are an average of the results after steady-state was reached in the reactor for approx. 2.5 h of experiment and the error bars represent the standard deviation over the time measured.

6.3.4 Plasma-catalytic activity

The description and schematic of the Rotating Gliding Arc (RGA) reactor have been presented in detail in [160]. Briefly, the RGA reactor consists of a cone electrode (cathode) mounted coaxially inside a hollow cylinder that acts as a grounded anode. The gas is injected tangentially in the reactor by two sets of gas injectors, forming a counter-clockwise vortex flow (as seen from the upper part of the reactor). The cathode is powered by a homemade dual-stage DC power supply. To fill the gap between the base of the reactor and the gas inlets, an additional ceramic piece (glass-mica) was added to avoid the catalyst falling to the base and not fluidize

To create a spouted bed in the RGA reactor, the catalyst powder (1.5 g) was added through the upper part of the reactor while argon (Ar) plasma was flowing in the reactor at a gas velocity of 21.6 cm s⁻¹ for Al₂O₃ supported catalyst and 26.3 cm s⁻¹ for SiO₂ supported catalyst. The latest represents 8.7 and 6.8 times the minimum fluidization velocity, respectively (see supplementary material A.2), thus ensuring proper catalyst fluidization. Afterwards, the reactor was closed, while electrical signals were monitored at all times. The RGA voltage and circuit current signals were monitored/measured online using a high-voltage probe (B&K Precision PR55) and a passive voltage probe (Tektronix P2200) across a 1 Ω shunt resistor, respectively, and displayed with a

benchtop oscilloscope (Tektronix MSO 2012, 100 MHz, 1 GS/s) but recorded with a PC oscilloscope (PicoScope 2408B).

A mix of Ar (99.999 %, Praxair), CO₂ (99.9 %, Praxair) and CH₄ (99.99 %, Megs) was injected through the reactor. The argon concentration was fixed between 70–75 vol% to ensure stable plasma operation. The volumetric CO₂/CH₄ ratio was fixed at 1.5 to reduce carbon deposition, based on our previous study [160], with total flow rates of 3.7 L_N min⁻¹ (GHSV = 148 L_N g_{cat}⁻¹ h⁻¹) and 4.5 L_N min⁻¹ (GHSV = 180 L_N g_{cat}⁻¹ h⁻¹) for Al₂O₃ and SiO₂ based catalyst, respectively. The exhaust gas was analyzed online by a calibrated mass spectrometer (Pfeiffer Omnistar GSD 301). The maximum RGA current delivered by the current driver was set by its internal resistance (300 Ω), giving rise to a peak arc current of 2.7 A. Each experiment was conducted three times, and the error bars reported reflect the standard deviation. No external heating was provided to the plasma-catalytic reactor.

The performance of the reforming reaction was calculated based on hydrogen and carbon monoxide selectivities (Eqs. 6.1 and 6.2), as well as the conversions of methane and carbon dioxide (Eqs. 6.3 and 6.4):

$$S_{H_2}(\%) = \frac{\dot{n}_{H_2out}}{2 (\dot{n}_{CH_4in} - \dot{n}_{CH_4out})} \times 100 \quad (6.1)$$

$$S_{CO}(\%) = \frac{\dot{n}_{COout}}{(\dot{n}_{CO_2in} - \dot{n}_{CO_2out}) + (\dot{n}_{CH_4in} - \dot{n}_{CH_4out})} \times 100 \quad (6.2)$$

$$X_{CH_4}(\%) = \frac{\dot{n}_{CH_4in} - \dot{n}_{CH_4out}}{\dot{n}_{CH_4in}} \times 100 \quad (6.3)$$

$$X_{CO_2}(\%) = \frac{\dot{n}_{CO_2in} - \dot{n}_{CO_2out}}{\dot{n}_{CO_2in}} \times 100 \quad (6.4)$$

The H₂/CO molar ratio and the carbon balances were defined as:

$$\frac{H_2}{CO} = \frac{\dot{n}_{H_2out}}{\dot{n}_{COout}} \quad (6.5)$$

$$B_C(\%) = \frac{\dot{n}_{CO_2out} + \dot{n}_{CH_4out} + \dot{n}_{COout}}{\dot{n}_{CO_2in} + \dot{n}_{CH_4in}} \times 100 \quad (6.6)$$

where, \dot{n}_i is the molar flow rate in (mol min^{-1}). The quantity of other hydrocarbons (C_2H_2 , C_2H_4) was neglected in the carbon balance since we found in our previous study [160] that it was ($< 0.5 \text{ mol}\%$). Hence, the MS was not calibrated for these species; however, the signal in $[\text{A}]/[\text{A}]$ was monitored during the experiments and can be found in the supplementary material B.2.4.

The energy cost of the syngas (EC) is defined as the amount of energy input per mol of syngas produced (MJ mol^{-1}), see eq. 6.7:

$$EC = \frac{P_{avg}}{\dot{n}_{\text{H}_2\text{out}} + \dot{n}_{\text{COout}}} \quad (6.7)$$

where P_{avg} is the time-averaged power (MJ s^{-1}) calculated using the same method as in [160] and \dot{n}_i is the molar flow rate of H_2 and CO (mol s^{-1}).

The energy efficiency (η) of the process was defined as:

$$\eta(\%) = \frac{\dot{n}_{\text{H}_2\text{out}} LHV_{\text{H}_2} + \dot{n}_{\text{COout}} LHV_{\text{CO}}}{P_{avg} + \dot{n}_{\text{CH}_4\text{in}} LHV_{\text{CH}_4}} \times 100 \quad (6.8)$$

where LHV_i is the low heating value of the gas i (CO , H_2 , CH_4) in (J mol^{-1})

The turnover frequency (TOF) was determined via H_2 chemisorption measurements, yielding the active surface area and eq. 6.9.

$$TOF (\text{s}^{-1}) = \frac{\text{reactant flow rate (mol s}^{-1}) \cdot \text{conversion at steady - state}}{\text{active surface area (mol g}^{-1}) \cdot \text{mass of catalyst (g)}} \quad (6.9)$$

6.4 Results and discussion

6.4.1 Thermo-catalytic activity

Fig. 6-1 shows the conversions of CO_2 and CH_4 as well as selectivities of H_2 and CO when the reaction was carried out over Al_2O_3 and SiO_2 based catalysts with three different Ni loadings (0, 15 and 30 %). Empty tube (i.e., homogeneous reaction) and support only (no nickel) experiments resulted in a CH_4 conversion of less than 0.5 %, while the CO_2 conversion was between 8% and 10 %. Thus, nickel is needed to facilitate the C—H bond and accelerate the C—O bond dissociation.

With increasing Ni content, the CO₂ and CH₄ conversions, as well as the CO and H₂ selectivities increased, approaching and reaching equilibrium, respectively. The CH₄ conversions' values were around the same for the 15Ni/Al₂O₃ and 15Ni/SiO₂ with 74 ± 1%. The same was observed for the 30Ni/Al₂O₃ and 30Ni/SiO₂ catalysts with slightly higher values of 80 ± 1%, yet below the chemical equilibrium. For CO₂, however, the behavior was different, and the conversions were considerably smaller. Over 15Ni/Al₂O₃, the conversion of CO₂ was 64 % and slightly higher compared to the 62 % over 30Ni/Al₂O₃. This can be explained by a bi-functional mechanism [54, 55], in which the CH₄ is activated on the metal only, whereas the CO₂ (which is a Lewis acid) can also adsorb and be activated on the basic sites provided by the Al₂O₃ [36, 51, 154]. Since the 15Ni/Al₂O₃ catalyst presents a higher surface area compared to the 30Ni/Al₂O₃ catalyst (212 and 164 m² g⁻¹, respectively), more CO₂ is converted. Moreover, the nickel supported on Al₂O₃ exhibited a higher H₂/CO ratio and H₂O signal due to the increased reverse water gas shift activity (CO₂ + H₂ ↔ CO + H₂O) than for the SiO₂ catalyst (see supplementary material B.1.3). For the inert SiO₂ catalyst, however, no additional CO₂ adsorption sites besides the nickel are available.

Interestingly, the 15 wt% Ni catalyst was more active than the 30 wt% Ni catalysts (i.e., higher turnover frequency TOF) based on the number of exposed Ni sites, as summarized in Table 6-1. This indicates that the 15 wt% Ni catalysts had smaller nickel clusters and higher nickel dispersion than the 30 wt% Ni, which was confirmed by H₂ uptake measurements (see Table 6-4). Thus, by comparing the absolute number of Ni active sites, it is shown that half of the amount of Ni (15 % Ni instead of 30 % Ni) is needed to obtain almost the same conversion of CO₂ and CH₄.

Table 6-1 Turnover frequency for Ni/Al₂O₃ and Ni/SiO₂ catalysts.

Catalyst	TOF (s ⁻¹)	
	CO ₂	CH ₄
30Ni/Al ₂ O ₃	1.3	1.1
15Ni/Al ₂ O ₃	1.8	1.5
30Ni/SiO ₂	1.2	1.0
15Ni/SiO ₂	1.6	1.3

The TOF_{CO_2}/TOF_{CH_4} ratio for all the catalysts is 1.2, which shows that the conversion of CO₂ is faster than the conversion of CH₄ for the Ni-supported catalyst. This is in agreement with previously

reported studies by Ferreira-Aparicio *et al.* [45], which assumed the dissociative adsorption of CH₄ as the rate determining step [48, 153, 161].

The TOF for CO₂ was higher than for CH₄, despite the smaller conversion of CO₂ compared to CH₄. This can be explained by the fact that the feed consists of 1.5 times more CO₂ than CH₄ as stated earlier.

Nonetheless, the stability of the catalyst over the period measured (160 min) decreased over time for SiO₂-based catalyst, whereas the Al₂O₃-based catalyst remained stable (see supplementary material B.1.2). This difference in catalyst stability is attributed to the weak interaction between Ni and SiO₂ that may lead to quick deactivation due to metal agglomeration [45, 48, 52].

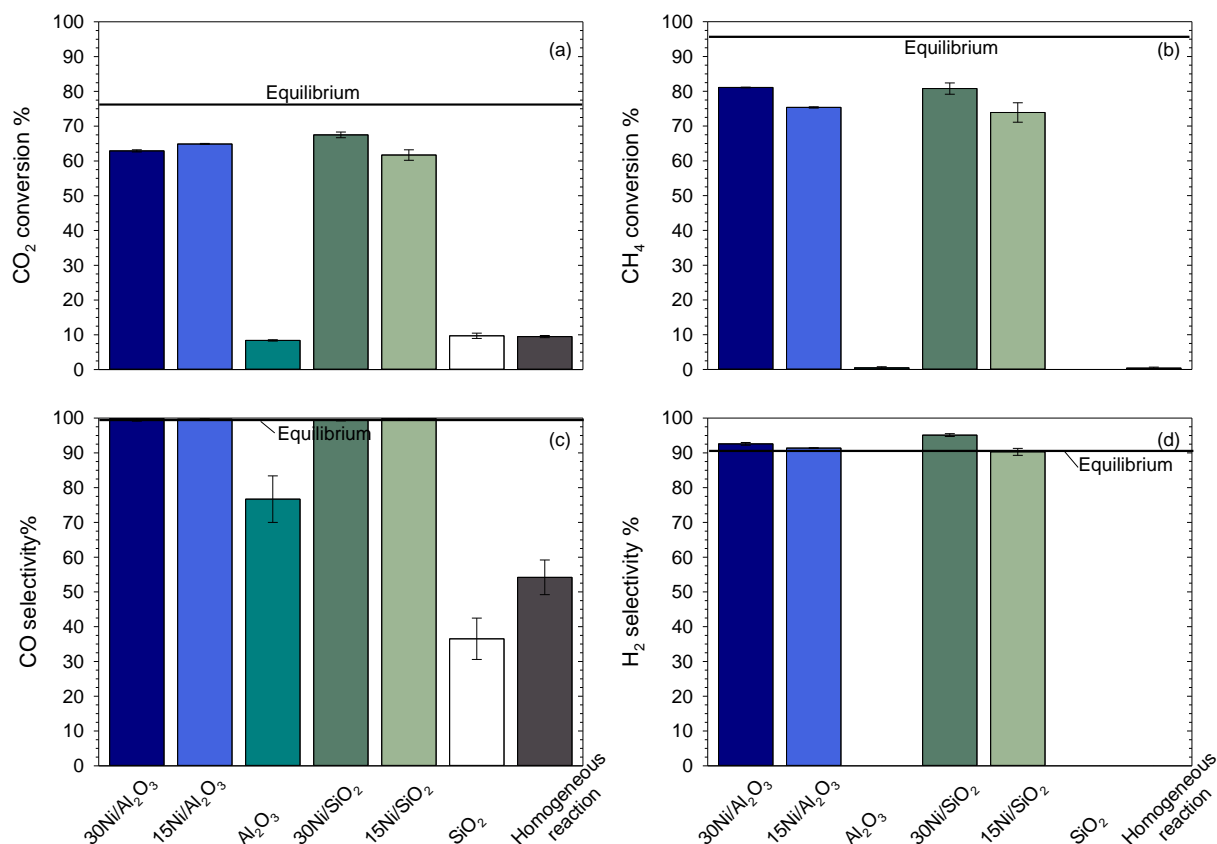


Fig. 6-1 Average conversions of (a) CO₂ and (b) CH₄. Average selectivities of (c) CO and (d) H₂ under catalytic conditions at 700 °C and 1 bar_{abs} with different Ni-based catalysts at GHSV = 148 L_N g_{cat}⁻¹ h⁻¹.

6.4.2 Plasma-catalytic activity

Typical voltage, current, and calculated instantaneous power signals are reported in Fig. 6-2 for the plasma-catalytic DRM at CO₂/CH₄ = 1.5, total gas flow rate of 3.7 L_N min⁻¹, and NiO/Al₂O₃

catalyst. The electric signals for the NiO/SiO₂ catalyst can be found in the supplementary material B.2.1. The voltage signature is comprised of three stages reproduced in a nearly periodic way: a capacitor-charging phase which builds up the voltage across the interelectrode gap (an exponential increase of the negative voltage signal), followed by a gaseous breakdown event (sharp voltage drop) and finally, the arcing phase (low voltage signal). Current flows through the RGA during the arcing phase, with the associated resistive power dissipation.

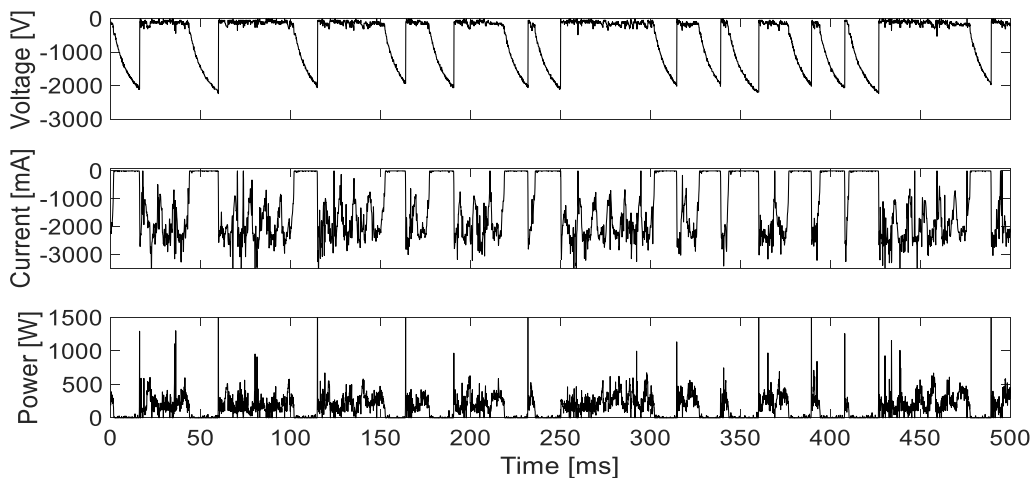


Fig. 6-2 Characteristic RGA discharge voltage, current and instantaneous power signals for plasma-catalytic DRM reaction at $\text{CO}_2/\text{CH}_4 = 1.5$, with a total flow rate of $3.7 \text{ L}_N \text{ min}^{-1}$ over NiO/Al₂O₃ catalyst.

Figs. 6-3 and 6-4 illustrate the results for DRM in the RGA-spouted bed reactor for plasma and plasma-catalysis experiments. Based on our previous studies [160] and new infrared camera measurements, the gas temperature in the catalytic powder bed was about 220 °C with a good volumetric distribution (Fig. 6-16, supplementary material B.2.1). At these conditions, according to thermodynamic equilibrium calculations, only a conversion of 0.2 % and 0.1 % is expected for CO₂ and CH₄, respectively. It is considered that the movement of the catalyst particles reduces the local overheating of the catalyst provided by the direct contact of the gliding arc discharge [80]. Two catalysts with 30 wt% Ni content supported on Al₂O₃ and SiO₂ (denoted as 30Ni/Al₂O₃(P) and 30Ni/SiO₂(P), respectively) were previously reduced in the fixed bed reactor under 20 vol% H₂ for 3 h and passivated to compare their performance to the fresh NiO catalyst since only superficial O was present on them (ideally easier to activate). Moreover, a 15 wt% Ni content fresh catalyst was previously treated under a 20 vol% CH₄ and 80 vol% Ar under plasma conditions for 50–75 min to

potentially reduce the catalyst (denoted as 15NiO/Al₂O_{3(CH4)} and 15NiO/SiO_{2(CH4)}, respectively) as reported by [81, 162].

An ANOVA statistical analysis was performed on the results to determine whether the experimental outcomes of the Al₂O₃ and SiO₂ catalyst groups were statistically different among their own group (see supplementary material B.2.2). In all cases, the ANOVA tests indicated statistical differences in the groups in general. Hence, a *t*-test two-sample assuming unequal variances was performed on all sample pairs individually (15 pairs for catalyst group) to determine if the samples were statistically different among them or not.

The conversions of CO₂ and CH₄ over the Al₂O₃ catalysts were smaller for the plasma-catalytic experiments than for the plasma-only experiment (Fig. 6-3 a and b). In detail, in the absence of any catalysts, conversion values of 11.5 ± 1 % for CO₂ and 13.8 ± 1 % for CH₄ were observed. For the 15NiO/Al₂O₃ and Al₂O₃ experiments, average CO₂ conversions of 10.9 % and CH₄ conversions of 11.8 % were determined. An increase in the nickel content to 30 wt% did not increase the conversion. The opposite was found for the CO₂ conversion (8%), while the CH₄ did not change (11.8 %). This negative effect of the Ni loading on the CO₂ conversion during plasma-catalytic dry reforming in a gliding arc-fixed bed reactor system has also been reported by Allah and Whitehead [81].

Interestingly, both reduced catalysts (30Ni/Al₂O_{3(P)} and 15NiO/Al₂O_{3(CH4)}) had a much smaller CO₂ and CH₄ conversion than the Ni-oxide catalysts. This might be due to a different reaction pathway between the plasma species interacting with the pre-reduced catalyst (passivated) compared to the fresh catalyst. For instance, the passivation layer in the catalyst might inhibit certain reactions occurring at the surface.

In terms of the CO and H₂ selectivities, adding a catalyst seems to be beneficial. For example, for the 15NiO/Al₂O_{3(CH4)} catalyst; a 11.2 % increase for CO (from 80.3 % to 91.5 %) and 9% for H₂ (from 71.5 % to 80.5 %) was observed (Fig. 6-3c and d). Without methane pretreatment, the 15NiO/Al₂O₃ catalyst had only slightly lower selectivity values (i.e., 88 % for CO and 76 % for H₂), but as stated earlier, it exhibited a higher reactant conversion. Increasing the nickel content to 30 wt% resulted in smaller product selectivities.

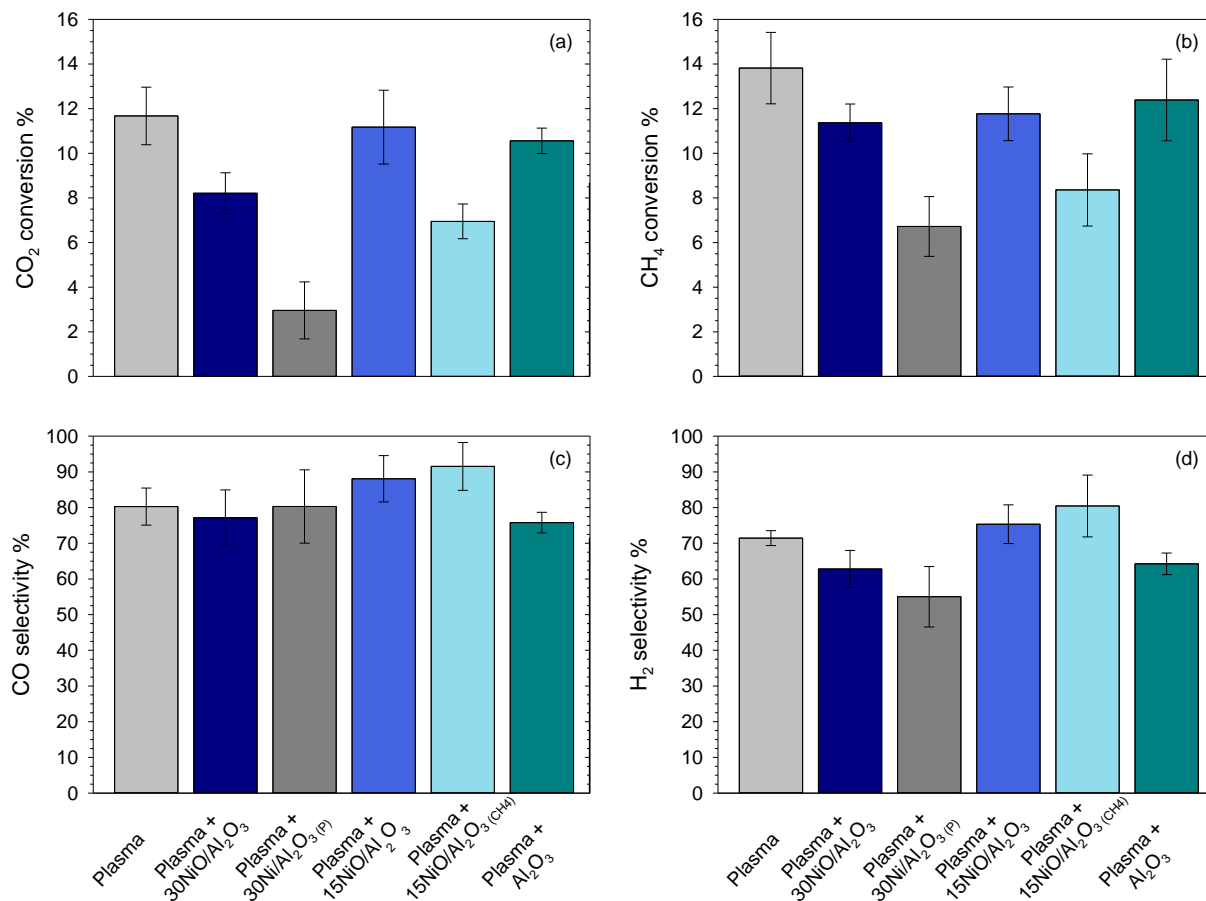


Fig. 6-3 Average conversions of (a) CO₂ and (b) CH₄. Average selectivities of (c) CO and (d) H₂ under plasma and plasma-catalytic conditions for different Ni/Al₂O₃ catalysts at GHSV = 148 L_N g_{cat}⁻¹ h⁻¹. Note: P = reduced – passivated, CH₄ = plasma pretreated with methane.

In the case of the SiO₂-based catalysts, the total flow rate was increased to 4.5 L_N min⁻¹ (i.e. 75 % Ar and keeping CO₂/CH₄ = 1.5) since with a lower flow rate, the Ni/SiO₂ catalyst partly melted and agglomerated inside of the reactor, making the RGA unstable. Inside the reactor, the gas temperature was measured to be around 220 °C, whereas the temperature inside the arc was much higher (between 700 and 2000 °C). Therefore, the spouted bed configuration may have led to repeated exposure of the SiO₂ particles to the arc's high-temperature region resulting in their partial melting. This was not observed for the Al₂O₃ samples, as the melting point is higher than for SiO₂ (i.e., ~2070 °C vs. ~1700 °C).

An increase in the arc length due to the increase in the flow rate also increased the maximum conversion and yield for reactants and products compared to the lower flow rate [132, 160]. The

conversions of CO₂ and CH₄ were larger in the absence of a catalyst than the values determined with SiO₂-based catalysts (Fig. 6-4 a and b). The CH₄ conversions for the 30NiO/SiO₂ and plasma only experiment were statistically similar (Table 6-10, supplementary material B.2.2).

Despite the lower conversion, the 30 wt% NiO/SiO₂ and 30 wt% Ni/SiO_{2(P)} had a higher CO selectivity than the plasma only run (97 % vs. 92 % vs. 88 %). However, for these catalysts, the observed H₂ selectivity was smaller than for the plasma DRM experiments without any catalysts. The Ni content and the pre-reduced catalyst did not seem to affect the reactants conversion and products selectivity of the plasma-catalytic DRM reaction over the SiO₂-supported catalyst, which can be attributed to the weak interaction between Ni and the support.

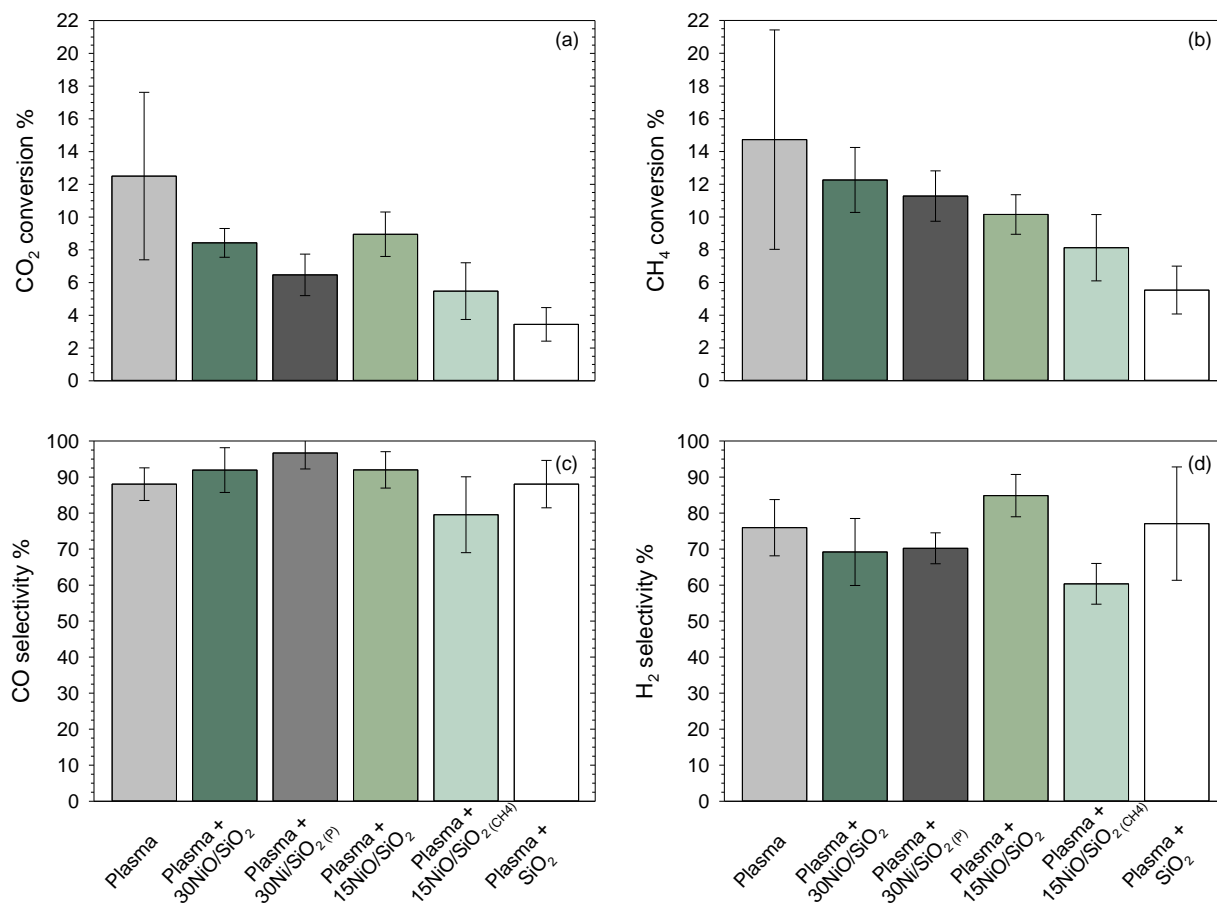


Fig. 6-4 Average conversions of (a) CO₂ and (b) CH₄. Average selectivities of (c) CO and (d) H₂ under plasma and plasma-catalytic conditions for different Ni/SiO₂ catalysts at GHSV = 180 L_N g_{cat}⁻¹ h⁻¹. Note:

P = reduced – passivated, CH₄ = plasma pretreated with methane.

Fig. 6-5 depicts the H_2/CO ratio for the different Ni-based catalysts under thermal and plasma-catalytic conditions. The blank support shows a very low (<0.5) H_2/CO ratio under typical thermal catalysis since almost no H_2 is produced. However, under plasma-catalytic conditions, this ratio increased 3.7 times in the case of blank Al_2O_3 and 1.8 times for blank SiO_2 since the plasma breaks down the CH_4 molecules, producing H_2 at low-temperature conditions. The highest H_2/CO ratio achieved under plasma-catalytic conditions was 0.82 for plasma ($3.7 L_N \text{ min}^{-1}$), $30NiO/Al_2O_3$ and Al_2O_3 , for which no statistical difference was found between these samples (see supplementary material B.2.2.2). For the SiO_2 based experiments, the highest average H_2/CO ratio was 0.80 for the plasma ($4.5 L_N \text{ min}^{-1}$), $30NiO/SiO_2$, SiO_2 and $15NiO/SiO_2(CH_4)$, for which no statistical difference was found among the samples

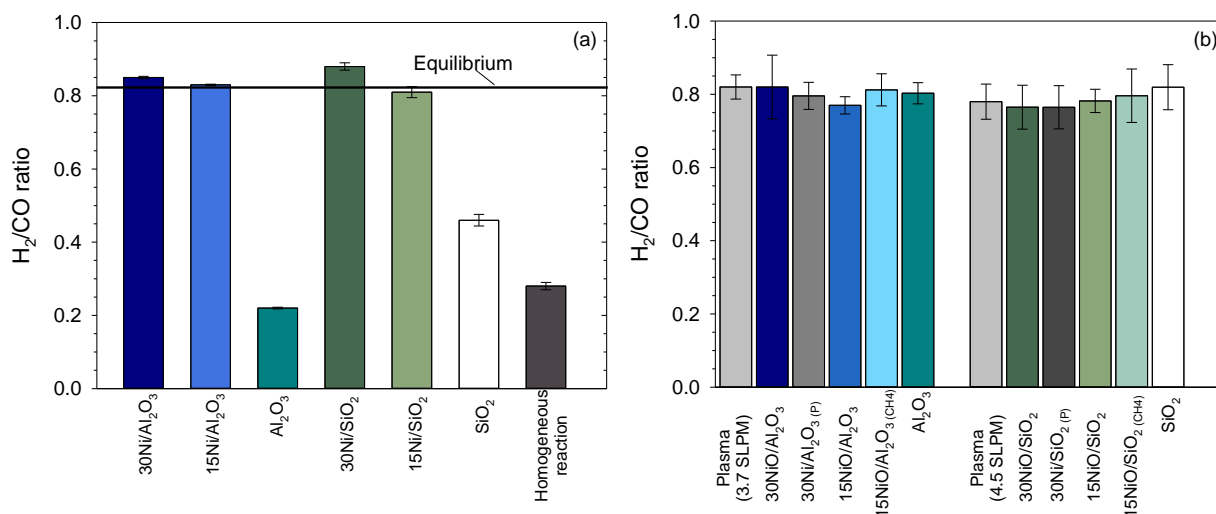


Fig. 6-5 H_2/CO ratio for different catalysts under (a) thermal catalysis and (b) plasma-catalytic conditions for Al_2O_3 and SiO_2 based Ni catalysts.

Moreover, the presence of a catalyst in the plasma zone decreased the production of C_2H_2 , a byproduct of the DRM reaction when carried out in plasma (see supplementary material B.2.4), thus increasing the H_2 selectivity. Besides, the amount of carbon deposited on the electrode after the experiment (Fig. 6-6) decreased, increasing the carbon balance (Table 6-2). The latest is discussed further in the next section.



Fig. 6-6 Stainless steel cathode after DRM reaction under (a) plasma-only and (b) plasma-catalytic conditions.

Under plasma conditions, the CO_2 and CH_4 conversions achieved were 11.7 % and 13.8 % for $3.7 \text{ L}_N \text{ min}^{-1}$ and 12.5 % and 14.7 % for $4.5 \text{ L}_N \text{ min}^{-1}$. This is equivalent to equilibrium conversions between 425–440 °C under thermo-catalytic conditions based on thermodynamic calculations. In conventional catalytic DRM, the dissociative adsorption of CH_4 is the rate determining step [48, 150, 153]. Since the conversions of CO_2 and CH_4 were higher in the absence of catalyst, these results suggest that the rate-determining step for a plasma-catalytic reaction is different, as concluded previously by Gallon [150]. Gallon stated that the catalytic surface reactions and the electron-impact plasma volume processes might be involved in the reaction mechanism. Additionally, the gas temperature inside of the plasma-catalytic reactor was about 220 °C (based on our previous studies [160]), which was too low to completely activate the DRM reaction by the catalyst (normally $>700 \text{ °C}$), making the plasma the main source for reforming of CH_4 [80]. Furthermore, the decline of CO_2 and CH_4 conversions when using a RGA-spouted catalytic bed was caused by a distortion of the plasma discharge by the catalyst, as reported by [80]. However, the free volume inside of the plasma-catalytic reactor is also changed. For the empty tube experiment, the ionized species and radicals interact in the whole accessible volume in the plasma zone (6.75 cm^3), whereas when the catalyst is inside, less gas volume is accessible to be ionized. Moreover, adding solids in the arcing zone reduces the volume accessible for the plasma and alters the arc itself. If we assume a free voidage of 50–70 % for the catalyst, this means that the solids actually occupy between 50% to 30 % of the volume. The latest is equivalent to reduce the plasma volume zone between $3.38\text{--}4.73 \text{ cm}^3$. If the total volume of the plasma zone is reduced, the residence time of the reactants in the plasma zone is also reduced, which would be equivalent to

increase the total flow rate in an empty tube experiment between 5.3–9.0 L_N min⁻¹. Thus, if we normalize the results based on void volume, adding catalyst might still be beneficial.

The energy cost (EC) of the DRM reaction using gliding arc discharge systems is 5–210 times lower than for other plasma systems using dielectric barrier discharges (DBD), as summarized in Table 6-2. This means that more energy needs to be supplied to produce the same amount of syngas as in the gliding arc reactors. All reported data in Table 6-2 are related to packed bed catalyst configurations, except the values presented in this work, which refer to spouted bed reactor. RGA – spouted bed a promising technology to increase syngas selectivity while decreasing carbon deposition.

Table 6-2 Comparison of performance parameters for different plasma-catalytic sources for DRM.

Plasma source	GHSV (L h ⁻¹ g _{cat} ⁻¹)	CO ₂ /CH ₄	Power (W)	Catalyst	Conversion (%)		Selectivity (%)		EC (MJ mol ⁻¹)	η (%)	Ref.
					CH ₄	CO ₂	H ₂	CO			
DBD	6	1.0	30	10wt% Ni/Al ₂ O ₃	26.1	16.3	34.6	48.8	4.2	10.4	[154]
DBD	3	1.0	50	10wt% Ni/Al ₂ O ₃	56.4	30.2	31.0	52.4	n/a	16.4	[62]
DBD*	0.9	1.0	38.4	>10wt% Ni/Al ₂ O ₃	44.0	26.0	~95	~95	2.3	n/a	[90]
DBD	12	1.0	45	NiC	63.5	60.3	42.4	49.7	n/a	n/a	[149]
DBD	n/a	1.0	2.1	10wt% Ni/Al ₂ O ₃	23.5	13.2	23.2	40.5	n/a	n/a	[144]
Corona	24	2.0	10	20wt% Ni/Al ₂ O ₃	35.6	23.4	54.2	91.4	n/a	n/a	[65]
Spark	24	1.0	39	BaZr _{0.05} Ti _{0.95} O ₃	86.0	82.4	88.7	67.4	0.22	n/a	[163]
GA*	12,700 h ⁻¹	1.0	128	Ni/CeO ₂ /Al ₂ O ₃	94	91	97	95	n/a	72	[164]
RGA	48	1.5 [#]	n/a	Ni/CeO ₂ /Al ₂ O ₃	~90	~19	~81	100	0.02	86	[77]
RGA	60	1.0	190	18 wt% NiO/Al ₂ O ₃	15.0	18.0	52.0	48.0	n/a	n/a	[81]
RGA	13,000 h ⁻¹	2.3	490	10 wt % Ni/Al ₂ O ₃	58.5	39.5	35.3	56	0.29	n/a	[165]
RGA-SB	180	1.5	64	15 wt% NiO/ SiO₂	10.2	9.0	84.9	92.0	0.44	10.6⁺	This work
RGA-SB	148	1.5	136	15 wt% NiO/Al₂O₃	11.8	11.2	75.3	88.1	0.90	9.4⁺	This work

GHSV= Gas Hourly Space Velocity; n/a – not reported/analyzed; *External heating was provided; # added O₂; DBD - dielectric barrier discharges; GA – gliding arc; RGA – rotating gliding arc; RGA-SB – rotating gliding arc spouted bed;

⁺The percentage of electrical energy that contributed to the DRM reaction are 29.5 and 60.2 % for 15NiO/Al₂O₃ and 15NiO/SiO₂, respectively.

6.4.3 Carbon balance and deposition

Table 6-3 shows the carbon balance (eq. 6.6) of the plasma-catalytic dry reforming of methane for the different Ni catalysts and plasma-only experiments. The carbon balance is over 95 %, regardless of the catalyst used. It can be noticed that the presence of the catalyst in the plasma zone slightly increases the carbon balance for both Al₂O₃- and SiO₂-supported catalysts. Besides, the carbon balance is higher in the case of SiO₂-supported catalysts. The higher total surface area of the SiO₂-supported catalyst, as well as the inert nature of the SiO₂ support, could lead to less carbon deposition. Moreover, the surface acidity of Al₂O₃ can contribute to coke deposition during the DRM reaction [52].

Table 6-3 Carbon balance for the different plasma and plasma-catalytic experiments.

Experiment	Carbon Balance %
Plasma (3.7 SLPM)	96.5 ± 0.6
Plasma + Al ₂ O ₃	96.9 ± 0.8
Plasma + 30NiO/Al ₂ O ₃	97.8 ± 0.6
Plasma + 30Ni/Al ₂ O ₃ (P)	99.1 ± 1.0
Plasma + 15NiO/Al ₂ O ₃	98.8 ± 0.8
Plasma + 15NiO/Al ₂ O ₃ (CH ₄)	99.5 ± 1.9
Plasma (4.5 SLPM)	98.4 ± 1.0
Plasma + SiO ₂	99.8 ± 0.7
Plasma + 30NiO/SiO ₂	99.0 ± 0.7
Plasma + 30Ni/SiO ₂ (P)	100 ± 0.7
Plasma + 15NiO/SiO ₂	99.7 ± 0.8
Plasma + 15NiO/SiO ₂ (CH ₄)	98.9 ± 1.0

Carbon deposition is one of the major drawbacks of DRM. This process is unavoidable and thermodynamically favored [40] and can occur due to CO-disproportionation, resulting in solid carbon, or due to coke formation (i.e. decomposition or condensation of hydrocarbons) [101]. TPO-TGA analyses were carried out to determine the type and amount of carbon deposited on the catalyst samples. Fig. 6-7a shows the corresponding relative mass change of three of the investigated catalyst samples that showed more significant signals of CO₂ evolution (Fig. 6-7b), i.e. 15NiO/Al₂O₃(CH₄), 15NiO/SiO₂(CH₄) and 30Ni/SiO₂(P), normalized by the catalyst sample mass. No

significant amount of carbon deposition was found on the fresh catalysts, the samples used for the thermo-catalytic experiments (except for 30Ni/Al₂O₃), and the rest of the samples used in the plasma-catalytic experiments (see supplementary material B.2.5). The samples that were pretreated with CH₄ showed higher signals for the carbon dioxide evolution than the catalyst samples used only for the plasma-catalytic DRM, since under plasma conditions, CH₄ decomposes in CH_x species that can condensate on the surface of the catalyst forming coke [101]. In Fig. 6-7b, four CO₂ peaks are observed for the different samples. The signals for carbon dioxide between 150 and 500 °C correspond to polymeric carbon (C_β), whereas the signals between 500 and 800 °C correspond to graphitic carbon (C_C) [9, 101]. The spent 15NiO/Al₂O₃(CH₄) catalyst (0.6 % more weight loss compared to the fresh sample) showed higher carbon deposition compared to the 15NiO/SiO₂(CH₄) (0.3 % more weight loss compared to the fresh sample). The same behavior was observed for the thermo-catalytic experiments, where higher carbon deposition was found in the spent Ni/Al₂O₃ catalysts compared to the catalysts supported on SiO₂. The latest can be attributed to the higher total surface area of the SiO₂ catalyst, as well as the inert nature of the SiO₂ support, which could lead to less carbon deposition [52]. For the fresh catalyst samples, only a small CO₂ peak at 950 °C was measured, indicating some graphitic carbon traces (see supplementary material B.2.5). For the thermo-catalytic experiments, only the 30Ni/Al₂O₃ sample showed a signal of CO₂ at 560 °C, corresponding to graphitic carbon with a weight loss of +4.3 % compared to the fresh sample (43 times more compared to the 30Ni/Al₂O₃ plasma-catalytic sample). In general, for the plasma-catalytic experiments, carbon deposition was less than 10 mg per gram of catalyst. The increase in mass for the 15NiO/SiO₂(CH₄) and 30Ni/SiO₂(P) catalysts from 270 to 370 °C and from 270 to 950 °C, respectively, could be attributed to the oxidation of the bulk nickel in the catalyst samples [9]. For the 15NiO/SiO₂(CH₄) catalyst, part of the NiO might be reduced during the pretreatment with CH₄ in the plasma reactor. The weak bond between the SiO₂ and the Ni leads to a lower reduction temperature (430 °C) than the Ni supported on Al₂O₃ (616 °C), which shows more stability during the catalytic and plasma-catalytic experiments.

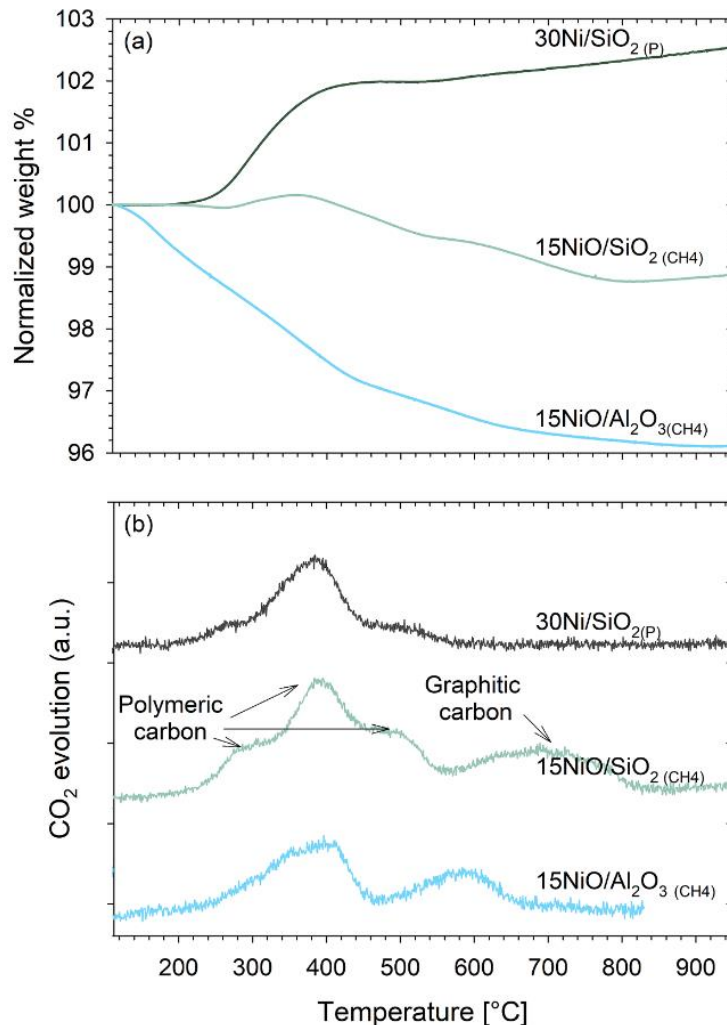


Fig. 6-7 (a) Normalized weight change and (b) CO₂ evolution during temperature-programmed oxidation (TPO) of the spent Ni-catalysts. Note: P = reduced + passivated, CH₄ = plasma pretreatment with CH₄.

Fig. 6-8 shows SEM pictures, and EDS spectra for fresh and spent 30NiO/Al₂O₃. It can be noticed that there is an increased amount of carbon deposited on the catalyst surface after plasma-catalytic DRM. These results are in accordance with the previous analyses. The same behavior was found for the 30NiO/SiO₂ (Fig. 6-18, supplementary material B.2.5). Some contributions to the carbon signal were from the sample grid as well as from carbon traces in the support, which was confirmed by the XPS analysis.

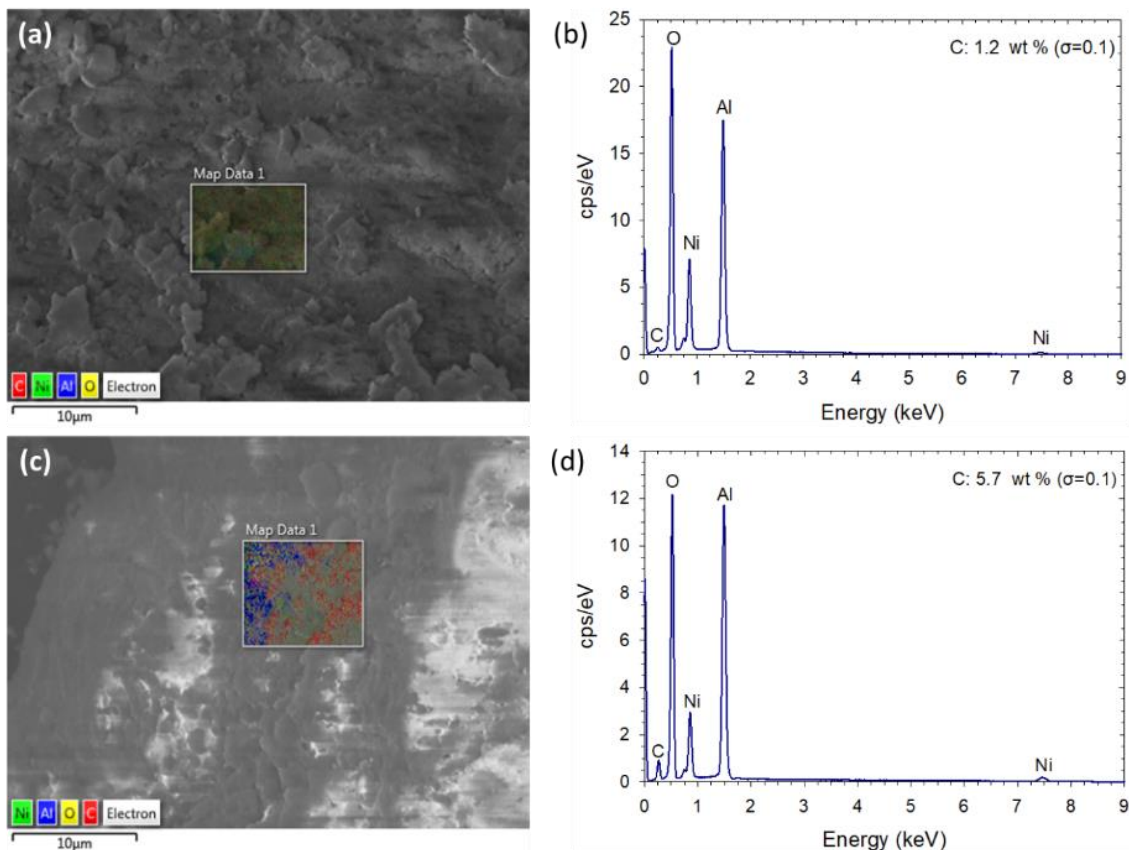


Fig. 6-8 SEM pictures and EDS spectra for 30NiO/Al₂O₃ for (a, b) fresh and (c, d) spent catalyst (after plasma).

6.4.4 Catalyst characterization

Tables 6-3 and 6-4 summarize the physicochemical properties of the fresh and spent Ni catalysts. The catalysts supported on SiO₂ present the highest surface area. It can be noticed that increasing the content of Ni from 15 to 30 wt% decreases the total surface area by 22 % and 13 % for the catalyst supported on Al₂O₃ and SiO₂, respectively. This is because more Ni atoms occupy the space on the support, which increases the H₂-uptake and the active surface area by 34 % and 27 % in Al₂O₃ and SiO₂ supported catalysts, respectively. In the case of the pore volume for the fresh catalyst, a decrease of 15% and 27 % for SiO₂- and Al₂O₃-supported catalyst was observed when the Ni content increased from 15 to 30 %, meaning that more Ni atoms were localized inside the pores of the support.

After the different Ni catalysts were in contact with plasma for the DRM reaction (spent catalyst), a reduction of the total surface area was measured, more noticeable with the 15NiO/Al₂O₃ catalyst,

which reduced the total surface area by 16 % (including the one pretreated with CH₄). For the 15NiO/SiO₂ catalyst, this reduction was only 4% after plasma-catalytic DRM and 40 % once that the catalyst was under a CH₄ atmosphere(Fig. 6-9, Table 6-4). This change is especially noticeable in the pore volume, which is attributed to a blockage of the pores by coke and carbon species produced by the CH₄ when treated by plasma, as presented in Fig. 6-9b, which explains the reduction of the active surface area for the 15NiO/SiO₂ (Table 6-5). No significant difference was measured for the pore diameter either by increasing Ni content or for fresh or spent catalyst.

Table 6-4 N₂ adsorption/desorption results (total surface area, average pore size and pore volume) for fresh and spent catalysts (AP = after plasma, P = passivated, CH₄ = after plasma pretreatment with CH₄).

Catalyst	S _{BET} ^a [m ² g ⁻¹]			D _{pore} ^b [nm]			V _{pore} ^c [cm ³ g ⁻¹]		
	Fresh	Spent		Fresh	Spent		Fresh	Spent	
		AP	P or CH ₄		AP	P or CH ₄		AP	P or CH ₄
30NiO/Al ₂ O ₃	164	154	156	8.6	8.8	8.3	0.42	0.40	0.41
15NiO/Al ₂ O ₃	212	178	180	8.5	8.8	8.4	0.58	0.49	0.49
Al ₂ O ₃	244	245	--	8.6	8.6	--	0.66	0.67	--
30NiO/SiO ₂	344	339	244	6.8	6.6	6.4	0.66	0.65	0.46
15NiO/SiO ₂	395	379	236	6.6	6.5	6.5	0.78	0.74	0.45
SiO ₂	426	410	--	6.8	6.6	--	0.90	0.85	--

^a S_{BET} = BET total specific surface area obtained from adsorption data in the p/p^0 range from 0.05-0.3; all reported data are within ± 4 m² g⁻¹ based on repeated analyses.

^b D_{Pore} = average pore diameters calculated using Barrett-Joyner-Halenda (BJH) method;

^c V_{Pore} = pore volume was obtained at $p/p^0 = 0.97$.

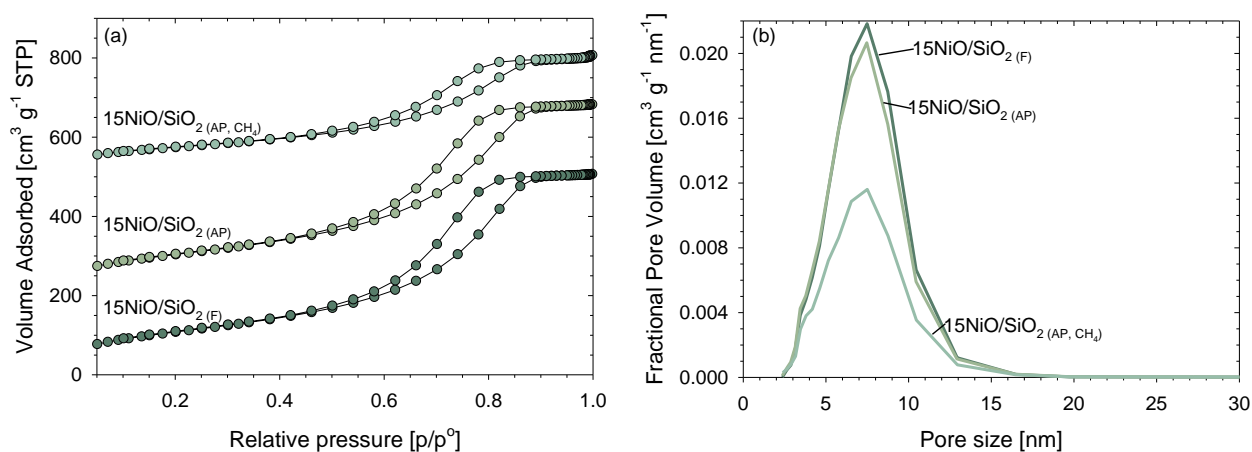


Fig. 6-9 (a) N_2 adsorption/desorption isotherms and (b) pore size distribution for $15NiO/SiO_2$ catalysts. (F) Fresh catalyst (AP) catalyst analyzed after interaction with plasma, (CH_4) Pretreated with methane.

A reduction in the H_2 -uptake of 10 % and 20 % was measured for $15NiO/Al_2O_3$ and $15NiO/SiO_2$, respectively, after plasma-catalytic DRM, suggesting that some nickel atoms were encapsulated by the carbon deposited on the catalyst surface during the reaction as shown in the previous section. A slight increase in metal dispersion was determined for the $15NiO/Al_2O_3$ catalyst that was pretreated with CH_4 , which could have been induced by the long contact time of the catalyst with the plasma. A study by Cheng *et al.* [64] reported a higher dispersion of Ni when pretreating the catalyst with a glow discharge prior to the calcination step, which shows that the direct contact of the catalyst with the plasma alters its chemical characteristics.

Table 6-5. H_2 uptake [$\mu mol g^{-1}$], specific surface area [$m^2 g^{-1}$], average nickel crystallite size [nm] and metal dispersion [%] for fresh and spent Ni catalysts.

Catalyst	H_2 -uptake			Active surface area			Ni Crystallite size, d			Metal dispersion, D		
	[$\mu mol g^{-1}$]			[$m^2 g^{-1}$]			[nm]			[%]		
	Fresh	Spent		Fresh	Spent		Fresh	Spent		Fresh	Spent	
	AP	P or CH_4		AP	P or CH_4		AP	P or CH_4		AP	P or CH_4	
$30NiO/Al_2O_3$	161 ± 2	159	149	12.6 ± 0.1	12.4	11.7	8.0 ± 0.1	8.1	8.6	6.3 ± 0.1	6.2	5.8
$15NiO/Al_2O_3$	110	96	118	8.6	7.6	9.2	5.9	6.7	5.5	7.2	7.6	9.2
$30NiO/SiO_2$	170 ± 12	178	75	13.3 ± 0.9	14.0	5.8	7.6 ± 0.5	7.2	17.3	6.7 ± 0.5	7.0	2.9
$15NiO/SiO_2$	124 ± 8	100	66	9.7 ± 0.7	7.8	5.2	5.2 ± 0.4	6.7	9.7	9.7 ± 0.7	7.6	5.2

6.4.5 X-ray diffraction

Fig. 6-10 shows the XRD patterns of the fresh and spent 30 wt% Ni catalysts on Al_2O_3 and SiO_2 . Reference patterns for NiO, $\gamma\text{-Al}_2\text{O}_3$ and SiO_2 are also shown for comparison and taken from the International Centre for Diffraction Data (ICDD) with the powder diffraction file (PDF) #044–1159, #050-0741 and #016-0152, respectively. Diffraction peaks associated with NiO (i.e., $2\theta = 37.2^\circ$, 43.3° , 62.8° , 75.4° , 79.4° and 95.0°) are very sharp and clearly seen for both NiO/ Al_2O_3 (Fig. 6-10a) and NiO/ SiO_2 (Fig. 6-10b) for fresh and spent catalysts, representing the high degree of crystallinity of the samples and confirming that the direct contact with the plasma did not affect the crystalline structure of the catalyst. The peaks at $2\theta = 45.7^\circ$ and 66.6° in Fig. 6 - 10a are associated with the crystal structure of Al_2O_3 .

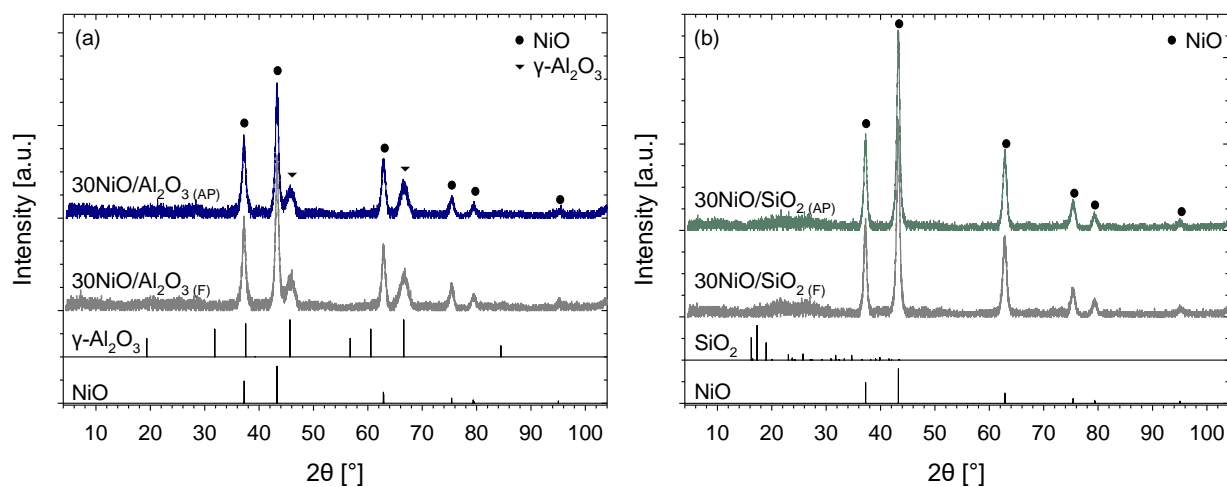


Fig. 6-10 XRD patterns of fresh catalyst and after plasma (a) 30NiO/ Al_2O_3 and (b) 30NiO/ SiO_2 support. Reference patterns of NiO and $\gamma\text{-Al}_2\text{O}_3$ and SiO_2 , PDF #044–1159, PDF #050-0741 and PDF #016-0152, respectively.

Additionally, the crystallite sizes for NiO particles were calculated using the Scherrer equation (eq. 6.10) and are reported in Table 6-6:

$$d = \frac{0.89 \cdot \lambda}{\beta \cdot \cos \theta} \quad (6.10)$$

where d is the mean crystallite size in nm, λ is the X-Ray wavelength (0.15406 nm), β is the Full Width Half Maximum (FWHM) in radians, and θ is the peak position in radians.

Table 6-6 Crystallite size of NiO catalysts fresh and after plasma DRM.

Catalyst	Crystallite size [nm]
30NiO/Al ₂ O ₃ (F)	12.0
30NiO/Al ₂ O ₃ (AP)	11.7
30NiO/SiO ₂ (F)	11.6
30NiO/SiO ₂ (AP)	12.2

*Note that the standard deviation for all samples is ± 1 nm

The results presented in Table 6-6 show that the crystallite size of NiO was not affected by contact with the plasma. Hence no sintering of the Ni catalyst occurs under plasma-catalytic DRM conditions. These results agree with previous studies [162, 166] that reported no significant change in crystallite size by plasma treatment in Pt/Al₂O₃ and NiO/Al₂O₃ catalysts, respectively.

6.4.6 X-ray photoelectron spectroscopy

To determine the effect of plasma exposure on the chemical state of the material, XPS analysis before and after plasma processing (Fig. 6-11) was performed for two types of catalysts: 30NiO/Al₂O₃ and 30NiO/SiO₂. XPS is a surface-sensitive analysis technique (<10 nm penetration depth) used to accurately analyze the chemical environment at the surface. The survey analysis showed a change in atomic composition for both types of catalysts induced by contact with plasma (Fig. 6-11a, b). In both cases, the nickel, oxygen, and aluminum (for 30NiO/Al₂O₃) compositions decrease. At the same time, the carbon composition increases, indicating the deposition of carbon onto the catalyst surface. Fig. 6-11c, d show high-resolution spectra for the Ni 2p of both types of catalysts. The identified peaks at ~853 and ~870 eV are characteristic of the 2p 3/2, and 2p 1/2 for Ni²⁺ chemical state of NiO, whereas the peaks at ~855 and ~873 eV correspond to a more oxidized state of nickel [167, 168]. However, the single peak of O 1s spectra (shown in Fig. 6-20, supplementary material B.2.6) at ~531 eV is attributed to metal-oxygen bond and does not show the presence of hydroxides. Thus, the more oxidized nickel could be a result of the synthesis stage where the reaction produces cation vacancies, or point defects, due to the presence of excess oxygen. These vacancies will then ionize to form Ni³⁺. This is commonly observed in NiO when synthesized using nickel (II) nitrate precursors followed by annealing [169].

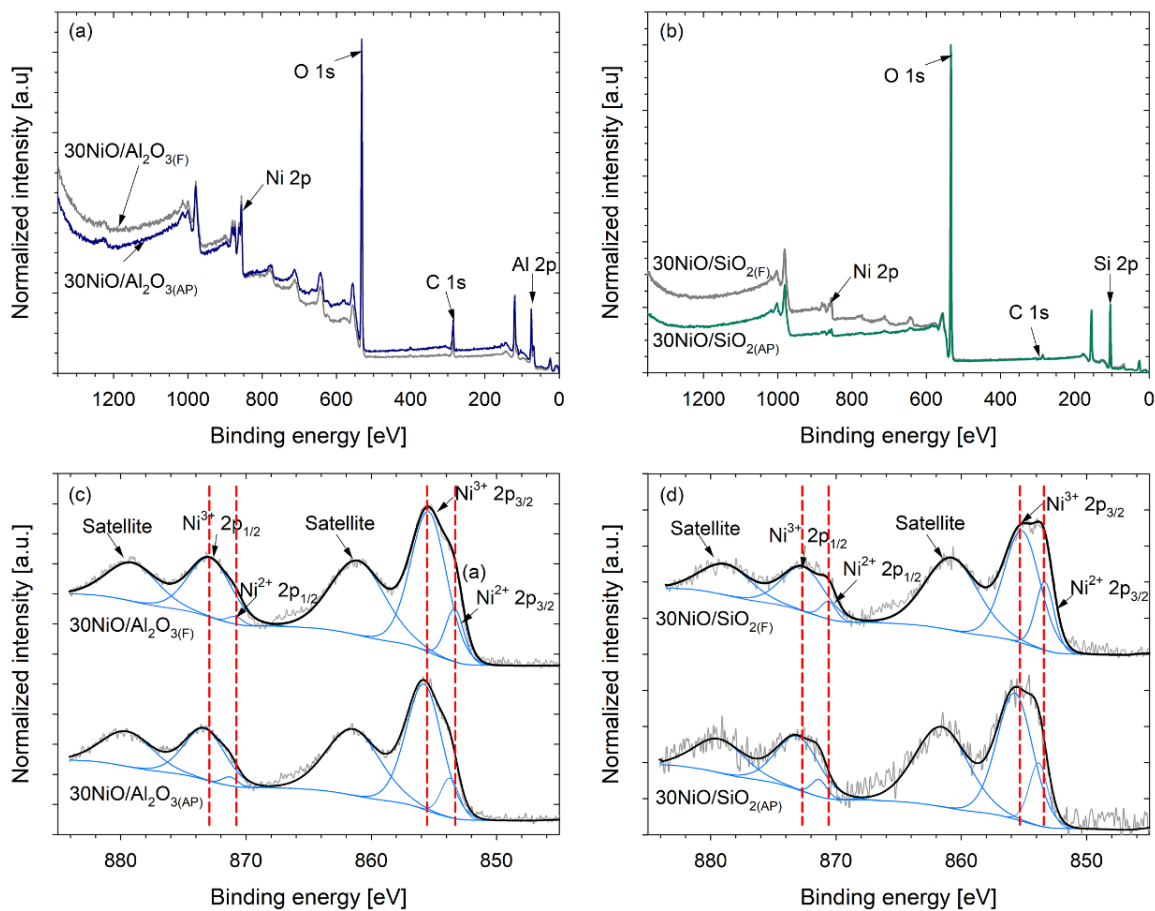


Fig. 6-11 XPS survey spectra of the catalyst materials before (F) and after contact with plasma (AP) for (a) 30NiO/Al₂O₃ and (b) 30NiO/SiO₂. High-resolution spectral analysis for catalyst materials at the (c) Ni 2p edge of 30NiO/Al₂O₃, d) Ni 2p of 30NiO/SiO₂.

After contact with plasma, there is a noticeable shift in peak positions towards a higher binding energy of 0.4 eV and 0.5 eV (measured from the Ni 2p 3/2) for the 30NiO/Al₂O₃ and 30NiO/SiO₂, respectively. This means that there is a change in the coordination environment of Ni to a more electronegative state as it becomes more Ni³⁺ ionic and the electron cloud density shifts towards Ni. Furthermore, there is a significant drop in the peak area for the Ni²⁺ after plasma treatment. The deconvoluted peak areas are listed in Table 6-13 (supplementary material B.2.6) and normalized based on the oxidized Ni³⁺, which quantitatively show the peak area for Ni²⁺ is halved after plasma. This indicates the plasma treatment introduces more defects. The shift of the peaks to higher binding energy reveals that the surface charge accumulates during the discharge [163]. Additionally, Zhu *et al.* [166] reported an increase in the binding energy for Pt-based catalyst after

plasma treatment, suggesting that the higher binding energy value originates from smaller particles produced by the plasma treatment. These smaller particles are more electron-deficient than the larger ones, shifting the binding energy to a higher value.

Moreover, a noticeable change in color from dark green to light green in the case of the Ni/Al₂O₃ catalyst and from black to gray for the Ni/SiO₂ catalyst (Fig. 6-21, supplementary material B-2.6) was observed after the plasma-catalytic reaction. Sugiyama *et al.* [170] reported a change in color of a Nb₂O₅ catalyst from white to blue after it was plasma-treated, attributed to the change in the catalyst surface chemistry. Since plasma does not damage the crystalline structure of the catalyst but changes its surface chemistry, it can improve the performance of the catalyst during a chemical reaction, i.e., lower carbon deposition and higher stability. For instance, Cheng *et al.* [64] studied the effect of an argon glow discharge during the catalyst synthesis, concluding that the plasma-treated catalyst shows an improved low-temperature activity, enhanced stability at high temperatures for DRM (up to 750°C) and better anti-carbon deposit performance than the catalyst prepared by the conventional method. Similar results were obtained by Yu *et al.* [171] for Pd/Al₂O₃ catalyst that concluded that plasma-treated catalyst increases catalytic activity for combustion of methane.

6.5 Conclusions

An atmospheric pressure RGA-spouted bed reactor has been developed for the plasma-catalytic dry reforming of methane. Two different Ni-based catalysts (supported on Al₂O₃ and SiO₂) were studied with two different Ni loadings to determine the effect of these catalyst parameters in the DRM reaction. More stable plasma operation was found with the Al₂O₃-supported catalyst than with SiO₂, which is attributed to the higher melting point of Al₂O₃ compared to SiO₂.

The presence of the catalytic material in the plasma zone decreases the conversion of CO₂ and CH₄ since the catalyst interferes with the formation of the arc, limiting the formation of active species produced by the plasma. Nonetheless, the presence of the spouted bed in the plasma zone increased the selectivity of the H₂ and CO since the catalyst might target their production, hindering the production of C₂ species. Moreover, plasma-catalyst interactions led to a significant decrease in the carbon deposition on the electrode. Polymeric carbon deposits were found on the catalysts's

surface when pretreated with plasma CH₄ due to methane cracking. However, only small amounts of polymeric carbon were found after plasma-catalytic DRM

The crystalline structure of the catalyst is not affected by direct contact with the plasma, whereas the change in the coordination of the Ni environment suggests the introduction of more surface defects. The change in surface chemistry of the catalyst could potentially enhance the catalyst stability and activity. The RGA-spouted bed reactor has the potential to increase not only product selectivity but also reactant conversion while improving the catalyst characteristics. Future work includes increasing the gas temperature in the plasma-catalytic reactor to potentially lead to a better synergistic effect between plasma and catalyst.

Acknowledgments

J. Martin-del-Campo acknowledges the financial support of CONACyT, the Faculty of Engineering through the McGill Engineering Doctoral Award, and the Department of Chemical Engineering through Eugenie Ulmer Lamothe award. The authors acknowledge the contributions of Xinyue Zhang in the catalyst preparation and Elmira Pajootan for conducting the SEM and XRD analysis. The authors thank the technical staff from the Department of Chemical Engineering of McGill University, especially Luciano Cusmich, Gerald Lepkyj, and Frank Caporuscio for their assistance. This work was financially supported by the Natural Sciences and Engineering Research Council of Canada, the Canadian Foundation for Innovation, and the Gerald Hatch Faculty Fellowship.

6.6 Supplementary material

A. Experimental

A.1. ICP results

Table 6-7 Target and actual nickel loadings for Al₂O₃ and SiO₂ supported catalyst determined by ICP - OES

Catalyst	Target	Actual [wt %]
30NiO/Al ₂ O ₃	30.0	28.9
15NiO/Al ₂ O ₃	15.0	18.0
*30NiO/SiO ₂	30.0	20.8
*15NiO/SiO ₂	15.0	10.3

*Note that the difference of 10% and 5% in the Ni content for the SiO₂ supported catalyst was due to incomplete dissolution of the SiO₂ matrix during the digestion.

A.2 Minimum fluidization velocity

The minimum fluidizing velocity (u_{mf}) was determined using eq. A-2.1 [31]:

$$u_{mf} = \frac{d_p^2 (\rho_s - \rho_g) \cdot g}{150 \mu} \cdot \frac{\varepsilon_{mf}^3 \varphi_s^2}{1 - \varepsilon_{mf}} \quad \text{for } Re_{mf} < 20 \quad (\text{A} - 2.1)$$

where u_{mf} is the minimum fluidization velocity (m s⁻¹), ρ_s is the solid density (kg m⁻³), ρ_g is the gas density (kg m⁻³), g is the gravitational acceleration (kg m s⁻²), d_p is the particle diameter (m), μ is the dynamic viscosity (Pa s), φ_s is the sphericity of the particle and ε_{mf} is the bed voidage.

The density and viscosity of the gas were calculated at 20 °C and 1 bar_{abs}, for a gas mixture of Ar 70%, CO₂ 18% and CH₄ 12%. On the other hand, for the catalyst characteristics, the bed voidage was assumed to be 0.55, while the sphericity was set at 0.58, which are typical values for Fischer-Tropsch catalyst [31]. The catalyst density was assumed based on the densities of Al₂O₃ and SiO₂, i.e. 3965 kg m⁻³ and 1538 kg m⁻³, respectively. Moreover, the calculations only considered the highest particle diameter in each case since the larger particle size are harder to fluidize. For the conditions described above, the u_{mf} were 2.5 cm s⁻¹, and 3.8 cm s⁻¹ for Al₂O₃ and SiO₂ supported catalyst, respectively.

B. Results and discussion

B.1 Thermo-catalysis

B.1.1 Reduction temperature

Fig. 6–12. shows the water evolution vs. temperature for the different Ni-based catalysts supported on Al_2O_3 and SiO_2 . The reduction temperature was determined as the last water peak measured on the TPR analyses.

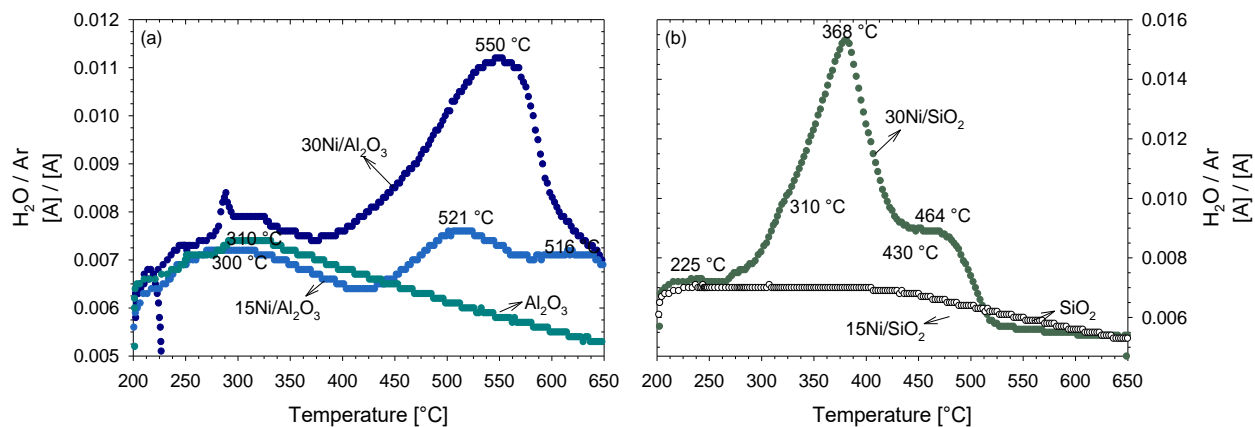


Fig. 6-12 Reduction temperatures for (a) Al_2O_3 and (b) SiO_2 based catalyst.

B.1.2 Catalyst stability

Fig. 6-13 shows the catalytic activity over time of the Ni-based catalyst supported on Al_2O_3 and SiO_2

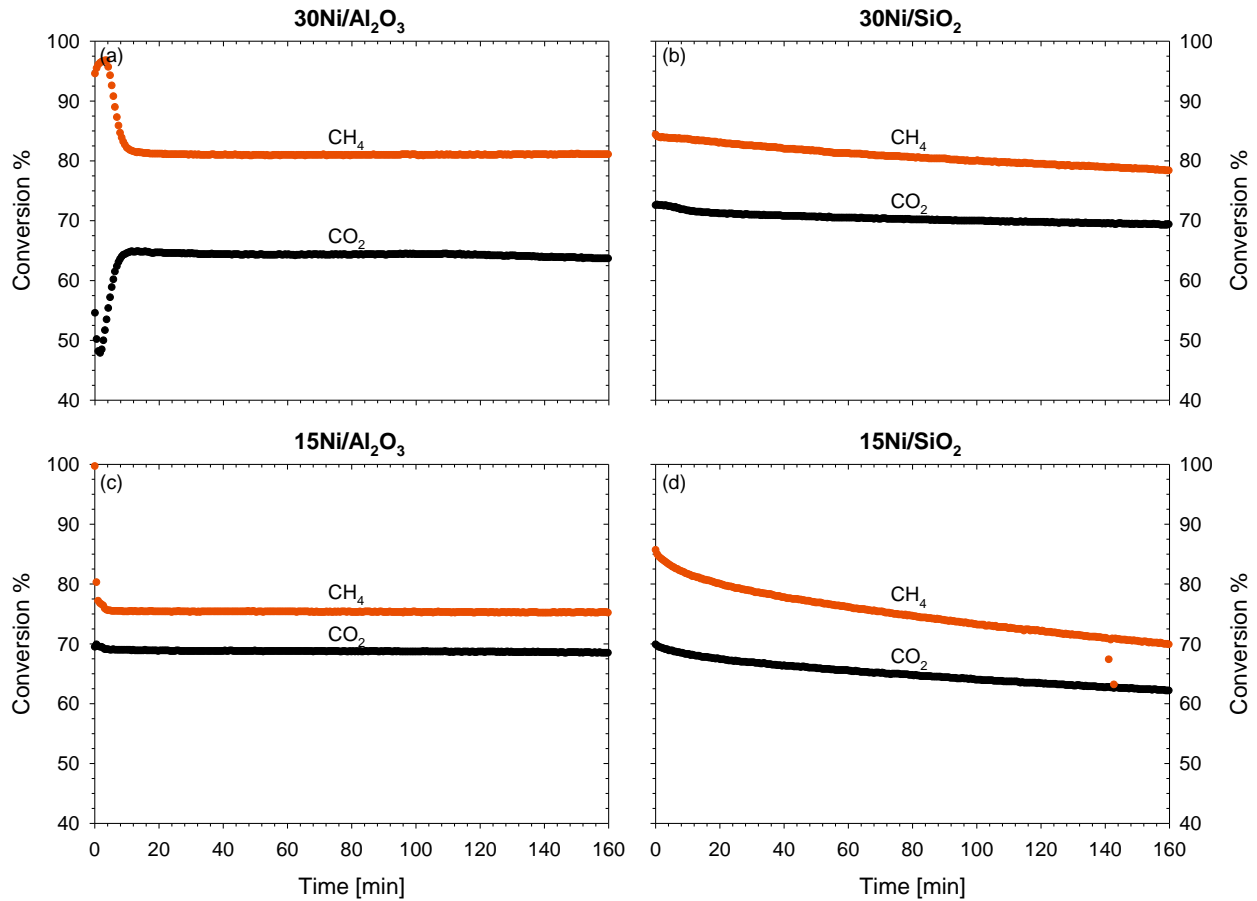


Fig. 6-13 Conversion of CO_2 and CH_4 over time for (a) $30\text{Ni}/\text{Al}_2\text{O}_3$, (b) $30\text{Ni}/\text{SiO}_2$, (c) $15\text{Ni}/\text{Al}_2\text{O}_3$ and (d) $15\text{Ni}/\text{SiO}_2$.

B.1.3 Water signal for thermal catalytic experiments

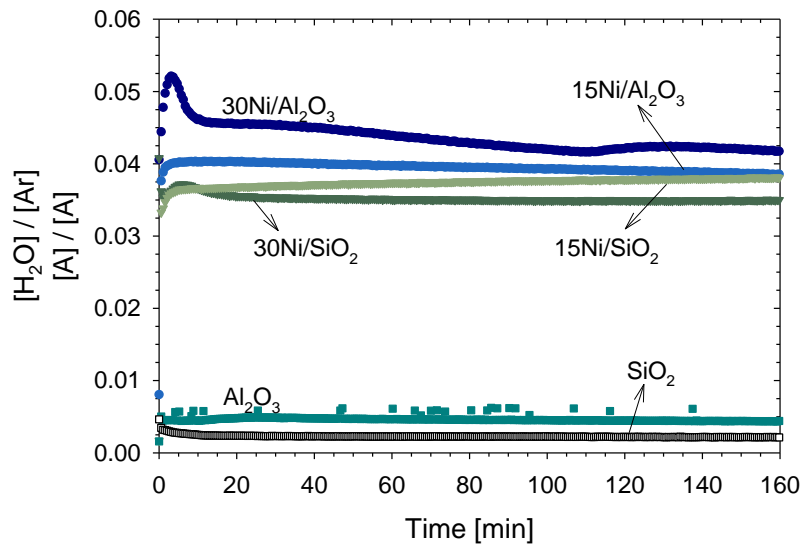


Fig. 6-14 Water signal over time for different Ni-based catalyst supported on Al₂O₃ and SiO₂.

B.2 Plasma-catalysis

B.2.1 Electrical signals

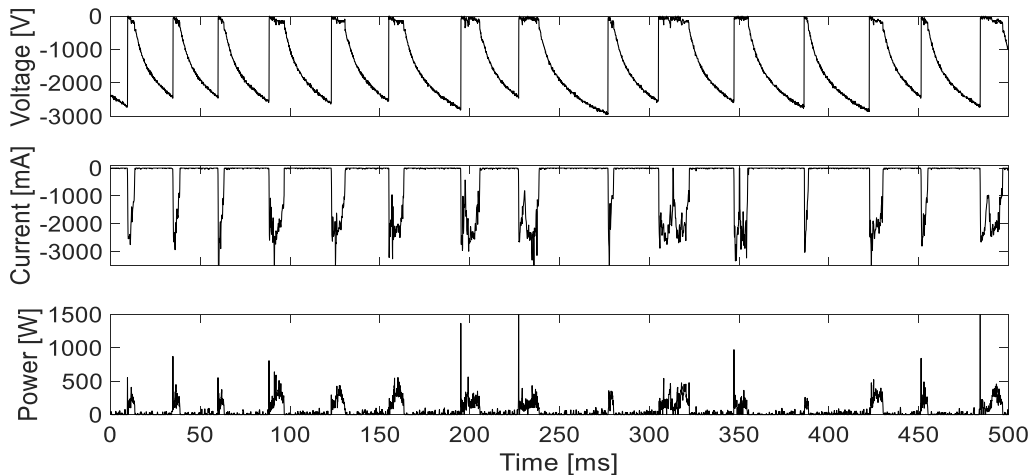


Fig. 6-15 Characteristic RGA discharge voltage, current and instantaneous power signals for plasma - catalytic DRM reaction at $\text{CO}_2/\text{CH}_4 = 1.5$, with a total flow rate of $4.5 \text{ L}_N \text{ min}^{-1}$ over Ni/SiO₂ catalyst.

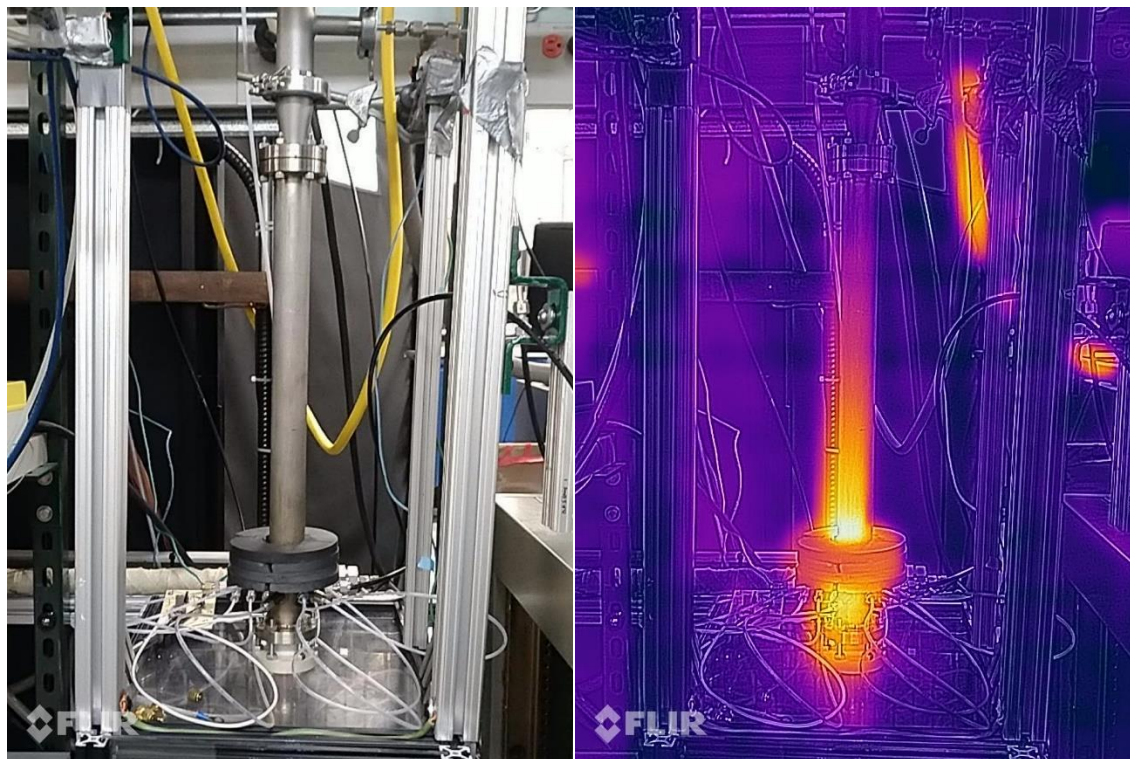


Fig. 6-16. Reactor assembly (on the left) and infrared photograph of the RGA reactor during DRM reaction (on the right). Taken with Cat S61 FLIR camera.

B.2.2 ANOVA and t-test statistical results

For Figures 6–3 and 6-4, ANOVA Statistical analyses and t-test were performed using the tool ANOVA: Single-factor and t-test: two sample assuming unequal variances, respectively from Microsoft Excel. The significance level was set at $\alpha=0.05$, and the null hypothesis failed to be rejected when $F < F_{crit}$ and $p\text{-value} > \alpha$ in the case of ANOVA. For the t-test, the null hypothesis is rejected if $t_{stat} < -t_{critical}$ and $t_{critical} < t_{stat}$. Alternatively, if $p(\text{two-tail}) > \alpha$, the null hypothesis fails to be rejected. The fail of rejection of the null hypothesis states that there is not enough evidence to state that there is a significant statistical difference between the evaluated means, with 95% confidence. Note that when p-value was close to α , α was set to 0.01, i.e. 99% of confidence to determine whether or not there was a significant difference between the samples.

The ANOVA tables (Tables 6-7 and 6-9) show the rejection of the null hypothesis, stating that there was a statistical difference between the groups analyzed. Hence, the t-test was performed between the different group of samples in each case. Tables 6-8 and 6–10 show the pairs of samples for which statistical difference was NOT found. For all the other pairs not shown in the tables, statistical difference was found.

Table 6-8 ANOVA results for plasma-catalytic experiments with Ni/Al₂O₃ catalysts.

Tested with ANOVA	Fig. 3 section	Description	F	p-value	Null hypothesis rejected
Al₂O₃ based catalyst	a	CO ₂ conversion	245.67	3.21 X 10 ⁻⁷⁴	yes
	b	CH ₄ conversion	118.47	1.45 X 10 ⁻⁵²	yes
	c	CO selectivity	25.42	1.22 X 10 ⁻¹⁸	yes
	d	H ₂ selectivity	68.64	1.9 X 10 ⁻³⁸	yes
		H ₂ /CO	5.84	5.41 X 10 ⁻⁰⁵	yes

Table 6-9. t-test results for plasma-catalytic experiments with Ni/Al₂O₃ catalysts.

Tested with t-test	Pair	P(t<=t) two tail	t-stat	t-crit two tail	Null hypothesis rejected
CO₂ conversion	Plasma – 15NiO/Al ₂ O ₃	0.20	1.3	2.00	no
	15NiO/Al ₂ O ₃ – Al ₂ O ₃	0.06	-1.91	2.02	no
CH₄ conversion	30NiO/Al ₂ O ₃ – 15NiO/Al ₂ O ₃	0.25	-1.16	2.02	no
	30NiO/Al ₂ O ₃ – Al ₂ O ₃	0.01	2.59	2.01 2.69 (α=0.01)	yes no
	15NiO/Al ₂ O ₃ – Al ₂ O ₃	0.09	1.71	2.00	no
CO selectivity	Plasma – 30Ni/Al ₂ O ₃ (P)	0.99	-0.01	2.06	no
	Plasma – 30Ni/Al ₂ O ₃ (F)	0.13	1.57	2.04	no
	30NiO/Al ₂ O ₃ – Al ₂ O ₃	0.45	-0.77	2.07	no
	30Ni/Al ₂ O ₃ (P) – Al ₂ O ₃	0.07	-1.91	2.08	no
	30NiO/Al ₂ O ₃ – 30Ni/Al ₂ O ₃ (P)	0.29	-1.09	2.03	no
	15NiO/Al ₂ O ₃ – 15NiO/Al ₂ O ₃ (CH ₄)	0.05	2.03	2.66	no
H₂ selectivity	30NiO/Al ₂ O ₃ – Al ₂ O ₃	0.27	1.12	2.05	no
H₂/CO	Plasma – 30NiO/Al ₂ O ₃	0.91	-0.10	2.06	no
	Plasma – 15NiO/Al ₂ O ₃ (CH ₄)	0.29	1.06	2.06	no
	30NiO/Al ₂ O ₃ – Al ₂ O ₃	0.21	-1.03	2.06	no
	30Ni/Al ₂ O ₃ (P) – Al ₂ O ₃	0.38	0.88	2.06	no
	15NiO/Al ₂ O ₃ (CH ₄) – Al ₂ O ₃	0.52	-0.65	2.06	no
	30NiO/Al ₂ O ₃ – 30Ni/Al ₂ O ₃ (P)	0.17	1.41	2.07	no
	30NiO/Al ₂ O ₃ – 15NiO/Al ₂ O ₃ (CH ₄)	0.52	0.65	2.05	no
	30NiO/Al ₂ O ₃ – 15NiO/Al ₂ O ₃	0.01	2.79	2.01 2.83 (α = 0.01)	yes no
	30Ni/Al ₂ O ₃ (P) – 15NiO/Al ₂ O ₃ (CH ₄)	0.14	-1.48	2.05	no

Table 6-10 ANOVA results for plasma-catalytic experiments with Ni/SiO₂ catalysts.

Tested with ANOVA	Fig. 4 section	Description	F	p-value	Null hypothesis rejected
SiO ₂ based catalyst	a	CO ₂ conversion	56.92	2.75 X 10 ⁻³³	yes
	b	CH ₄ conversion	36.35	1.80 X 10 ⁻²⁴	yes
	c	CO selectivity	16.74	5.09 X 10 ⁻¹³	yes
	d	H ₂ selectivity	19.82	3.19 X 10 ⁻¹⁵	yes
		H ₂ /CO	3.60	0.004	yes

Table 6-11. t-test results for plasma-catalytic experiments with Ni/SiO₂ catalysts.

Tested with t-test	Pair	P(t<=t) two tail	t-stat	t-crit two tail	Null hypothesis rejected
CO ₂ conversion	30NiO/SiO ₂ – 15NiO/SiO ₂	0.10	-1.7	2.00	no
	30Ni/SiO ₂ (P) – 15NiO/SiO ₂ (CH ₄)	0.05	2.08	2.72	no
CH ₄ conversion	Plasma – 30NiO/SiO ₂	0.03	2.24	2.03 2.72 (α=0.01)	yes no
	30NiO/SiO ₂ – 30Ni/SiO ₂ (P)	0.04	2.08	2.01 2.69 (α=0.01)	yes no
CO selectivity	Plasma – SiO ₂	0.99	-0.005	2.01	yes no
	30Ni/SiO ₂ – SiO ₂	0.02	-2.36	2.00 2.66 (α=0.01)	yes no
	15NiO/SiO ₂ – SiO ₂	0.02	-2.41	2.01 2.68 (α=0.01)	yes no
	30Ni/SiO ₂ – 15NiO/SiO ₂	0.96	-0.04	2.01	no
H ₂ selectivity	Plasma- SiO ₂	0.73	-0.35	2.01	no
	30NiO/SiO ₂ – SiO ₂	0.02	2.36	2.01 2.68 (α=0.01)	yes no
	30NiO/SiO ₂ (P) – SiO ₂	0.03	2.26	2.03 2.68 (α=0.01)	yes no
	30NiO/SiO ₂ – 30Ni/SiO ₂ (P)	0.60	-0.52	2.01	no
	15NiO/SiO ₂ – SiO ₂	0.01	-2.53	2.03 2.68 (α=0.01)	yes no

H₂/CO	Plasma- SiO ₂	0.03	-2.19	2.05 2.67 ($\alpha=0.01$)	yes no
	Plasma – 30Ni/SiO ₂	0.25	1.16	2.05	no
	Plasma – 30Ni/SiO ₂ (P)	0.14	1.52	2.05	no
	Plasma – 15NiO/SiO ₂	0.53	0.62	2.05	no
	Plasma – 15NiO/SiO ₂ (CH ₄)	0.68	-0.41	2.05	no
	30NiO/SiO ₂ – 30NiO/SiO ₂ (P)	0.42	0.81	2.05	no
	30NiO/SiO ₂ – 15NiO/SiO ₂	0.24	-0.69	2.05	no
	30NiO/SiO ₂ (P) – 15NiO/SiO ₂ (CH ₄)	0.14	-1.50	2.05	no
	30NiO/SiO ₂ – 15NiO/SiO ₂ (CH ₄)	0.26	-1.14	2.05	no
	15NiO/SiO ₂ (CH ₄) – SiO ₂	0.24	1.18	2.05	no
	15NiO/SiO ₂ (CH ₄) – 15NiO/SiO ₂	0.42	-0.81	2.05	no

B.2.4 Acetylene signal for plasma-catalytic experiments

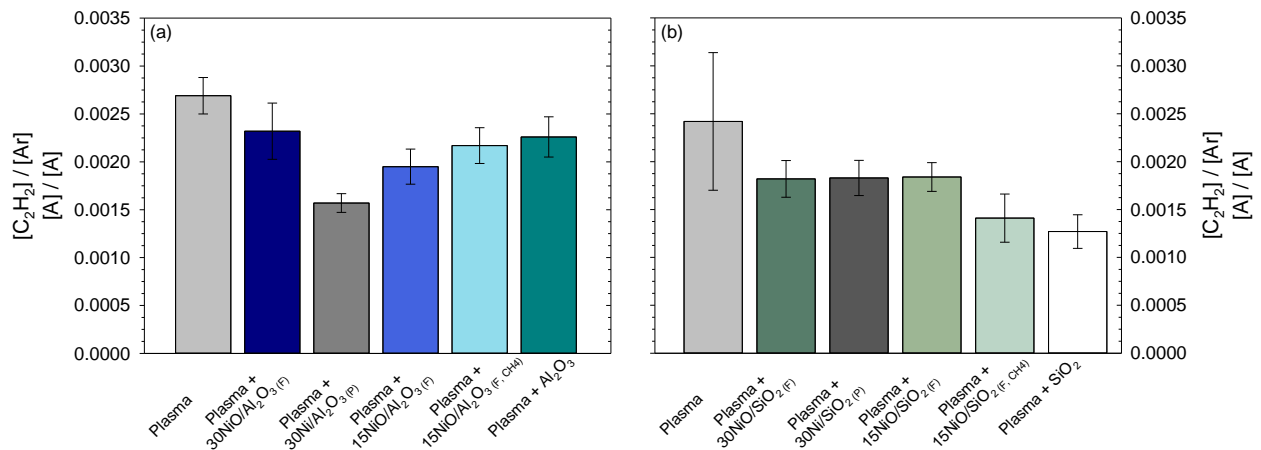


Fig. 6-17 $[C_2H_2]/[Ar]$ signal for the different catalyst supported on (a) Al_2O_3 , total flow rate $3.7 L_N \text{ min}^{-1}$ and (b) SiO_2 , total flow rate $4.5 L_N \text{ min}^{-1}$.

B.2.5 Carbon deposition

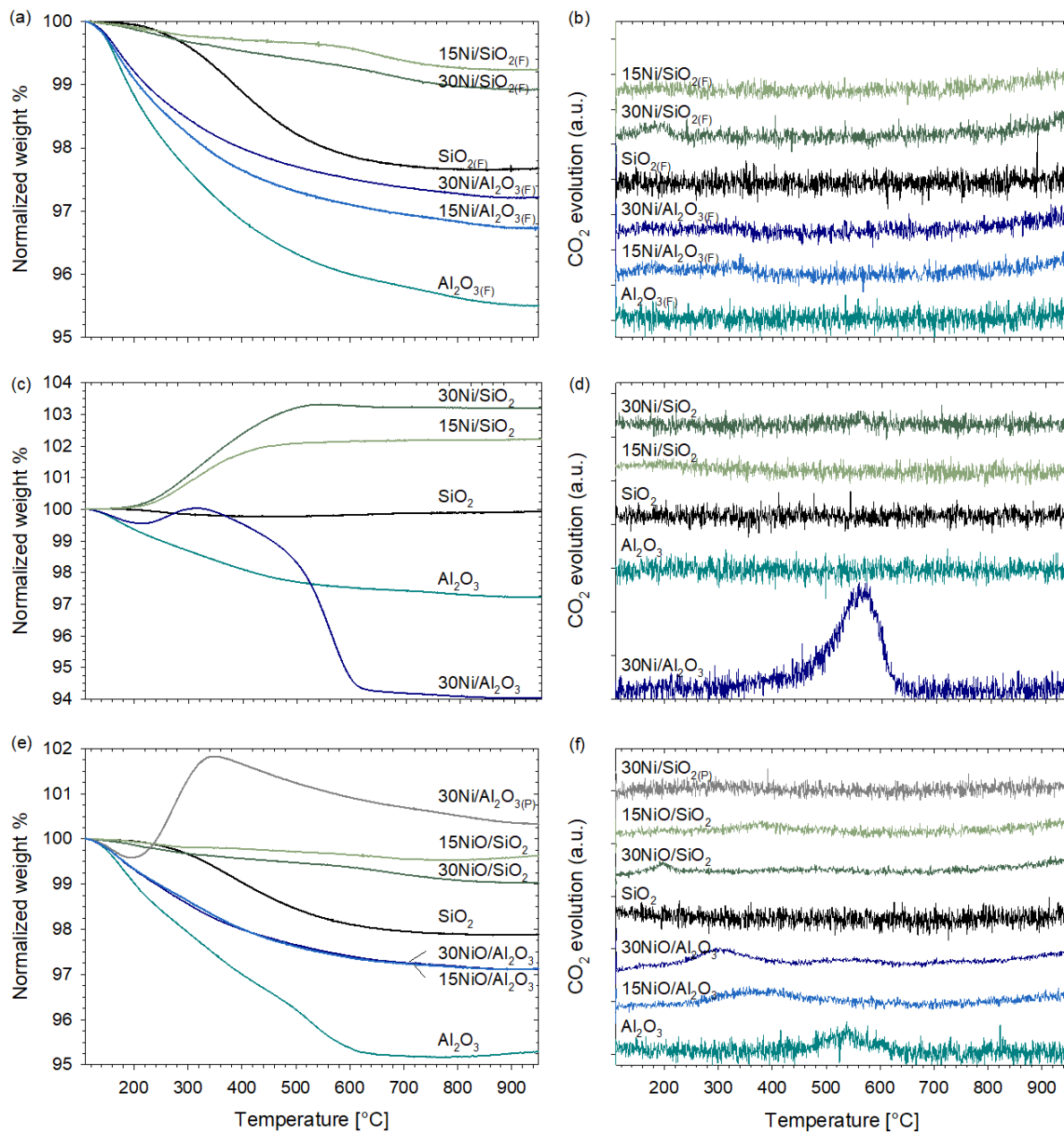


Fig. 6-18 TGA-TPO results for Ni-based catalysts (a, b) fresh, (c,d) used in thermo-catalytic experiments and (e,f) used in plasma-catalytic experiments.

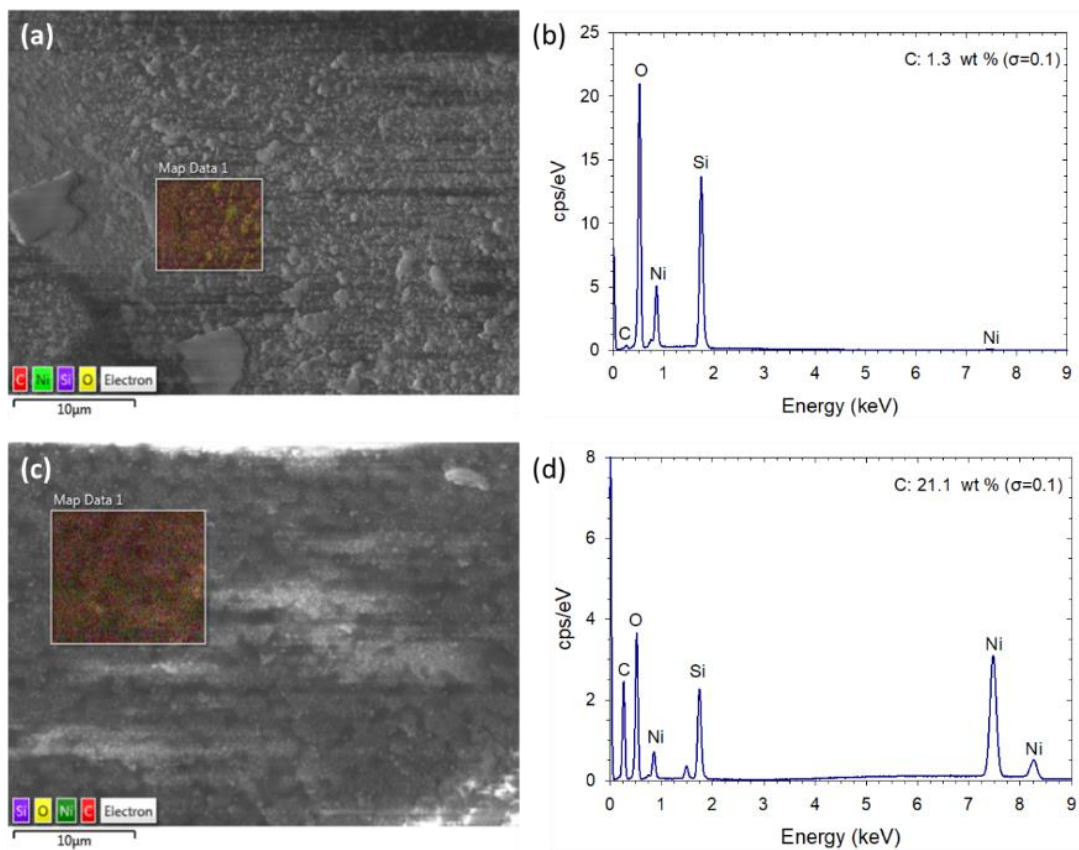


Fig. 6-19 SEM pictures and EDS spectra for 30NiO/SiO₂ for (a, b) fresh and (c, d) spent catalyst (after plasma).

B.2.6 X-Ray Photoelectron Spectroscopy

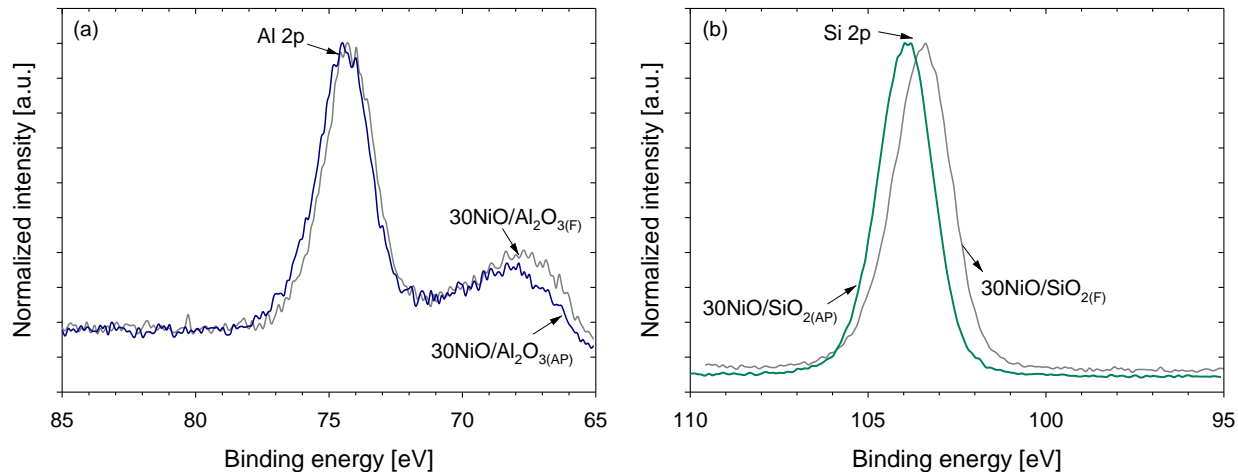


Fig. 6-20 High-resolution spectral analysis for fresh (F) and spent (AP) catalysts at the (a) Al 2p of 30NiO/Al₂O₃, and (b) Si 2p of 30NiO/SiO₂.

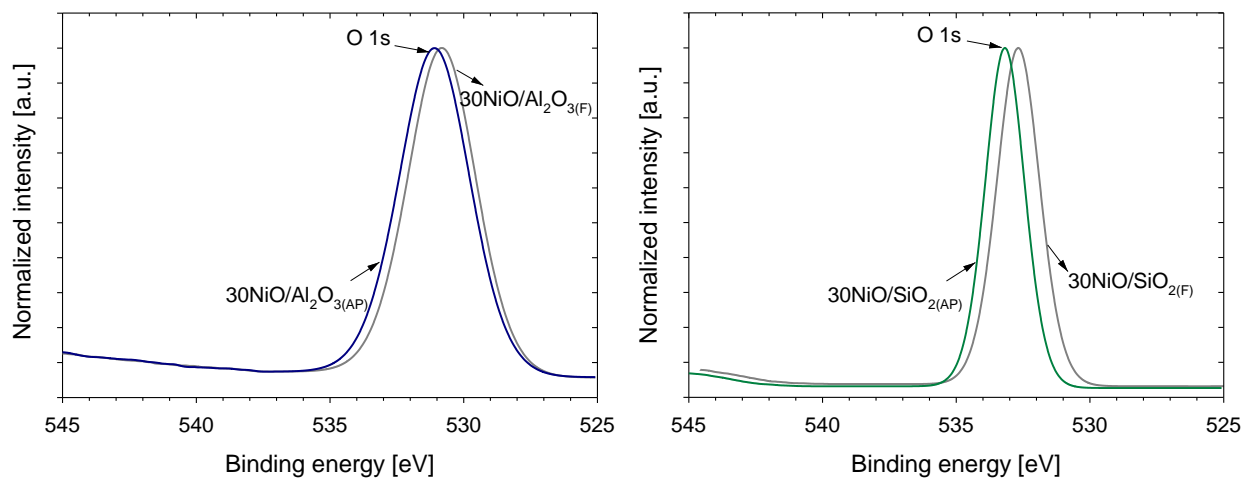


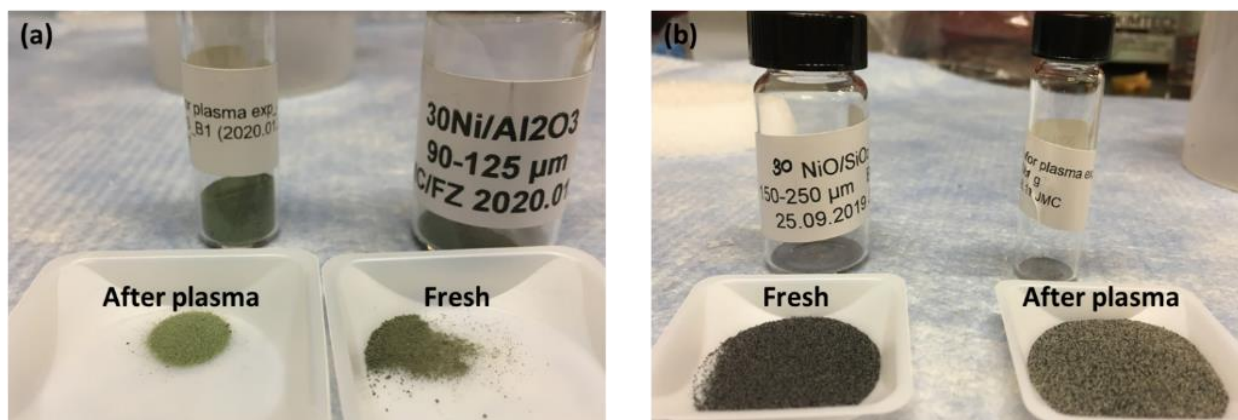
Fig. 6-21 High-resolution spectral analysis for fresh (F) and spent (AP) catalysts at the O 1s (a) 30NiO/Al₂O₃, and (b) 30NiO/SiO₂

Table 6-12 Atomic compositions of the catalyst

Surveys		Atomic %				
Catalyst		O	Ni	Al	C	Si
30NiO/Al ₂ O ₃	F	45.4	6.2	39.1	9.4	NA
	AP	44.2	4.9	38.7	12.2	NA
30NiO/SiO ₂	F	65.1	2.7	NA	3.4	28.8
	AP	64.5	1.2	NA	3.7	30.3

Table 6-13 Change in Ni 2p 3/2 peak ratios for catalysts.

Catalyst	Area Ratios		
	Ni ²⁺	Ni ³⁺	
30NiO/Al ₂ O ₃	F	0.38	1
	AP	0.16	1
30NiO/SiO ₂	F	0.31	1
	AP	0.26	1

Fig. 6-22 Fresh and spent catalyst (after contact with plasma) (a) 30NiO/Al₂O₃ and (b) 30NiO/SiO₂.

7

Conclusions and Future work

7.1 Summary and Main Findings

The work presented in this dissertation explores and studies different alternatives for the current limitations of two promising CO₂ valorization processes, i.e., CO₂ methanation and dry reforming of methane.

First, in the case of the more industrially mature CO₂ methanation process, a graphic approach for the design and operation of bubbling fluidized bed reactors was developed. In particular, methanation reactors should be able to operate in a flexible range of total inlet flow rates (capacity) since the production of H₂ depends on the excess of renewable energies available. Working diagrams for BFB reactors are scarce, and several authors have reported diagrams in which the fluidization regimes are shown. However, these diagrams do not mention possible operating conditions for BFB reactors. The work presented in Chapter 4 aims to determine the interdependency of operating temperature, pressure, particle diameter, and the fluidization characteristics for BFB reactors. The working diagrams are designed based on the hydrodynamic equations for BFB reactors, and the thermodynamics of the CO₂ methanation reaction at different operating temperatures and pressures are also considered. The first type of working diagrams presented in Chapter 4, section 4.5, shows a decision window to choose bed diameter given specific operating conditions (e.g., temperature, pressure, and particle size) that ensures that the superficial gas velocity is high enough to provide proper fluidization conditions and at the same time is far enough of the terminal velocity. It was found that the bed diameter increases with temperature, this as a result of gas expansion in the reactor. On the other hand, increasing the pressure at a

specific gas temperature leads to slimmer reactors. Operating in a flexible range of pressures makes the design of the reactor easier (slimmer, less material) and gives more flexibility to fluidize different particle sizes. The next section (4.6) in Chapter 4 is more interesting from the operating point of view since a decision window to determine the operating capacity of the reactor (given a specific bed diameter) is determined. It was found that increasing the operating temperature in the BFB reactor leads to lower operating capacity (turndown ratio). The latter is helpful in case of less H_2 availability to keep fluidization conditions and avoid the collapse of the bed. However, increasing the operating temperature reduces the energy output as the production of CH_4 is thermodynamically unfavored. At the same time, the energy consumption increases and, thus, the total cost of the process. On the other hand, operating with a flexible pressure range provides the flexibility to operate at different reactor capacities with the same particle size and keeping the same fluidization conditions, avoiding de-fluidization. In the case study presented for an industrial reactor, it is shown that the reactor can operate safely in a flexible range of pressures between 1 and 10 bara, corresponding to capacities of 10 to 120%, respectively. Moreover, higher pressures are preferred from the thermodynamic point of view, as CO_2 conversion is favored. In general, the methodology shown in Chapter 4 to build working diagrams for determining design and operating parameters can be applied to any gas phase reaction by considering the reaction thermodynamics.

The second CO_2 valorization technique studied was dry reforming of methane. A major advantage of DRM is that it upgrades two greenhouse gases, CO_2 and CH_4 . Nonetheless, the commercialization and scaling up of the DRM reaction is limited by its thermodynamics. Hence, research on new technologies is needed. A non-thermal plasma technology known as rotating gliding arc was developed in Chapter 5 for the DRM process. The RGA can produce syngas at room temperature. Different operating conditions such as peak current, total inlet flow rate, CO_2/CH_4 ratio, and gas inlet temperature were studied to determine the effect of these parameters on the performance of DRM. The first sections of Chapter 5 discussed the evaluation of the reaction performance (conversion, yield, and energy efficiency) when the latter parameters were changed. It was found that the peak current was one of the main parameters contributing to the conversion of CO_2 and CH_4 , as a higher peak current led to higher electron density. Hence, more electron impact reactions were taking place in the plasma discharge zone. Another interesting finding was that at lower peak current (0.74 A), the conversion of CO_2 increased when the total flow rate increased from 3.7 to 4.7 SLPM. This finding is similar to the one previously reported

by [129], and it was not expected since an increase in total flow rate also leads to a decrease of residence time in the plasma discharge zone. The increase in conversion was attributed to two factors: a) increasing the flow probably directs to the CO_2 activation into a more efficient pathway through vibrational excitation, and b) the length of the arc increased with the flow rate, increasing the volume of the discharge zone. On the other hand, it was found that the H_2/CO ratio only depends on the CH_4/CO_2 ratio and not on the other parameters, such as the total inlet flow rate or peak current. Besides, the H_2/CO ratio can be controlled to produce the desired fraction of these products in the syngas for further applications. Acetylene was found as the main gaseous byproduct of the reforming reaction. The concentration and kinetics of C_2H_2 depend only on the CH_4 concentration. The apparent reaction order for the formation of C_2H_2 was determined, and it was found that increasing the partial pressure of CH_4 by a factor of 2, increases the C_2H_2 formation by approx. a factor of 8. Regarding the section on plasma-induced gas heating, two key points were found: a) the gas heating when the plasma discharge was turned on is very fast at the beginning (5 to 10 degrees per minute). However, a steady-state was achieved, and the gas temperature was increased by approx. 200 °C, and b) the CO_2/Ar mix heats faster than $\text{CH}_4/\text{CO}_2/\text{Ar}$ mix, due to the lower specific heat value of CO_2 compared to the CH_4 . In the energy section of Chapter 5, it was found that the energy efficiency increased with increasing peak current and CO_2 in the feed, as well as with decreasing total flow rate. Moreover, at high peak current (1.50 A) more than 25% of the total electrical energy fed into the system was utilized by the DRM reaction at all the total flow rates studied. At lower peak current (0.74 A), only the total flow rate of 4.7 SLPM achieved a similar percentage of electrical energy utilization. This analysis confirmed that the best operating condition for the lower peak current (0.74 A) was at a total flow rate of 4.7 SLPM for every CO_2/CH_4 ratio. The optical emission characterization of the discharge showed several active species present on the plasma. The most intense signals corresponded to the C_2 Swan bands, which are associated with hydrocarbon decomposition and which intensity decreased with increasing CO_2 concentration in the feed. Overall, the results showed that a higher concentration of CO_2 in the feed is beneficial for the reforming reaction. In the following sections of Chapter 5, the carbon byproducts of the DRM reaction were analyzed. Among the solid carbon deposits, stainless-steel particles as a result of electrode erosion were found, as well as some signals in the Raman spectrum corresponding to graphene sheets.

Finally, Chapter 6 follows up on the work developed in Chapter 5 to explore an alternative technology to improve the performance of DRM. This technology is known as plasma-catalysis. The work aimed to investigate whether or not there was a synergistic effect when combined plasma and catalyst in a single-stage plasma-catalytic reactor for DRM. Different characteristics of Ni-based catalysts were investigated, including two different catalyst supports, three different Ni loadings, pre-reduced and fresh catalyst, as well as the effect of CH₄ plasma pretreatment of the catalyst to potentially reduce the catalyst as previously reported by [81, 162]. The thermo-catalytic DRM is the conventional way to carry out the reaction due to its highly endothermic nature; however, temperatures above 700 °C are required as well as an efficient catalyst. The performance of the different catalysts in the DRM reaction was compared under thermal-catalytic conditions at 700 °C and 1 bar_{abs}. It was found that there was only a slight increase in conversion and yield when the reaction was carried out using 30% wt. than when using 15% wt. Ni catalyst. The turnover frequency showed that the absolute number of Ni active sites was higher in the 15% wt. Ni catalyst, making it a better candidate for the DRM reaction. Moreover, the Al₂O₃-supported catalyst showed higher stability over time than the SiO₂ one, which steadily lost activity during the time on stream measured (160 min) due to the weak bond between Ni and SiO₂. In the case of plasma-catalysis using the Al₂O₃-supported catalyst, a negative effect on conversion, yield and selectivity was found when increasing the Ni content from 15 to 30% wt. Additionally, a negative effect in conversion of CO₂ and CH₄, as well as yield of H₂ and CO, was found for the pre-reduced catalyst compared to the fresh catalyst, attributed to a different reaction pathway of the plasma species interacting with the catalysts. In the case of the SiO₂-supported catalysts, the plasma operation was rather unstable, causing melting and agglomeration of the catalyst in the reactor at flow rates below 4.5 SLPM. Nonetheless, compared to the Al₂O₃ catalyst, no statistical difference was found between the Ni 30% wt. fresh, the pre-reduced catalyst and the Ni 15% wt. for the conversion and yield of CO₂, CH₄ and H₂ and CO, respectively. This was also attributed to the weak bond between the inert support and the Ni. For both cases, the conversion of methane was favored over the conversion of CO₂, following thermodynamic equilibrium. The introduction of a catalytic material in the plasma reactor apparently decreased the conversion and yield of the DRM reaction. However, considering that the catalyst occupies part of the plasma volume, then the arc has access to a reduced volume for the creation of active species. This is equivalent to increase the total flow rate between 1.5 to 2 times in an empty tube experiment. Based on our previous studies presented

in Chapter 5, we found that increasing the flow rate 1.3 to 1.8 times actually decreases the conversion between 1.1 and 3 times. Hence, the introduction of the catalyst in the plasma reactor might actually be beneficial since only a decrease between 1.2 and 1.5 was measured. Temperature Programmed Oxidation showed the formation of polymeric carbon in the catalyst pre-treated with CH_4 , which also showed lower conversion of reactants and products for both supports due to the catalyst poisoning with coke and solid carbon deposition produced by the CH_x species in the plasma reactor. Additionally, a reduction of acetylene and carbon deposition was found when having a catalytic bed in the plasma zone. It was also confirmed that the interaction of the catalyst with the plasma does not affect its crystalline structure. However, it changes the surface chemistry of the catalyst, making the Ni more electronegative, i.e., the interaction with the plasma introduces more defects. The latest can potentially improve catalyst stability and activity.

7.2 Contributions to Knowledge

The numerical and experimental works presented in this thesis led to several contributions to knowledge for the two CO_2 valorization technologies studied. These contributions are:

1. *The development of working diagrams for the design and operation of BFB reactors.* The working diagrams developed serve as a tool to: a) for an existing reactor, identify the range of pressure, temperature, catalyst diameter, and total flow rate that the reactor can be operated and b) for a range of temperature or pressure, and particle size, to determine the best reactor diameter to ensure good fluidization and avoid catalyst entrainment and de-fluidization or collapse of the bed.
2. *Concentration of products showing a transient behavior when a plasma discharge was applied.* The experiments carried out in Chapter 5 show a transient behavior of the yield of CO and H_2 . This finding shows that when the reforming reaction is treated by the plasma discharge, the concentration of products changes over time, stabilizing after approx. 5 min. This behavior is more evident at lower flow rates, and it is comparable to the one shown when the reaction is carried out under thermal-catalytic conditions.
3. *The decrease in the conversion of reactants for longer plasma reforming experiments.* Usually, plasma experiments are short (some minutes) compared to catalytic experiments (some hours) since the interaction of the reactant with the active species in the plasma discharge is

instantaneous. For the longer experiments, it was found that after 20 min., even if the gas temperature in the reactor increased, the conversion and yield of reactants and products decreased due to two reasons: a) the energy given to the reaction was mostly transformed into thermal energy rather than into chemical energy and b) more solid carbon was deposited in the electrodes, making the effect of the discharge less efficient.

4. *The effect of reactant gas temperature.* It was observed that the reactant temperature did not affect the capabilities of the plasma discharge to carry out DRM. This is an unexpected result given the endothermic nature of the reaction. The explanation for this effect is that gas temperatures in the plasma zone are normally between 1000 to 3000 K, which is 2 to 6 times higher than the preheated gas temperature. Thus, giving more energy to preheat the gas only makes the process more energy deficient.
5. *The dependence of the average discharge power with gas composition and total flow rate.* Changing the composition of the gas mixture and the total inlet flow rate affected the average power of the discharge. To the best knowledge of the candidate, this is an unexpected result, and it was attributed to the differences between the resistivity of the gas mixtures and the radiative losses.
6. *The development of a single-stage RGA-spouted bed plasma-catalytic reactor for DRM.* The setup developed for the experiments in Chapter 6 to the best knowledge of the candidate is quite novel, and this specific plasma-catalytic configuration has not been previously reported.
7. *The effect of pre-reduced and fresh catalyst in the plasma-catalytic DRM.* The experiments carried out in Chapter 6 for Ni/Al₂O₃ catalyst showed that higher conversions and yields were obtained with the fresh catalyst rather than with the pre-reduced catalyst. This is an unexpected result given that only superficial oxygen is present in the pre-reduced catalyst, forming weaker bonds with the Ni, and ideally easier to remove, and hence activate the catalyst. This difference in the catalyst performance was attributed to a different reaction path between the plasma species interacting with the catalyst.
8. *The effect of different catalyst supports in the operation of the RGA.* The stability of the plasma discharge was affected by the type of support used for the catalyst. In the case of SiO₂-supported catalyst, lower flow rates led to melting and agglomeration of the catalyst inside of the reactor. However, Al₂O₃-supported catalyst showed good stability for the flow rates

reported. This difference between the catalysts was attributed to the different melting points of the supports, being higher for the Al_2O_3 .

9. *The determination of positive or negative effects in a RGA-fluidized bed reactor.* The presence of a catalytic bed in the plasma discharge leads to a negative effect regarding conversion of CO_2 and CH_4 , as well as yield of H_2 and CO . However, it also leads to a positive effect regarding product selectivity while strongly decreasing carbon deposition. Even though the reaction pathways in thermal and plasma-catalytic reactions are different, the presence of a catalyst in the plasma zone might target the production of syngas in a similar way that in the thermal-catalytic reaction in which no C_2 species are produced as a byproduct of the reaction.

7.3 Future Work

The following aspects can improve the further understanding of the work presented in this dissertation:

- Confirm the theoretical approach of working diagrams with experimental data. Using the working diagrams to design and operate a laboratory-scale BFB reactor would confirm the graphic approach and add value to the work presented in Chapter 4. Besides, further aspects of the fluidization can be studied, improving the characteristics of the working diagrams.
- Improve the capabilities of the power supply for RGA. Certain aspects regarding the performance of the reaction, such as conversion, yield, and energy efficiency, can be further improved by improving the power supply characteristics, for example, optimizing the power delivered by the power supply.
- Determine plasma discharge characteristics. A deeper Optical Emission Spectroscopy analysis could be performed to understand better certain plasma characteristics such as electron density, electron temperature, T_e , vibrational temperature, T_v , and rotational temperature T_r . These characteristics would contribute to a better understanding of the plasma discharge as well as its capabilities.
- Increase the plasma volume. Ideally, increasing the plasma volume in the reactor would lead to higher yield of syngas as well as CO_2 and CH_4 conversions. This could be made by changing the configuration of the cathode in the reactor.

- Investigate the effect of higher gas temperature in the plasma-catalytic reactor. Increasing the gas temperature in the plasma-catalytic reactor could potentially activate the catalyst completely and lead to a better synergistic effect between plasma and catalyst.
- Investigate the effect of in-situ catalyst reduction in the plasma-catalytic reactor. Better catalytic performance could be achieved if the catalyst is reduced inside of the plasma-catalytic reactor under a H₂ atmosphere, utilizing at the same way the energy provided by the plasma source.
- Investigate different catalysts for plasma driven-catalysis DRM. Boron nitride nanotubes (BNNT's) can potentially be used as catalyst support due to their high thermal resistivity, high surface area and low bulk density. The BNNT's can be coated with metal nanoparticle catalysts via pulsed laser deposition, in which only some micrograms of active metal are used, leading to high metal dispersion and possibly better catalytic performance.

Nomenclature

Parameters

ΔH_{298K}	kJ mol^{-1}	Heat of reaction
ΔG_f^θ	kJ mol^{-1}	Gibbs energy
c_p	$\text{J g}^{-1} \text{K}^{-1}$	specific heat value
d	nm	mean crystallite size
D_{pore}	nm	average pore diameter
$E(t)$	J	cumulative energy
h	mm	height of the cone electrode
$I(t)$	A	current
k		constant of reaction
LHV_i	J mol^{-1}	low heating value of species i
\dot{n}_i	mol min^{-1}	molar flow rate of species i
$P(t)$	W	instantaneous power
P_{avg}	W	time-averaged power
p_i	mol s^{-1}	partial pressure of species i
Q	L min^{-1}	volumetric flow rate
R	mm	large radius of the cone electrode

r_1	mm	inner radius of ground electrode
r_2	mm	small radius of the cone electrode
r_i	mol s ⁻¹	rate of reaction of species i
S_{BET}	m ² g ⁻¹	BET total specific surface area
S_i	%	selectivity of species i
T_e	°C / eV	electron temperature
T_h	°C	temperature of heavy species
TOF	s ⁻¹	turnover frequency
$V(t)$	V	voltage
V_{pore}	cm ³ g ⁻¹	pore volume
X_i	%	conversion of species i
Y_i	%	yield of species i
α		order of reaction / significance level
η	%	energy efficiency
θ	ms	residence time

Abbreviations

BET	Brunauer, Emmet and Teller method
BFB	Bubbling fluidized bed
BNNT's	Boron nitride nanotubes
CWVM	Cockcroft-Walton voltage multiplier
DBD	Dielectric barrier discharge

DRM	Dry reforming of methane
EC	Energy cost
EDS	Energy dispersive X-ray spectroscopy
EED	Electron energy distribution
FBR	Fixed bed reactor
FT	Fischer-Tropsch
FWHM	Full width half maximum
GA	Gliding arc
GC	Gas chromatography
GHG	Greenhouse gases
GHSV	Gas hourly space velocity
ICP-OES	Inductively coupled plasma - optical emission spectroscopy
IPC	In-plasma catalysis
MS	Mass spectroscopy
MW	Microwave discharges
NTP	Non-thermal plasmas
OES	Optical emission spectroscopy
P2G	Power to gas
PPC	Post-plasma catalysis
RC	Resistor-capacitor
RF	Radio-frequency discharges
RGA	Rotating gliding arc
RGA-SB	Rotating gliding arc - Spouted bed

SEI	Specific energy input
SEM	Scanning electron microscopy
SLPM	Standard liters per minute
TCD	Thermal conductivity detector
TCHP	Thermochemical heat pipe
TGA	Thermogravimetric analysis
TPO	Temperature programmed oxidation
TPR	Temperature programmed reduction
T_r	Rotational temperature
T_v	Vibrational temperature
XPS	X-ray photoelectron spectroscopy
XRD	X-Ray diffraction

Subscripts

AP	Spent catalyst (after contact with plasma)
CH ₄	plasma pretreatment with CH ₄ catalyst
F	Fresh catalyst
P	Reduced-passivated catalyst

Gas species

Ar	argon
C ₂ H ₂	acetylene
C ₂ H ₄	ethylene
CH ₄	methane
CO	carbon monoxide
CO ₂	carbon dioxide
H ₂	hydrogen
H ₂ O	water

References

1. Bush E, Gillett N, Watson E, et al (2019) Understanding Observed Global Climate Change. In: Bush E, Lemmen DS (eds) Canada's Changing Climate Report. Government of Canada, Ottawa, Ontario, pp 24–72
2. Canada G of (2019) Energy and Greenhouse Gas Emissions (GHGs). In: Nat. Resour. Canada. <https://www.nrcan.gc.ca/science-data/data-analysis/energy-data-analysis/energy-facts/energy-and-greenhouse-gas-emissions-ghgs/20063>. Accessed 24 Mar 2020
3. (2019) Global Emissions, Solutions Center for Climate and Energy. <https://www.c2es.org/content/international-emissions/>. Accessed 24 Mar 2020
4. Puliyalil H, Lašič Jurković D, Dasireddy VDBC, Likozar B (2018) A review of plasma-assisted catalytic conversion of gaseous carbon dioxide and methane into value-added platform chemicals and fuels. *RSC Adv* 8:27481–27508. <https://doi.org/10.1039/C8RA03146K>
5. Government of Canada (2018) Technical Backgrounder: Federal methane regulations for the upstream oil and gas sector. <https://www.canada.ca/en/environment-climate-change/news/2018/04/federal-methane-regulations-for-the-upstream-oil-and-gas-sector.html>. Accessed 24 Mar 2020
6. Razali NAM, Lee KT, Bhatia S, Mohamed AR (2012) Heterogeneous catalysts for production of chemicals using carbon dioxide as raw material: A review. *Renew Sustain Energy Rev* 16:4951–4964. <https://doi.org/10.1016/j.rser.2012.04.012>
7. Götz M, Lefebvre J, Mörs F, et al (2016) Renewable Power-to-Gas: A technological and economic review. *Renew Energy* 85:1371–1390. <https://doi.org/10.1016/j.renene.2015.07.066>
8. Québec Government (2019) Quantity of renewable natural gas to be delivered by a distributor. *Gaz Off du Quebec* 465
9. Witte J, Calbry-Muzyka A, Wieseler T, et al (2019) Demonstrating direct methanation of real biogas in a fluidised bed reactor. *Appl Energy* 240:359–371. <https://doi.org/10.1016/j.apenergy.2019.01.230>
10. Aljishi A, Veilleux G, Lalinde JAH, Kopyscinski J (2018) The effect of synthesis parameters on ordered mesoporous nickel alumina catalyst for CO₂ methanation. *Appl Catal A Gen* 549:263–272. <https://doi.org/10.1016/j.apcata.2017.10.012>

11. Hernandez Lalinde JA (2019) Investigation of CO₂ methanation over order mesoporous Ni/Al₂O₃ catalyst using a catalytic plate reactor with spatially resolved measurement capability. McGill University
12. Bogaerts A, Neyts EC (2018) Plasma Technology: An Emerging Technology for Energy Storage. *ACS Energy Lett* 3:1013–1027. <https://doi.org/10.1021/acsenerylett.8b00184>
13. Zhang H, Li XD, Zhang YQ, et al (2012) Rotating Gliding Arc Codriven by Magnetic Field and Tangential Flow. *IEEE Trans Plasma Sci* 40:3493–3498. <https://doi.org/10.1109/TPS.2012.2220984>
14. Whitehead JC (2016) Plasma–catalysis: the known knowns, the known unknowns and the unknown unknowns. *J Phys D Appl Phys* 49:243001. <https://doi.org/10.1088/0022-3727/49/24/243001>
15. Pan SY, Chiang PC, Pan W, Kim H (2018) Advances in state-of-art valorization technologies for captured CO₂ toward sustainable carbon cycle. *Crit Rev Environ Sci Technol* 48:471–534. <https://doi.org/10.1080/10643389.2018.1469943>
16. Huang C-H, Tan C-S (2014) A Review: CO₂ Utilization. *Aerosol Air Qual Res* 14:480–499. <https://doi.org/10.4209/aaqr.2013.10.0326>
17. De Falco M (2017) CO₂ Valorization Technologies. Rome, Italy
18. Olajire AA (2013) Valorization of greenhouse carbon dioxide emissions into value-added products by catalytic processes. *J CO₂ Util* 3–4:74–92. <https://doi.org/10.1016/j.jcou.2013.10.004>
19. Aresta M, Dibenedetto A, Angelini A (2013) Catalysis for the Valorization of Exhaust Carbon: from CO₂ to Chemicals, Materials, and Fuels. *Technological Use of CO₂*. *Chem Rev* 114:1709–1742. <https://doi.org/10.1021/cr4002758>
20. Snoeckx R, Bogaerts A (2017) Plasma technology – a novel solution for CO₂ conversion? *Chem Soc Rev* 46:5805–5863. <https://doi.org/10.1039/C6CS00066E>
21. Edwards JH, Maitra AM (1995) The chemistry of methane reforming with carbon dioxide and its current and potential applications. *Fuel Process Technol Process Technol* 42:269–289
22. Witte J, Settino J, Biollaz SMA, Schildhauer TJ (2018) Direct catalytic methanation of biogas – Part I: New insights into biomethane production using rate-based modelling and detailed process analysis. *Energy Convers Manag* 171:750–768. <https://doi.org/10.1016/j.enconman.2018.05.056>
23. Türks D, Mena H, Armbruster U, Martin A (2017) Methanation of CO₂ on Ni/Al₂O₃ in a Structured Fixed-Bed Reactor—A Scale-Up Study. *Catalysts* 7:152. <https://doi.org/10.3390/catal7050152>
24. Schildhauer TJ, Biollaz SMA (2016) *Synthetic Natural Gas from Coal, Dry Biomass, and Power-to-Gas Applications*. John Wiley & Sons, Inc., Hoboken, NJ, USA
25. Liu J, Shen W, Cui D, et al (2013) Syngas methanation for substitute natural gas over Ni-

- Mg/Al 2O₃ catalyst in fixed and fluidized bed reactors. *Catal Commun* 38:35–39. <https://doi.org/10.1016/j.catcom.2013.04.014>
26. Kopyscinski J (2010) Production of synthetic natural gas in a fluidized bed reactor: Understanding the hydrodynamic, mass transfer, and kinetic effects. ETH Zurich
 27. Görke O, Pfeifer P, Schubert K (2005) Highly selective methanation by the use of a microchannel reactor. *Catal Today* 110:132–139. <https://doi.org/10.1016/j.cattod.2005.09.009>
 28. Liu Z, Chu B, Zhai X, et al (2012) Total methanation of syngas to synthetic natural gas over Ni catalyst in a micro-channel reactor. *Fuel* 95:599–605. <https://doi.org/10.1016/j.fuel.2011.12.045>
 29. Kopyscinski J, Schildhauer TJ, Biollaz SMA (2010) Production of synthetic natural gas (SNG) from coal and dry biomass – A technology review from 1950 to 2009. *Fuel* 89:1763–1783. <https://doi.org/10.1016/j.fuel.2010.01.027>
 30. Grace JR (2016) Fluidized-bed catalytic reactors. In: *Multiphase Catalytic Reactors*. John Wiley & Sons, Inc., Hoboken, NJ, USA, pp 80–94
 31. Kunii D, Levenspiel O (1991) *Fluidization Engineering*. Elsevier, United States of America
 32. Geldart D (1986) *Gas Fluidization Technology*, 1st ed. John Wiley & Sons, New York
 33. Martin H (2010) M5 Heat Transfer in Fluidized Beds. In: *VDI Heat Atlas*. Springer Berlin Heidelberg, pp 1301–1309
 34. Kai T, Furusaki S (1987) Methanation of carbon dioxide and fluidization quality in a fluid bed reactor: the influence of a decrease in gas volume.pdf. *Chem Eng Sci* 42:335–339
 35. A. Abba I, R. Grace J, T. Bi H (2002) Variable-gas-density fluidized bed reactor model for catalytic processes. *Chem Eng Sci* 57:4797–4807. [https://doi.org/10.1016/S0009-2509\(02\)00289-0](https://doi.org/10.1016/S0009-2509(02)00289-0)
 36. Chung W-C, Chang M-B (2016) Review of catalysis and plasma performance on dry reforming of CH₄ and possible synergistic effects. *Renew Sustain Energy Rev* 62:13–31. <https://doi.org/10.1016/j.rser.2016.04.007>
 37. Pan KL, Chung WC, Chang MB (2014) Dry Reforming of CH₄ With CO₂ to Generate Syngas by Combined Plasma Catalysis. *IEEE Trans Plasma Sci* 42:3809–3818. <https://doi.org/10.1109/TPS.2014.2360238>
 38. Boudart M (1995) Turnover Rates in Heterogeneous Catalysis. *Chem Rev* 95:661–666
 39. Herrera-Delgado K, Maier L, Tischer S, et al (2015) Surface Reaction Kinetics of Steam- and CO₂-Reforming as Well as Oxidation of Methane over Nickel-Based Catalysts. *Catalysts* 5:871–904. <https://doi.org/10.3390/catal5020871>
 40. Nikoo MK, Amin NAS (2011) Thermodynamic analysis of carbon dioxide reforming of methane in view of solid carbon formation. *Fuel Process Technol* 92:678–691. <https://doi.org/10.1016/j.fuproc.2010.11.027>

41. Liu J-L, Wang X, Li X-S, et al (2020) CO₂ conversion, utilisation and valorisation in gliding arc plasma reactors. *J Phys D Appl Phys* 53:253001. <https://doi.org/10.1088/1361-6463/ab7c04>
42. Tu X, Whitehead JC (2014) Plasma dry reforming of methane in an atmospheric pressure AC gliding arc discharge: Co-generation of syngas and carbon nanomaterials. *Int J Hydrogen Energy* 39:9658–9669. <https://doi.org/10.1016/j.ijhydene.2014.04.073>
43. Fischer F, Tropsch H (1928) Conversion of methane into hydrogen and carbon monoxide. *Chemie* 3:39–46
44. Nakamura J, Uchijima T (1993) Methane reforming with carbon dioxide. *Shokubai* 478–484
45. Ferreira-Aparicio P, Guerrero-Ruiz A, Rodríguez-Ramos I, Rodríguez-Ramos I (1998) Comparative study at low and medium reaction temperatures of syngas production by methane reforming with carbon dioxide over silica and alumina supported catalysts. *Appl Catal A Gen* 170:177–187. [https://doi.org/10.1016/S0926-860X\(98\)00048-9](https://doi.org/10.1016/S0926-860X(98)00048-9)
46. Pakhare D, Spivey J, Zhao H, et al (2014) A review of dry (CO₂) reforming of methane over noble metal catalysts. *Chem Soc Rev* 43:7813–7837. <https://doi.org/10.1039/C3CS60395D>
47. Li Y, Wang Y, Zhang X, Mi Z (2008) Thermodynamic analysis of autothermal steam and CO₂ reforming of methane. *Int J Hydrogen Energy* 33:2507–2514. <https://doi.org/10.1016/j.ijhydene.2008.02.051>
48. Aramouni NAK, Touma JG, Tarboush BA, et al (2018) Catalyst design for dry reforming of methane: Analysis review. *Renew Sustain Energy Rev* 82:2570–2585. <https://doi.org/10.1016/j.rser.2017.09.076>
49. Ferreira-Aparicio P, Rodríguez-Ramos I, Guerrero-Ruiz A (1997) Methane interaction with silica and alumina supported metal catalysts. *Appl Catal A Gen* 148:343–356. [https://doi.org/10.1016/S0926-860X\(96\)00237-2](https://doi.org/10.1016/S0926-860X(96)00237-2)
50. Bradford MCJ, Vannice MA (1999) CO₂ reforming of CH₄. *Catal Rev - Sci Eng* 41:1–42. <https://doi.org/10.1081/CR-100101948>
51. Arora S, Prasad R (2016) An overview on dry reforming of methane: strategies to reduce carbonaceous deactivation of catalysts. *RSC Adv* 6:108668–108688. <https://doi.org/10.1039/C6RA20450C>
52. Zhang R, Xia G, Li M, et al (2015) Effect of support on the performance of Ni-based catalyst in methane dry reforming. *J Fuel Chem Technol* 43:1359–1365. [https://doi.org/10.1016/S1872-5813\(15\)30040-2](https://doi.org/10.1016/S1872-5813(15)30040-2)
53. Takayasu O, Takegahara Y, Matsuura I (1995) Thermogravimetric study in connection with the CO₂-reforming reaction of CH₄. *Energy Convers Manag* 36:597–600. [https://doi.org/10.1016/0196-8904\(95\)00076-P](https://doi.org/10.1016/0196-8904(95)00076-P)
54. Bitter JH, Seshan K, Lercher JA (1998) Mono and bifunctional pathways of CO₂/CH₄ reforming over Pt and Rh based catalysts. *J Catal.* <https://doi.org/10.1006/jcat.1998.2022>

55. Ferreira-Aparicio P, Rodríguez-Ramos I, Anderson JA, Guerrero-Ruiz A (2000) Mechanistic aspects of the dry reforming of methane over ruthenium catalysts. *Appl Catal A Gen* 202:183–196. [https://doi.org/10.1016/S0926-860X\(00\)00525-1](https://doi.org/10.1016/S0926-860X(00)00525-1)
56. Capezzuto P, Cramarossa F, Molinari E (1977) Methane and n-butane oxidation with CO₂ under radiofrequency plasmas of moderate pressures. *Rev Phys Appliquee* 12:1205–1208. <https://doi.org/10.1051/rphysap:019770012090120500>
57. Fridman A, Kennedy LA (2011) *Plasma Physics and Engineering*, 2nd editio. CRC Press, Boca Raton
58. Zhou LM, Xue B, Kogelschatz U, Eliasson B (1998) Nonequilibrium Plasma Reforming of Greenhouse Gases to Synthesis Gas. *Energy & Fuels* 12:1191–1199. <https://doi.org/10.1021/ef980044h>
59. Brock SL, Shimojo T, Suib SL, et al (2002) Application of non-thermal atmospheric pressure ac plasmas to the carbon dioxide reforming of methane. *Res Chem Intermed* 28:13–24. <https://doi.org/10.1163/156856702760129465>
60. Tu X, Gallon HJ, Whitehead JC (2013) Plasma-assisted reduction of a NiO/Al₂O₃ catalyst in atmospheric pressure H₂/Ar dielectric barrier discharge. *Catal Today* 211:120–125. <https://doi.org/10.1016/j.cattod.2013.03.024>
61. Wang Q, Yan B-H, Jin Y, Cheng Y (2009) Investigation of Dry Reforming of Methane in a Dielectric Barrier Discharge Reactor. *Plasma Chem Plasma Process* 29:217–228. <https://doi.org/10.1007/s11090-009-9173-3>
62. Tu X, Whitehead JC (2012) Plasma-catalytic dry reforming of methane in an atmospheric dielectric barrier discharge: Understanding the synergistic effect at low temperature. *Appl Catal B Environ* 125:439–448. <https://doi.org/10.1016/j.apcatb.2012.06.006>
63. Li D, Li X, Bai M, et al (2009) CO₂ reforming of CH₄ by atmospheric pressure glow discharge plasma: A high conversion ability. *Int J Hydrogen Energy* 34:308–313. <https://doi.org/10.1016/j.ijhydene.2008.10.053>
64. Cheng D-G, Zhu X, Ben Y, et al (2006) Carbon dioxide reforming of methane over Ni/Al₂O₃ treated with glow discharge plasma. *Catal Today* 115:205–210. <https://doi.org/10.1016/j.cattod.2006.02.063>
65. Aziznia A, Bozorgzadeh HR, Seyed-Matin N, et al (2012) Comparison of dry reforming of methane in low temperature hybrid plasma-catalytic corona with thermal catalytic reactor over Ni/γ-Al₂O₃. *J Nat Gas Chem* 21:466–475. [https://doi.org/10.1016/S1003-9953\(11\)60392-7](https://doi.org/10.1016/S1003-9953(11)60392-7)
66. Li M-W, Xu G-H, Tian Y-L, et al (2004) Carbon Dioxide Reforming of Methane Using DC Corona Discharge Plasma Reaction. *J Phys Chem A* 108:1687–1693. <https://doi.org/10.1021/jp037008q>
67. Seyed-Matin N, Jalili AH, Jenab MH, et al (2010) DC-Pulsed Plasma for Dry Reforming of Methane to Synthesis Gas. *Plasma Chem Plasma Process* 30:333–347. <https://doi.org/10.1007/s11090-010-9225-8>

68. Li M-W, Tian Y-L, Xu G-H (2007) Characteristics of Carbon Dioxide Reforming of Methane via Alternating Current (AC) Corona Plasma Reactions. *Energy & Fuels* 21:2335–2339. <https://doi.org/10.1021/ef070146k>
69. Tan Z, Ai P (2017) CO₂ reforming of biogas to obtain synthesis gas using non-thermal plasma. *J Energy Inst* 90:864–874. <https://doi.org/10.1016/J.JOEL.2016.08.008>
70. Pacheco J, Soria G, Valdivia R, et al (2014) Warm Plasma Reactor With Vortex Effect Enhanced Used for CH₄–CO₂ Reforming. *Ieee Trans Plasma Sci* 42:2800–2801. <https://doi.org/10.1109/TPS.2014.2337290>
71. Sreethawong T, Thakonpatthanakun P, Chavadej S (2007) Partial oxidation of methane with air for synthesis gas production in a multistage gliding arc discharge system. *Int J Hydrogen Energy* 32:1067–1079. <https://doi.org/10.1016/j.ijhydene.2006.07.013>
72. Indarto A, Choi J-W, Lee H, Song HK (2006) Effect of additive gases on methane conversion using gliding arc discharge. *Energy* 31:2986–2995. <https://doi.org/10.1016/j.energy.2005.10.034>
73. Wu A, Yan J, Zhang H, et al (2014) Study of the dry methane reforming process using a rotating gliding arc reactor. *Int J Hydrogen Energy* 39:17656–17670. <https://doi.org/10.1016/J.IJHYDENE.2014.08.036>
74. Tao X, Bai M, Li X, et al (2011) CH₄–CO₂ reforming by plasma – challenges and opportunities. *Prog Energy Combust Sci* 37:113–124. <https://doi.org/10.1016/j.pecs.2010.05.001>
75. Fridman A, Nester S, Kennedy LA, et al (1999) Gliding arc gas discharge. *Prog Energy Combust Sci* 25:211–231. [https://doi.org/10.1016/S0360-1285\(98\)00021-5](https://doi.org/10.1016/S0360-1285(98)00021-5)
76. McNall M, Coulombe S (2018) Characterization of a rotating gliding arc in argon at atmospheric pressure. *J Phys D Appl Phys* 51:445203. <https://doi.org/10.1088/1361-6463/aade44>
77. Li K, Liu J-L, Li X-S, et al (2016) Warm plasma catalytic reforming of biogas in a heat-insulated reactor: Dramatic energy efficiency and catalyst auto-reduction. *Chem Eng J* 288:671–679. <https://doi.org/10.1016/j.cej.2015.12.036>
78. Zhu F, Zhang H, Yan X, et al (2017) Plasma-catalytic reforming of CO₂-rich biogas over Ni/γ-Al₂O₃ catalysts in a rotating gliding arc reactor. *Fuel* 199:430–437. <https://doi.org/10.1016/j.fuel.2017.02.082>
79. Chun YN, Yang YC, Yoshikawa K (2009) Hydrogen generation from biogas reforming using a gliding arc plasma-catalyst reformer. *Catal Today* 148:283–289. <https://doi.org/10.1016/j.cattod.2009.09.019>
80. Lee H, Sekiguchi H (2011) Plasma–catalytic hybrid system using spouted bed with a gliding arc discharge: CH₄ reforming as a model reaction. *J Phys D Appl Phys* 44:274008. <https://doi.org/10.1088/0022-3727/44/27/274008>
81. Allah ZA, Whitehead JC (2015) Plasma-catalytic dry reforming of methane in an atmospheric pressure AC gliding arc discharge. *Catal Today* 256:76–79.

- <https://doi.org/10.1016/j.cattod.2015.03.040>
82. Pacheco J, Soria G, Pacheco M, et al (2015) Greenhouse gas treatment and H₂ production, by warm plasma reforming. *Int J Hydrogen Energy* 40:17165–17171. <https://doi.org/10.1016/j.ijhydene.2015.08.062>
 83. Neyts EC (2016) Plasma-Surface Interactions in Plasma Catalysis. *Plasma Chem Plasma Process* 36:185–212. <https://doi.org/10.1007/s11090-015-9662-5>
 84. Fridman, A.Kennedy LA (2004) *Plasma Physics and Engineering*. Taylor & Francis, United States of America
 85. Fridman A, Gutsol A, Gangoli S, et al (2008) Characteristics of Gliding Arc and Its Application in Combustion Enhancement. *J Propuls Power* 24:1216–1227. <https://doi.org/10.2514/1.24795>
 86. Hwang N, Lee J, Lee DH, Song Y-H (2012) Interactive Phenomena of a Rotating Arc and a Premixed CH₄ Flame. *Plasma Chem Plasma Process* 32:187–200. <https://doi.org/10.1007/s11090-012-9349-0>
 87. Ramakers M, Trenchev G, Heijkers S, et al (2017) Gliding Arc Plasmatron: Providing an Alternative Method for Carbon Dioxide Conversion. *ChemSusChem* 10:2642–2652. <https://doi.org/10.1002/cssc.201700589>
 88. Cleiren E, Heijkers S, Ramakers M, Bogaerts A (2017) Dry Reforming of Methane in a Gliding Arc Plasmatron: Towards a Better Understanding of the Plasma Chemistry. *ChemSusChem* 10:4025–4036. <https://doi.org/10.1002/cssc.201701274>
 89. Kim H-H, Teramoto Y, Negishi N, Ogata A (2015) A multidisciplinary approach to understand the interactions of nonthermal plasma and catalyst: A review. *Catal Today* 256:13–22. <https://doi.org/10.1016/j.cattod.2015.04.009>
 90. Wang Q, Yan B-H, Jin Y, Cheng Y (2009) Dry Reforming of Methane in a Dielectric Barrier Discharge Reactor with Ni/Al₂O₃ Catalyst: Interaction of Catalyst and Plasma. *Energy & Fuels* 23:4196–4201. <https://doi.org/10.1021/ef900286j>
 91. Tu X, Gallon HJ, Whitehead JC (2011) Electrical and spectroscopic diagnostics of a single-stage plasma-catalysis system: effect of packing with TiO₂. *J Phys D Appl Phys* 44:482003. <https://doi.org/10.1088/0022-3727/44/48/482003>
 92. Wang L, Yi Y, Wu C, et al (2017) One-Step Reforming of CO₂ and CH₄ into High-Value Liquid Chemicals and Fuels at Room Temperature by Plasma-Driven Catalysis. *Angew Chemie Int Ed* 56:13679–13683. <https://doi.org/10.1002/anie.201707131>
 93. Gallon HJ, Tu X, Whitehead JC (2012) Effects of reactor packing materials on H₂ production by CO₂ reforming of CH₄ in a dielectric barrier discharge. *Plasma Process Polym* 9:90–97. <https://doi.org/10.1002/ppap.201100130>
 94. Chen G, Georgieva V, Godfroid T, et al (2016) Plasma assisted catalytic decomposition of CO₂. *Appl Catal B Environ* 190:115–124. <https://doi.org/10.1016/j.apcatb.2016.03.009>
 95. Malik MA, Schoenbach KH, Abdel-Fattah TM, et al (2017) Low Cost Compact

- Nanosecond Pulsed Plasma System for Environmental and Biomedical Applications. *Plasma Chem Plasma Process* 37:59–76. <https://doi.org/10.1007/s11090-016-9747-9>
96. McNall M (2018) Characterization of a Rotating Gliding Arc in Argon at Atmospheric Pressure
 97. Haber J, Block JH, Delmon B (1995) Manual of methods and procedures for catalyst characterization (technical report)
 98. Yates JG (1983) Fundamentals of fluidized-bed chemical processes, 3rd ed. Butterworths Monographs in Chemical Engineering, University College, London
 99. Yang W-C (2003) Handbook of fluidization and fluid-particles Systems. Marcel Dekker, New York
 100. Kopyscinski J, Schildhauer TJ, Biollaz SMA (2011) Methanation in a fluidized bed reactor with high initial CO partial pressure: Part I—Experimental investigation of hydrodynamics, mass transfer effects, and carbon deposition. *Chem Eng Sci* 66:924–934. <https://doi.org/10.1016/j.ces.2010.11.042>
 101. Kopyscinski J, Schildhauer TJ, Biollaz SMA (2011) Fluidized-Bed Methanation: Interaction between Kinetics and Mass Transfer. *Ind Eng Chem Res* 50:2781–2790. <https://doi.org/10.1021/ie100629k>
 102. Kopyscinski J, Schildhauer TJ, Biollaz SMA (2009) Employing Catalyst Fluidization to Enable Carbon Management in the Synthetic Natural Gas Production from Biomass. *Chem Eng Technol* 32:343–347. <https://doi.org/10.1002/ceat.200800413>
 103. Rauch R, Kiennemann A, Sauciuc A (2013) Fischer-Tropsch Synthesis to Biofuels (BtL Process). In: *The Role of Catalysis for the Sustainable Production of Bio-fuels and Bio-chemicals*. Elsevier, pp 397–443
 104. Zhang HL, Degrève J, Dewil R, Baeyens J (2015) Operation Diagram of Circulating Fluidized Beds (CFBs). *Procedia Eng* 102:1092–1103. <https://doi.org/10.1016/j.proeng.2015.01.232>
 105. Shaul S, Rabinovich E, Kalman H (2012) Generalized flow regime diagram of fluidized beds based on the height to bed diameter ratio. *Powder Technol* 228:264–271. <https://doi.org/10.1016/j.powtec.2012.05.029>
 106. Bi HT, Grace JR (1995) Flow Regime Diagrams for Gas-Solid Fluidization and Upward Transport. *Int J Multiph Flow* 21:1229–1236
 107. Mahmoudi S, Chan CW, Brems A, et al (2012) Solids flow diagram of a CFB riser using Geldart B-type powders. *Particuology* 10:51–61. <https://doi.org/10.1016/j.partic.2011.09.002>
 108. Rabinovich E, Kalman H (2011) Flow regime diagram for vertical pneumatic conveying and fluidized bed systems. *Powder Technol* 207:119–133. <https://doi.org/10.1016/j.powtec.2010.10.017>
 109. Grace JR (1986) Contacting modes and behaviour classification of gas-solid and other

- two-phase suspensions. *Can J Chem Eng* 64:353–363.
<https://doi.org/10.1002/cjce.5450640301>
110. Takeuchi H, Hiramata T, Biswas J, Leung LS (1986) A Quantitative Definition and Flow Regime Diagram for Fast Fluidization. *Powder Technol* 47:195–199
 111. Ghaib K, Nitz K, Ben-Fares F-Z (2016) Chemical Methanation of CO₂: A Review. *ChemBioEng Rev* 3:266–275. <https://doi.org/10.1002/cben.201600022>
 112. Mebrahtu C, Krebs F, Abate S, et al (2019) CO₂ Methanation: Principles and Challenges. In: *Studies in Surface Science and Catalysis*. Elsevier Inc., pp 85–103
 113. Ghaib K, Nitz K, Ben-Fares F-Z (2016) Chemical Methanation of CO₂: A Review. *ChemBioEng Rev* 3:266–275. <https://doi.org/10.1002/cben.201600022>
 114. Ghaib K, Ben-Fares F-Z (2018) Power-to-Methane: A state-of-the-art review. *Renew Sustain Energy Rev* 81:433–446. <https://doi.org/10.1016/j.rser.2017.08.004>
 115. Haider A, Levenspiel O (1989) Drag coefficient and terminal velocity of spherical and nonspherical particles. *Powder Technol* 58:63–70. [https://doi.org/10.1016/0032-5910\(89\)80008-7](https://doi.org/10.1016/0032-5910(89)80008-7)
 116. Li H, Tan Y, Ditaranto M, et al (2017) Capturing CO₂ from Biogas Plants. *Energy Procedia* 114:6030–6035. <https://doi.org/10.1016/j.egypro.2017.03.1738>
 117. Gao J, Wang Y, Ping Y, et al (2012) A thermodynamic analysis of methanation reactions of carbon oxides for the production of synthetic natural gas. *RSC Adv* 2:2358. <https://doi.org/10.1039/c2ra00632d>
 118. Witte J, Kunz A, Biollaz SMA, Schildhauer TJ (2018) Direct catalytic methanation of biogas – Part II: Techno-economic process assessment and feasibility reflections. *Energy Convers Manag* 178:26–43. <https://doi.org/10.1016/j.enconman.2018.09.079>
 119. Maqueo PDG, Coulombe S, Bergthorson JM (2019) Energy efficiency of a nanosecond repetitively pulsed discharge for methane reforming. *J Phys D Appl Phys* 52:.. <https://doi.org/10.1088/1361-6463/ab199b>
 120. (2011) North American Power Plant Air Emissions. Montreal, Quebec, Canada
 121. NASA: Global climate change (2018) Climate change: How do we know? <https://climate.nasa.gov/evidence/>. Accessed 28 Jun 2018
 122. National Academy of Sciences (2014) Climate Change: Evidence and Causes. National Academies Press, Washington, D.C.
 123. Lavoie J-M (2014) Review on dry reforming of methane, a potentially more environmentally-friendly approach to the increasing natural gas exploitation. *Front Chem* 2:81. <https://doi.org/10.3389/fchem.2014.00081>
 124. Olsbye U, Wurzel T, Mleczko L (1997) Kinetic and Reaction Engineering Studies of Dry Reforming of Methane over a Ni/La/Al₂O₃ Catalyst. *Ind Eng Chem Res* 35:5180–5188. <https://doi.org/10.1021/ie9702461>

125. Liu J-L, Park H-W, Chung W-J, Park D-W (2016) High-Efficient Conversion of CO₂ in AC-Pulsed Tornado Gliding Arc Plasma. *Plasma Chem Plasma Process* 36:437–449. <https://doi.org/10.1007/s11090-015-9649-2>
126. Chen Q, Yang X, Sun J, et al (2017) Pyrolysis and Oxidation of Methane in a RF Plasma Reactor. *Plasma Chem Plasma Process* 37:1551–1571. <https://doi.org/10.1007/s11090-017-9844-4>
127. Zhang H, Du C, Wu A, et al (2014) Rotating gliding arc assisted methane decomposition in nitrogen for hydrogen production. *Int J Hydrogen Energy* 39:12620–12635. <https://doi.org/10.1016/J.IJHYDENE.2014.06.047>
128. Chen H, Lee H, Chen S, et al (2008) Review of plasma catalysis on hydrocarbon reforming for hydrogen production—Interaction, integration, and prospects. *Appl Catal B Environ* 85:1–9. <https://doi.org/10.1016/j.apcatb.2008.06.021>
129. Zhang H, Li L, Li X, et al (2018) Warm plasma activation of CO₂ in a rotating gliding arc discharge reactor. *J CO₂ Util* 27:472–479. <https://doi.org/10.1016/J.JCOU.2018.08.020>
130. Lesueur H, Czernichowski A, Chapelle J (1994) Electrically assisted partial oxidation of methane. *Int J Hydrogen Energy* 19:139–144. [https://doi.org/10.1016/0360-3199\(94\)90118-X](https://doi.org/10.1016/0360-3199(94)90118-X)
131. Bo Z, Yan J, Li X, et al (2008) Plasma assisted dry methane reforming using gliding arc gas discharge: Effect of feed gases proportion. *Int J Hydrogen Energy* 33:5545–5553. <https://doi.org/10.1016/j.ijhydene.2008.05.101>
132. Lu N, Sun D, Xia Y, et al (2018) Dry reforming of CH₄-CO₂ in AC rotating gliding arc discharge: Effect of electrode structure and gas parameters. *Int J Hydrogen Energy* 43:13098–13109. <https://doi.org/10.1016/J.IJHYDENE.2018.05.053>
133. Istadi, Amin NAS (2006) Co-generation of synthesis gas and C₂+ hydrocarbons from methane and carbon dioxide in a hybrid catalytic-plasma reactor: A review. *Fuel* 85:577–592. <https://doi.org/10.1016/j.fuel.2005.09.002>
134. Bogaerts A, Berthelot A, Heijkers S, et al (2017) CO₂ conversion by plasma technology: insights from modeling the plasma chemistry and plasma reactor design. *Plasma Sources Sci Technol* 26:
135. Czernichowski A (2001) Glidarc Assisted Preparation of the Synthesis Gas from Natural and Waste Hydrocarbons Gases. *Oil Gas Sci Technol* 56:181–198. <https://doi.org/10.2516/ogst:2001018>
136. Liu C-J, Xu G-H, Wang T (1999) Non-thermal plasma approaches in CO₂ utilization. *Fuel Process Technol* 58:119–134
137. Sun SR, Wang HX, Mei DH, et al (2017) CO₂ conversion in a gliding arc plasma: Performance improvement based on chemical reaction modeling. *J CO₂ Util* 17:220–234. <https://doi.org/10.1016/j.jcou.2016.12.009>
138. Sudhakaran MSP, Trinh HQ, Karuppiyah J, et al (2017) Plasma Catalytic Removal of p-Xylene from Air Stream Using γ -Al₂O₃ Supported Manganese Catalyst. *Top Catal*

- 60:944–954. <https://doi.org/10.1007/s11244-017-0759-3>
139. Hammer T, Kappes T, Baldauf M (2004) Plasma catalytic hybrid processes: gas discharge initiation and plasma activation of catalytic processes. *Catal Today* 89:5–14. <https://doi.org/10.1016/j.cattod.2003.11.001>
 140. Eliasson B, Liu C-J, Kogelschatz U, et al (2000) Direct Conversion of Methane and Carbon Dioxide to Higher Hydrocarbons Using Catalytic Dielectric-Barrier Discharges with Zeolites. *Ind Eng Chem Res* 39:.. <https://doi.org/10.1021/ie990804r>
 141. Ghorbanzadeh AM, Lotfalipour R, Rezaei S (2009) Carbon dioxide reforming of methane at near room temperature in low energy pulsed plasma. *Int J Hydrogen Energy* 34:293–298. <https://doi.org/10.1016/j.ijhydene.2008.10.056>
 142. Scapinello M, Martini LM, Dilecce G, Tosi P (2016) Conversion of CH₄ / CO₂ by a nanosecond repetitively pulsed discharge. *J Phys D Appl Phys* 49:.. <https://doi.org/10.1088/0022-3727/49/7/075602>
 143. Kraus M, Egli W, Haffner K, et al (2002) Investigation of mechanistic aspects of the catalytic CO₂ reforming of methane in a dielectric-barrier discharge using optical emission spectroscopy and kinetic modeling. *Phys Chem Chem Phys* 4:668–675. <https://doi.org/10.1039/b108040g>
 144. Ray D, Manoj P, Reddy K, et al (2017) Ni-Mn/ γ -Al₂O₃ assisted plasma dry reforming of methane. *Catal Today* 309:212–218. <https://doi.org/10.1016/j.cattod.2017.07.003>
 145. Ray D, Subrahmanyam C (2016) CO₂ decomposition in a packed DBD plasma reactor : influence of packing materials. *RSC Adv* 6:39492–39499. <https://doi.org/10.1039/C5RA27085E>
 146. Fazekas P, Keszler AM, Bódis E, et al (2015) Optical emission spectra analysis of thermal plasma treatment of poly(vinyl chloride). *Open Chem* 13:549–556. <https://doi.org/10.1515/chem-2015-0069>
 147. Hodkiewicz J (2010) *Characterizing Carbon Materials with Raman Spectroscopy*. Madison, WI, USA
 148. Kameshima S, Tamura K, Ishibashi Y, Nozaki T (2015) Pulsed dry methane reforming in plasma-enhanced catalytic reaction. *Catal Today* 256:67–75. <https://doi.org/10.1016/j.cattod.2015.05.011>
 149. Wang H, Han J, Bo Z, et al (2019) Non-thermal plasma enhanced dry reforming of CH₄ with CO₂ over activated carbon supported Ni catalysts. *Mol Catal* 475:110486. <https://doi.org/10.1016/j.mcat.2019.110486>
 150. Gallon HJ (2010) *Dry Reforming of Methane Using Non-Thermal Plasma-Catalysis*. The University of Manchester
 151. Wang Q, Cheng Y, Jin Y (2009) Dry reforming of methane in an atmospheric pressure plasma fluidized bed with Ni/ γ -Al₂O₃ catalyst. *Catal Today* 148:275–282. <https://doi.org/10.1016/j.cattod.2009.08.008>

152. Heintze M, Pietruszka B (2004) Plasma catalytic conversion of methane into syngas: the combined effect of discharge activation and catalysis. *Catal Today* 89:21–25. <https://doi.org/10.1016/j.cattod.2003.11.006>
153. Kim J, Go DB, Hicks JC (2017) Synergistic effects of plasma–catalyst interactions for CH₄ activation. *Phys Chem Chem Phys* 19:13010–13021. <https://doi.org/10.1039/C7CP01322A>
154. Mei D, Ashford B, He Y-L, Tu X (2017) Plasma-catalytic reforming of biogas over supported Ni catalysts in a dielectric barrier discharge reactor: Effect of catalyst supports. *Plasma Process Polym* 14:1600076. <https://doi.org/10.1002/ppap.201600076>
155. Schmidt-Szalowski K, Krawczyk K, Mlotek M (2007) Catalytic effects of metals on the conversion of methane in gliding discharges. *Plasma Process Polym* 4:728–736. <https://doi.org/10.1002/ppap.200700052>
156. Młotek M, Sentek J, Krawczyk K, Schmidt-Szałowski K (2009) The hybrid plasma–catalytic process for non-oxidative methane coupling to ethylene and ethane. *Appl Catal A Gen* 366:232–241. <https://doi.org/10.1016/j.apcata.2009.06.043>
157. Fridman, A.; Skop, H.; Savaliev, A.; Nester, S.; Kennedy L (1997) Nonequilibrium gliding arc in fluidized bed. 802–806
158. Gupta CK, Sathiyamoorthy D (1999) *Fluid bed Technology in Materials Processing*. CRC Press LLC
159. Du C, Qiu R, Ruan J (2018) *Plasma Fluidized Bed*. Springer Singapore, Singapore
160. Martin-del-Campo J, Coulombe S, Kopyscinski J (2020) Influence of Operating Parameters on Plasma-Assisted Dry Reforming of Methane in a Rotating Gliding Arc Reactor. *Plasma Chem Plasma Process* 40:857–881. <https://doi.org/10.1007/s11090-020-10074-2>
161. Bradford MCJ, Vannice MA (1996) Catalytic reforming of methane with carbon dioxide over nickel catalysts II. Reaction kinetics. *Appl Catal A Gen* 142:97–122. [https://doi.org/10.1016/0926-860X\(96\)00066-X](https://doi.org/10.1016/0926-860X(96)00066-X)
162. Gallon HJ, Tu X, Twigg M V., Whitehead JC (2011) Plasma-assisted methane reduction of a NiO catalyst—Low temperature activation of methane and formation of carbon nanofibres. *Appl Catal B Environ* 106:616–620. <https://doi.org/10.1016/j.apcatb.2011.06.023>
163. Chung W-C, Chang M-B (2016) Dry reforming of methane by combined spark discharge with a ferroelectric. *Energy Convers Manag* 124:305–314. <https://doi.org/10.1016/j.enconman.2016.07.023>
164. Liu J-L, Li Z, Liu J-H, et al (2019) Warm-plasma catalytic reduction of CO₂ with CH₄. *Catal Today* 330:54–60. <https://doi.org/10.1016/j.cattod.2018.05.046>
165. Zhu F, Zhang H, Yan X, et al (2017) Plasma-catalytic reforming of CO₂-rich biogas over Ni/γ-Al₂O₃ catalysts in a rotating gliding arc reactor. *Fuel* 199:430–437. <https://doi.org/10.1016/j.fuel.2017.02.082>

166. Zhu X, Huo PP, Zhang YP, Liu CJ (2006) Characterization of argon glow discharge plasma reduced Pt/Al₂O₃ Catalyst. *Ind Eng Chem Res* 45:8604–8609. <https://doi.org/10.1021/ie060735y>
167. Nesbitt HW, Legrand D, Bancroft GM (2000) Interpretation of Ni2p XPS spectra of Ni conductors and Ni insulators. *Phys Chem Miner* 27:357–366. <https://doi.org/10.1007/s002690050265>
168. Sone BT, Fuku XG, Maaza M (2016) Physical & electrochemical properties of green synthesized bunsenite NiO nanoparticles via *Callistemon Viminalis*' extracts. *Int J Electrochem Sci* 11:8204–8220. <https://doi.org/10.20964/2016.10.17>
169. Dubey P, Kaurav N, Devan RS, et al (2018) The effect of stoichiometry on the structural, thermal and electronic properties of thermally decomposed nickel oxide. *RSC Adv* 8:5882–5890. <https://doi.org/10.1039/c8ra00157j>
170. Sugiyama K, Anan G, Shimada T, et al (1999) Catalytic ability of plasma heat-treated metal oxides on vapor-phase Beckmann rearrangement. *Surf Coatings Technol* 112:76–79. [https://doi.org/10.1016/S0257-8972\(98\)00783-X](https://doi.org/10.1016/S0257-8972(98)00783-X)
171. Yu KL, Liu CJ, Zhang YP, et al (2004) The preparation and characterization of highly dispersed PdO over alumina for low-temperature combustion of methane. *Plasma Chem. Plasma Process.* 24:393–403